Multiplexed biochemical imaging reveals the extent and complexity of non-genetic heterogeneity in DNA damage-induced caspase dynamics.

Maximilian Werner Fries

King's College

University of Cambridge

February 2018

This dissertation is submitted for the degree of Doctor of Philosophy.

Summary of the dissertation to obtain a Doctor of Philosophy

Maximilian Werner Fries | King's College | University of Cambridge | February 2018

Title | **Multiplexed biochemical imaging reveals the extent and complexity of non-genetic heterogeneity in DNA damage-induced caspase dynamics.**

Summary | Genetically identical cells show a heterogeneous response to a multitude of signals such as growth factors and DNA damage. While this heterogeneity has been shown to be a major determinant of treatment success in several diseases including cancer, little is known about how differences in biochemical signalling networks underlie such heterogeneity.

State-of-the-art methodologies to study biochemical networks are often invasive and enable to quantify biochemical events only on cell populations or at a single point in time for a single cell, and therefore, cannot adequately quantify the fast, asynchronous and heterogeneous responses. In order to address these limitations, we have developed a unique sensing platform based on fluorescence lifetime imaging microscopy (FLIM) capable to multiplex at least three biosensors by utilizing Förster Resonance Energy Transfer (FRET) efficiently.

After an overall introduction in Chapter 1, I describe the rational design and characterization of novel FRET pairs aiming to utilize the visible spectrum efficiently in combination with FLIM in Chapter 2. We combined blue, green and red donor fluorescent proteins that are excited at the same wavelength (840 nm for two-photon excitation) with genetically encoded quenchers, i.e. non-fluorescent chromoproteins as acceptors. This sensing platform enables the simultaneous detection of three biochemical reactions within single living cells providing new opportunities to characterize and understand non-genetic heterogeneity.

In Chapter 3, I will demonstrate the first application of this novel platform by studying the activity of three key enzymes in DNA damage-induced cell death, caspase-2, -3, and -9. We confirm the heterogeneous nature of Cisplatin-induced cell death in genetically identical cells but reveal the existence of at least three subpopulations of cells characterized by distinct caspase dynamics. By combining biochemical and morphological information we infer the existence of different biochemical network topologies that are associated with alternative death phenotypes each cell adopts, such as apoptosis and programmed necrosis.

Finally, deconvolution of cellular populations and direct measurement of a three-node caspase network - formerly impossible - permitted us to design perturbations of cell fate choices utilizing clinically relevant inhibitors. These perturbations resulted in changes in cell fate in response to Cisplatin, a clinically desirable outcome that suggests new avenues for combinatorial drugging and a new strategy to reveal cancer vulnerabilities that may be otherwise confounded by typical genetic and non-genetic heterogeneity.

To Anna and Jonathan

Declaration

I hereby declare that this dissertation is the result of my own work and includes nothing which is the outcome of work done in collaboration except where specifically indicated in the text and figure legends. Due to the collaborative nature of this work, the first person plural (“we”) is used throughout this dissertation.

This dissertation is not substantially the same as any that I have submitted, or, is being concurrently submitted for a degree or diploma or other qualification at the University of Cambridge or any other University or similar institution. I further state that no substantial part of my dissertation has already been submitted, or, is being concurrently submitted for any such degree, diploma or other qualification at the University of Cambridge or any other University or similar institution.

I further confirm that this dissertation does not to exceed 60,000 words excluding figures, tables, appendices and bibliography as set by the Degree Committee for Clinical Medicine and Clinical Veterinary Medicine.

Maximilian Werner Fries

February 2018

Acknowledgements

This work would have been impossible without the support and contribution of many. First of all, I would like to thank Dr Alessandro Esposito for his outstanding day-to-day supervision and support. He was the reason I came to Cambridge in the first place, a decision I never regretted. Ale, thank you for not only for being the best supervisor I could have wished for, but, more importantly, for becoming a good friend.

I would like to thank Professor Ashok Venkitaraman for his guidance throughout this project. I am immensely grateful for the myriad of opportunities for professional and personal development both Ashok and Alessandro provided.

Dr Kalina Haas has been a crucial part of this project and I would like to thank her for her key contribution to data analyses, great discussions and for teaching me much about Matlab.

I am also deeply grateful to present and past members of the group, Emma Richardson, Callum Campbell, Dr David Perera, Dr Siddharth De, Pablo Oriol Valls, Bryn Hardwick, Meredith Roberts-Thomson, Dr Suzan Ber-Esposito and Dr Marina Popleteeva for contributing to this work in many different ways. Working with you was a huge privilege.

Finally, the exceptional financial support by the Gates Cambridge Trust not only enabled me to study in Cambridge in the first place but also to intermit my studies to become a father for which I owe the Trust my profoundest gratitude.

Maximilian Werner Fries

February 2018

Summary

Genetically identical cells show a heterogeneous response to a multitude of signals such as growth factors and DNA damage. While this heterogeneity has been shown to be a major determinant of treatment success in several diseases including cancer, little is known about how differences in biochemical signalling networks underlie such heterogeneity.

State-of-the-art methodologies to study biochemical networks are often invasive and enable to quantify biochemical events only on cell populations or at a single point in time for a single cell, and therefore, cannot adequately quantify the fast, asynchronous and heterogeneous responses. In order to address these limitations, we have developed a unique sensing platform based on fluorescence lifetime imaging microscopy (FLIM) capable to multiplex at least three biosensors by utilizing Förster Resonance Energy Transfer (FRET) efficiently.

After an overall introduction in Chapter 1, I describe the rational design and characterization of novel FRET pairs aiming to utilize the visible spectrum efficiently in combination with FLIM in Chapter 2. We combined blue, green and red donor fluorescent proteins that are excited at the same wavelength (840 nm for two-photon excitation) with genetically encoded quenchers, i.e. non-fluorescent chromoproteins as acceptors. This sensing platform enables the simultaneous detection of three biochemical reactions within single living cells providing new opportunities to characterize and understand non-genetic heterogeneity.

In Chapter 3, I will demonstrate the first application of this novel platform by studying the activity of three key enzymes in DNA damage-induced cell death, caspase-2, -3, and -9. We confirm the heterogeneous nature of Cisplatin-induced cell death in genetically identical cells but reveal the existence of at least three subpopulations of cells characterized by distinct caspase dynamics. By combining biochemical and morphological information we infer the existence of different biochemical network topologies that are associated with alternative death phenotypes each cell adopts, such as apoptosis and programmed necrosis.

Finally, deconvolution of cellular populations and direct measurement of a three-node caspase network - formerly impossible - permitted us to design perturbations of cell fate choices utilizing clinically relevant inhibitors. These perturbations resulted in changes in cell fate in response to Cisplatin, a clinically desirable outcome that suggests new avenues for combinatorial drugging and a new strategy to reveal cancer vulnerabilities that may be otherwise confounded by typical genetic and non-genetic heterogeneity.

Contents

List of Figures

List of Tables

Abbreviations frequently used in this work

1PE	One-photon excitation
2PE	Two-photon excitation
B/C/G/Y/R FP	Blue/Cyan/Green/Yellow/Red Fluorescent Protein
CX, cX	Caspase-X
DDR	DNA-Damage Response
DNA	Desoxyribonucleic acid
FLIM	Fluorescence Lifetime Imaging Microscopy
FRET	Foerster Resonance Energy Transfer
iCX	Caspase-X inhibitor
PCR	Polymerase Chain Reaction
REA	Relative enzymatic activity
siRNA	small-interfering ribonucleic acid
STS	Staurosporine
UCL	Uncleavable

Chapter 1 Overall introduction | Studying biochemistry in single living cells

1.1 Dynamic signalling networks determine cell fate at the single-cell level

Biochemical networks determine the fate of a cell by regulating cellular responses to internal and external signals. Most networks process more than one signal that encodes for different cellular outputs. Different signals may be distinguished by various, non-mutually exclusive mechanisms, such as a change in the abundance of network components, their activity, post-translational modifications and subcellular location. Importantly, those mechanisms are rarely static but change dynamically over time (Kholodenko et al., 2010; Purvis and Lahav, 2013)

Experimental investigation of network dynamics suffers, however, from significantly underappreciated issues. Methods such as genomics, transcriptomics, proteomics or metabolomics allow the simultaneous characterization of tens of thousands of biomolecules enabling the enumeration of most of the network components; however, these methods are intrinsically invasive requiring cell fixation or extraction. Although single-cell 'omics' approaches are becoming feasible, it is very unlikely that such methodologies will be ever expanded to single-cell live measurements. Therefore, causality between phenotypic cell fate changes and biochemical networks over time can be only inferred from time snapshots of networks measured on single cells at best, but more routinely on ensemble measurements.

Population-based studies have provided and will still provide invaluable insights into network topology (how individual genes or gene products interact with each other) and dynamics. For example, by demonstrating how differences in the dynamics of the same network lead to different cell fates (Santos et al., 2007). Santos *et al*. used a combination of quantitative Western Blot and siRNA-mediated perturbation of the RAF/MEK(MAPKK1)/ERK(MAPK1)-

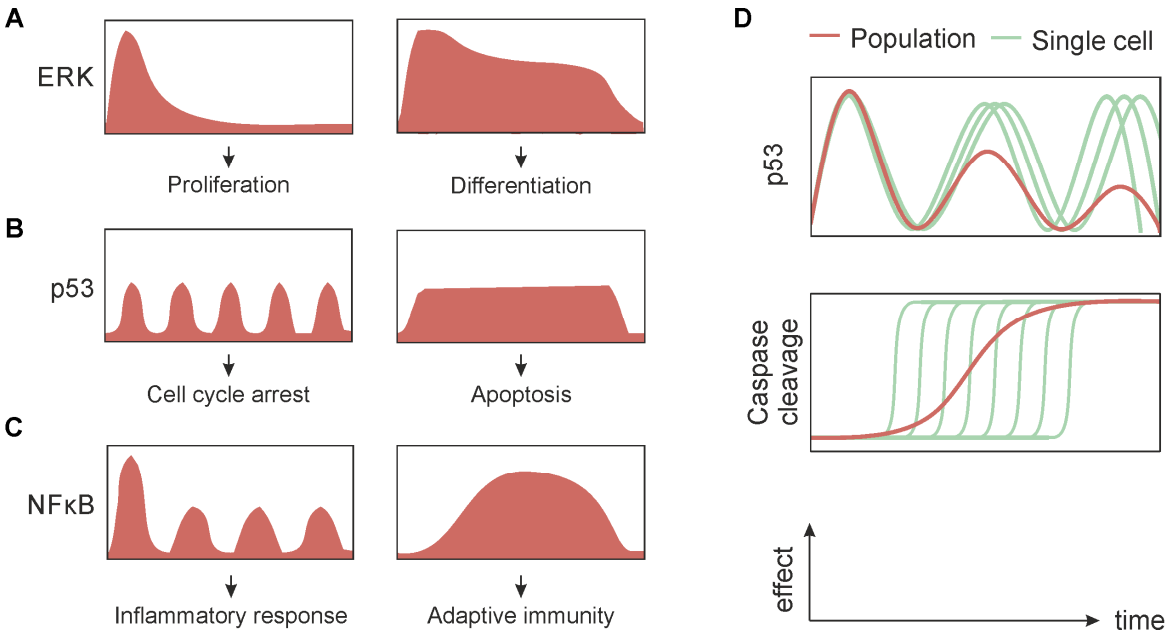

Figure 1.1 **– Signalling dynamics determine cell fate at a single-cell level.**

A, B, C: Dynamics of ERK, p53 and NFκB determine cell fate. D: Heterogeneity in single-cell responses results in misinterpretation of real kinetics if studied on a population average. Adapted from Purvis et. al, 2013.

signalling network to show that transient activation of ERK induced by Epidermal Growth Factor (EGF) leads to proliferation, while sustained activation induced by Neuronal Growth Factor (NGF) leads to differentiation (Santos et al., 2007; Fig. 1.1A). Using a computational approach called Modular Response Analysis (MRA), Santos and colleagues were able to determine the direction and strength of signalling in the MAPK (Mitogen Activated Protein Kinase) signalling three-nodes (RAF, MEK and ERK) network and use the topological information so obtained to engineer cell fate with the use of small molecule inhibitors. In fact, using a Protein Kinase C inhibitor that does not target MAPK signalling directly, but interferes with one of the feedback loops within the MAPK pathway, Santos and colleagues could rationally convert the transient EGF-induced MAPK response to a sustained NGF-like response and convert the pro-proliferative EGF effect into EGF-induced differentiation. This demonstrates how the knowledge of network dynamics can help design perturbations to change cell fates. However, this otherwise powerful approach was unable to assess the cell-to-cell heterogeneity of a response, which may mask asynchronous and subtle signalling events.

The effect of such heterogeneity on the study of network dynamics is best exemplified with the p53 dynamics in response to DNA damage (Lahav et al., 2004). Using fluorescence imaging

Lahav *et. al.* observed that the p53 levels oscillate after γ-irradiation and that the pulse frequency determines cell fate (Fig. 1.1B). In each single cell, the pulses have a fixed height and duration and are undampened over time. In contrast, measuring p53 levels by Western Blot led Bar-Or *et al.* to the conclusion that such pulses a dampened, because on a single-cell level later pulses were increasingly out of phase, leading to a decrease of the signal in average (Lev Bar-Or et al., 2000; Fig. 1.1D, top). Similarly, time-lapse imaging revealed that caspase-3 is activated in a fast, switch-like fashion, and not gradually as judged by Western Blot on an asynchronous population (Tyas et al., 2000; Fig. 1.1D, bottom). Using fluorescence microscopy, other processes have been found to exhibit heterogeneous network dynamics including the immune-signalling of NFkB (Nuclear Factor κB); Tay et al., 2010; Fig. 1.1C) as well as the EGF receptor signalling (Shankaran et al., 2009).

Finally, Ryu *et al.* have directly addressed the single-cell heterogeneity that Santos *et al.* were unable to address in their seminal work discussed above (Ryu et al., 2015; Santos et al., 2007). Using the same system as Santos *et al.* in which EGF- and NGF-dependent dynamics determine cell fate, but measuring ERK dynamics at single-cell level using a FRET biosensor, they showed that the ERK response to EGF/NGF is highly heterogeneous between cells, undetectable by Santos' method. Furthermore, refinement of Santos' original model using single-cell data allowed to accurately predict that the delivery of multiple EGF pulses should lead to a change in cell fate to differentiation, in the absence of any genetic of chemical perturbation, showing that frequency of growth factor stimulation, and not only the identity can remodel pathways. While this crucial finding could have wide implications for the study of network dynamics, it was only enabled with the prior knowledge of the existence of differential feedback loops described by Santos (Santos et al., 2007), because only one network component, ERK, could be measured with this approach. The inability to combine single-cell measurements with the read-out of several network nodes is a central impediment to fully grasp the complexity of cellular networks, from which all studies discussed above have suffered so far.

Importantly, non-genetic as well as genetic heterogeneity in cellular signalling has pronounced consequences in human disease, where it, for example, determines resistance to chemotherapeutic drugs in cancer treatment affecting patient survival (Caiado et al., 2016; for a more detailed introduction to heterogeneity in cancer also see Chapter 2). Moreover, it has been suggested that the failure to sufficiently incorporate not only network topology but also dynamics at the single-cell level into the models to predict targets for development of new drugs has made them unsuccessful (Huang, 2013; Jørgensen and Linding, 2010; Pawson and

Linding, 2008). Thus, Pawson and Linding coin the term “Network Medicine” to describe a novel approach to treating diseases, i.e. by targeting network dynamics, for example by using a larger number of small perturbations in contrast to targeting one of few central network nodes. However, the degree of quantitative, single-cell information required for these predictions, can not be obtained using current single-cell techniques, as they are often limited to monitor one or two biochemical reactions at a time.

To overcome this limitation, we set out to redesign quantitative imaging assays from their foundations with the long-term aim to convert a power technique such MRA described by Santos *et. al.*, i.e. measurement of multiple events and targeted perturbation to quantify their dynamics, into a single-cell assay capable to resolve the heterogeneity in network topologies and cell fate choices, or in other words, to perform what we call “Single-Cell Biochemistry”.

1.2 Single-Cell Biochemistry allows the study of heterogeneity in dynamic networks

The Single-Cell Biochemistry platform combines targeted perturbation of signalling nodes with the simultaneous sensing of at least three network nodes in single living cells using multiplexed FRET sensors that are read-out by a fast and highly efficient spectrally-resolved fluorescence-lifetime imaging (FLIM) setup and in-house developed analysis software (Fig. 1.2).

In Chapter 2 of this dissertation, I describe the rational design of the FRET pairs for three-colour imaging by testing and optimizing a large number of fluorescent protein pairs.

In Chapter 3, I show how those novel FRET pairs can be used to monitor the activity of three key caspases (caspase-2, 3, and -9) in the cell death network of the human cervical cancer HeLa cell line in response to the DNA damaging agent Cisplatin.

Importantly, the novel FLIM hardware and software developed within the group permitted us to minimize acquisition times and increase dynamic range. These capabilities were exploited to measure hundreds of cells in live-cell imaging for 16 hours over 13 different fields of view at the comparatively high temporal resolution of 15 min. Utilizing a very efficient optical design and detection system, we were able to minimize phototoxicity.

I will show that this approach allows us to study the order of caspase activation and their true, single-cell kinetics, establishing an so far undescribed role of caspase-9 activity downstream

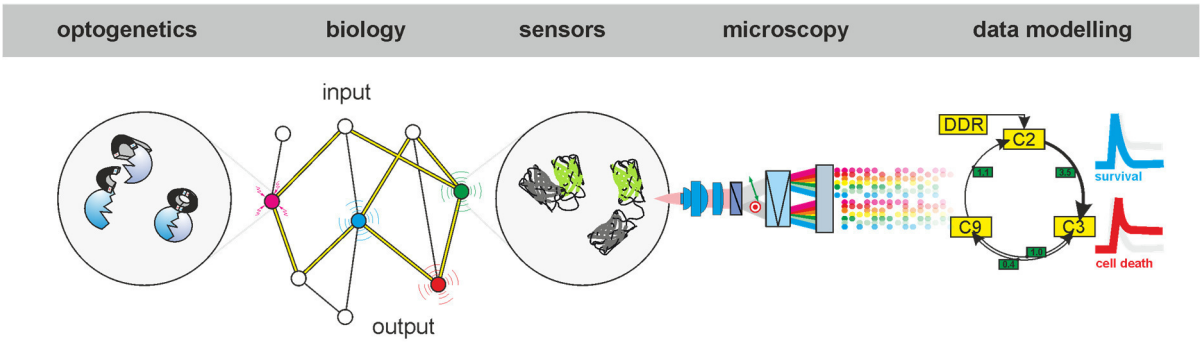

Figure 1.2 **– Concept of Single-Cell Biochemistry**

A chosen biological network consisting of multiple network nodes is probed using an array of FRET-based biosensors that are read-out using a novel fast and high-efficient fluorescence-lifetime imaging platform and in-house developed data analysis and modelling. To achieve fully controllable and single-cell specific perturbation, light-controlled optogenetics tools are being developed. Adapted from A. Esposito.

of caspase-2 and -3 activation. I will further show that the presence or absence of caspase-9 activation characterizes two distinct cell populations, with the absence of caspase-9 resulting in a delay in cell death. Furthermore, Cisplatin-treated cells not only die from apoptosis but also a necrotic form of cell death, adding another level of non-genetic heterogeneity. The death phenotype is correlated with the time of cell death, suggesting a link between biochemical as well as phenotypic observations. Using inhibitors to directly perturb caspase activity, this link is further investigated, showing that perturbation of any caspase prevents the efficient execution of apoptosis, delays cell death and shifts the cell fate towards necrosis. Finally, using treatments that sensitize caspases, cell death was found accelerated and no shift towards necrosis was observed, supporting a model where a delay in cell death due to the lack of caspase-9 in a subpopulation of cells or disruption of the caspase network results in a shift from apoptotic to necrotic cell death.

In summary, Single-Cell Biochemistry combines key requirements for investigating signalling dynamics. First, it allows the simultaneous time-lapse imaging of at least three biochemical reactions in single living cells, which, second, permits the direct validation of biochemical models, using single-cell rather than population kinetics, and third, can deconvolve cell-to-cell heterogeneity with a high temporal resolution. Crucially, this biochemical information can be directly connected to microscopic cell fate such as changes in cell death.

Finally, Single-Cell Biochemistry allows reverse engineering and testing targeted network perturbations to alter cell fate choices and thereby expose vulnerabilities of diseases such as cancer at a single-cell level, such as the requirement for caspase-9 for fast apoptosis, that previously went unnoticed due to a high degree of genetic and non-genetic heterogeneity.

Chapter 2 Rational design of FRET-based biosensors for Single-Cell Biochemistry

2.1 Introduction

2.1.1 Fluorescence microscopy as a tool to correlate biochemical events with cell fate in single cells

To study biochemical signalling in single cells and to correlate it with cell fate, the ideal biological tool needs to meet three requirements: First, a high spatial resolution to monitor and distinguish not only single cells but also subcellular signalling as well as any microscopic changes correlated with cell fate. Second, a high temporal resolution that allows quantitative monitoring of asynchronous biochemical events over time. And, third, high biochemical resolution, i.e. it needs to permit detection of biochemical events and separate multiple events that occur simultaneously. Only fluorescence microscopy is suited to meet all these requirements as it preserves both the integrity and the identity of individual cells. For instance, flow cytometry is often used to monitor a multitude of markers in single cells, but it cannot monitor changes over time on individual cells nor provide a subcellular resolution (Grecco et al., 2016). Single-cell genomics, epigenomics, transcriptomics, proteomics and metabolomics, all suffer from the same limitation (Kandpal et al., 2009), even though providing single-cell information, they only provide a snapshot in time.

The power of fluorescence microscopy is its low-invasive non-destructive nature that allows monitoring the same cell over days and weeks combined with an ever-expanding toolbox of genetically encodable tools to monitor (i.e., fluorescence-based reporters) and probe (i.e., optogenetics) cell biochemistry. Fluorescent reporters can be broadly distinguished into those that are genetically encoded and reporters of chemical synthesis (Terai and Nagano, 2013; Xia et al., 2013). Synthetic probes benefit from high brightness and their simplicity but are

difficult to tune and adapt to new applications. Furthermore, their use in living cells is often hindered by non-existing delivery methodologies and limited stability over a long time.

Genetically encoded fluorescent sensors

In contrast, genetically encoded sensors have received particular attention because of their versatility for a multitude of applications including live cells, their modularity that allows fast adaptation to new requirements and their tunability using genetic engineering (Sanford and Palmer, 2017). Genetically encoded sensors have been used to sense a wide-range of physiological quantities and processes, including pH, redox, metals, ions, metabolites, physical force, crowding, voltage and signalling (Newman et al., 2011; Sample et al., 2014; Sanford and Palmer, 2017). A common characteristic of genetically encoded fluorescent sensors are fluorescent proteins, which, since the first steps of using the Green Fluorescent Protein (GFP) from the jellyfish *Aequorea victoria* two decades ago were made (Tsien, 1998), have rapidly expanded to span the whole visible spectrum and become an invaluable tool for cell biology and beyond (Rodriguez et al., 2017).

It is possible to distinguish five classes of genetically encoded fluorescent sensors based on their mode of action (Sanford and Palmer, 2017):

First, translocation sensors are based on the signal-dependent change in their subcellular localization, mostly between the cytoplasm to the nucleus or plasma membrane. This change is elicited by the modification of a targeting motif such as a nuclear localization signal by the signal/enzyme of interest. For example, imaging fluorescently-tagged ERK shuttling between nucleus and cytoplasm has provided key insights into growth-factor signalling dynamics (Ryu et al., 2015; Shankaran et al., 2009). While their modularity and relative ease of multiplexing are major advantages, their low dynamic range and signal-to-noise ratio makes accurate quantification challenging and the specific requirements for processes that can be sensed limits the number of applications. Also, for accurate quantification, a marker for the target location is required, limiting the number of processes that can be studied simultaneously.

Second, sensors based on complementation consist of two or more non-fluorescent split fragments that when complemented in response to a signal mature and become fluorescent. For example, a split GFP has been rationally designed to become fluorescent upon protease cleavage of a linker peptide (To et al., 2016). While this class has low basal fluorescence, a high dynamic range and a good potential for multiplexing because it comprises a single fluorophore, maturation of chromophores takes several minutes and is irreversible, therefore

lacking temporal resolution for fast and reversible processes. Also, as an intensiometric sensor, i.e. based on the change in fluorescence intensity, other processes that result in local concentration changes such as cell shrinkage cannot be distinguished from a true signal.

Third, environmentally-sensitive fluorophores that change spectroscopic properties when the chromophore, usually protected in the β-barrel of the fluorescent protein, is exposed to environmental changes. For instance, the β-barrel can be designed to allow ions to access the chromophore leading to quenching or changes in emission or excitation spectra allowing for sensing of ions and pH (Llopis et al., 1998; Miyawaki et al., 1997). Such sensors are well-suited for multiplexing, but suffer from the same limitation as complementation sensors, because they rely on intensity changes. Furthermore, not all fluorescent proteins are suitable for this approach.

Fourth, the novel class of dimerization sensors consists of two proteins, a fluorescent protein whose fluorescence is quenched when monomeric and a second protein that de-quenches the fluorescence upon heterodimerization. The dimerization is induced by the modification of a linker that brings the two proteins in close proximity (Alford et al., 2012a, 2012b). Such tools have been used to sense protease, ions and kinase activation, and recent improvements have also enabled ratiometric imaging, overcoming the limitations of an intensiometric readout (Ding et al., 2015). Together, these make this novel class a promising alternative to conventional reporters, however, multiplexing is currently limited as only a green, yellow and red version of this special protein pair have been found so far.

FRET-based sensors

Fifth and last, FRET biosensors constitute the largest and most diverse class of genetically-encoded biosensors (Newman et al., 2011). FRET, or Förster resonance energy transfer, is the non-radiative transfer of energy from a donor to an acceptor fluorophore that occurs when they are in close proximity (typically < 10 nm) and if the emission spectrum of the donor overlaps sufficiently with the absorption spectrum of the acceptor (Bajar et al., 2016a; Förster, 1948). FRET efficiency (E) describes the percent of the energy that is transferred from the donor to the acceptor and is a function of the distance between the donor and acceptor dipoles (r):

$$E = \frac{1}{1 + (\frac{r}{R_0})^6}$$

R_0 is known as the Förster Radius or Förster Distance and describes the distance at which E is 50%. It depends on the photophysical parameters of donors and acceptors, including the inter-dipole orientation (or κ^2, generally assuming the value of $^2/_3$ in the approximation of freely rotating dipoles), the quantum yield of the donor, the extinction coefficient of the acceptor and the spectral overlap of donor emission and acceptor excitation spectrum. To be able to measure the distance between two β-barrel FPs with a diameter of around 4 nm each, an R_0 of at least 4 nm is required. Higher R_0 – within limits – increases the change in FRET efficiency upon a given change in distance, i.e. the dynamic range of the pair (see Bajar *et al.*, 2016 for an example).

FRET-based biosensors can be grouped into two classes depending on whether donor and acceptor are covalently bound or not (Bajar et al., 2016a): In intermolecular FRET sensors, donor and acceptor are fused to different molecules and FRET efficiency can be used to measure their proximity (Stryer and Haugland, 1967). Considering the size of most globular proteins of a few nanometers, the typical limit of ~10 nm for FRET to occur enables to study direct protein-protein interaction with a spatial resolution that is hardly achievable with other fluorescent techniques including super-resolution microscopy.

In comparison, in intramolecular FRET sensors, donor and acceptor are fused together with a linker that carries a sensor domain. When modification of the linker leads to a change in orientation or proximity of donor and acceptor, this can be measured by a change in FRET. Using various linkers, biosensors measuring pH, ion concentration, metabolites, phosphorylation, methylation, acetylation, ubiquitination, viscosity, mechanical stress, GTPase and protease activities have been developed with varying degrees of sensitivity, dynamic range and reversibility (for an extensive list see: Newman et al., 2011; Sample et al., 2014). This versatility is one of the major advantages of FRET biosensors. Due to their modular nature, linkers, as well as fluorophores, can be relatively easily modified using standard genetic tools allowing adaptation to new applications. Furthermore, changes in FRET are instantaneous and, except for protease sensors, reversible, allowing measurements of very fast processes such as Ca^{2+} signalling (Miyawaki et al., 1997).

Measuring FRET

A further advantage is that FRET can be measured with multiple methods, utilizing any characteristics of fluorescence, such as spectrum, lifetime and polarization, allowing to tailor the detection for each application (Bajar et al., 2016a).

In spectral imaging-based FRET (siFRET) FRET efficiency is derived from the spectra of donor and acceptor whose individual contribution to the overall spectrum is a surrogate for the FRET efficiency. Sensitized emission FRET (seFRET) is a popular method for FRET detection, because of its ease and speed. Most commonly, changes in FRET are measured by the ratio of donor and acceptor emission upon donor excitation, as FRET causes emission of the acceptor. Acceptor-photobleaching FRET (apFRET) is based on the de-quenching of donor emission through irreversible bleaching of the acceptor, but is not usable in live cells and does not allow measuring FRET changes over time. Polarization-resolved FRET (prFRET) monitors the polarization of the acceptor emission upon donor excitation which becomes partially depolarized if FRET occurs because the dipole orientation changes. Uniquely, prFRET permits measurement of HomoFRET between two spectrally identical fluorophores, and has a high dynamic range and very short acquisition times.

Finally, in fluorescence lifetime imaging FRET (FLIM-FRET), the decay of the fluorescence emission of the donor is measured and the lifetime determined from the nanosecond decay pattern. Upon FRET, the fluorescence lifetime of the donor is reduced allowing a highly accurate and sensitive determination of the FRET efficiency. Two technologies are used to measure fluorescence lifetime: Frequency-domain FLIM measures the demodulation of frequency-modulated excitation light, a characteristic that is dependent on the fluorescent lifetime. In time-domain FLIM, the fluorescence lifetime is derived from the arrival times of single photons after an ultrashort (pico- to femtosecond) excitation pulse.

For both methods, FRET efficiency (E) can be obtained from the lifetime of the donor in the presence (τ_{DA}) and absence (τ_D) of the acceptor:

$$E = 1 - (\frac{\tau_{DA}}{\tau_D})$$

FLIM-FRET has several advantages compared to other, intensity-based detection methods, and is therefore sometimes considered the ‘gold-standard’ for FRET detection (Bajar et al., 2016a). FLIM directly quantifies a molecular property of a donor fluorophore (i.e., the average time that the donor spends in its excited state) that is directly proportional to changes in FRET efficiencies (the surrogate measure of biochemical events). Therefore, FLIM-FRET is broadly insensitive to changes in fluorophore concentrations, variations in intensities caused by optics and spectral cross-talk. Typically, time-domain FLIM methods such as TCSPC (Time-correlated single-photon counting) do not require calibrations, corrections and very efficiently use the limited photon-budgets available in biological experiments (Day and Davidson, 2012).

Two disadvantages are described frequently. First, long measurement times of up to several minutes are common to acquire sufficient photons for a good estimation of the fluorescence lifetime. However, recent technological advances such as integrated single-photon avalanche photodiodes (Li et al., 2010), fast and sensitive hybrid photomultiplier tube detectors (Becker et al., 2010) and modulated solid-state cameras (Esposito et al., 2005; Raspe et al., 2016; Zhao et al., 2012) allow to greatly reduce acquisition times to a few seconds while maintaining low excitation intensity suitable for live-cell imaging. Furthermore, the required know-how to operate and the costs of procuring FLIM instrumentation have decreased significantly and more commercial fully integrated systems are now available on the market and in core imaging facilities.

In summary, fluorescence lifetime imaging and FRET-based biosensors provide quantitative and robust measurements on biochemical reactions in live cells. However, significant limitations in measuring several biochemical reactions in the living cell, in particular with FRET-based biosensors, still persist. Therefore, one of the goals of this study was to redevelop FRET-based assays to enable quantitative and simultaneous measurements of at least small three-node biochemical networks in the living cell.

2.1.2 Key challenges in the design of FRET-based biosensors

When designing FRET-based biosensors, two key challenges frequently arise, a low FRET efficiency and the formation of visible aggregates.

Low FRET efficiency

Maximizing the FRET efficiency, as well as the dynamic range of a sensor, are crucial for a sensitive, quantitative and reproducible measurement of biological events. As discussed in the previous section, FRET efficiency depends on the photophysical properties of donor and acceptor, their distance and relative orientation. Thus, approaches to maximize FRET efficiency have been focussed on these characteristics.

Varying the donor-acceptor distance by changing the linker length is a frequently used strategy to improve FRET efficiency (Evers et al., 2006; Komatsu et al., 2011; Shimozono et al., 2006). In addition to changing the linker, the termini of donor and acceptor can be shortened to decrease the distance, which can increase FRET efficiency (van der Krogt et al., 2008), but is limited by the minimal structure required for fluorescence and the potential reduction of rotational freedom (Li et al., 1997). Furthermore, depending on the design of the FRET sensor,

short linkers that minimize the distance are not always possible, because short linkers can sterically hinder the function of the sensor. Thus, long flexible linkers are frequent in FRET sensor designs (Piston and Kremers, 2007). However, new approaches such as HiFRET which uses electrostatic 'helper interactions' to increase the affinity of donor and acceptor in the presence of a long linker can help to achieve high FRET efficiencies with long linkers (Grünberg et al., 2013).

A change in the dipole orientation has primarily been achieved by swapping the position of donor and acceptor around the linker as well as the use of circular-permutated fluorescent proteins (cpFPs; Baird et al., 1999; Topell et al., 1999). In cpFPs, the amino- and carboxy-termini are either joined or inserted at different positions of the β-barrel resulting in an inclination of the cpFP relative to its fusion partner, which is well-suited to optimize FRET efficiency (van der Krogt et al., 2008; Nagai et al., 2004).

Finally, improving the properties of the fluorescent proteins constituting the FRET pair are obviously crucial, including fast maturation, high photostability and sufficient spectral overlaps. For donors for FLIM-FRET a high quantum yield is favourable, while acceptors ideally have high extinction coefficient. The latter can be doubled by creating tandem-dimers (Campbell et al., 2002; Fradkov et al., 2002) which often results in a marked increase in FRET efficiency (van der Krogt et al., 2008).

Aggregation

The formation of visible aggregates (also termed 'speckles' in some publications) is a common feature of fluorescent proteins and their fusions across all spectra and can severely limit their usability.

Different causes for the aggregation of fluorescent proteins have been reported. For instance, DsRed and its derivatives mRFP1 and dsRed2 can accumulate in lysosomes by an autophagy-related mechanism (Katayama et al., 2008). Poor folding of a fluorescent protein can also cause aggregation regardless of their quaternary structure (Kremers et al., 2006). Last, oligomerization of the fluorescent proteins used in a FRET pair is a frequent cause for aggregation. The likely cause for such oligomerization is that in nature fluorescent proteins and chromoproteins often occur as dimers (e.g., GFP) or tetramers (e.g., dsRed); these oligomers show strong aggregation, in particular when fused to other proteins (Fradkov et al., 2002) and/or expressed at high levels (van der Krogt et al., 2008). Monomerization of FPs achieved by destabilization of dimer interfaces through mutagenesis and by cloning tandem-dimers often

halts aggregation (Campbell et al., 2002; Fradkov et al., 2002; van der Krogt et al., 2008). Tandem-dimers are a fusion of two identical copies of a fluorescent protein and may promote intramolecular dimerization over inter-molecular dimerization, effectively generating a 'pseudo-monomer' and inhibiting aggregation.

Destabilization of dimerization interfaces (Bajar et al., 2016b; Merzlyak et al., 2007) and tandem-dimer fusions (Fradkov et al., 2002; Shaner et al., 2005) can be used either alone or in combination (Campbell et al., 2002; van der Krogt et al., 2008), depending on the specific fluorescent protein. Importantly, even when monomerization has been confirmed by biochemical means in cell-free systems (such as size-exclusion chromatography), fluorescent proteins might still oligomerize and aggregate in cells, as elegantly shown by using the natural tendency of endoplasmic reticulum to accumulate for testing FPs in cells (Costantini et al., 2012; Cranfill et al., 2016). Also, even if original tetramers have been pseudo-monomerized as tandem-dimers, the tandem-dimers themselves can dimerize again to form a *de facto* tetramer showing reduced, but still visible, aggregation (Fradkov et al., 2002).

This observation of oligomerization of supposed monomers supports a notion of van der Krogt *et al*. that FRET pairs in particular, even if they consist of monomers, are more prone to aggregation since the presence of two fluorescent protein moieties in close proximity increases the avidity (van der Krogt et al., 2008). In their example, the introduction of non-dimerizing mutations into CFP-YFP did not affect aggregation, while the tandem-dimerization of Venus (replacing YFP) abolished aggregation. This suggests that tandem-dimerization is not only useful for monomerization of FPs generally, but by tandem-dimerization of seemingly monomeric FPs as acceptors in FRET pairs the propensity to form aggregates can be reduced while gaining FRET efficiency through the doubling of the extinction coefficient.

Apart from mutagenesis and tandem-dimerization further strategies have been suggested to reduce oligomerization. For instance, the concentration of FRET pairs inside cells strongly influences aggregation (van der Krogt et al., 2008). High expression can relatively easily be overcome by avoiding bright cells or by creating stable cell lines selected for moderate expression, but the drawback is that higher laser powers need to be used for imaging increasing phototoxicity. Moreover, in applications where FRET pairs are expressed in small spaces or the cellular volume decreases significantly, as during apoptosis in our work, an increase of local concentration can result in the creation of new aggregates (with increased FRET probably due to additional intra-molecular energy transfer in crowded environments) during the experiment, without the possibility to avoid such cells during the setup.

Importantly, aggregation is also dependent on the cells of choice, as noted by others (van der Krogt et al., 2008) and exemplified by a recent study showing mCherry, which never aggregated even at high levels in a large number of cancer cells strongly aggregated in neuronal cells (Laviv et al., 2016). This suggests that a change in cell line, if experimentally possible, can be an easy way to avoid aggregation.

In summary, a growing number of solutions to overcome key challenges in the design of FRET-based biosensor provide a toolbox for our endeavour to design a suite of FRET pairs suitable for multiplexing. In this Chapter, I will describe how we used a number of those to address an issue arising during the development of such pairs.

2.1.3 Multiplexing FRET pairs permits simultaneous readout of multiple biochemical events in single cells

To achieve the goal of multiplexing FRET pairs several different approaches have been used, but all are limited to two simultaneously imaged FRET pairs.

Multiplexing with two excitation lines

Two spectrally-resolved FRET sensors are read out sequentially using two excitation wavelengths. This has first been achieved by using CFP and YFP as spectrally resolved donors that work with the same RFP acceptor. Using intramolecular FRET, the interaction of two Ras isoforms, labelled with CFP or YFP, and a binding domain labelled with tHcRed as acceptor was studied using FLIM measuring donor fluorescence lifetimes (Peyker et al., 2005). In an intramolecular FRET setup, CFP and YFP were each fused to dsRed with linker carrying a protease cleavage site and the increase in donor fluorescence upon loss of FRET measured (Kawai et al., 2005). Avoiding sharing of an acceptor which can have complex effects on FRET measurements (Bunt and Wouters, 2017), true spectrally distinct pairs have been first used to study RAS and Ca^{2+} signalling by FLIM (ECFP/mVenus, TagRFP-mPlum; Grant et al., 2008). Importantly, FLIM imaging of the donors proved essential for this combination, because of the low quantum yield of mPlum that was not sufficient to measure its sensitized emission. Using brighter, but less red-shifted acceptors, that are suitable for seFRET, several groups have reported dual-colour FRET imaging monitoring FRET pairs for a range of applications, including subcellular caspase-3 cleavage (mTFP-mCitrine, mAmetrine-tdTomato; Ai et al., 2008), Src kinase and Matrix Metalloprotease activity (CFP/YFP, mOrange-mCherry; Ouyang et al., 2010), caspase-3 and Ca^{2+} imaging (mTFP-mCitrine, mAmetrine-tdTomato; Ding et al.,

2011), PKA and cAMP activity (Cerulean-mCherry, mVenus-mCherry; Aye-Han et al., 2012) and Src kinase and Ca^{2+} signalling (mTagBFP-sfGFP, mVenus-mKOκ; Su et al., 2013). Using anisotropy FRET imaging, Warren *et al.* combined a standard CFP/YFP Ca^{2+} sensor with a homoFRET probe consisting of mCherry fused to the membrane-anchor of Akt kinase, which allows measuring Akt clustering by intermolecular FRET (Warren et al., 2015).

While important insights have been gained using two excitation wavelengths, the delay between the acquisition of each pair which, depending on the detection setup, can be seconds to minutes, prevents the fully simultaneously imaging required for fast events. Furthermore, multiple exposures with different laser lines make phototoxicity more likely.

Multiplexing with a single excitation line

Using a single excitation wavelength for both donors has been made possible by the development of fluorescent proteins with a long Stokes shift (the difference between excitation and emission peak wavelengths; LSS). This permitted to study very fast processes such as cAMP and cGMP signalling by combining ECFP-EYFP sensors with LSS donor T-Sapphire linked to the RFP dimer2 that can be read out using ratiometric seFRET (Niino et al., 2009). Similarly, caspase-3 and fast Ca^{2+} imaging were studied using ECFP-mVenus and LSS-mOrange-mKate sensors (Shcherbakova et al., 2012). To reduce spectral bleed-through of the first acceptor into the second pair that can lead to false-positive FRET efficacy changes, ‘dark’ acceptors (Ganesan et al., 2006) with a low quantum yield have been introduced in a number of studies. Niino *et al.* monitored cAMP and cGMP signalling with mTagBFP-sREACh and CFP/YFP using seFRET (Niino et al., 2010). However, because of the low quantum yield of sREACh, mTagBFP intensity was measured non-ratiometrically and therefore only providing relative FRET changes. Two recent studies used FLIM, which is ideal for dark acceptors since only the donor fluorescence lifetime is measured to obtain absolute changes in FRET efficiency, to monitor CaMKII and RhoA signalling with mEGFP-dimVenus and mCyRFP-mMaroon pairs (Laviv et al., 2016) and PKA and ERK kinase activity with mTFP-ShadowG and LSS-mOrange-mKate2 (Demeautis et al., 2017).

A different approach is based on the combination of three fluorophores that are either in a sequential, ‘two-step’ configuration in which the acceptor for donor 1 is also donor for acceptor 2 (Watrob et al., 2003), or in a ‘three-way’ configuration where one donor shares two acceptors that may also exhibit FRET between them (Galperin et al., 2004). So far, this approach has only been used to study three interactions in protein complexes, with the exception for two-step FRET which was used by Wu *et al.* to measure two different caspase

activities by creating a CFP-YFP-mRFP fusion with two protease linkers read out by seFRET using flow cytometry (Wu et al., 2006).

Example for multiplexing three biochemical events using FRET

Finally, one study has described simultaneously multiplexing of three FRET sensors for PKA, cAMP and Ca^{2+} consisting of only three different FPs (mTurquoise2-cpVenus, mTurquoise2-mCherry, mCherry-cpVenus) that are imaged using three excitation wavelengths and a combination of ratiometric and spectral imaging FRET (Woehler, 2013). For unmixing, reference excitation and emission spectra are acquired for the individual pairs and then used to extract apparent FRET efficiencies from time-lapse data of the co-expressed sensors. While allowing very fast imaging and relative simple analysis, the use of three excitation wavelengths is undesirable for multiplexing, especially when extending to a higher number of fluorophores. Also, as discussed earlier, the use of intensiometric readouts makes this approach less quantitative as for example FLIM, and more prone to concentration artefacts resulting from, for example, a local increase in concentration due to cell shrinkage. Homogeneous and stable expression levels of all sensors in all cells are possible only in a few biological applications limiting the usefulness of this otherwise elegant approach.

Design principles for three-colour single excitation FLIM-FRET suite

In order to overcome the limitations in quantitative biochemical multiplexing of state-of-the-art techniques, we decided to rationalize the utilization of the visible spectrum and planned to combine (Fig. 2.1):

i) Three donors with varying Stokes shifts that allow excitation with a single wavelength and simultaneous detection
ii) Three ‘dark’ acceptors exhibiting high extinction coefficients and low quantum yields with spectral overlaps matched to their respective donor fluorophore, permitting us to minimize spectral cross-talk.
iii) FLIM-based detection in order to obtain quantitative biochemical read-outs utilizing only fluorescence emitted by donor fluorophores.
iv) Two-photon excitation to provide efficient separation between excitation and emission paths, z-sectioning and 3D imaging with non-descanned hybrid detectors which minimize optical losses. This strategy permits us to increase sensitivity and reduce acquisition times. Hybrid detectors could achieve photon count rates in excess of what common FLIM electronics were capable of at the beginning of this

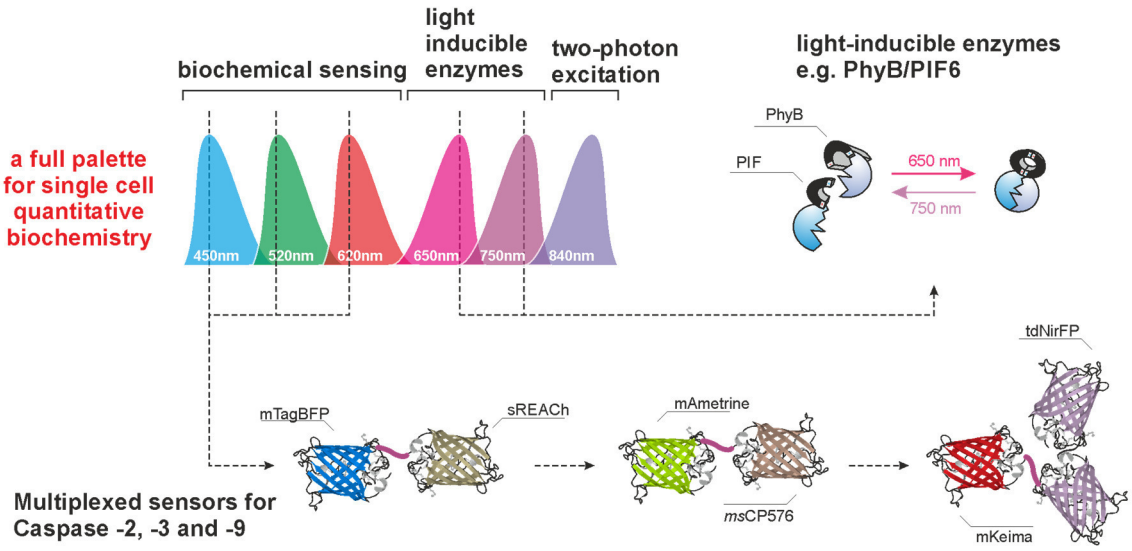

Figure 2.1 – **Efficient utilization of the visible spectrum for single-cell live biochemistry**

For multiplexing, we designed three FRET pairs that are excited at 840 nm two-photon excitation. The efficient utilization of visible spectrum permits us to increase the number of FRET pairs that can be imaged simultaneously and provides the opportunity for future integration with light-inducible enzymes that are currently under development in our laboratory. This scheme will permit to perturb and quantify small networks of biochemical reactions in living cells. The best three FRET pairs for multiplexing, developed as described in Chapter 2, are shown here. Adapted from A. Esposito.

v) project and, therefore, we customized read-out electronics achieving very fast (about one order of magnitude faster than standard electronics) and sensitive detection.

vi) Finally, developing novel unmixing algorithms to achieve fast model-free and computational efficient data pipelines that permitted us to retrieve quantitative biochemical information from complex photophysical information.

In this chapter, I will describe in detail the development and validation of these FRET pairs. In order to characterize them in a simple and biologically relevant context, we used short peptide linkers between donor and acceptor fluorescent proteins that carry well-characterized caspase (Cysteine-aspartic proteases) (Tyas et al., 2000) recognition sequences that are preferentially cleaved by three caspases that have been implicated in the DNA damage response: caspase-2, -3 and -9. These sensors are experimentally simple to activate and known to provide a high dynamic range. Therefore, this strategy permitted us both to have a “molecular workbench” to test novel FRET pairs, microscopy and analysis tools, while addressing important questions related to dynamics and heterogeneity of caspase activation in response to DNA damage at the same time.

2.2 Material and methods

Detailed information for all reagents used in this study can be found in Table S4.

2.2.1 Molecular cloning

All reagents were from New England Biolabs unless stated otherwise. Detailed information about the oligonucleotides and template sequences can be found in supplemental Tables S1 and S2, respectively.

To create the initial set of FRET sensors, the donors (mTagBFP, mAmetrine, and mKeima) and acceptors (sREACh, msCP576 and mNeptune; cloning performed by Bryn Hardwick and Meredith Roberts-Thomson (sREACh and msCP576) and Dr David Perera (mNeptune)) were amplified by PCR (Accuprime Pfx polymerase; Invitrogen) and purified using the QIAquick PCR Purification kit (Qiagen). The purified PCR products and the recipient vector pcDNA3.1(-) vector (Invitrogen) were digested with NheI and KpnI restriction enzymes for 1 hour at 37ºC, separated on a 0.8% Agarose (Biogene) gel and extracted using the QIAquick Gel Extraction (Qiagen) per manufacturer's instructions. Ligation of vector and insert were performed using T4 ligase for 16 hours at 4ºC. After insertion of the donor, linker oligonucleotides were phosphorylated with Polynucleotide Kinase in T4 ligase buffer, annealed and ligated into NotI and KpnI sites using T4 DNA ligase for 2 hours at 16ºC, followed by the acceptors using KpnI and PmeI and as described for the donors. Linker sequences were (cleavage motif underlined): Uncleavable, LGGTGSGSGSASGG; caspase-2, LGGTGSGSGVDVADG and LGGTGSGSGVDTTDG; caspase-3: LGGTGSGSGDEVDG and LGGTGSGSGDEVDRG; caspase-7: LGGTGSGSGQKDVKDG; caspase-9 (short): LGGTGSGSGLEHDG; caspase-9 (long): SPGSTLGGTGSGSGLEHDGPSGSA.

Ligated plasmids were then transformed into in-house prepared competent DH5α bacteria using heat-shock. Plasmid DNA was prepared using the Plasmid Mini Kit (Qiagen) and screening performed by analytical digest and separation on an Agarose gel. Positive clones were confirmed by Sanger Sequencing (Source Bioscience), re-transformed into DH5α and plasmid DNA obtained using Plasmid Plus Maxi Kit (Qiagen) to reduce endotoxin contamination prior to transfection.

To change the linker in an existing construct, the construct was digested with KpnI and NotI, new linker oligos processed and ligated using T4 ligase as described above for the original linker.

New donors and acceptors were inserted into the existing constructs by digesting the template and purified PCR-amplified insert with NheI/KpnI or NotI/PmeI, respectively, followed by gel-extraction as above and ligation using Quick-Stick ligase (Bioline) for 30 min at room temperature.

Codon optimization for expression of msCP576 in human cell lines was performed with the GeneArt gene synthesis online tool (Thermo Fisher Scientific). The optimized gene (msCP576h) was designed to integrate NotI/PmeI restriction sites utilized for subsequent subcloning into the corresponding sites in the mAmetrine-msCP576 containing plasmids by PCR-based restriction cloning as described above. ShadowG, bfloGFPc1, Ultramarine, hmKeima8.5 and mGarnet were codon-optimized as GeneArt Strings with suitable NheI/KpnI or NotI/PmeI sites. GeneArt Strings were used directly for restriction digest and ligated into both into FRET sensor backbones and an empty pcDNA3.1(-) as described for new donors and acceptors above.

Tandem-dimer NirFP was created by co-worker Emma K. Richardson (who also created all constructs containing single copies of NirFP) using scar-less SapI-fusion cloning as described for tdTomato (Shaner et al., 2004). To link two copies of NirFP with a 14 amino-acid flexible linker (GHGTGSTGSGSSGT), NirFP was PCR-amplified from the pNirFP-C vector using two different set of primers, with the first adding a NheI restriction site to the N-terminus and the first seven linker residues followed by the SapI site to the C-terminus, and the second PCR adding the SapI N-terminally followed by the last seven linker residues and a NotI site. Purified and gel-extracted PCR products were digested with SapI followed by gel extraction. The digested products were then ligated for 16 hours at 16ºC overnight using T4 DNA ligase and the ligated products gel-extracted. To insert tdNirFP into the recipient vector, both insert and vector (pcDNA3-NirFP-mKeima) were digested with NheI and NotI, correct bands gel-extracted and ligated for 16 hours at 16ºC overnight using T4 DNA ligase. The ligations were transformed into DH5α bacteria and plasmid DNA prepared and sequence confirmed as described above.

Using a simplified and commercial scar-less fusion approach, Ultramarine and iRFP682 were tandem-dimerized with the same linker as used for tdNirFP above, but using the NEBuilder HiFi DNA Assembly kit. Two copies of either cDNA were amplified using two different sets of

overlapping primers designed using the NEBuilder online tool. The PCR products and pcDNA3-tdNirFP-mKeima backbone were digested using NheI and NotI restriction enzymes purified by gel extraction. Next, all three components (backbone and two PCR products) were ligated with their overlapping ends using the NEBuilder HiFi DNA Assembly Master Mix with a molar ratio of vector:insert of 1:2 while using 100 ng vector for 15 min at 50ºC. The products were transformed into DH5α bacteria and plasmid DNA prepared and sequence verified as described above.

2.2.2 Cell culture

HeLa cells (CCL 2, ECACC #93021013) were obtained from the European Collection of Cell Cultures, maintained in DMEM (Gibco) supplemented with 10% fetal calf serum at 37ºC and 5% CO_2 in humified atmosphere and passaged by trypsinization (Trypsin-EDTA; Gibco).

2.2.3 Sample preparation for fluorescence lifetime imaging

15,000 HeLa cells were seeded on 8-well LabTek II chambered coverglass (#1.5, Nunc cat. # 155409). Transient transfection was performed 24 hours later with 125 ng of indicated plasmids using Effectene (Qiagen) (Fig. 2.3-4, 2.6, 2.9-11, 2.14A-F, 2.15A-H) or Jetprime (Polyplus) (all other figures) according to the manufacturer's instructions. 24 hours (Effectene) or 6 hours (Jetprime) after transfection cells were washed with PBS (Phosphate Buffered Saline) and fresh medium added, which contained 40 uM Biliverdin (Sigma) for iRFP713 and iRFP682. 25 µM of the irreversible and cell-permeable caspase inhibitors (see Tab. S4 for details) or DMSO (Dimethylsulfoxide) was added 2 hours before addition of 4 µM Staurosporine (Santa Cruz) or Ethyl Acetate (Sigma) as solvent control. Where indicated in pilot experiments, 10 µM Etoposide (Sigma) or DMSO was used for 16 hours instead of Staurosporine. At indicated time points, cells were fixed with 4% formaldehyde (Agar Scientific) for 10 min at room temperature (RT) and kept in PBS at 4ºC until use.

2.2.4 Spectral scans, fluorescence lifetime imaging and data analysis

Imaging was performed with a Leica SP5 confocal laser scanning microscope (Leica Microsystems) equipped with a Ti:Sapphire two-photon laser (Coherent) tuned to 840 nm if not stated otherwise.

Emission spectra were acquired using the XYλ mode of the Leica SP5 with a 40x oil objective (Leica HCX PL APO CS 40.0x1.25 OIL UV), 256x256 pixel image size, 400 Hz scan speed, 10 nm detection bandwidth and step size using the internal PMTs (photo-multiplier-tubes). The analysis was performed by exporting raw data for single cells from LAS Lite (Leica) to Microsoft Excel where the background was subtracted and normalized to the sum per cell or field of view. The average was calculated and normalized to the maximum. The relative contribution of acceptor fluorescence to donor emission was determined as the ratio of the area under the curve of donor-only and UCL control.

Confocal images to visualize expression were acquired with a Leica SP5 with a 40x oil objective (Leica HCX PL APO CS 40.0x1.25 OIL UV), 1024x1024 pixel image size, 400 Hz scan speed, 16x line average, variable zoom and detection bandwidth optimized for maximum signal using the internal PMTs. If 1PE was used as indicated in the figure legend, the pin hole was closed to 1 airy units. Brightness, contrast and look-up table were adjusted using Fiji (ImageJ, NIH).

For FLIM, the emission light was filtered according to the fluorophores used (mTagBFP: 467-499 nm; mAmetrine: 506-545 nm; mKeima: 604-679 nm; all Semrock) and photons detected with a hybrid PMT operating in photon-counting mode connected to a module allowing time-correlated single-photon-counting (SPC-150; Becker & Hickl GmbH). Images were acquired with a 40x oil objective (Leica HCX PL APO CS 40.0x1.25 OIL UV), 256x256 pixel image size and 400 Hz scan speed within 60 sec acquisition time. The fluorescence lifetime was calculated with SPCImage V4.9 (Becker & Hickl) fitting a monoexponential decay with adjusted threshold for background reduction and 1x binning. Intensity and lifetime images were exported from SPCImage. To generate lifetime distributions, the raw data was normalized to the sum of each FOV and multiple fields of view averaged in Microsoft Excel. Relative enzymatic activity (REA) and FRET efficiency (E) were calculated with average lifetimes obtained by summing the first moments of the lifetime distributions: $REA = \frac{\tau - \tau_{UCL}}{\tau_D - \tau_{UCL}}$ and $E = 1 - \frac{\tau}{\tau_D}$. τ = average measured lifetime, τ_{UCL} = lifetime UCL-control, τ_D = lifetime donor-only control.

2.2.5 Western Blot

For analysis of caspase sensor cleavage, 400,000 HeLa cells were seeded per 6 cm dish and 24 hours later transfected with 500 ng (Donor-only control) or 100 ng (UCL-control, sensors

and empty-vector control) plasmid DNA using the JetPRIME reagent (Polyplus) according to the manufacturer's instructions. The medium was changed 6 hours later. 24 hours after transfection, fresh medium was added containing 25 µM caspase-inhibitors followed by 4 µM Staurosporine (Santa Cruz) or Ethyl Acetate (Sigma) as solvent control two hours later, as detailed for imaging above. At indicated time points after treatment, the supernatant was removed, cells washed twice with PBS, detached with Trypsin-EDTA, collected in full medium and pooled with the supernatant. Cells were pelleted by centrifugation at 1000 rpm for 5 min at 4ºC, washed once in ice-cold PBS, resuspended in 100 µl PBS and transferred to a microcentrifuge tube followed by centrifugation at 13,000 rpm for 10 min at 4ºC. The pellet was stored at -80C until further processing.

Lysis was performed by resuspending the pellet in 50 µl RIPA buffer (50 mM Tris pH 7.4, 150 mM NaCl, 0.5% (w/v) Sodium deoxycholate, 0.1% SDS, 1% (v/v) IGEPAL) supplemented with 1 mM PMSF protease inhibitor (Sigma) and 1x Protease Inhibitor Complete (Roche) prior to use and incubated for 30 min on ice followed by centrifugation at 13,000 rpm for 10 min at 4ºC. The protein concentration of the supernatant was determined by BCA assay (Pierce). 10 µg of lysate was denatured with 1x sample loading buffer (Life Technologies) for 10 min at 70ºC. Samples were separated on a 26-well 4-12% Bis-Tris SDS-PAGE gel (Life Technologies) and transferred onto a Hybond ECL (GE Healthcare) nitrocellulose membrane using wet transfer at 30 V for 120 min at 4ºC or 40 mA or 20 V for 16 hours at 4ºC. The membrane was stained with Ponceau-S solution (Sigma, cat. #7170) for 5 min to confirm efficient and even transfer. Blocking with 5% (w/v) milk in TBS-T (Tris Buffered Saline + 0.05% Tween-20) was followed by incubation with the primary antibody in blocking solution overnight at 4ºC (see Table S3 for details of all antibodies used). After washing 4x 5 min in TBS-T, the membrane was incubated with fluorescently-labeled secondary antibodies (IRDye; Licor) for 1 h at room temperature, washed 4x 5 min with TBS-T and scanned using the Licor Odyssey scanner. Quantification of the bands was performed Image Studio version 5.25 (Licor) and ratios between cleaved and uncleaved sensor calculated in Microsoft Excel.

2.2.6 Data analysis and presentation

If not stated otherwise, all analyses were performed in Microsoft Excel (Microsoft) and graphs prepared with GraphPad Prism version 5.0 (GraphPad Software). Foerster radii (r_0) of donor-acceptor pairs were estimated with an in-house developed Matlab script using published information on photophysical properties.

2.3 Results

Each of the following sections describes the development of a blue, green and red light emitting FRET pair that was specifically designed for multiplexing, including discussions of FRET pairs that were deemed not good enough for subsequent experiments. Details of all tested fluorescent proteins and FRET pairs can be found in Tables 2.1 and 2.2 (located at the end of this chapter), respectively.

To assess the suitability of FRET pairs, at least two constructs were created for each pair, one "UCL-control", where donor and acceptor fluorophore are linked with a short 14 amino acid

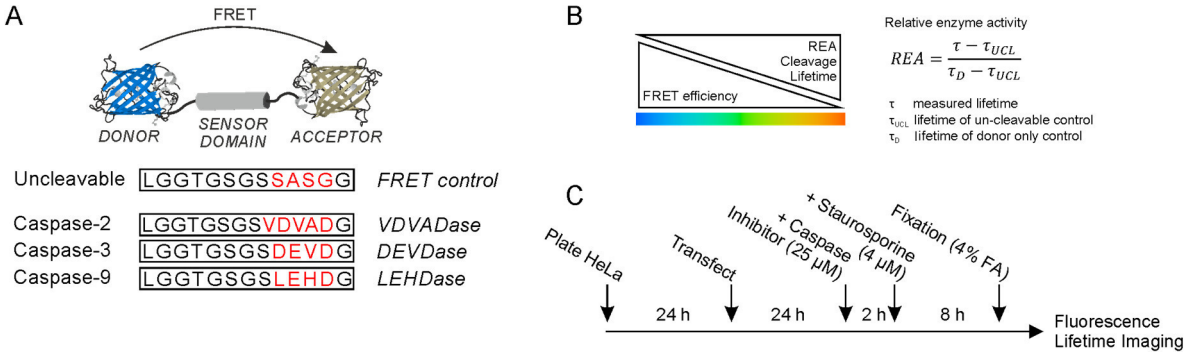

Figure 2.2 – **Design principles of FRET pairs and experimental setup**

A: FRET pairs consist of a donor and acceptor fluorophore linked by a short peptide linker that is either proteolytically stable (uncleavable) or contains a specific substrate cleavage motif (in red) for the indicated caspase.

B: Representation of the principles of FLIM data analysis for cleavage-based caspase sensors used for experiments in this chapter.

C: General experimental protocol used for the validation of caspase FRET sensor in this chapter.

long peptide linker that is insensitive ("uncleavable", UCL) to caspase cleavage, and a "Donor-only" control, that consists of the donor FP with the UCL linker but lacks the acceptor (Figure 2.2A). Constructs were transiently expressed in HeLa cells, fixed in formaldehyde, their emission spectra recorded and FRET efficiency determined using FLIM (Figure 2.2B, C).

Those FRET pairs that showed sufficiently high FRET efficiency, consistent measurements, lack of secondary emission peaks, and did not exhibit significant aggregation were converted to caspase sensors introducing cleavage sites in the linkers in order to test their suitability to measure enzymatic activities (Figure 2.2B). Caspase-dependent cell death was induced by treatment with 4 µM Staurosporine (STS, a pan-kinase inhibitor) for 8 hours. Cells were also

pre-treated with irreversible inhibitors for the respective caspases (Figure 2.2C) to assess the specificity and dynamic range of the sensors.

2.3.1 Development of a blue FRET pair for multiplexing

As a donor for the blue FRET pair mTagBFP was chosen because it was the brightest blue fluorescent protein excitable at 840 nm two-photon excitation (2PE) at the time. We first tested sREACh as dark acceptor because it has been reported to work well for FRET with mTagBFP (Niino et al., 2010). sREACh is an optimized version of REACh2 that exhibits optimal spectral overlap with mTagBFP, but solves folding issues compared to REACh2. Compared to the parent YFP, sREACh was reported to exhibit a residual fluorescence of ~5% (Murakoshi et al., 2008) that we considered sufficiently low for multiplexing with green FRET probes. However, spectral imaging of the mTagBFP-sREACh pair let us estimate that sREACh still contributed ~12% to the total fluorescence (Fig. 2.3A), because of FRET and direct acceptor excitation. Although higher than expected under the chosen conditions, this residual fluorescence is still low enough to be properly unmixed by spectral or multicolour FLIM.

We, therefore, introduced the canonical caspase-2 cleavage site VDVAD (Zhivotovsky and Orrenius, 2005) into the mTagBFP-sREACh linker and tested its suitability to sense caspase-2 activity by FLIM. The sensor was well expressed in HeLa cells and exhibited 33% FRET (Fig. 2.3B-D). Some aggregation of sREACh was visible in the green part of the spectrum in very bright cells, which did not affect fluorescence lifetime and can easily be avoided by choosing cells with moderate expression. STS treatment resulted in an increase in fluorescence lifetime

relative to the untreated and UCL control (Fig. 2.3D-E). This change in fluorescence lifetime corresponded to an average of 65% relative enzyme activity (REA; Fig. 2.3F), indicating that 65% of the sensor was cleaved. When the irreversible caspase-2 inhibitor Z-VDVAD was added, the fluorescence lifetime decreased only slightly, indicating limited specificity of this sensor. (Fig. 2.3E-F). As a note, several cells did not exhibit caspase-2 cleavage in one of three experiments performed resulting in the local maximum around 1500 ps (Fig. 2.3E) which in turn explains the large standard deviation in panel F.

To increase the specificity for caspase-2, the substrate cleavage motif was changed from VDVAD to VDTTD. This change has been reported to increase the sensitivity by 4-fold and the specificity for caspase-2 over the caspase-3 substrate motif DEVD(G) by 2-fold (Fig. 2.4A; Kitevska et al. 2014). In our assay, the change to VDTTD indeed resulted in a higher sensitivity to caspase activation indicated by the increase in REA from 65% to 81% upon STS treatment.

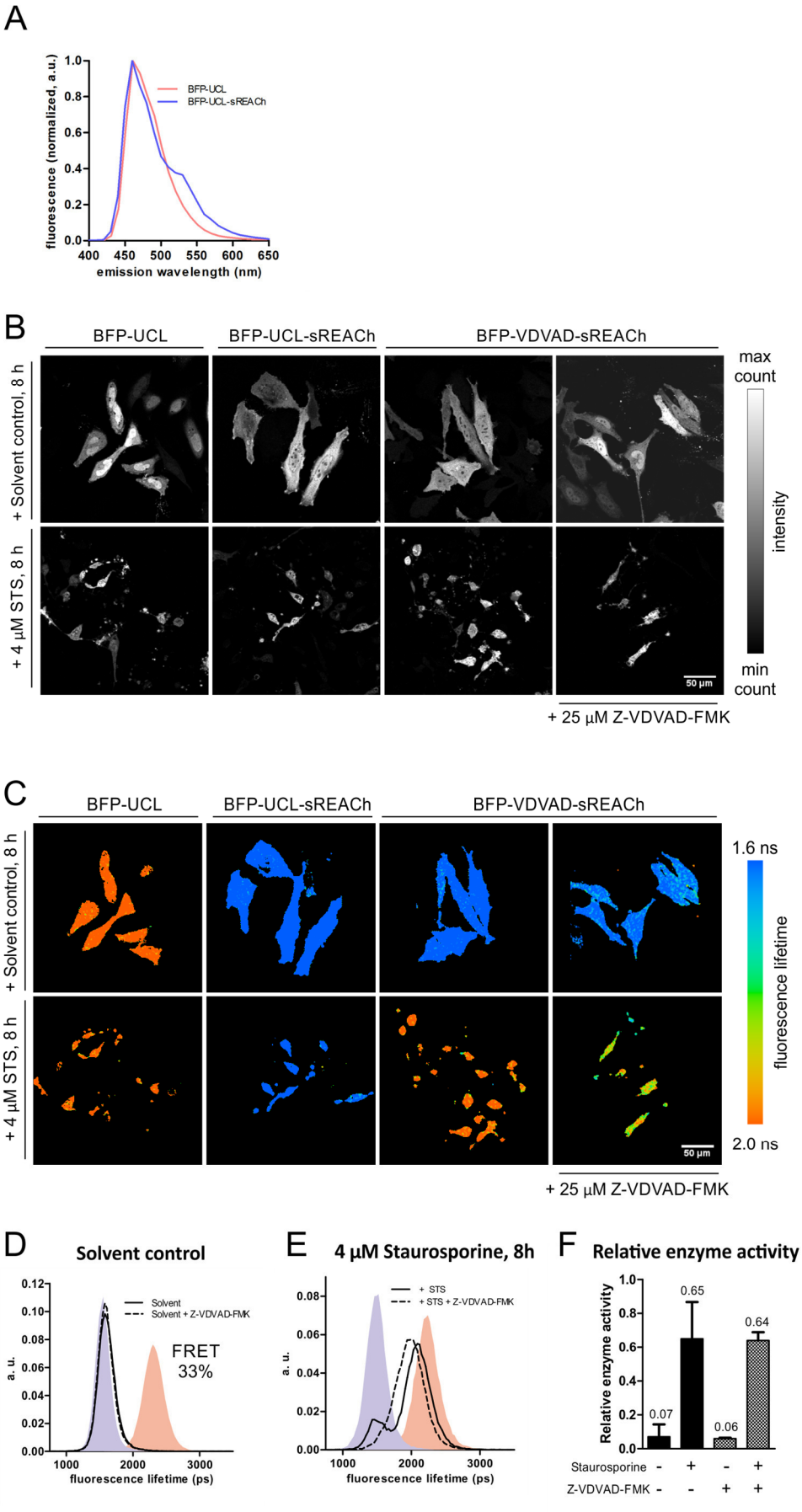
A
fluorescence (normalized, a.u.)
emission wavelength (nm)
BFP-UCL
BFP-UCL-sREACh
B
BFP-UCL
BFP-UCL-sREACh
BFP-VDVAD-sREACh
+ Solvent control, 8 h
+ 4 µM STS, 8 h
max count
intensity
min count
50 µm
+ 25 µM Z-VDVAD-FMK
C
BFP-UCL
BFP-UCL-sREACh
BFP-VDVAD-sREACh
+ Solvent control, 8 h
+ 4 µM STS, 8 h
1.6 ns
fluorescence lifetime
2.0 ns
50 µm
+ 25 µM Z-VDVAD-FMK
D
Solvent control
Solvent
Solvent + Z-VDVAD-FMK
FRET
33%
a. u.
fluorescence lifetime (ps)
E
4 µM Staurosporine, 8h
+ STS
+ STS + Z-VDVAD-FMK
a. u.
fluorescence lifetime (ps)
F
Relative enzyme activity
Relative enzyme activity
0.07
0.65
0.06
0.64
Staurosporine - + - +
Z-VDVAD-FMK - - + +

Figure 2.3 – **Characterization of a mTagBFP-sREACh as caspase-2 FRET biosensor for FLIM**

A: Fluorescence emission upon excitation with 840 nm two-photon excitation of donor-only controls (red) and uncleavable controls (blue).

B: Representative intensity images (photon counts per pixel) of HeLa cells transiently transfected with indicated constructs after 8 hours STS or control treatment in the absence or presence of irreversible caspase-2 inhibitor Z-VDVAD-FMK.

C: Fluorescence lifetime images of cells shown in B.

D, E: Fluorescence lifetime distribution of control-treated cells (D) and cells treated with 4 µM STS (E) for 8 hours in the absence (solid lines) or presence (dashed lines) of indicated inhibitors at 25 µM. Blue and red shaded curves show distributions of UCL and donor-only controls, respectively.

F: Relative enzyme activity values computed from the respective lifetime distributions as shown in Fig. 2.2B. Bars show means and standard deviations.

Data are from three independent experiments with at least 20 cells per experiment and condition.

The specificity as judged by the decrease of REA upon inhibitor treatment has also increased (65% to 64% (VDVAD); 84% to 60% (VDTTD)) (Fig. 2.4B-F).

To complete the characterization of this sensor, expression and cleavage were analysed by Western Blot on whole cell lysates of HeLa cells that were prepared using the same protocol as for the FLIM experiments (Figure 2.4G). Both linker sequences were included for comparison. All constructs showed good expression at the expected molecular weights. We

found that the lower molecular weight fragments that are present in all samples are due to fragmentation of the fluorescent proteins during denaturation in SDS-containing loading buffer, since lowering the temperature for denaturation reduced the amount of fragmentation (not shown). This has previously been observed for DsRed-like fluorophores (such as mTagBFP) with the breakpoint just before the chromophore resulting in the observed band pattern (Costantini et al., 2012).

Upon STS treatment both linkers were efficiently cleaved, whereas the controls remained unchanged. Treatment with the caspase-2 inhibitor Z-VDVAD-FMK resulted in partial rescue of cleavage, in line with the partial rescue observed by FLIM. Quantification of the cleavage showed that as observed by FLIM, VDTTD was cleaved more efficiently than VDVAD (1.7-fold) upon STS treatment and showed a slight increase in rescue upon inhibitor treatment (1.2-fold, Figure 2.4H)

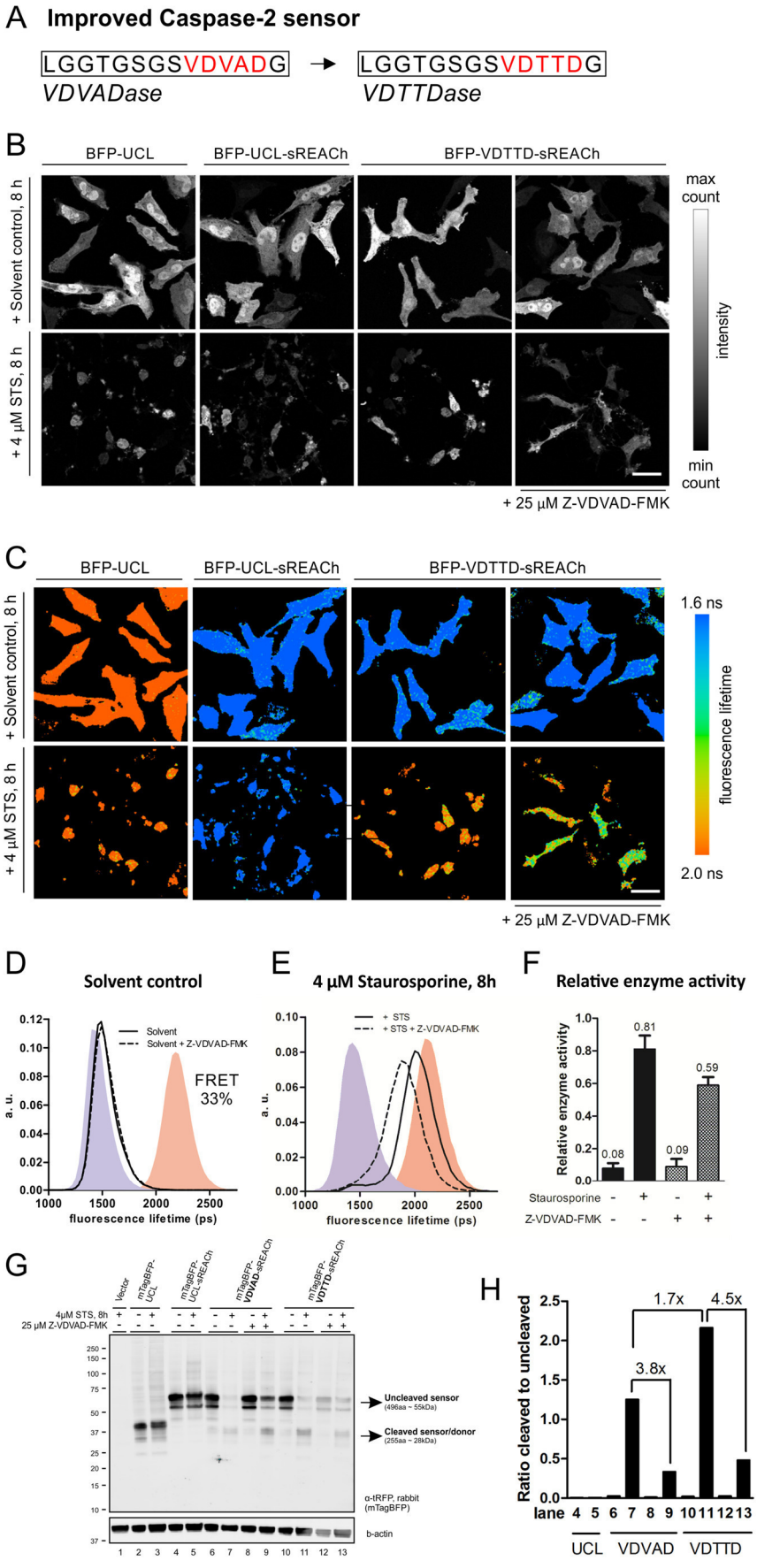
A Improved Caspase-2 sensor
LGGTGSGSVDVADG
VDVADase
LGGTGSGSVDTTDG
VDTTDase
B
BFP-UCL
BFP-UCL-sREACh
BFP-VDTTD-sREACh
+ Solvent control, 8 h
+ 4 µM STS, 8 h
max count
intensity
min count
+ 25 µM Z-VDVAD-FMK
C
BFP-UCL
BFP-UCL-sREACh
BFP-VDTTD-sREACh
+ Solvent control, 8 h
+ 4 µM STS, 8 h
1.6 ns
fluorescence lifetime
2.0 ns
+ 25 µM Z-VDVAD-FMK
D
Solvent control
Solvent
Solvent + Z-VDVAD-FMK
FRET 33%
a. u.
fluorescence lifetime (ps)
E
4 µM Staurosporine, 8h
+ STS
+ STS + Z-VDVAD-FMK
a. u.
fluorescence lifetime (ps)
F
Relative enzyme activity
Relative enzyme activity
0.08
0.81
0.09
0.59
Staurosporine
Z-VDVAD-FMK
G
Vector
mTagBFP-UCL
mTagBFP-UCL-sREACh
mTagBFP-VDVAD-sREACh
mTagBFP-VDTTD-sREACh
4µM STS, 8h
25 µM Z-VDVAD-FMK
Uncleaved sensor
(496aa ~ 55kDa)
Cleaved sensor/donor
(255aa ~ 28kDa)
α-tRFP, rabbit
(mTagBFP)
b-actin
H
Ratio cleaved to uncleaved
1.7x
4.5x
3.8x
lane
UCL
VDVAD
VDTTD

Figure 2.4 – **Improvement of caspase-2 sensing of mTagBFP-sREACh FRET pair**

A: Original and improved peptide linker sequences are shown with the caspase-2 cleavage site in red.

B: Representative intensity images (photon counts per pixel) of HeLa cells transiently transfected with indicated constructs after 8 hours STS or control treatment in the absence or presence of irreversible caspase-2 inhibitor Z-VDVAD-FMK.

C: Representative fluorescence lifetime images of cells in B. Scale bars are 50 µm.

D, E: Fluorescence lifetime distribution of control-treated cells (D) and cells treated with 4 µM STS (E) for 8 hours in the absence (solid lines) or presence (dashed lines) of indicated inhibitors both at 25 µM. Blue and red shaded curves show distributions of UCL and donor-only controls, respectively.

F: Relative enzyme activity values computed from the respective lifetime distributions. Bars show means and standard deviations. B-F: Data from three independent experiments with at least 20 cells per experiment and condition.

G: Western Blot of HeLa cells transiently transfected with indicated constructs and treated as in B-F. mTagBFP expression was detected using a tRFP antibody and beta-actin is shown as loading control. Multiple bands correspond to FP cleavage during denaturation (see main text for details).

H: Quantification of the Western Blot shown in G for the indicated lanes, and shown as the ratio of cleaved over the uncleaved sensor with fold changes indicated. G-H: Data from one experiment.

Development of additional blue fluorescent FRET pairs for multiplexing

Aiming to find truly non-fluorescent alternatives for sREACh that would be better suited for multiplexing, we screened literature for chromoproteins that may suitable acceptor for mTagBFP. We tested CRY2PHR, bfloGFPc1 and ShadowG (Figure 2.5, Tables 2.1-2.2),

which all have been reported to be nonfluorescent (Bomati et al., 2014; Kennedy et al., 2010; Murakoshi et al., 2015).

CRY2PHR showed no residual fluorescence and 11% FRET, but strongly aggregated in all cells (Fig. 2.5A-C). To reduce the aggregation, CY2PHR was systematically truncated to find the minimal domain that could be still mediate chromophore formation and exhibit FRET, but all fragments showed similar or increased aggregation and lower FRET efficiencies (Fig. 2.5D-E).

BfloGFPc1 was also completely dark and exhibited 16% FRET efficiency, which increased to 21% after removal of a GFP-like N-terminal sequence (MVSKGEEDNMA) that we had added during synthesis to promote folding (Fig. 2.5F-G). Both bfloGFPc1 constructs showed aggregation in approximately a third of the cells (Fig. 2.5H).

Next, we tested ShadowG, a chromoprotein derived from sREACh by others with the aim to reduce its residual quantum yield (Murakoshi et al., 2015). ShadowG showed a two-fold decrease of residual fluorescence compared to sREACh in our experimental conditions and

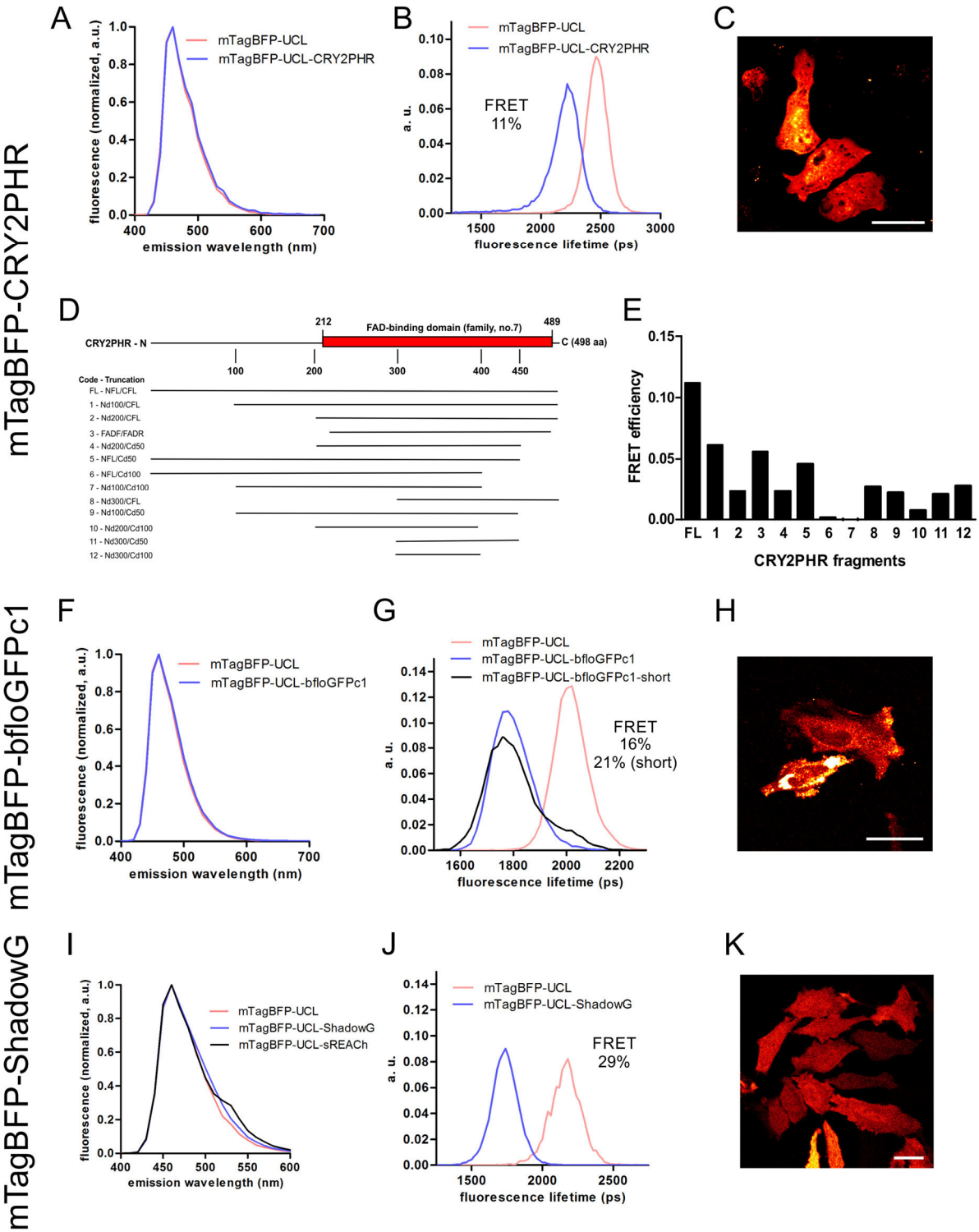

Figure 2.5 – **Alternative FRET pairs tested to replace mTagBFP-sREACh**

A-E: **mTagBFP-CRY2PHR.** A: Fluorescence emission spectra of transiently transfected HeLa cells upon 840 nm 2PE for donor-only (red line) and UCL-control (blue line). B: Fluorescence lifetime distribution for cells in panel A showing 11% FRET. C: Representative intensity (photon counts per pixel) from FLIM measurements of HeLa cells expressing mTagBFP-UCL-CRY2PHR, coloured to show aggregation in bright yellow. D: Schematic of

CRY2PHR domain structure with coverage of 12 cloned truncations constructs. E: FRET efficiency measured by FLIM for constructs shown in E.

F-H: **mTagBFP-bfloGFPc1**. F: Fluorescence emission of transiently transfected HeLa cells upon 840 nm 2PE for donor-only (red line) and UCL-control (blue line). G: Fluorescence lifetime distribution for cells in F showing 16% FRET efficiency for long version and 21% for short version (see main text). H: Confocal image of representative HeLa cells expressing mTagBFP-bfloGFPc1 coloured to show aggregation in white.

I-K: **mTagBFP-ShadowG** I: Fluorescence emission of transiently transfected HeLa cells upon 840 nm 2PE for donor-only (red line) and UCL-control (blue line). J: Fluorescence lifetime distribution for cells in panel I showing 29% FRET efficiency. H: Representative confocal images of HeLa cells expressing mTagBFP-UCL-ShadowG showing homogeneous expression without visible aggregation.

A-B, E-G and I-J show averages of at least 10 cells per construct from one experiment. Scale bars are 30 µm.

exhibited ~30% FRET. Similarly to sREACh, moderate aggregation of ShadowG was observed in the green channel, but without affecting fluorescence lifetime measurements (Figure 2.5I-K). Taken together, mTagBFP-ShadowG is a slightly better FRET pair compared to mTagBFP-sREACh. However, as this FRET pair was cloned after a significant amount of experiments on caspase biology had already been performed and ShadowG still exhibited residual fluorescence emission, all following experiments were carried out with sREACh.

In summary, we identified in mTagBFP-VDTTD-sREACh as a suitable caspase-2 FRET-sensor for multiplexing.

2.3.2 Development of a green FRET pair for multiplexing

As donor for the green fluorescent pair, mAmetrine was chosen due to it exceptional brightness and long Stokes shift that allows two-photon excitation at 840 nm (Table 2.1). Due to its putative high Förster radius, we selected a chromoprotein previously identified in the stony coral *Montipora spongodes* as acceptor, msCP576, originally reported simply as Keima clone number 20 (Kogure et al., 2006). msCP576 was used to evolve the long Stokes shifted red fluorescent protein mKeima and, at the best of our knowledge, it has not been used since for any application.

In contrast to sREACh, no residual fluorescence of msCP576 was detected, making it an ideal dark acceptor (Figure 2.6A). Furthermore, mAmetrine-msCP576 exhibited 44% FRET efficiency as measured by FLIM, providing opportunities for higher dynamic ranges compared to mTagBFP-sREACh with 33% (Fig. 2.6 C-F).

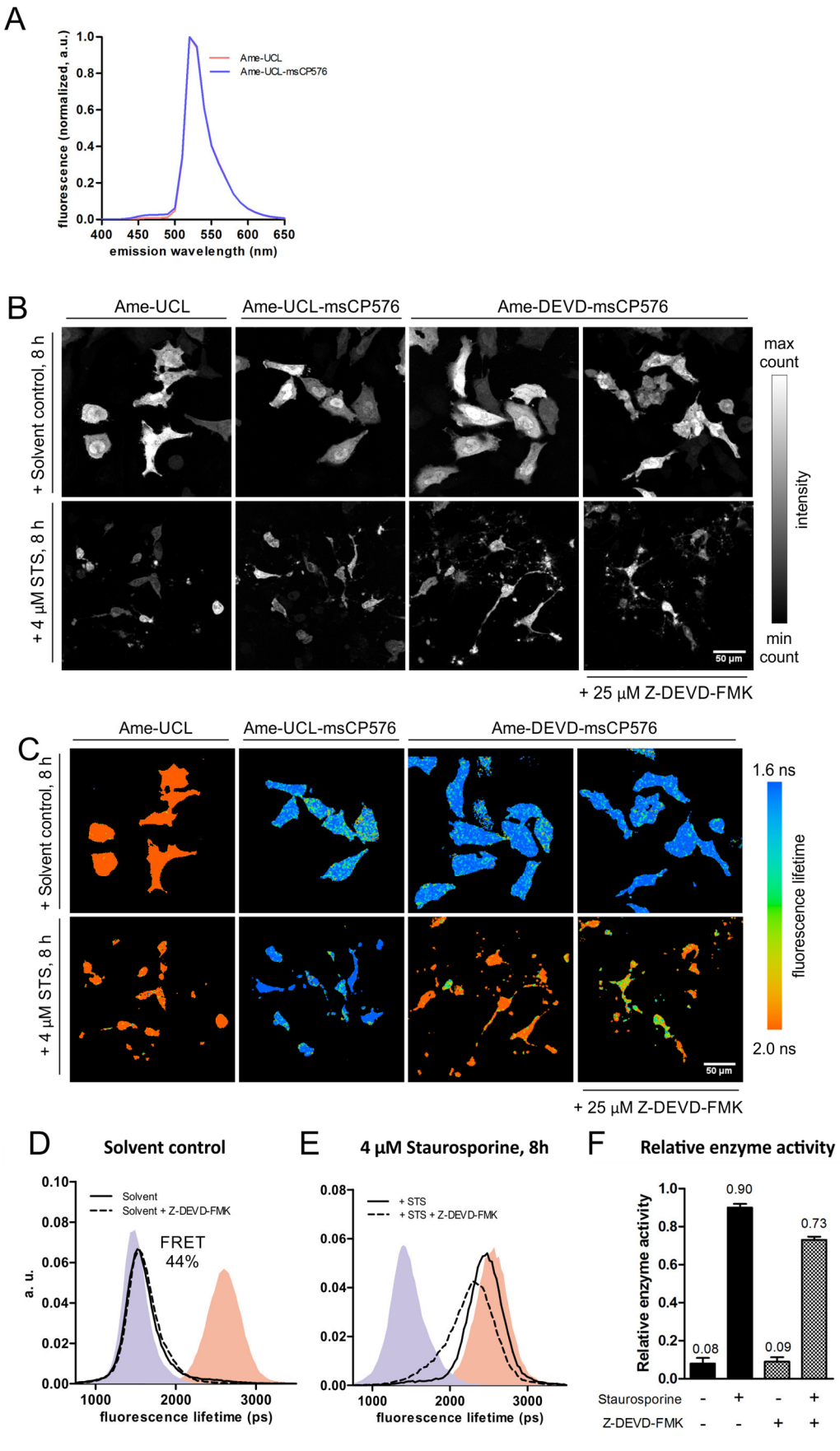
A
fluorescence (normalized, a.u.)
emission wavelength (nm)
Ame-UCL
Ame-UCL-msCP576
B
Ame-UCL
Ame-UCL-msCP576
Ame-DEVD-msCP576
+ Solvent control, 8 h
+ 4 µM STS, 8 h
max count
intensity
min count
50 µm
+ 25 µM Z-DEVD-FMK
C
Ame-UCL
Ame-UCL-msCP576
Ame-DEVD-msCP576
+ Solvent control, 8 h
+ 4 µM STS, 8 h
1.6 ns
fluorescence lifetime
2.0 ns
50 µm
+ 25 µM Z-DEVD-FMK
D
Solvent control
Solvent
Solvent + Z-DEVD-FMK
FRET
44%
a. u.
fluorescence lifetime (ps)
E
4 µM Staurosporine, 8h
+ STS
+ STS + Z-DEVD-FMK
fluorescence lifetime (ps)
F
Relative enzyme activity
Relative enzyme activity
0.08
0.90
0.09
0.73
Staurosporine
Z-DEVD-FMK

Figure 2.6 – **Characterization of mAmetrine-msCP576 as caspase-3 FRET biosensor for FLIM**

A: Fluorescence emission upon excitation with 840 nm two-photon excitation of donor-only controls (red line) and uncleavable controls (blue line). Ame, mAmetrine.

B: Representative intensity images (photons per pixel) of HeLa cells transiently transfected with indicated constructs after 8 hours STS or control treatment in the absence or presence of irreversible caspase-3 inhibitor Z-DEVD-FMK.

C: Representative fluorescence lifetime images of cells in B. Scale bars are 50 µm.

D, E: Fluorescence lifetime distribution of control-treated cells (D) and cells treated with 4 µM STS (E) for 8 hours in the absence (solid lines) or presence (dashed lines) of indicated inhibitors at 25 µM. Blue and red shaded curves show distributions of UCL and donor-only controls, respectively.

F: Relative enzyme activity values computed from the respective lifetime distributions. Bars show means and standard deviations.

Data are from three independent experiments with at least 20 cells per experiment and condition.

Next, a linker was inserted containing DEVDG as canonical substrate cleavage motif for caspase-3 (Fig. 2.2; Tyas et al., 2000). Treatment with STS resulted in near complete cleavage of the linker as indicated by a relative enzymatic activity of ~90%. Caspase-3 inhibition partially prevented cleavage (Fig. 2.6 D-F) reducing REA to ~70%.

However, we noticed that the expression of this sensor was low and barely sufficient for imaging and that in those rare cells with high expression, visible aggregates exhibiting low fluorescence lifetime occurred (Fig. 2.7A). Aggregation is a frequent issue with new fluorescent proteins and chromoproteins such as msCP576. For mAmetrine-msCP576, we hypothesized that incorrect expression of msCP576 was caused by the suboptimal mammalian codon usage of the original coral gene that, in turn, may cause also aggregation if msCP576 would be frequently mistranslated (Dobson, 2004). We, therefore, replaced msCP576 with a humanized version of the gene (msCP576h) obtained by gene synthesis introducing 147 silent point mutations (Fig. 2.7B-C). As shown in Figure 2.7A, the expression was markedly increased by the optimization while maintaining FRET. Aggregation in highly expressing cells still occurred, but only in very bright cells and, therefore, we decided to select mAmetrine-msCP576h as FRET pair amenable for multiplexing. Stable monoclonal cell lines selected for medium-expression level of the construct should harness the advantages of this FRET pair yet not exhibiting aggregation.

Next, we aimed to increase the specificity of the sensor for caspase-3 because the limited rescue by Z-DEVD-FMK (Fig. 2.6F) upon STS treatment suggested a specificity lower than desirable. The canonical linker DEVDG (in general referred to as DEVD) has been shown to be cleaved efficiently by caspase-8 and caspase-7, and to a lesser degree by caspase-1 and

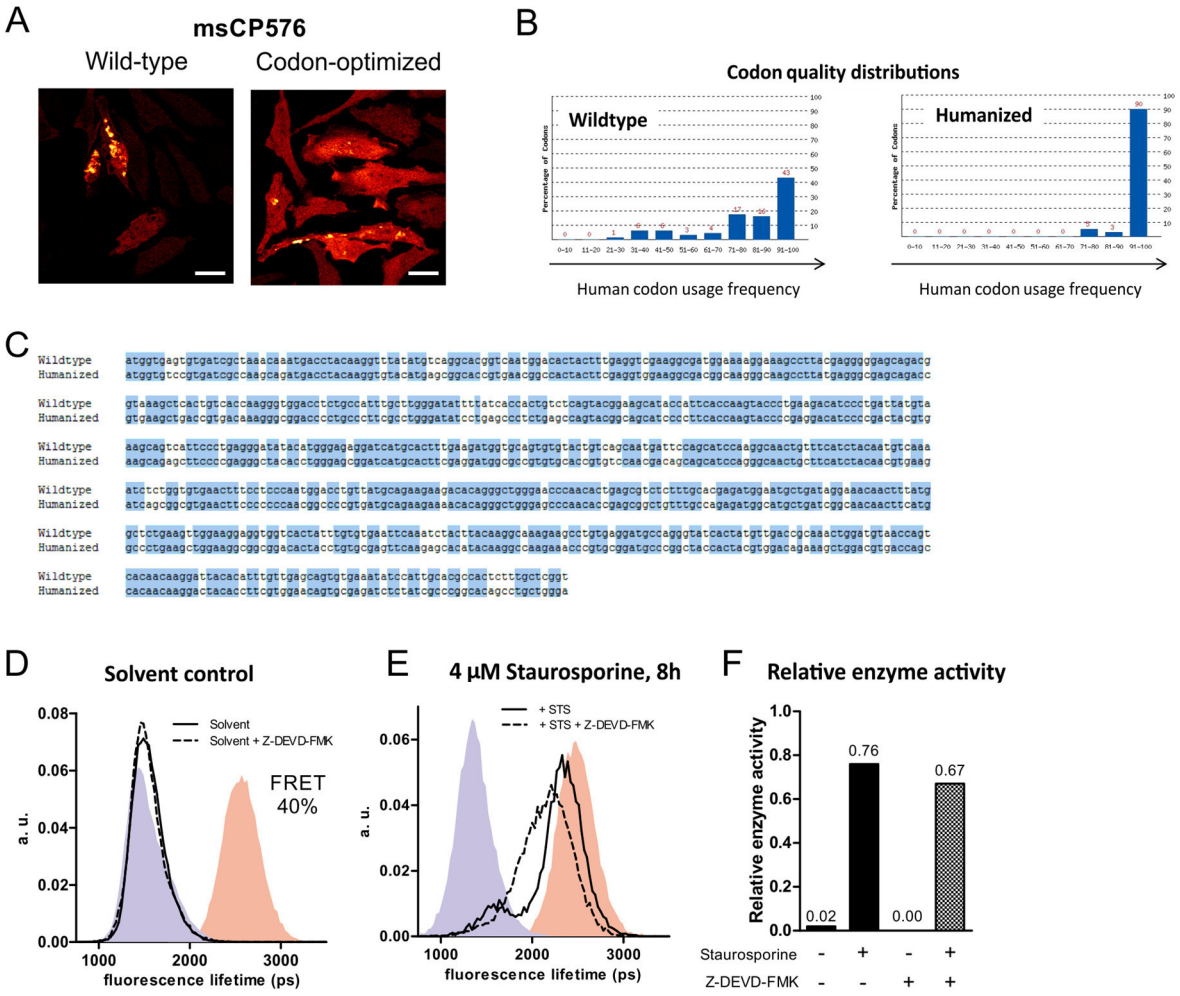

Figure 2.7 – **Optimization of mAmetrine-msCP576 by msCP576 codon optimization**

A: Representative confocal images for wild-type (left) and codon-optimized (right) mAmetrine-DEVD-msCP576 FRET pair expressed in HeLa cells upon 840 nm 2PE excitation are shown. Scale bars are 30 µm.

B: Human codon usage frequency for wild-type (left) and codon-optimized (right) msCP576 created during synthesis of the new gene.

C: Sequence comparison of the wild-type and codon-optimized cDNA of msCP576, with consensus highlighted in blue.

D, E: Fluorescence lifetime distribution of HeLa cells expressing the mAmetrine-msCP576h caspase-3 FRET sensor containing the codon-optimized msCP576h treated with solvent control (D) 4 µM STS (E) for 8 hours in the absence (solid lines) or presence (dashed lines) of indicated inhibitors at 25 µM. Blue and red shaded curves show distributions of UCL and donor-only controls, respectively.

F: Relative enzyme activity values computed from the respective lifetime distributions.

A, D-F: Data are from one experiment with at least 20 cells per condition.

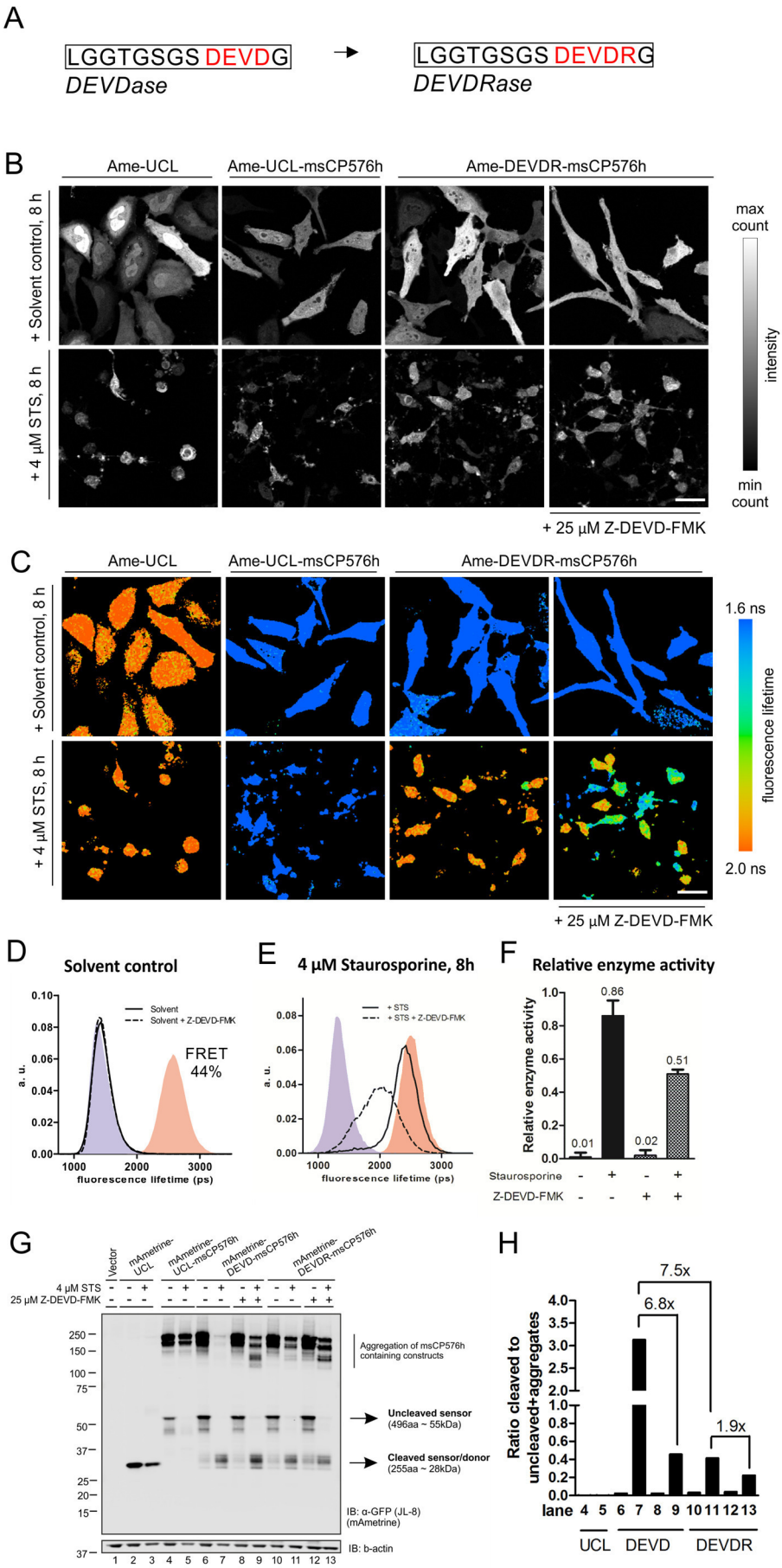
A
LGGTGSGS DEVDG
DEVDase
LGGTGSGS DEVDRG
DEVDRase
B
Ame-UCL
Ame-UCL-msCP576h
Ame-DEVDR-msCP576h
+ Solvent control, 8 h
+ 4 µM STS, 8 h
max count
intensity
min count
+ 25 µM Z-DEVD-FMK
C
Ame-UCL
Ame-UCL-msCP576h
Ame-DEVDR-msCP576h
+ Solvent control, 8 h
+ 4 µM STS, 8 h
1.6 ns
fluorescence lifetime
2.0 ns
+ 25 µM Z-DEVD-FMK
D
Solvent control
Solvent
Solvent + Z-DEVD-FMK
FRET 44%
a. u.
fluorescence lifetime (ps)
E
4 µM Staurosporine, 8h
+ STS
+ STS + Z-DEVD-FMK
a. u.
fluorescence lifetime (ps)
F
Relative enzyme activity
Relative enzyme activity
0.86
0.51
0.01
0.02
Staurosporine
Z-DEVD-FMK
G
Vector
mAmetrine-UCL
mAmetrine-UCL-msCP576h
mAmetrine-DEVD-msCP576h
mAmetrine-DEVDR-msCP576h
4 µM STS
25 µM Z-DEVD-FMK
Aggregation of msCP576h containing constructs
Uncleaved sensor (496aa ~ 55kDa)
Cleaved sensor/donor (255aa ~ 28kDa)
IB: α-GFP (JL-8) (mAmetrine)
IB: b-actin
H
7.5x
6.8x
1.9x
Ratio cleaved to uncleaved+aggregates
lane
UCL
DEVD
DEVDR

Figure 2.8 – **Improvement of caspase-3 sensing of mAmetrine-msCP576h FRET pair**

A: Original and improved peptide linker sequences are shown with the caspase-3 cleavage site in red.

B: Representative intensity images (photons per pixel) of HeLa cells transiently transfected with indicated constructs containing msCP576h after 8 hours 4 µM STS or control treatment in the absence or presence of irreversible caspase-3 inhibitor Z-DEVD-FMK at 25 µM. Ame, mAmetrine.

C: Representative fluorescence lifetime images of cells in B. Scale bars are 50 µm.

D, E: Fluorescence lifetime distribution of control-treated cells (D) and cells treated with 4 µM STS (E) for 8 hours in the absence (solid lines) or presence (dashed lines) of indicated inhibitors both at 25 µM. Blue and red shaded curves show distributions of UCL and donor-only controls, respectively.

F: Relative enzyme activity values computed from the respective lifetime distributions. Bars show mean and standard deviation.

B-F: Data from three independent experiments with at least 20 cells per experiment and condition.

G: Western Blot of HeLa cell lysates transiently transfected with indicated constructs and treated as in B-F. mAmetrine expression was detected using a GFP (JL-8) antibody and b-actin is shown as loading control. Multiple bands correspond due FP cleavage during denaturation and higher molecular weight bands are functional, aggregated sensors (see main text).

H: Quantification of Western Blot in panel G for the indicated lanes, and shown as the ratio of cleaved over the sum of uncleaved and aggregated sensor with fold changes indicated.

G-H: Data from one experiment.

caspase-6 *in vitro* (Stennicke et al., 2000). In contrast, the change to DEVDR was reported to result in a decrease of cleavage for all those caspases by 1-2 orders of magnitude (300-fold

for caspase-8, 108-fold for caspase-1, 88-fold for caspase-7, 36-fold for caspase-6) while only decreasing processing by caspase-3 by 14-fold, and thereby resulting in the net increase in specificity for caspase-3 (ibid.). Furthermore, assessing the effect of the change to DEVDR in cells, Albeck *et al.* showed a 4-fold decrease of processing by caspase-8 upstream of mitochondrial outer membrane permeabilization compared to DEVD (MOMP; Albeck et al. 2008). In our hands, the DEVDR-based caspase-3 sensor was indeed significantly more specific for caspase-3, resulting in a loss of REA of ~40% (from ~90% to 50%) instead of ~10% (80% to 70%) upon caspase-3 inhibitor treatment for the DEVDG linker (Fig. 2.8B-G). Thus, the efficiency of cleavage in response to STS was maintained, while increasing specificity (compare Fig. 2.6F and 2.8F).

We completed the characterization of the sensor by monitoring sensor expression and cleavage by Western Blot,including both linker sequences (Fig. 2.8G-H). The FRET pairs are generally well expressed and exhibit the expected molecular weights albeit showing the degradation bands already discussed for mTagBFP-sREACh (Fig. 2.4G). Furthermore, specific high-molecular-weight bands between 200-250 kDa were present for all mAmetrine-msCP576-containing constructs. These bands likely correspond to the aggregation we

observed microscopically in highly expressing cells and seem to be resistant to denaturation, but are cleaved when treated with STS, indicating the presence of a functional sensor. We, therefore, summed the intensity of the putative aggregates as well as the monomeric 55 kDa

band for the quantification of the Western Blot. As shown in Figure 2.8H, the change to DEVDR resulted in a 7.5-fold decrease in cleavage upon STS treatment, in line with the reported decrease *in vitro* (Stennicke et al., 2000). We noted that this decrease in sensitivity was not observed by FLIM (Compare Fig. 2.6F and Fig. 2.8F). Upon caspase-3 inhibitor treatment, DEVD showed a 6.8-fold decrease in cleavage compared to 1.9-fold for DEVDR indicating that at least on Western Blot, the increase in specificity observed by FLIM could not be observed.

These discrepancies between Western Blot and FLIM measurements are currently investigated further by performing repeats of the Western Blot, but based on the FLIM results from three independent experiments with very little variation between the experiments, we decided to continue with the DEVDR linker for further FLIM-based studies.

In summary, we found mAmetrine-DEVDR-msCP576h to be an excellent FRET pair for multiplexing and a suitable sensor for caspase-3 substrate cleavage by FLIM.

Adaptation of mAmetrine-msCP576h as caspase-9 sensor

Because of its excellent suitability for multiplexing and major challenges in constructing a red fluorescent caspase-9 sensor, we replaced the DEVDR linker with LEHD (Thornberry et al., 1997) to be able to sense caspase-9 sensor cleavage and multiplex the blue caspase-2 sensor both with caspase-3 and caspase-9. This flexibility is also useful when the red part of the spectrum is used for other, non-FRET-based, detection.

When treated with STS, FRET efficiency decreased by 20% corresponding to 50% REA (Fig. 2.9A-E). Upon Z-LEHD-FMK inhibitor treatment, cleavage was almost completely lost, indicating a very high specificity of the linker for caspase-9. Those observations were confirmed by Western Blot (Fig. 2.9F-G). The incomplete cleavage of the caspase-9 sensor compared to near complete cleavage of the tested caspase-2 and caspase-3 sensor is likely reflecting differences in the enzymatic activity of these enzymes, with caspase-9 enzyme activity being low (Garcia-Calvo et al., 1999) and reported to be inactivated rapidly after activation (Malladi et al., 2009).

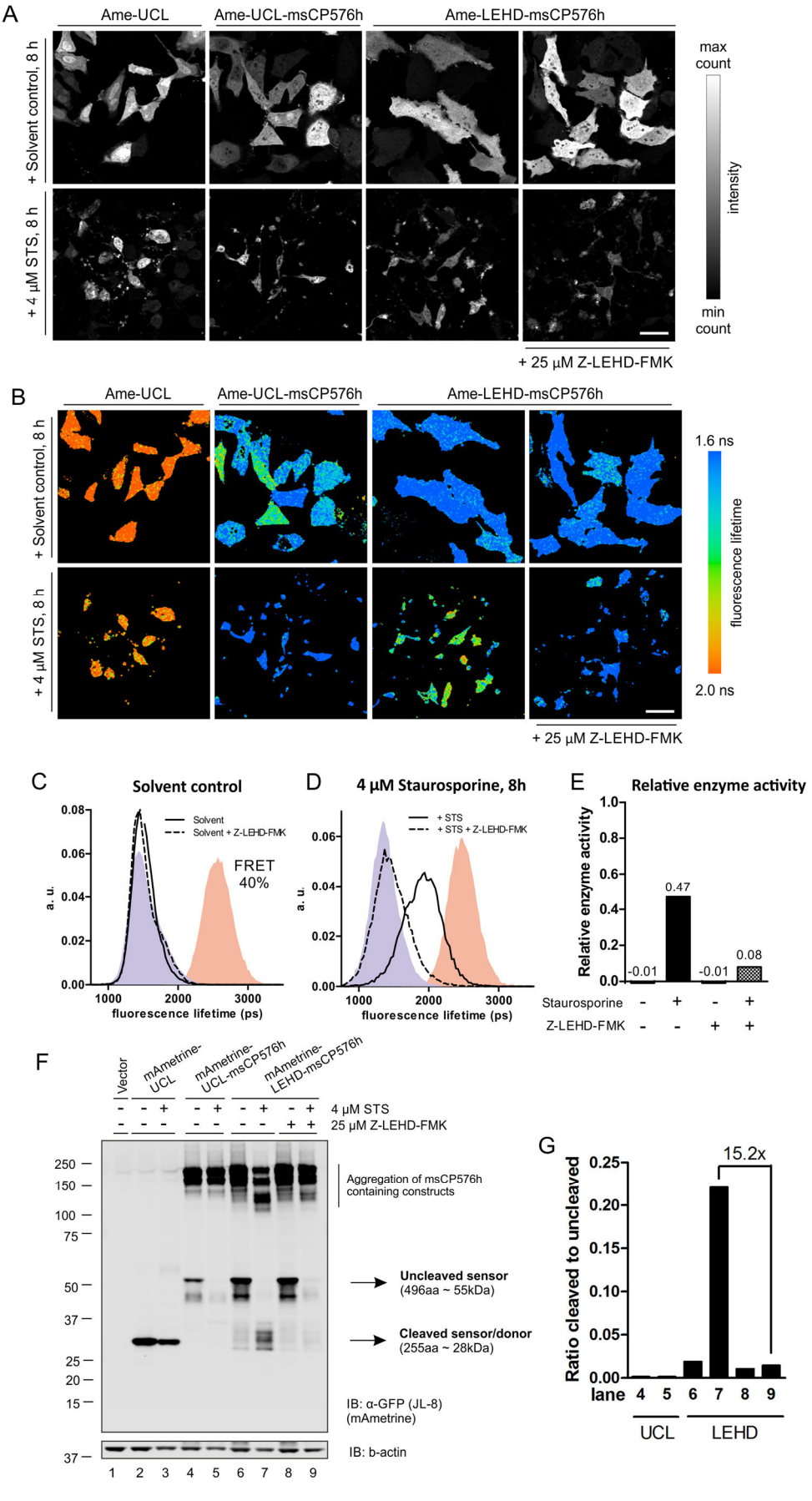
A
Ame-UCL
Ame-UCL-msCP576h
Ame-LEHD-msCP576h
+ Solvent control, 8 h
+ 4 µM STS, 8 h
max count
intensity
min count
+ 25 µM Z-LEHD-FMK
B
Ame-UCL
Ame-UCL-msCP576h
Ame-LEHD-msCP576h
+ Solvent control, 8 h
+ 4 µM STS, 8 h
1.6 ns
fluorescence lifetime
2.0 ns
+ 25 µM Z-LEHD-FMK
C
Solvent control
Solvent
Solvent + Z-LEHD-FMK
FRET 40%
a. u.
fluorescence lifetime (ps)
D
4 µM Staurosporine, 8h
+ STS
+ STS + Z-LEHD-FMK
a. u.
fluorescence lifetime (ps)
E
Relative enzyme activity
Relative enzyme activity
0.47
-0.01
-0.01
0.08
Staurosporine - + - +
Z-LEHD-FMK - - + +
F
Vector
mAmetrine-UCL
mAmetrine-UCL-msCP576h
mAmetrine-LEHD-msCP576h
4 µM STS
25 µM Z-LEHD-FMK
Aggregation of msCP576h containing constructs
Uncleaved sensor (496aa ~ 55kDa)
Cleaved sensor/donor (255aa ~ 28kDa)
IB: α-GFP (JL-8) (mAmetrine)
IB: b-actin
G
15.2x
Ratio cleaved to uncleaved
lane 4 5 6 7 8 9
UCL
LEHD

Figure 2.9 – **Adaptation of mAmetrine-msCP576 as caspase-9 biosensor**

A: Representative intensity images (photons per pixel) of HeLa cells transiently transfected with indicated constructs after 8 hours in 4 µM STS or control treatment in the absence of presence of irreversible caspase-9 inhibitor Z-LEHD-FMK at 25 µM.

B: Representative fluorescence lifetime images of cells in A. Scale bars are 50 µm.

C, D: Fluorescence lifetime distribution of control-treated cells (C) and cells treated with 4 µM STS (D) for 8 hours in the absence (solid lines) or presence (dashed lines) of Z-LEHD-FMK at 25 µM. Blue and red shaded curves show distributions of UCL and donor-only controls, respectively.

E: Relative enzyme activity values computed from the respective lifetime distributions. Bars show mean and standard deviation.

A-E: Data from three independent experiments with at least 20 cells per experiment and condition.

F: Western Blot of HeLa cell lysates transiently transfected with indicated constructs and treated as in A-F. mAmetrine expression was detected using a GFP (JL-8) antibody and b-actin is shown as loading control. Multiple bands correspond due FP cleavage during denaturation and higher molecular weight bands are functional, aggregated sensors (see main text).

G: Quantification of Western Blot in G for the indicated lanes, and shown as the ratio of cleaved over the sum of uncleaved and aggregated sensor with fold changes indicated. F-G: Data from one experiment.

2.3.3 Development of a red FRET pair for multiplexing

The development of a red fluorescent FRET pair that is excitable at 840 nm together with the green and the blue fluorescent pairs described above has been a central challenge in the development of this multiplexing platform.

First, we have tested all the long Stokes shift red fluorescent proteins (LSS-RFPs) available at the time: mKeima, LSS-mKate1, LSS-mKate2 and mBeRFP (see table Table 2.1 for details). As shown in Figure 2.10A, all LSS-RFPs show varying levels of green fluorescence at 840 nm two-photon excitation, which were generally found to be more pronounced than originally published, at least in our experimental conditions. Since for fast and efficient multiplexing minimal spectral overlap between the FRET pairs is crucial, mKeima was chosen as donor for the development of red FRET pairs, because it exhibited the least green fluorescence. Previously, mKeima had only been used as internal standard for spectral FRET imaging for CFP/YFP-like pairs, but not as FRET donor/acceptor itself (Kumagai et al., 2011).

As acceptors, three proteins were identified that exhibited a sufficiently high extinction coefficient and spectral overlap with mKeima to provide a high Förster radius, thus being good candidates for acceptors when paired with mKeima (Tables 2.1 and 2.2.): cjBlue, iRFP713 and NirFP.

First, the tetrameric non-fluorescent chromoprotein cjBlue was tested (Chan et al., 2006). We found that mKeima-cjBlue strongly aggregated in more than 90% of the cells rendering it unusable (Fig. 2.10B). When the emission at 840 nm 2PE was measured in few cells with less aggregation, no contribution to the overall fluorescence from cjBlue was observed, indicating that cjBlue is indeed non-fluorescent under our experimental conditions (Fig. 2.10C). In those cells, we could quantify a FRET efficiency of 16% for mKeima-cjBlue by FLIM (Fig. 2.10D). This demonstrates that mKeima-cjBlue could be a useful FRET pair if the aggregation issue

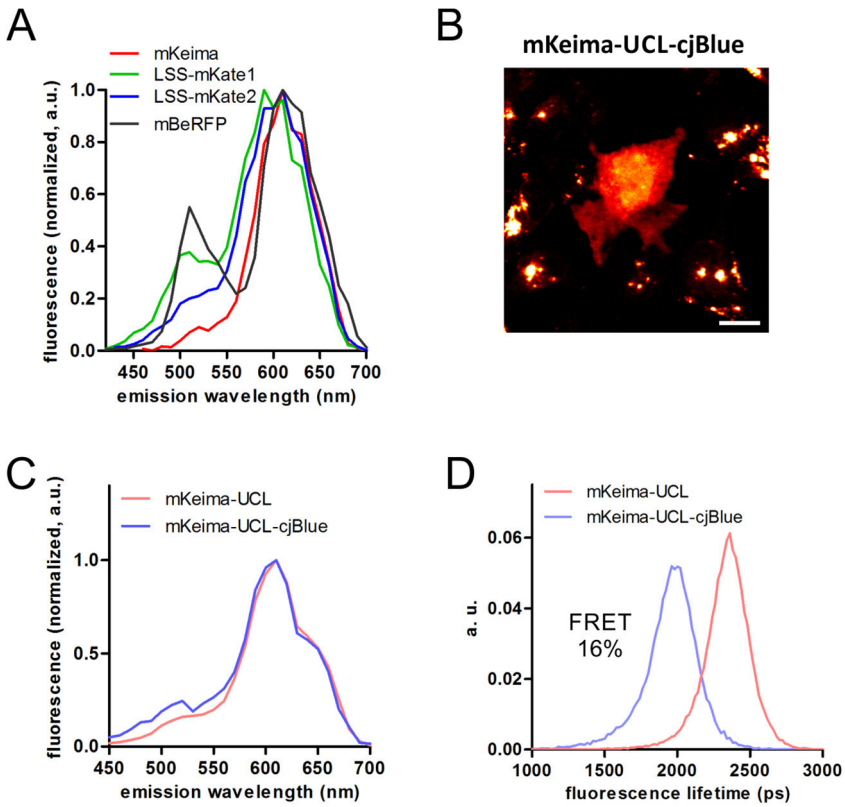

Figure 2.10 – **Donor and acceptor fluorophores for long Stokes shift red fluorescent FRET pairs**

A: Fluorescence emission spectra of HeLa cells transiently transfected with the indicated LSS-RFPs at 840 nm two-photon excitation. Lines are the average of at least 10 cells each and from one experiment.

B: Representative confocal image of HeLa cells transiently expressing mKeima-UCL-cjBlue, coloured to show aggregates in hotter colours. All visible aggregates around the cell in the centre of the field of view are inside neighbouring cells. Scale bar is 30 µm.

C: Fluorescence emission spectra of indicated constructs transiently expressed in HeLa cells at 840 nm 2PE.

D: Fluorescence lifetime distribution of indicated constructs transiently expressed in HeLa resulting in a FRET efficiency of 16%.

C-D: Data from one experiment with at least 5 cells per construct. Only cells with no or little visible aggregates were imaged.

was solved. To this end, co-workers performed mutagenesis on cjBlue to disrupt the tetramerization domain, based on the monomerizing mutations for related proteins Rmts5 and

DsRed (not shown). However, our attempts in monomerizing mKeima-cjBlue were not successful and, therefore, cjBlue was not further utilized.

Second, iRFP713 was used as an acceptor for mKeima. Dimeric iRFP713 belongs to a class of near-infrared fluorescent proteins that were evolved from bacterial phytochrome photoreceptors and that require the incorporation of the cofactor Biliverdin (BV) for maximal fluorescence (Filonov et al., 2011). Mammalian cells produce low levels of BV that is sufficient for 60% of maximal fluorescence, but the addition of exogenous BV is required for full fluorescence. Therefore, to test the mKeima-iRFP713 FRET pair, cells were incubated in a high, but nontoxic concentration of BV for 16 hours prior to the experiment. At 840 nm 2PE, iRFP713 did not seem to contribute to overall fluorescence at least in the spectral band we used to image mKeima (Fig. 2.11A). The use of short-pass filter at 700 nm that was required to separate the excitation and the emission optical paths for two-photon microscopy prevented us to detect possible fluorescence over 700 nm (ibid.).

The FRET pair was well expressed in HeLa cells with fewer than 10% of cells showing small fluorescent aggregates (Fig. 2.11D, upper row). The construct was excluded from the nucleus, likely due to the larger size of iRFP713 compared to GFP-like proteins (~250 amino acids for GFP, ~300 for iRFP). However, strong aggregation was observed in all dead, shrunk cells, likely due to the increase of the local concentration of the construct in a smaller volume, which could promote aggregation (Fig. 2.11D, lower row). These aggregates also exhibited a lower fluorescence lifetime (illustrated by a broadening of the blue distribution in Fig. 2.11G) and therefore higher FRET efficiency, likely caused by inter-molecular FRET caused by molecular crowding (Fig. 2.11E-H). Whereas 15% FRET efficiency was measured in untreated cells, dead cells exhibited 25% for the uncleavable (UCL) control (Fig. 2.11H). FRET was dependent on the presence of exogenous added BV, as was the appearance of low-lifetime aggregates which were less pronounced in the absence of BV (Fig. 2.11 D-H).

Despite this change in lifetime and aggregation in shrunk cells, we could still confirm sensor cleavage by FLIM (Fig. 2.11G-H) as well as Western Blot (Fig. 2.11B, C). Thus, mKeima-iRFP713 promised to be a good FRET pair with two limitations. First, it is not well-suited for applications where the cell volume decreases strongly, such as the study of cell death, which results in aggregations with high apparent FRET that complicate the analysis. Second, exogenous addition of BV is required for FRET, at least in HeLa cells, which must be

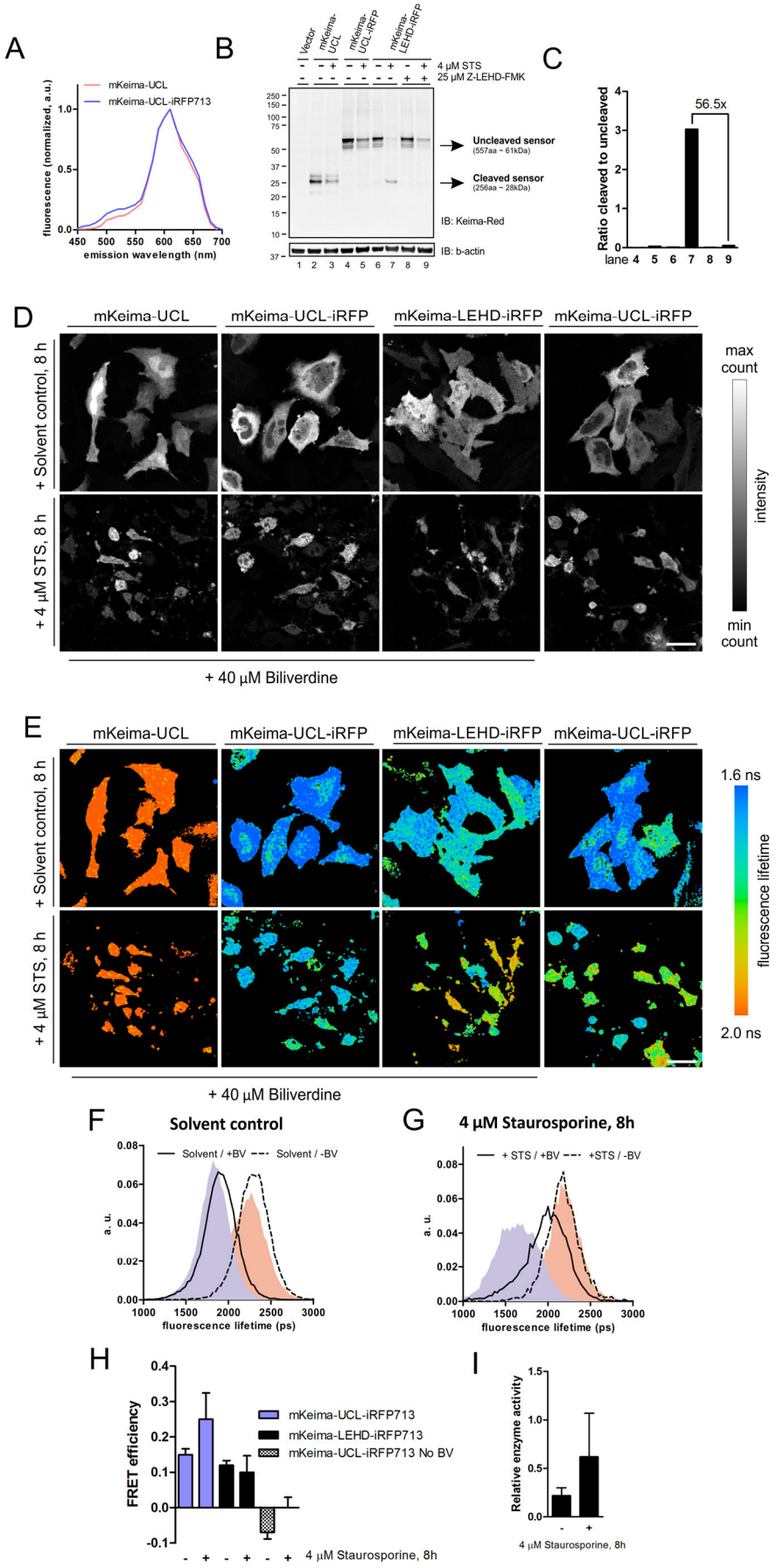
A
mKeima-UCL
mKeima-UCL-iRFP713
fluorescence (normalized, a.u.)
emission wavelength (nm)
B
Vector
mKeima-UCL
mKeima-UCL-iRFP
mKeima-LEHD-iRFP
4 µM STS
25 µM Z-LEHD-FMK
Uncleaved sensor
(557aa ~ 61kDa)
Cleaved sensor
(256aa ~ 28kDa)
IB: Keima-Red
IB: b-actin
C
Ratio cleaved to uncleaved
56.5x
lane
D
mKeima-UCL
mKeima-UCL-iRFP
mKeima-LEHD-iRFP
mKeima-UCL-iRFP
+ Solvent control, 8 h
+ 4 µM STS, 8 h
max count
intensity
min count
+ 40 µM Biliverdine
E
mKeima-UCL
mKeima-UCL-iRFP
mKeima-LEHD-iRFP
mKeima-UCL-iRFP
+ Solvent control, 8 h
+ 4 µM STS, 8 h
1.6 ns
flucrescence lifetime
2.0 ns
+ 40 µM Biliverdine
F
Solvent control
Solvent / +BV
Solvent / -BV
a. u.
fluorescence lifetime (ps)
G
4 µM Staurosporine, 8h
+ STS / +BV
+STS / -BV
a. u.
fluorescence lifetime (ps)
H
FRET efficiency
mKeima-UCL-iRFP713
mKeima-LEHD-iRFP713
mKeima-UCL-iRFP713 No BV
4 µM Staurosporine, 8h
I
Relative enzyme activity
4 µM Staurosporine, 8h

Figure 2.11 – **Characterization of mKeima-iRFP713 as caspase-9 FRET biosensor for FLIM**

A: Fluorescence emission of indicated constructs transiently expressed in HeLa cells at 840 nm 2PE. 40 µM Biliverdin was added 24 hours before formaldehyde fixation. Data from one experiment with 10 cells measured per sample.

B: Western Blot of HeLa cells transiently transfected with indicated constructs and treated with 4 µM STS or solvent control for 8 hours. 40 µM Biliverdin was added 16 hours before addition of STS and was absent in the medium during the duration of treatment. mKeima expression was detected using the mKeima-Red antibody and β-actin is shown as loading control. Multiple bands correspond to FP cleavage during denaturation (see main text for details).

C: Quantification of Western Blot in B for the indicated lanes, and shown as the ratio of the cleaved uncleaved sensor with fold changes indicated. B-C: Data from one experiment.

D: Representative intensity images (photons per pixel) of HeLa cells transiently transfected with indicated constructs and treated as in B. No Biliverdin was added to cells in the last panel.

E: Representative fluorescence lifetime images of cells in D. No Biliverdin was added to cells in the last panel. Scale bars are 50 µm.

F, G: Fluorescence lifetime distribution of control-treated cells (F) and cells treated with 4 µM STS (G) for 8 hours after 16 hours incubation with (solid lines, mKeima-LEHD-iRFP713) or without (dashed lines, mKeima-UCL-iRFP713) 40 µM Biliverdin. Blue and red shaded curves show distributions of UCL and donor-only controls, respectively. Data are from one experiment with at least 10 cells measured for each curve.

H: FRET efficiency derived from indicated lifetime distributions in F-G. Bars show the mean and standard deviation of at least 10 cells of a single experiment for each condition and construct.

I: Relative enzymatic activity for mKeima-LEHD-iRFP713 sensor constructs computed from the respective lifetime distributions shown in F-G.

incorporated into the experimental design. Intriguingly, mKeima-iRFP713 is a promising pair for *in vivo* FRET imaging since physiological levels of BV in animals are sufficient for full fluorescence, and therefore likely full FRET efficiency, as well as the advantage of using 2PE excitation at 840 nm which allows deeper tissue penetration.

The third acceptor we investigated was NirFP (also known as eqFP670; Tables 2.1 and 2.2). Expression of mKeima-UCL-NirFP resulted in strong aggregation in more than 50% of all cells (Fig. 2.12A). When performing measurements on the cells with less or no aggregation, a contribution of NirFP to the overall emission could not be detected (Fig. 2.12B). FLIM measurements showed a FRET efficiency of 37% (Fig. 2.12C). Next, we swapped the position of donor and acceptor, which, in our hands, can affect both FRET efficiency as well as aggregation. We found an increase in the number of cells showing aggregation for NirFP-UCL-mKeima, but with the aggregates appearing smaller (Fig. 2.12D). We, therefore, continued the development with NirFP-UCL-mKeima. The creation of tandem-dimers by fusing two copies of the same fluorescent protein with a short flexible linker has been used to reduce aggregation of dimeric FPs, such as tandem-dimer (td)Tomato (Shaner et al., 2004). As discussed in the introduction, it is suggested that the fusion promotes intramolecular dimerization between the

two copies in the same molecule over inter-molecular dimerization with other molecules, thus resulting in effective monomerization of a tandem-dimer construct. We employed the same approach as described for tdTomato to create tandem-dimer NirFP (tdNirFP) linking two copies of dimeric NirFP with a short 14-residue linker (Fig. 2.12E). Indeed, aggregation was completely absent in the resulting tdNirFP-UCL-mKeima FRET pair (Fig. 2.12F). tdNirFP contributed 12% to the overall fluorescence compared to the donor only (Fig. 2.12G), which corresponds to the emission of tdNirFP at 650 nm that is slightly red-shifted compared to NirFP (Fig. 2.12H), due to direct excitation, sensitized emission or both.

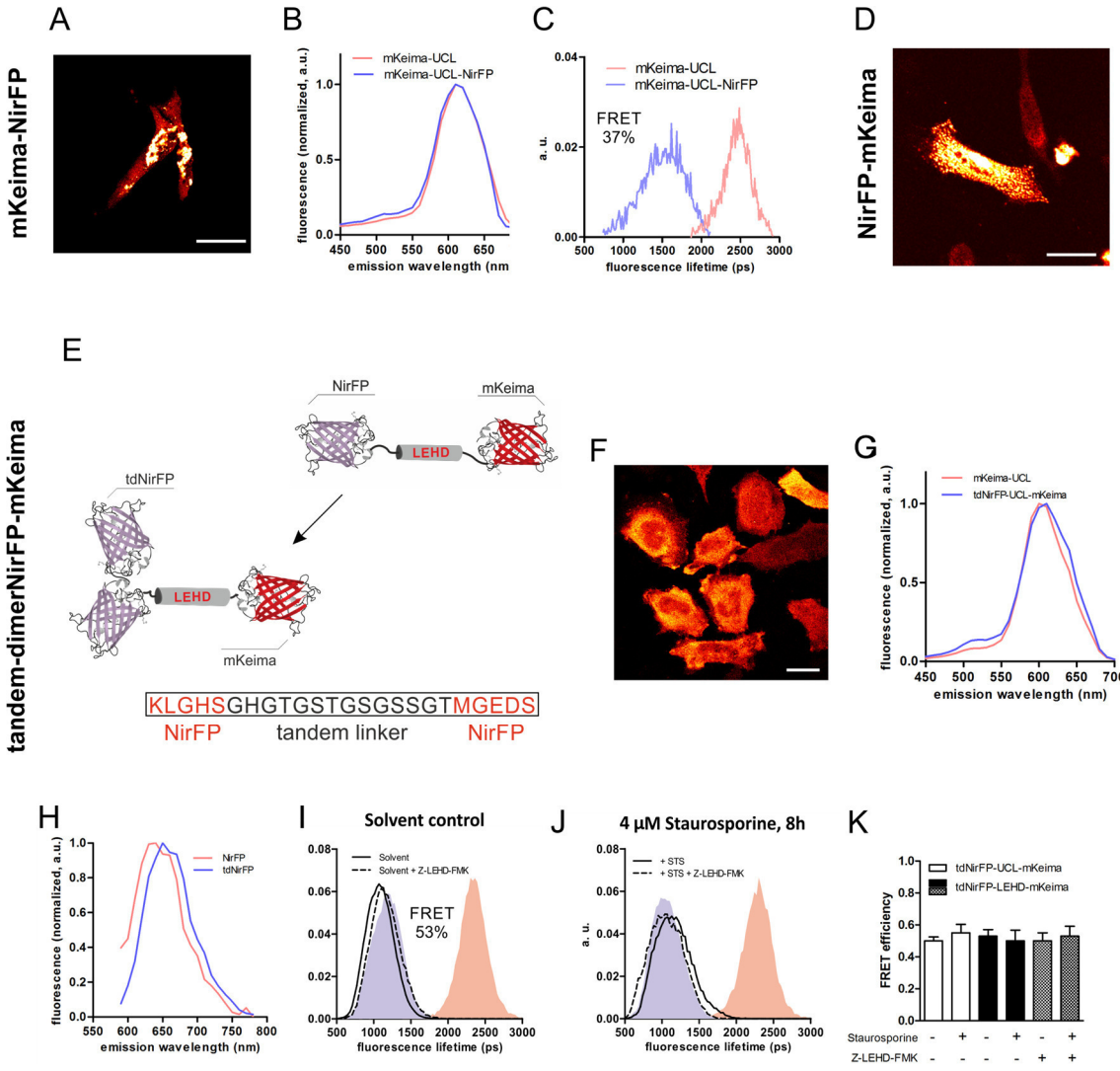

Figure 2.12 – **Development of tdNirFP-mKeima, a first-in-class long Stokes shift red fluorescent FRET pair**

A: Representative confocal image of HeLa cells transiently expressing mKeima-UCL-NirFP with 405 nm 1PE with aggregates shown in hotter colours.

B: Fluorescence emission of the indicated constructs expressed in HeLa cells at 840 nm 2PE. Only cells with little to no aggregation were imaged.

C: Fluorescence lifetime distribution cells in B, corresponding to 37% FRET efficiency.

D: Representative confocal image of HeLa cells transiently expressing NirFP-UCL-mKeima with 405 nm 1PE with aggregates shown hotter colours. Note the different appearance of aggregates as compared to A.

E: Schematic of the configuration of tandem-linker NirFP and the used linker sequence with N- and C-termini of adjacent NirFPs in red.

F: Representative confocal image of HeLa cells transiently expressing tdNirFP-UCL-mKeima at 840 nm 2PE demonstrating the absence of any visible aggregation.

G-H: Fluorescence emission of HeLa cells transiently transfected with indicated constructs at 840 nm 2PE (G) and 594 nm 1PE (H).

I-J: Fluorescence lifetime distribution of control-treated cells (I) and cells treated with 4 µM STS (J) for 8 hours in the absence (solid lines) or presence (dashed lines) of caspase-9 inhibitor Z-LEHD-FMK at 25 µM. Blue and red shaded curves show distributions of UCL and donor-only controls, respectively

K: FRET efficiency computed from I-J. Mean with standard deviations are shown.

All data are from a single experiment and the average of at least 10 cells are shown per construct and condition in B-C, G-K. Scale bars are 30 µm.

TdNirFP-UCL-mKeima exhibits a FRET efficiency of 53% (Fig. 2.12I), making it to our knowledge the best red FRET pair yet reported, as well as the only red FRET pair that is excitable in the blue part of the visible spectrum, at 840 nm 2PE. However, when the standard 14-residue long caspase-9 substrate cleavage linker was introduced and cells treated with STS, no change in fluorescence lifetime was observed (Fig. 2.12I-K), indicating that the linker is not cleaved. As the same linker in a different pair, mAmetrine-msCP576h, was efficiently cleaved upon STS treatment, the linker alone cannot be the reason for the loss of cleavage. We, therefore, hypothesized that the tandem-dimer could sterically prevent caspase-9 from processing the linker. Therefore, we extended the linker by 10 amino acids including prolines and glycines to provide a longer flexible linker (Fig. 2.13A). The new linker restored cleavage by STS as shown both by Western Blot (Fig. 2.13B-C) and FLIM (Fig. 2.13D-H). Similarly to the cleavage of the green mAmetrine-LEHD-msCP576h sensor, we observed only a ~50% maximal cleavage (Compare Fig. 2.9E and 2.13H). Treatment with the caspase-9 inhibitor Z-LEHD-FMK resulted in a two-fold decrease in cleavage, a specificity similar to those of the caspase-2 and caspase-3 sensors reported above (Fig. 2.13H). Notably, the decrease upon treatment with inhibitors was an order of magnitude smaller that determined by Western Blot (Fig. 2.13C). Along with similar discrepancies between FLIM and Western Blot observed for DEVD/DEVDR caspase-3 (Fig. 2.8H) and LEHD caspase-9 (Fig. 2.9H, 2.11C) linker, this

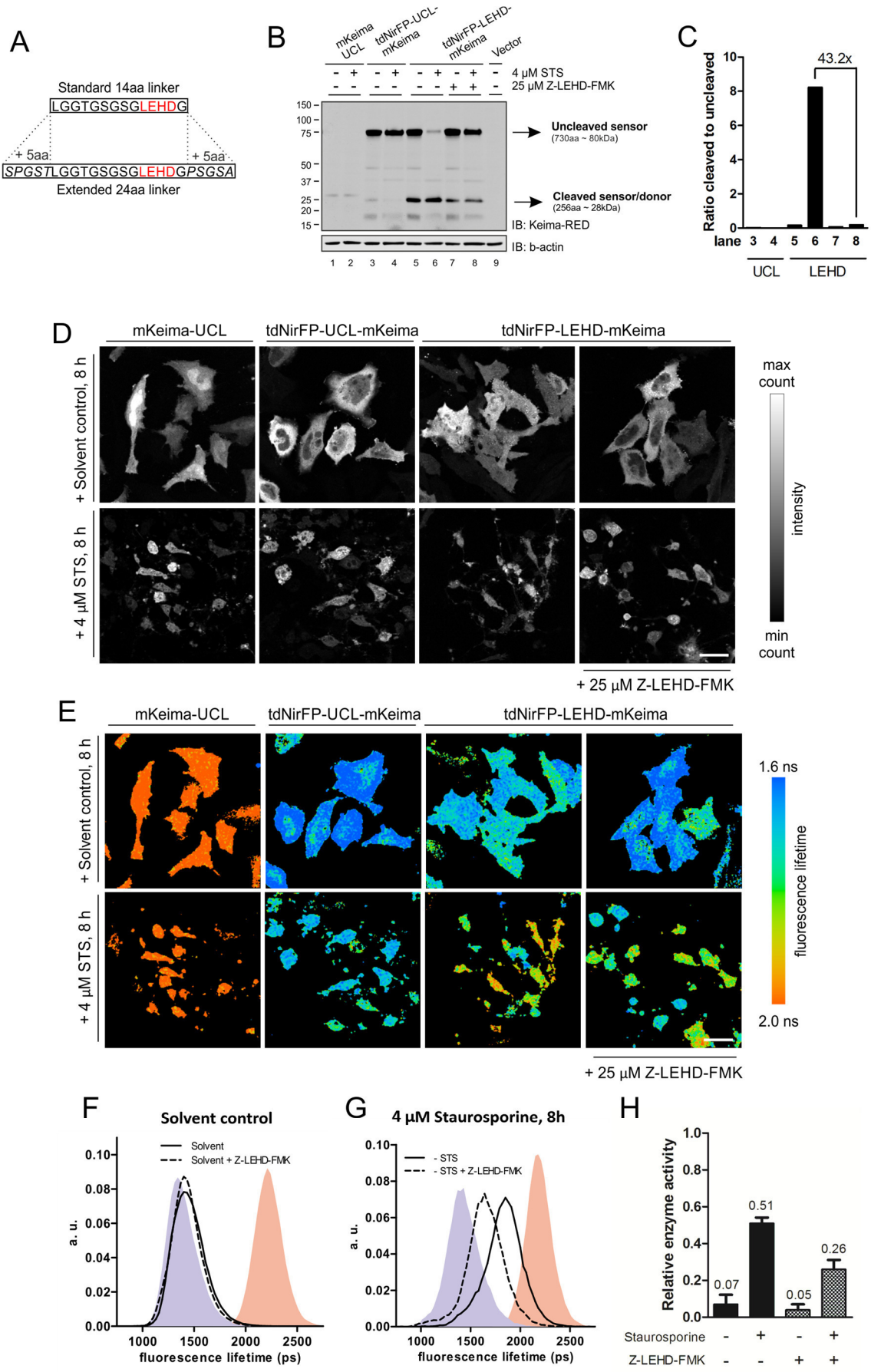
A
Standard 14aa linker
LGGTGSGSGLEHDG
+ 5aa
+ 5aa
SPGSTLGGTGSGSGLEHDGPSGSA
Extended 24aa linker
B
mKeima UCL
tdNirFP-UCL-mKeima
tdNirFP-LEHD-mKeima
Vector
4 µM STS
25 µM Z-LEHD-FMK
Uncleaved sensor
(730aa ~ 80kDa)
Cleaved sensor/donor
(256aa ~ 28kDa)
IB: Keima-RED
IB: b-actin
C
Ratio cleaved to uncleaved
43.2x
lane 3 4 5 6 7 8
UCL
LEHD
D
mKeima-UCL
tdNirFP-UCL-mKeima
tdNirFP-LEHD-mKeima
+ Solvent control, 8 h
+ 4 µM STS, 8 h
max count
intensity
min count
+ 25 µM Z-LEHD-FMK
E
mKeima-UCL
tdNirFP-UCL-mKeima
tdNirFP-LEHD-mKeima
+ Solvent control, 8 h
+ 4 µM STS, 8 h
1.6 ns
fluorescence lifetime
2.0 ns
+ 25 µM Z-LEHD-FMK
F
Solvent control
Solvent
Solvent + Z-LEHD-FMK
a. u.
fluorescence lifetime (ps)
G
4 µM Staurosporine, 8h
- STS
- STS + Z-LEHD-FMK
a. u.
fluorescence lifetime (ps)
H
Relative enzyme activity
0.07
0.51
0.05
0.26
Staurosporine
Z-LEHD-FMK

Figure 2.13 – **Characterization of tdNirFP-mKeima as FRET biosensor for caspase-9 substrate cleavage**

A: Schematic representation of the longer and more flexible caspase-9 linker used to overcome impaired cleavage by caspase-9.

B: Western Blot of HeLa cell lysates transiently transfected with indicated constructs and treated with 4 µM STS or solvent control for 8 hours in the absence or presence of caspase-9 inhibitor Z-LEHD-FMK at 25 µM. mKeima expression was detected using the mKeima-Red antibody and b-actin is shown as loading control. Additional specific bands are due to FP fragmentation during denaturation.

C: Quantification of Western Blot in B for the indicated lanes, and shown as the ratio of the cleaved uncleaved sensor with fold changes indicated. B-C: Data are from one experiment.

D: Representative intensity images (photons per pixel) of HeLa cells transiently transfected with indicated constructs and treated as in B. Scale bar is 50 µm.

E: Representative fluorescence lifetime images of cells in D.

F, G: Fluorescence lifetime distribution of control-treated cells (F) and cells treated with 4 µM STS (G) for 8 hours in the presence (solid lines) or absence (dashed lines) of 25 µM Z-LEHD-FMK. Blue and red shaded curves show distributions of UCL and donor-only controls, respectively.

H: Relative enzymatic activity for tdNirFP-LEHD-mKeima sensor computed from the respective lifetime distributions shown in F-G. Bars show mean and standard deviation.

D-H: Data from three independent experiments with at least 20 cells per construct and condition.

suggests that observations about specificity and sensitivity made with those techniques are of limited use for a direct comparison.

Compared to the shorter linker, FRET efficiency decreased by 18% to 35% (Fig. 2.13E), likely due to the larger distance between donor and acceptor or to changes in dipole-dipole orientation between donor and acceptor that may occur if donor and acceptors experience different steric hindrances in the two constructs. More importantly, we did not detect any of the issues experienced with other near-infrared acceptors (aggregation and unspecific FRET), making of tdNirFP-mKeima our best choice for the multiplexing platform.

In summary, tdNirFP-mKeima is an excellent first-in-class FRET pair that is well suited for multiplexing with blue and green fluorescent FRET pairs with a single blue excitation wavelength and serves as a good caspase-9 substrate cleavage sensor.

Alternative red-fluorescent long Stokes shift FRET pairs for multiplexing

With new fluorescent proteins being published frequently, we continuously tested new combinations and benchmarked them against tdNirFP-mKeima. Table 2.2 reports results for all tested pairs, which will be described in the following section to guide further development and highlight common challenges in the development of this class of FRET pairs.

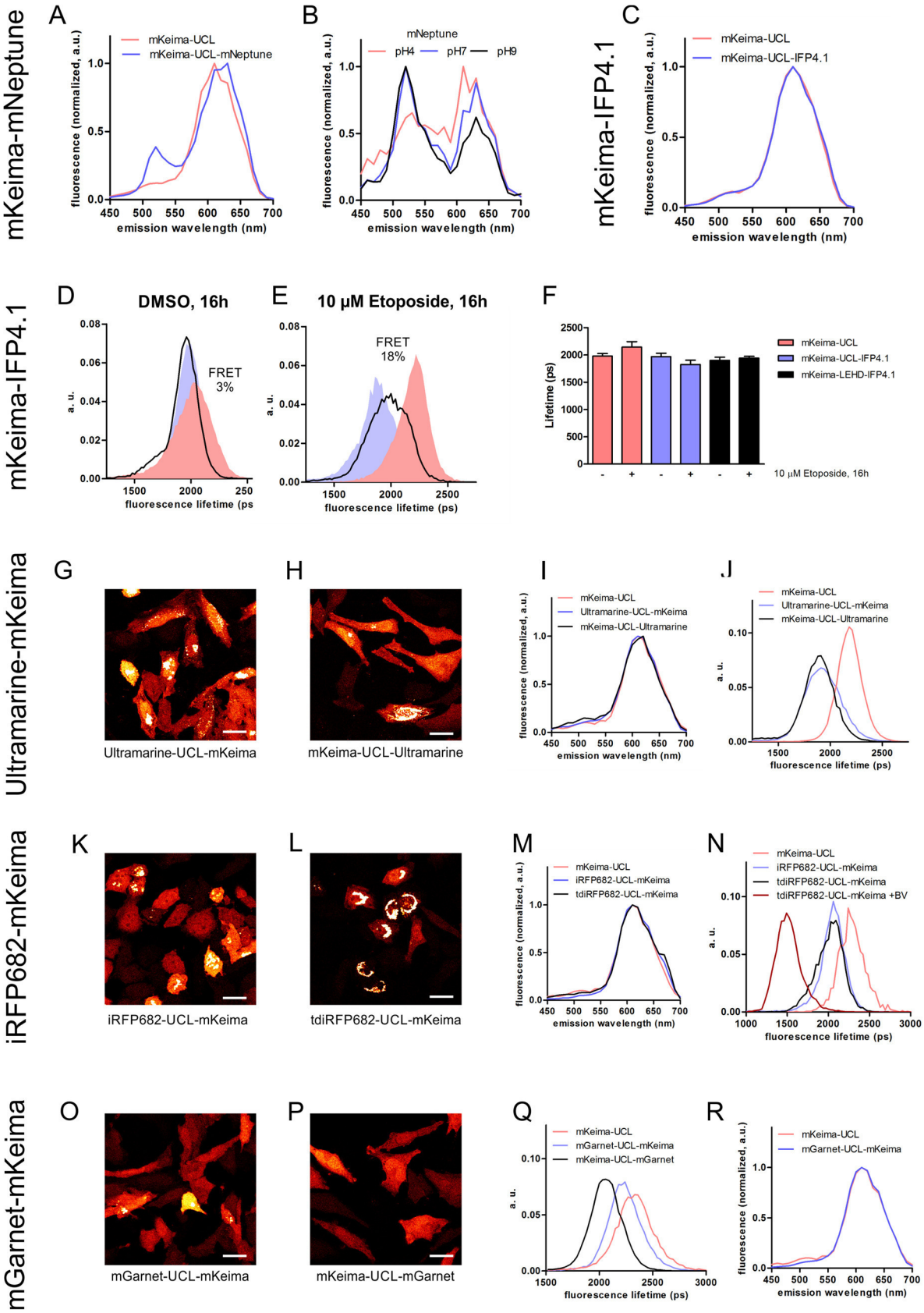
mKeima-mNeptune
A
mKeima-UCL
mKeima-UCL-mNeptune
fluorescence (normalized, a.u.)
emission wavelength (nm)
B
mNeptune
pH4
pH7
pH9
C
mKeima-IFP4.1
mKeima-UCL
mKeima-UCL-IFP4.1
mKeima-IFP4.1
D
DMSO, 16h
FRET
3%
a. u.
fluorescence lifetime (ps
E
10 µM Etoposide, 16h
FRET
18%
F
Lifetime (ps)
mKeima-UCL
mKeima-UCL-IFP4.1
mKeima-LEHD-IFP4.1
10 µM Etoposide, 16h
Ultramarine-mKeima
G
Ultramarine-UCL-mKeima
H
mKeima-UCL-Ultramarine
I
mKeima-UCL
Ultramarine-UCL-mKeima
mKeima-UCL-Ultramarine
J
iRFP682-mKeima
K
iRFP682-UCL-mKeima
L
tdiRFP682-UCL-mKeima
M
iRFP682-UCL-mKeima
tdiRFP682-UCL-mKeima
N
tdiRFP682-UCL-mKeima +BV
mGarnet-mKeima
O
mGarnet-UCL-mKeima
P
mKeima-UCL-mGarnet
Q
mGarnet-UCL-mKeima
mKeima-UCL-mGarnet
R

Figure 2.14 – **Assessment of alternative FRET acceptors for mKeima**

A: Fluorescence emission of HeLa cells transiently expressing mKeima-UCL or mKeima-UCL-mNeptune at 840 nm 2PE.

B: Fluorescence emission of HeLa cells expressing mNeptune in PBS with varying pH at 840nm 2PE.

C: Fluorescence emission of HeLa cells transiently expressing mKeima-UCL or mKeima-UCL-IFP4.1 at 840 nm 2PE. 40 µM Biliverdin was added 24 hours prior to fixation.

D, E: Fluorescence lifetime distribution of HeLa cells transiently expressing mKeima-LEHD-IFP4.1 (solid line) after 16 hours of treatment with 10 µM Etoposide (E) or solvent control (D). Blue and red shaded curves show distributions of UCL and donor-only controls, respectively. Cells were pre-treated with 40 µM Biliverdin 24 hours prior to addition of Etoposide.

F: Fluorescence lifetime derived from distributions in D-E. Bars show the mean and standard deviation of at least 10 cells in a single experiment.

G, H: Representative confocal images of HeLa cells transiently expressing indicated constructs at 840nm 2PE with aggregates shown in hotter colours.

I: Fluorescence emission of cells in G-H at 840 nm 2PE, with cells with little to no aggregation chosen for analysis.

J: Fluorescence lifetime distribution of HeLa cells expressing indicated constructs with little to no aggregation. Both orientations exhibit 10% FRET efficiency.

K, L: Representative confocal images of HeLa cells transiently expressing indicated constructs at 840 nm 2PE with aggregates shown in hotter colours.

M: Fluorescence emission of HeLa cells transiently indicated constructs at 840 nm 2PE. No Biliverdin was added.

N: Fluorescence lifetime distribution of HeLa cells expressing indicated constructs with little to no aggregation. As shown, tdiRFP682-UCL-mKeima was also treated with 40 µM Biliverdin 24 hours prior to fixation. BV treatment increased FRET from 5% to 40%.

O, P: Representative confocal images of HeLa cells transiently expressing indicated constructs at 840 nm 2PE with aggregates in panel O shown in hotter colours, which are absent in P.

Q: Fluorescence lifetime distribution HeLa cells expressing indicated constructs with little to no aggregation corresponding to 3% and 10% for mGarnet-UCL-mKeima and mKeima-UCL-mGarnet, respectively.

R: Fluorescence emission of HeLa cells transiently expressing indicated constructs at 840 nm 2PE.

All data are from a single experiment and the average of at least 10 cells are shown per construct and condition. Scale bars in all panels are 30 µm.

mNeptune is a widely used bright monomeric RFP that with a Förster radius of 5 nm could be a good acceptor for mKeima (Lin et al., 2009). However, a strong, pH-sensitive green emission upon 840 nm 2PE excitation made it unsuitable for multiplexing with green fluorescent FRET pairs (Fig. 2.14A-B). Recently, new versions of mNeptune have been published that are optimized for higher pH stability and reduced green emission which could be more suitable for multiplexing and remain to be tested with mKeima (Chu et al., 2014).

IFP4.1 belongs to the same class of bacterial phytochromes as iRFP713, but has a 57% lower extinction coefficient and is more strongly dependent on the addition of Biliverdin (Filonov et al., 2011; Shu et al., 2009). However, in contrast to the dimeric iRFP713, it has been described as a monomer which could reduce the tendency to aggregate. When pre-treated with high

levels of BV for 16 h, analogous to iRFP713, no contribution to the overall fluorescence could be detected (Fig. 2.14C). Despite the addition of BV, only 3% FRET efficiency could be measured in untreated cells (Fig. 2.14D). In Etoposide-treated dead cells, which was used at that time as an alternative to STS, the fluorescence lifetime for the UCL control decreased and, surprisingly, increased for donor-only control and therefore FRET increased to 18% (Fig. 2.14E-F). This is reminiscent to the decrease in fluorescence lifetime observed for mKeima-iRFP713, suggesting that a similar mechanism, i.e. molecular crowding leading to intramolecular FRET, could be responsible. However, we observed no visible aggregation in dead cells, which could still be present, but too small to be detected microscopically. Still, as for iRFP713, a shift in fluorescence lifetime upon Etoposide treatment was observed, corresponding to around 50% REA (Fig. 2.14E-F). Overall, IFP4.1 is not a good replacement for iRFP713 nor for tdNirFP.

Ultramarine is a non-fluorescent chromoprotein derived from the weakly fluorescent RFP Rtms5 and has been shown to work well as a dark acceptor for a range of cyan to green fluorescent proteins and could with a Förster radius of 4.6 nm be a suitable acceptor for mKeima (Pettikiriarachchi et al., 2012). Despite being reported as a pure monomer, mKeima-Ultramarine showed strong aggregation in 40-50% of the cells, while Ultramarine-mKeima showed similar aggregation in 70-80% of the cells (Fig. 2.14G-H). When analysing cells without aggregation, Ultramarine did not contribute to the overall fluorescence and resulted in 10% FRET efficiency in both configurations (Fig. 2.14I-J). Notably, we created tandem-dimers for Ultramarine, but rather than abolishing aggregation, they caused strong aggregation in all the cells (not shown), indicating that tandem-dimerization is not a general solution for all

instances of aggregation. In summary, Ultramarine, as well as tdUltramarine, are unsuitable to replace tdNirFP as acceptor.

iRFP682 was derived from iRFP713 and reported to exhibit higher fluorescence in the absence of exogenous Billiverdin as co-factor, indicating a more efficient incorporation of endogenous BV (Shcherbakova and Verkhusha, 2013). Assuming that the increased brightness is caused by an increased molar extinction coefficient, we hypothesized that this could lead to higher FRET in the absence of BV as well. With a Förster radius similar to that of mKeima-tdNirFP, iRFP682 could be a suitable alternative (Tab. 2.2). iRFP682-UCL-mKeima, and to a larger extent, tdiRFP682-UCL-mKeima showed strong aggregation when expressed in HeLa cells (Fig. 2.14K-L). mKeima-UCL-tdiRFP682 was not expressed at all (not shown). This unexpected effect of tandem-dimerization can likely be explained by the completely different

structure of iRFPs compared to NirFP. In contrast to the β-barrel structure of NirFP and many other avGFP like proteins, iRFPs form a symmetrical bilobal conformation with the dimerization interface located between two symmetric PAS domains (Stepanenko et al., 2014) that, as our results indicate, cannot be blocked by the same tandem-dimerization approach. Despite the aggregation, we were able to acquire emission spectra (Fig. 2.14M) as well as FLIM measurements (Fig. 2.14N) in some cells. Both tested constructs exhibited 10% FRET efficiency, which increased to 40% upon BV addition. This shows that iRFP682-mKeima could be a good FRET pair if the aggregation issue could be solved.

Finally, mGarnet, an RFP evolved from mKate, has a very high extinction coefficient comparable to iRFP713, but is a pure monomer and does not require a cofactor for maximal absorption (Tab. 2.1, Hense et al. 2015). Hence, mGarnet-UCL-mKeima could be a suitable FRET pair. However, moderate aggregation was found in 20% of the cells, which was overcome by changing the orientation of donor and acceptor (Fig. 2.14O-P). This change in orientation to mKeima-UCL-mGarnet increased the initial 3% FRET efficiency (in cells without aggregation) to 10% (Fig. 2.14Q). No contribution of mGarnet to the overall fluorescence was observed (Fig. 2.14R). Taken together, mKeima-UCL-mGarnet is clearly inferior to tdNirFP-mKeima, however, we note that tandem-dimerization of mGarnet could increase its FRET efficiency, an approach we have not pursued so far.

Testing other long Stokes shift red-fluorescent donors

When we started to multiplex mTagBFP, mAmetrine and mKeima in the same cells, we noted that the low relative brightness of mKeima (16% of mAmetrine, 31% of mTagBFP; Fig. 3.4E) can be a major challenge in setting excitation powers high enough to achieve sufficient signal from mKeima and low enough to avoid phototoxicity or saturation of detectors by the very bright mAmetrine (Table 2.1). We, therefore, tested two additional donor fluorophores, mBeRFP (Yang et al., 2013) and hmKeima8.5 (Guan et al., 2015) that have been reported to be three times and two times brighter than mKeima, respectively.

mBeRFP showed strong green fluorescence when it was tested initially (Fig. 2.10A), but since its higher brightness would improve multiplexing considerably and our unmixing approach could possibly tolerate the increased green fluorescence, we tested both tdNirFP as well as iRFP713, the top two acceptors so far, for FRET with mBeRFP.

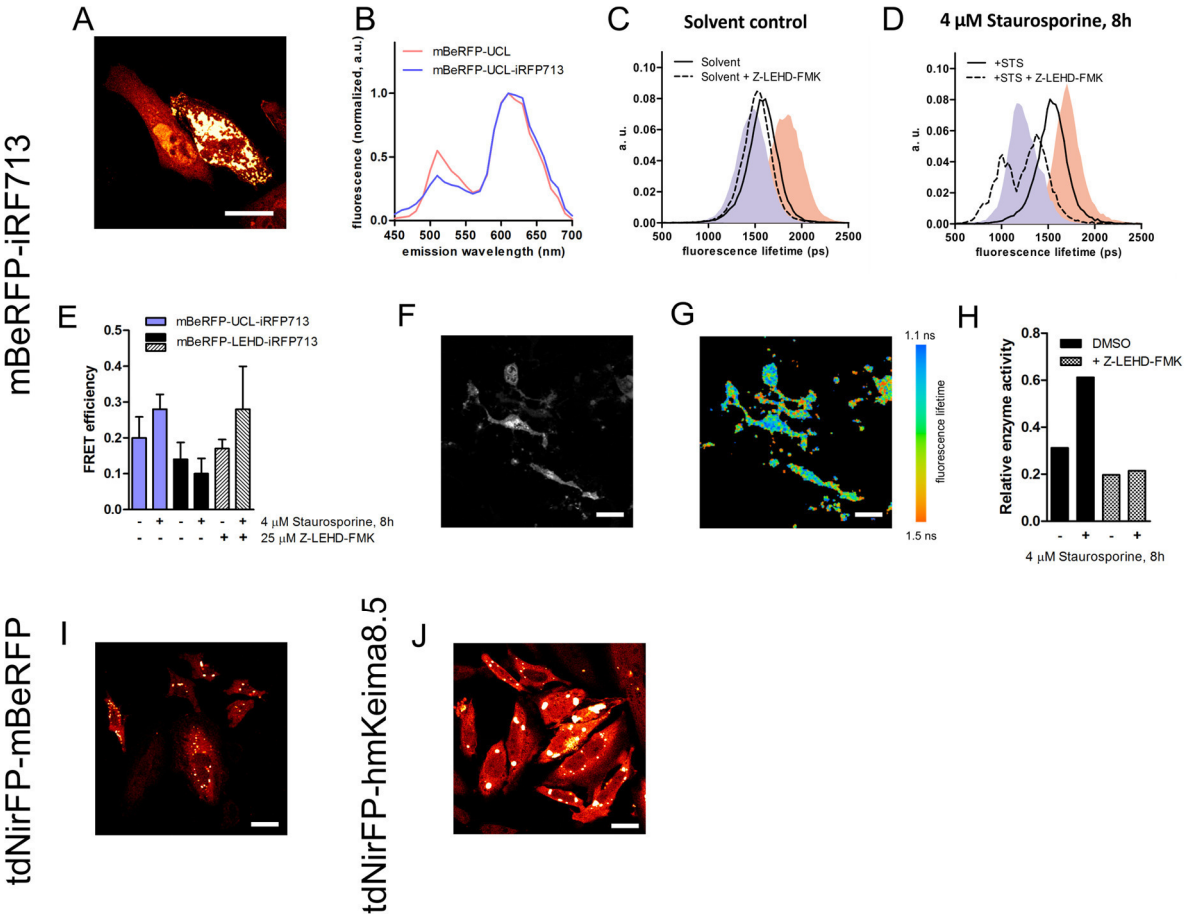

Figure 2.15 – **Assessment of alternative long Stokes shift red fluorescent FRET donors with selected acceptors**

A: Representative confocal images of HeLa cells transiently expressing mBeRFP-UCL-iRFP713 at 840 nm 2PE with aggregates shown in hotter colours.

B: Fluorescence emission of HeLa cells transiently indicated constructs at 840 nm 2PE. 40 µM Biliverdin was added 24 hours prior to fixation

C, D: Fluorescence lifetime distribution of HeLa cells transiently transfected with mBeRFP-LEHD-iRFP713 treated with solvent control (C) or 4 µM STS (D) for 8 hours in the presence (solid lines) or absence (dashed lines) of 25 µM Z-LEHD-FMK. Blue and red shaded curves show distributions of UCL and donor-only controls, respectively. Cells were pre-treated with 40 µM Biliverdin 16 hours prior to addition of STS.

E: FRET efficiency calculated from lifetime distributions in C-D. Bars show mean and standard deviation from at least 10 cells each and from a single experiment.

F, G: Representative intensity (F) and lifetime (G) image of HeLa cells transiently expressing mBeRFP-UCL-iRFP713 and treated with 4 µM STS for 8 hours showing low lifetime aggregates in shrunk cells.

H: Relative enzymatic activity for mBeRFP-LEHD-iRFP713 computed from the respective lifetime distributions in C-D.

I, J: Representative confocal images of HeLa cells transiently expressing tdNirFP-UCL-mBeRFP (I) or tdNirFP-UCL-hmKeima8.5 (J) at 840 nm 2PE with aggregates shown in hotter colours.

All data are from a single experiment and the average of at least 10 cells are shown per construct and condition. Scale bars in all panels are 30 µm.

mBeRFP-UCL-iRFP713 showed strong aggregation in about 50% of all cells, and in contrast to mKeima-UCL-iRFP713, already in healthy cells in the absence of STS treatment (Fig. 2.15A).

Performing measurements on the cells that did not show aggregates, we observed the characteristic green emission of mBeRFP (Fig. 2.15B). As for mKeima-UCL-

iRFP713, the aggregation increased in shrunk cells coinciding with a decrease in fluorescence lifetime and an increase in FRET efficiency from 20% to 28% in the presence of BV (Fig. 2.15C-G). Still, FRET was reduced upon STS treatment for the sensor and rescued upon caspase-9 inhibitor treatment (Fig 2.15H), indicating that it would be a suitable pair if aggregation was reduced.

Last, we tested tdNirFP with mBeRFP as well as hmKeima8.5 but found that both pairs strongly aggregated in all cells precluding any further use (Fig. 2.15I-J). Therefore, none of the LSS-RFPs we tested is superior to mKeima, primarily because of enhanced aggregation when fused to acceptor chromophores.

2.3.4 Multiplexing more than three FRET pairs

A significant advantage of our sensing platform compared to other possible strategies is the utilization of a single excitation laser line. On the one hand, this diminishes the requirement for sequential exposures and, on the other hand, it allows extending the number of biochemical events that could be measured in a single cell when used with additional excitation lines and an additional set of FRET pairs. With two or three excitation lines, it is conceivable to excite two to three additional FRET pairs, bringing the total number of FRET pairs for multiplexing up to six (Fig. 2.16A). We tested one of such pairs, Clover-mRuby2, as proof of concept.

We found that Clover is well excited at 1010 nm 2PE (Fig. 2.16B). However, incomplete maturation of mRuby2 (see grey lines in Fig. 2.16B) was observed, indicating that there is a continuum of partially functional FRET pairs with heterogeneous FRET efficiency. The reason for this incomplete maturation is likely the green-to-red maturation of mRuby2 that is reported

to be five times slower than for Clover (Lam et al., 2012) and is common for red fluorescent proteins (van der Krogt et al., 2008).

When tested for FLIM in a pilot experiment as a caspase-7 sensor using QKDVKD as substrate cleavage motif, the incomplete maturation manifested in a wide fluorescence lifetime

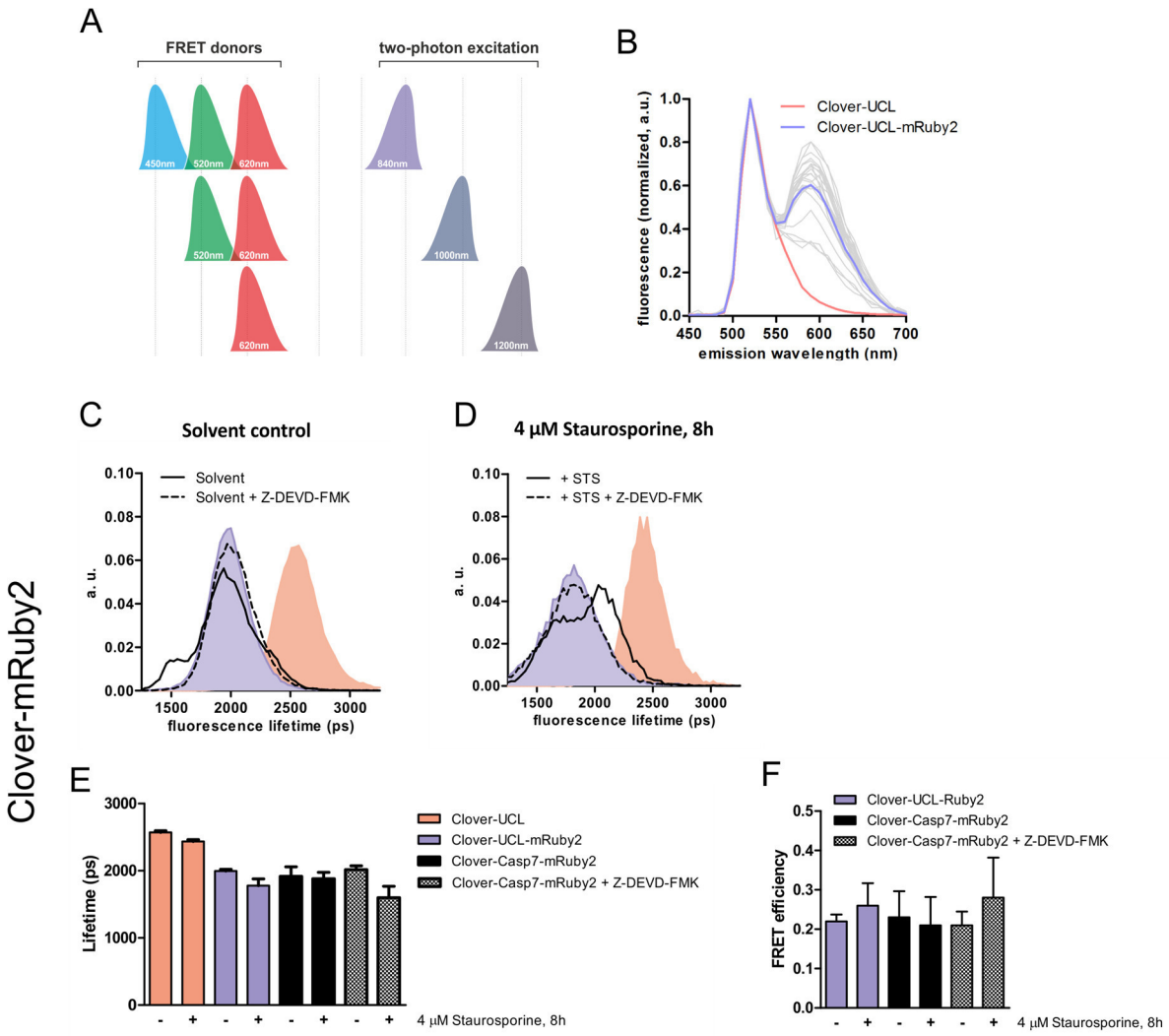

Figure 2.16 – **Characterization of Clover-mRuby2 as a FRET pair to extend the multiplexing platform**

A: Extension of the multiplexing platform using two additional excitation wavelengths for two more sets of FRET sensors

B: Fluorescence emission in HeLa cells transiently transfected with indicated constructs at 1010 nm 2PE. Grey lines show spectra of 23 individual cells that are averaged in the blue line demonstrating incomplete and heterogeneous maturation of mRuby2.

C, D: Fluorescence lifetime distribution of HeLa cells transiently transfected with caspase-7 biosensor Clover-QKDVKD-mRuby2 treated with solvent control (C) or 4 µM STS (D) for 8 hours in the presence (solid lines) or absence (dashed lines) of 25 µM Z-DEVD-FMK. Blue and red shaded curves show distributions of UCL and donor-only controls, respectively.

E, F: Fluorescence lifetime (E) and FRET efficiency (F) for indicated constructs computed from distributions shown in C-D. Bars show the mean and standard deviation of at least 10 cells each.

B-F: Data are from a single experiment.

distribution, that was exacerbated by STS treatment (Full width at half maximum (Control/STS): 330/450 nm; mAmetrine-UCL-msCP576h: 300/300 nm; Fig. 2.16C-D). We also

observed a decrease in fluorescence lifetime for both mClover-UCL as well as Clover-UCL-Ruby2 in dead cells in the absence of clearly visible aggregates (Fig. 2.16E), and corresponding changes in FRET around a baseline of 20%, with a partial response of the caspase-7 sensor (Fig. 2.16E-F). Such a decrease in fluorescence lifetime in dead cells is

reminiscent of iRFP713-containing pairs and could be indicative of similar molecular-crowding induced intramolecular FRET, which could be confounded by the incomplete maturation. Both issues would need to be addressed before being usable as fourth FRET pair. The recent development of the faster maturating mRuby3 (Bajar et al., 2016b) promises to be a potential alternative and remains to be tested.

2.4 Discussion

Simultaneous multiplexing of more than two spectrally-resolved FRET pairs in live cells has so far been challenging due to the lack of suitable pairs. Here, after a process of extensive screening and rational design of donor and acceptor combinations, we identified a set of three FRET pairs to enable the robust quantification of three biochemical events in the living cell (Fig. 2.17). This is of particular interest to monitor the dynamics of small three-nodes networks to directly measure their dynamics and heterogeneity across different cells or to falsify larger network models generated from ‘omics’ platforms and bioinformatics that are often not tested in living cells.

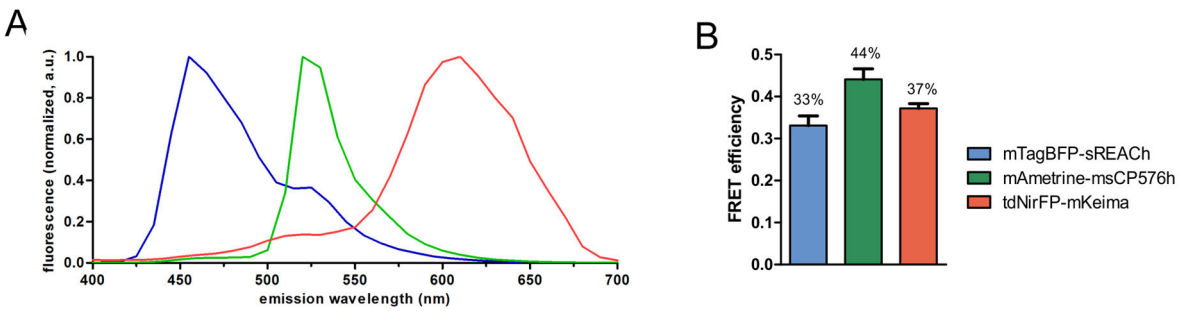

Figure 2.17 – **Summary of the complete FRET pair suite for three-colour FLIM**

A: Fluorescence emission of mTagBFP-UCL-sREACh (solid blue), mAmetrine-UCL-msCP576h (solid green), tdNirFP-UCL-mKeima (solid red) and respective donor-only controls (dashed lines) at 840 nm 2PE. Mean of three independent experiments with at least 20 cells per construct is shown.

B: FRET efficiency of FRET pairs in A. Bars are mean and standard deviation of experiments in A.

While mTagBFP-sREACh has been developed by others (Niino et al., 2010), mAmetrine-msCP576h and tdNirFP-mKeima have been developed in this work. By using spectrally separated donor fluorophores excitable at a single wavelength and dark acceptors, these pairs allow using the visible spectrum efficiently, minimizing spectral contamination between the pairs (Fig. 2.17A). All three pairs exhibit high FRET efficiencies above 30% and therefore

conferring a high dynamic range to the caspase biosensors created by introducing substrate cleavage motifs into the FRET linker (Fig. 2.17B).

2.4.1 Strategies for future improvement of the FRET pairs for multiplexing

mTagBFP-sREACh

Although mTagBFP-sREACh proved to be a very suitable pair for multiplexing, the residual sREACh fluorescence emission decreases the signal-to-noise ratio of multiplexing. Therefore, a darker acceptor for mTagBFP is desirable for future optimization of this sensing platform. We found that ShadowG is a better acceptor showing a decrease of fluorescence compared to sREACh by about 2-fold, and will be used for the further steps in the ongoing development of this multiplexing platform. While this dissertation was in preparation, an improved version of sREACh named ShadowY has been reported to exhibit seven times less residual quantum yield and 50% increased extinction coefficient compared to sREACh resulting in an R_0 of 5.4 nm, comparable to sREACh (Murakoshi, 2017). Another potential acceptor could be Dark Venus, a non-fluorescent mutant of Venus that has been successfully used as a dark acceptor for the CFP mTurquoise (Klarenbeek et al., 2015). Importantly, tandem-dimerization of Dark Venus increased FRET efficiency from 32% to 49% compared to the monomer and abolished aggregation, similarly to our observation for tdNirFP. Therefore, it may be possible to improve the blue sensor utilizing tandem-dimers of sREACh (R_0 increased from 5.4 nm to 6.1 nm), ShadowG (R_0 increased from 5.6 nm to 6.3 nm), dark Venus (R_0 5.1 nm) or ShadowY (R_0 6.1 nm), both to potentially increase the dynamic range of sensors and remove residual aggregation of the sensors.

mAmetrine-msCP576h

mAmetrine-msCP576h is an excellent FRET pair with high FRET efficiency and a completely dark acceptor, making it ideal for FRET-FLIM experiments in general and multiplexing in particular. The only limitation of this FRET pair is aggregation in highly expressing cells, effects

that can be easily avoided during careful generation of cell lines. Therefore, none of the strategies that we described was employed to reduce aggregation of the green sensor. However, on the basis of its tetrameric quaternary structure, we can speculate that an approach similar to the evolution of tetrameric DsRed into monomeric derivatives mRFP1, mCherry and tdTomato (Campbell et al., 2002; Shaner et al., 2004) including targeted mutagenesis of the dimer interface, circular-permutation and tandem-dimerization could be used to reduce aggregation. Tandem-dimer msCP576h has a nominal Förster radius of 6.3 nm compared to 5.6 nm of the original protein, suggesting a high potential FRET gain. Alternatively, two mutants of mCherry with low quantum yield (<0.04), termed ‘dark mCherries’ have been created as monomeric dark acceptors for red/orange donor FPs (Nakahata et al., 2016). With Förster radii of 5.3 nm and 5.1 nm, they may also be suitable alternatives for msCP576.

tdNirFP-mKeima

The development of tdNirFP-mKeima, the reddest genetically encoded long Stokes shift red-fluorescent FRET pair reported so far, was the most challenging optimization we carried out. Yet, tdNirFP-mKeima may still benefit from substantial improvement to recover brightness and dynamic range, without compromising the long Stokes shift and aggregation propensity. Previously, orange/red FRET pairs have been reported by others, including long Stokes shift pairs dKeima570-tdFP615 (Miyamoto et al., 2015) and mCyRFP-mMaroon (Laviv et al., 2016), as well as short Stokes shift pairs TagRFP-mPlum (Grant et al., 2008), mKate2-iRFP713 and eqFP650-iRFP713 (Zlobovskaya et al., 2016), TagRFP-KFP (Rusanov et al., 2010), and mRuby2-dark-mCherry/mRuby2-Ultramarine (Nakahata et al., 2016; see Tab. 2.1 for more information on all FPs). However, all these pairs have unfavourable spectral characteristics that do not allow a combination with our mTagBFP and mAmetrine pairs, being either too blue-shifted leading to an increased spectral contribution to mAmetrine, or too red-shifted to be excitable with a single 840 nm excitation line. Nonetheless, as discussed in section 2.3.4, these pairs may be useful in extending our sensing platform with additional excitation lines.

Alternative acceptors for mKeima

New red fluorescent proteins are published frequently providing a continuous new crop of potential acceptors for mKeima. We estimated the Förster radius of recently published fluorescent proteins to compare these to tdNirFP-mKeima: mCardinal (5.3 nm), TagRFP675 (5.2 nm) and mNeptune2.5 (4.9 nm), mMaroon (5.3 nm), TagRFP657 (4.7 nm), tdFP615 (5.4 nm) and mPlum (4.3 nm) exhibit a shorter Förster radius compared to tdNirFP-mKeima

(5.8 nm). A new chromoprotein, sgCP, that shares 79% sequence identity with cjBlue was recently published (Chiang et al., 2015). sgCP exhibits twice the cjBlue's extinction coefficient and a nominal Förster radius of 5.8 nm, but considering its tetrameric structure will likely be prone to aggregation as cjBlue and require extensive optimization including tandem-dimerization, circular permutation and/or targeted mutagenesis. Among the alternative acceptors we already tested, mGarnet showed the least amount of aggregation, but only 10% FRET efficiency. Varying the linker length and creating a tandem-dimer could, therefore, be simple ways to improve this FRET pair without the need to address aggregation that is present in all other acceptors tested.

We also tested acceptors from the new and growing class of bacterial and plant phytochromes with most exhibiting red- and far-red emission. We identified phytochromes that could, in principle, act as good acceptor for FRET. The requirement of exogenous chromophore supplementation in cell culture may limit their applications, but phytochromes may be particularly useful *in vivo,* where endogenous Biliverdin is sufficiently high. For example, the FRET pairs mKeima-iRFP713, mKeima-iRFP682 and mBeRFP-iRFP713 could be extremely useful when combined with two-photon microscopy permitting deep tissue *in vivo* imaging. However, in our experimental conditions, we experienced a strong tendency to aggregate for these FRET pairs. Our limited attempts for monomerization were unsuccessful, but targeted efforts may unlock the potential of such FRET pairs. More generally, the failure of the tandem-dimer of iRFP682, but also of Ultramarine, to reduce aggregation indicates that while tandem-dimerization can be a successful tool (as shown for tdNirFP), it cannot be generalized for all donor and acceptor combinations. Notably, new monomeric IFP-derivatives with decreased co-factor dependency, mIFP (Yu et al., 2015) and miRFP (Shcherbakova et al., 2016), have been recently cloned and may be good candidates to overcome both aggregation and supplementation of Biliverdin.

Replacing mKeima with a brighter LSS-RFP

Finally, the most significant improvement that could be attempted in the future is increasing the low brightness of mKeima. mKeima exhibits a relative intensity of ~30% compared to mTagBFP and ~15% of mAmetrine and tendency to photobleach faster than the other donor fluorophores. mKeima's brightness is thus not ideal because it requires finding a compromise between photo-toxicity, photo-bleaching and saturation of detectors imaging mAmetrine. As illustrated in the next chapter, this compromise can be found, but it requires careful standardization of the experiments, an experienced experimentalist and a compromise on the

eventual signal-to-noise ratio of the biochemical measurement. The only two available alternatives for mKeima are hmKeima8.5 (1.5-fold brighter) and mBeRFP (2.7-fold brighter), but they both resulted in stronger aggregation when used with tdNirFP as acceptor. We did not attempt further monomerization of these FRET pairs, but swapping of donor-acceptor (as for mKeima-mGarnet), utilization of other acceptors (e.g., Ultramarine and (td)iRFP682), may provide an improved LSS far-red FRET pair.

Further optimization of the linkers or design principles of the FRET pairs (e.g. HiFRET (Grünberg et al., 2013)) may also provide significant improvements in the performance of this biochemical multiplexing platform. As issues such as aggregation have been observed by others to be dependent on cell lines (van der Krogt et al., 2008), using a different cell line could be a further strategy to improve these pairs.

However, as we wanted to demonstrate the usefulness of this strategy in a biological application, we used this first triplet of FRET pairs to study cell death in response to DNA damage (see Chapter 3).

2.4.2 Extension of the FRET multiplexing platform

Simultaneous quantification of three biochemical reactions by FRET is a critical strategic step to permit researchers to study biochemical networks in single living cells. The readout of more biochemical events may be desirable, especially compared the level of multiplexing achievable with Western Blotting or flow cytometry. Our approach provides already the essential advantage to interrogate individual living cells over time like no other technique can achieve. However, there are several approaches that could be used to extend the multiplexing even beyond three reactions.

As illustrated in Figure 2.16A using additional excitation wavelength for additional FRET pairs is one possible option. For 1000 nm 2PE, the tested Clover-mRuby2, the improved Clover3-mRuby3 pair or Clover3 with faster-maturing mScarlet (Bajar et al., 2016b; Bindels et al., 2017; Lam et al., 2012) could be combined with mCyRFP-mMaroon (Laviv et al., 2016). For excitation at 1200 nm, a number of red FRET pairs have been reported as described above, among which eqFP650-iRFP713 is the most red-shifted, but could suffer from BV dependency. Therefore, new combinations could be explored, using the bright mCardinal or mNeptune2.5 as donors with iRFP682 or iRFP713 as acceptor. One challenge when designing such additional pairs is direct excitation of fluorescent acceptors in other FRET pairs, for example, exciting tdNirFP, mMaroon and Ruby3 with 1200 nm 2PE. Even if this contribution would be

small enough to allow unmixing, this would be significantly detrimental to the signal-to-noise ratio of the biochemical readouts. Therefore, the most suitable strategy is the use of dark acceptors like Ultramarine, cjBlue, sgBP and msCP576h.

It should be also noted that increasing the number of fluorescence properties imaged can both extend the type of measurements that can be performed and the biochemical resolving power in microscopy. For instance, fluorescence polarization enables the measurement of homo-FRET (FRET between two identical fluorescent proteins) or FRET between a chemically distinct but spectrally similar donor and acceptor pairs because of the significant depolarization of sensitized emission. mCherry variants have been described in such a configuration which would also fit well with a second excitation at 1000 nm 2PE as described above (Lindenburg et al., 2013). Furthermore, the detection of time-resolved spectra, other pairs or even all properties of fluorescence (polarization, lifetime and spectra) as in a hyper-dimensional imaging platform envisioned by our group (Esposito et al., 2013) can increase the multiplexing capabilities in fluorescence microscopy, either providing a better biochemical resolution or a growing number of FRET sensors that can be imaged simultaneously in a living cell.

Finally, avoiding the development of new FRET pairs altogether, spatial separation of the same pair in different compartments would allow studying two spatially segregated biochemical events simultaneously with the same FRET pair. With targeting motifs available for a wide range of compartments, such segregation can be easily achieved (Komatsu et al., 2011) and has been previously used for multiplexing of three FRET sensors (DiPilato et al., 2004; Piljic and Schultz, 2008). Furthermore, a large number of non-FRET-based sensors consisting of a single fluorophore (Kunkel et al., 2005; Niino et al., 2010; Piljic and Schultz, 2008; Sergeeva et al., 2017) could be used to complement the current set of sensors provided they are spectrally separated from the FRET pairs.

Apart from the availability of suitable FRET pairs, the number of fluorescent proteins that can be expressed in a cell without affecting viability will likely limit the extent of multiplexing. While high expression levels are needed for imaging, high expression of multiple proteins can affect cell viability and function, which we noticed when creating stable cell lines constitutively expressing our three-colour suite (see Chapter 3). Inducible expression systems (e.g. tetracycline-inducible promoter such as ‘Flp-In’ systems) allow to tightly confine transgene expression to the time of the experiment to avoid any effects on cell growth and viability during cell line maintenance. Furthermore, inducible promoters allow titration of the expression to optimally balance brightness with effects on viability. Transient transfections are an alternative

to overcome long-term effects on viability, but these are often toxic in the short-term and variable in efficiency. Finally, combining FRET pairs with cell-permeable organic FRET probes could be a potential way to avoid any effect of expression of genetic probes.

In summary, an extension of the FRET multiplexing platform is not only biologically desirable but, as shown in this section, feasible with available tools and technologies.

2.4.3 Specificity of caspase linkers

Whereas linker cleavage was efficient during STS-induced cell death, the rescue using irreversible caspase-inhibitor of the peptide-mimetic Z-VAD-FMK family was often incomplete when assayed by Western Blot and FLIM imaging of the sensors. Introducing different motifs (VDTTD, DEVDR) resulted in an increased, but still limited, specificity. It should be noted, that because the inhibitors are peptide-mimetics of the canonical VDVAD, DEVD and LEHD sequences, they suffer from the same, or in the case of VDVAD and DEVD, worse specificity than the actual sensors, further confounding the interpretation. For this reason, these motifs have been systematically optimized creating a new class of chemical inhibitors, and, if labelled with a fluorescent dye, activity-based probes for caspases (Berger et al., 2006; Edgington et al., 2009, 2012). However, because they contain non-natural amino acids, these tools cannot be used in genetically encoded sensor.

Considering the available literature, a limited specificity of such substrate-based sensors is not surprising due the cross-talk and overlapping cleavage specificities between caspases (Berger et al., 2006; Delgado et al., 2013; Kitevska et al., 2014; McStay et al., 2008; Stennicke et al., 2000). Therefore, when using consensus motifs found in cellular substrates, the observation of cross-talk can be expected, because it recapitulates the situation in the cell where multiple caspases cleave one substrate. Thus, speaking of a sensor for a given caspase (e.g., caspase-2, -3 or -9) is a simplification used for clarity of language, a simplification widely used in the relevant literature, but when interpreting results we shall always consider that these sensors more accurately described as VDTTDase, DEVDRase and LEHDase activity sensors.

Relative specificity is an issue for most measurements and perturbations in biology. Therefore, falsifying observations based on FRET sensors requires, like for any other assay, appropriate control experiments and execution of orthogonal assays. For instance, siRNA-mediated knockdowns have been widely used to study caspases (Dorstyn et al., 2012; Lassus et al., 2002; Oliver et al., 2011). However, knockdowns can be of limited use when studying enzymes, since even a small percentage of remaining enzymes can be sufficient to fully cleave a caspase

linker. Complete genetic knock-outs are better suited for this reason but are more resource demanding and impossible for essential genes. Moreover, chronic depletion of specific proteins can induce adaptation of the related biochemical networks thus rendering them non-representative of the biochemical networks an experimenter intended to study. Western Blot for caspase processing as an orthogonal assay can also contribute to understanding the involvement of different caspases, even though not all caspases require processing for activity. Combining immunoprecipitation of active caspases and Western Blot, the identity of the most upstream caspase can be assessed (Tu et al., 2006).

Another explanation for limited specificity could be the experimental setup which uses a highly potent, but not well-characterized cell death inducer such as Staurosporine (Chae et al., 2000) and only assesses one, late endpoint. At this point, all caspases are fully activated and most cellular proteins proteolytically cleaved, not only by caspases but the many other proteases that get activated during the late stages of cells death. Indeed, studies assessing specificity of caspases (Berger et al., 2006; Kitevska et al., 2014; McStay et al., 2008; Stennicke et al., 2000) either study caspases using recombinant proteins or in cell-free assays, or if studied in cells, perform end-point studies with high doses of inducer and a single time point. Studying caspase activation over time could, therefore, allow studying differences that these approaches are unable to observe.

Indeed, several studies successfully used both fluorometric as well as FRET-based caspase sensors based on linker sequences used in this work to study DNA-damage (Lin et al., 2006; VDVAD and DEVD) or metabolite-stress induced intrinsic apoptosis (Viswanath et al. 2001; DEVD, IETD, LEHD), as well as TRAIL-induced extrinsic apoptosis (Albeck et al., 2008b; Spencer et al., 2009; DEVDR and IETD). All of these studies showed differential cleavage of the sensors, suggesting that under those conditions, the canonical sequences can indeed be highly specific.

Accordingly, in the next chapter, we will use the optimized FRET pair suite developed here to study caspase activation in single cells in response to a more targeted inducer (Cisplatin) over extended periods of time and in combination with a number of inhibitors as well as Western Blotting as an orthogonal assay. Using this combination we can indeed show that there are cells that are responding with single sensors or different combination of sensors, strongly arguing that under those experimental conditions, the sensors developed in this chapter are specific.

Table 2.1 - **Photophysical properties of fluorescent proteins discussed in this study.** All values as reported in the given reference. N.d., not determined. Sorted in each class by ascending emission maximum.

	Excitation maximum (nm)	Emission maximum (nm)	Quantum Yield	Extinction Coefficient (M^{-1} cm^{-1})	Quaternary structure	Lifetime (ns)	Reference
Non-fluorescent chromoproteins (Extinction Coefficient ≤ 0.01)							
CRY2PHR	350/450	-	-	-	n.d.	n.d.	(Banerjee et al., 2007; Kennedy et al., 2010)
msCP576 (No. 20)	576	-	-	64000	tetramer	n.d.	(Kogure et al., 2006)
sgBP	608	-	-	123000	tetramer	n.d.	(Chiang et al., 2015)
cjBlue	610	-	-	66700	tetramer	n.d.	(Chan et al., 2006)
ShadowG	486	510	0.005	89000	monomer	n.d.	(Murakoshi et al., 2015)
ShadowY	519	531	0.01	136000	monomer	0.17	(Murakoshi and Shibata, 2017)
Blue fluorescent proteins							
mTagBFP	399	456	0.63	52000	monomer	2.2	(Subach et al., 2008)
Green fluorescent proteins							
EGFP	488	507	0.6	56000	dimer	2.4	Clontech
Clover	505	515	0.76	111000	monomer	n.d.	(Lam et al., 2012)
mClover3	506	518	0.78	109000	monomer	n.d.	(Bajar et al., 2016a)
bfloGFPc1	493	521	0.15	98800	dimer	n.d.	(Bomati et al., 2014)
mAmetrine	406	526	0.58	45000	monomer	2.6	(Ai et al., 2008)
sREACh	517	531	0.07	77500	monomer	n.d.	(Murakoshi et al., 2008)

	Excitation maximum (nm)	Emission maximum (nm)	Quantum Yield	Extinction (M^{-1} cm^{-1}) Coefficient	Quaternary structure	Lifetime (ns)	Reference
Orange fluorescent proteins							
mOrange	548	562	0.69	71000	monomer	n.d.	(Shaner et al., 2004)
Red and far-red fluorescent protein							
hmKeima8.5	438	612	0.11	32000	monomer	n.d.	(Guan et al., 2015)
dKeima570	440	570	0.15	14000	dimer		(Kogure et al., 2006)
mKeima	440	620	0.24	14400	monomer	2.93	(Kogure et al., 2006)
mBeRFP	446	611	0.27	65000	monomer	2.0	(Yang et al., 2013)
LSS-mKate2	460	605	0.17	26000	monomer	n.d.	(Piatkevich et al., 2010)
LSS-mKate1	463	624	0.08	31200	monomer	n.d.	(Piatkevich et al., 2010)
mCyRFP	528	594	0.65	35000	monomer	3.55	(Laviv et al., 2016)
tdTomato	554	581	0.69	138000	Tandem dimer	n.d.	(Shaner et al., 2004)
TagRFP	555	584	0.48	100000	Monomer	2.3	(Merzlyak et al., 2007)
mRuby3	558	592	0.45	128000	monomer	n.d.	(Bajar et al., 2016a)
mRuby2	559	600	0.38	113000	monomer	n.d.	(Lam et al., 2012)
mScarlet	569	594	0.70	100000	monomer	3.9	(Bindels et al., 2017)
KFP1 (non kindled)	580	600	0.001	123000	Monomer	n.d.	(Chudakov et al., 2003)

	Excitation maximum (nm)	Emission maximum (nm)	Quantum Yield	Extinction (M^{-1} cm^{-1}) Coefficient	Quaternary structure	Lifetime (ns)	Reference
mKate2	588	633	0.40	62500	monomer	n.d.	(Shcherbo et al., 2009)
mPlum	590	649	0.10	41000	monomer	n.d.	(Wang et al., 2004)
eqFP650	592	650	0.24	65000	dimer	n.d.	(Shcherbo et al., 2010)
mGarnet	598	670	0.09	95000	monomer	0.8	(Hense et al., 2015)
TagRFP675	598	675	0.08	46000	monomer	n.d.	(Piatkevich et al., 2013)
mNeptune2.5	599	643	0.28	95000	monomer	n.d.	(Chu et al., 2014)
tdFP615#	~600	615	0.20	79000	tandem-dimer	n.d.	(Miyamoto et al., 2015)
mNeptune	600	650	0.20	67000	monomer	n.d.	(Lin et al., 2009)
mCardinal	604	659	0.19	87000	monomer	n.d.	(Chu et al., 2014)
eqFP670 (NirFP)	605	670	0.07	70000	dimer	n.d.	(Shcherbo et al., 2010)
mMaroon	609	657	0.11	80000	monomer	n.d.	(Bajar et al., 2016b)
TagRFP657	611	657	0.10	34000	monomer	n.d.	(Morozova et al., 2010)
iRFP682	663	682	0.11	90000	dimer	n.d.	(Shcherbakova and Verkhusha, 2013)
IFP1.4	684	708	0.07	92000	monomer	n.d.	(Shu et al., 2009)
iRFP713	690	713	0.06	98000	dimer	n.d.	(Filonov et al., 2011)

spectroscopic properties reported for FP615 (not tandem-dimer)

Table 2.2 - **Overview of all FRET pairs and configurations tested for multiplexing platform.** D: Donor, A: Acceptor. Short linker: 14 amino acids, LGGTGSGSGSASGG. Long linker: 24 amino acids, SPGSTLGGTGSGSGSASGGPSGSA

Donor	Acceptor	Foerster Radius	Orien-tation	Linker	FRET efficiency	Aggregation/Other observations	References	Figure
mTagBFP	sREACh	5.42	D-A	Short	33%	Green fluorescent aggregation in bright cells	(Niino et al., 2010)	2.3
	CRY2PHR	-	D-A	Short	14%	Strong aggregation in all cells	This work	2.5
	CRY2PHR fragments	n.d.	D-A	Short	< 6%	Aggregation increased compared to full-length in all cells and expression decreased	This work	2.5
	bfloGFPc1	5.79	D-A	Short	16%	Aggregation in 30% of cells	This work	2.5
	bfloGFPc1short	5.79	D-A	Short	21%	Aggregation in 30% of cells	This work	2.5
	ShadowG	5.86	D-A	Short	29%	Green fluorescent aggregation in bright cells	(Murakoshi et al., 2015)	2.5
mAmetrine	msCP576h	5.58	D-A	Short	44%	Aggregation in very bright cells	This work	2.6
Clover	mRuby2	6.4	D-A	Short	22%	No aggregation, used at 1010nm 2PE, incomplete maturation observed	(Lam et al., 2012)	2.16
mKeima	mNeptune	4.92	D-A	Short	n.d.	No aggregation, not unusable due to pH-dependent green emission	This work	2.14
	iRFP713	5.89	D-A	Short	15%	Aggregates show low lifetime peak and are visible in some healthy and all shrunk cells, Co-factor Biliverdin required for FRET	This work	2.11
	IFP4.1	5.39	D-A	Short	3%	Co-factor Biliverdin required for FRET (more dependent than iRFP713), low lifetime decrease in shrunk cells	This work	2.14
	cjBlue	5.31	D-A	Short	16%	Moderate to strong aggregation in all cells; aggregation maintained in C-terminal truncations	This work	2.10
	NirFP	5.14	D-A	Short	37%	Strong aggregation in >50% of cells	This work	2.12
	NirFP	5.14	A-D	Short	n.d.	Strong aggregation in all cells, aggregates smaller than D-A orientation	This work	2.12

Donor	Acceptor	Foerster Radius	Orien-tation	Linker	FRET efficiency	Aggregation/Other observations	References	Figure
mKeima	tdNirFP	5.77	A-D	Short	53%	Little aggregation in few cells, no linker cleavage	This work	2.12
	tdNirFP	5.77	A-D	Long	37%	Little aggregation in few cells, good linker cleavage	This work	2.13
	Ultramarine	4.55	A-D	Short	10%	Strong aggregation in 70-80% of cells	This work	2.14
	Ultramarine	4.55	D-A	Short	10%	Strong aggregation in 40-50% of cells	This work	2.14
	tdUltramarine	5.10	D-A	Long	n.d.	Strong aggregation in all cells	This work	2.14
	tdUltramarine	5.10	A-D	Long	n.d.	Strong aggregation in all cells	This work	2.14
	iRFP682	5.94	A-D	Long	5%	Moderate aggregation in 50% of the cells	This work	2.14
	tdiRFP682	6.67	A-D	Long	5% (40% with BV)	Strong aggregation in more than 50% of cells, Maximum FRET requires Biliverdin	This work	2.14
	tdiRFP682	6.67	D-A	Long	n.d.	Not expressed	This work	2.14
	mGarnet	5.34	A-D	Short	3%	Moderate aggregation in 20% of cells	This work	2.14
	mGarnet	5.34	D-A	Short	10%	No aggregation	This work	2.14
hmKeima8.5	tdNirFP	6.24	A-D	Long	n.d.	Strong aggregation in 70-80% of cells	(Guan et al., 2015)	2.15
mBeRFP	iRFP720	5.67	D-A	Short	20%	Strong aggregation in 50% of the cells with low lifetime, green fluorescence of mBeRFP not ideal for multiplexing	This work	2.15
	tdNirFP	6.02	A-D	Short	n.d.	Strong aggregation in all cells	This work	2.15

Chapter 3 Non-genetic heterogeneity in the caspase response to Cisplatin-induced DNA damage

3.1 Introduction

3.1.1 Intra-tumour heterogeneity leads to fractional killing and resistance in response to DNA damage

Cells are constantly exposed to DNA damage caused by a multitude of endogenous and environmental sources. Such lesions can lead to mutations in genes as well as chromosomal aberrations, which in turn can result in the development of tumours and promote tumour progression (Jackson and Bartek, 2009). In response to DNA damage, a complex network of mechanisms - collectively referred to as the DNA Damage Response (DDR) - dedicated to sense and repair DNA lesions and signal their presence is activated to maintain genomic integrity. If the damage is incorrectly repaired or remains unresolved, tumour suppressive mechanisms may be engaged resulting in cell death or the permanent withdrawal from the cell cycle by senescence. DDR is compromised during the early evolution of most tumours confirming its critical tumour suppressive role (Bartkova et al., 2005; Gorgoulis et al., 2005; Halazonetis et al., 2008); therefore, the DDR has been one of the main pharmacological targets as cancer cells tend to be more sensitive to DNA damage compared to normal cells (Roos et al., 2015). Indeed, localized induction of DNA damage by radiotherapy and the systemic administration of genotoxic drugs are the most-widely used and effective first-line treatments for cancer (Matt et al., 2016). Unfortunately, the effectiveness of tumour therapy is frequently limited by tumour cells that exhibit tolerance or resistance to treatment (Holohan et al., 2013) resulting in the survival of a subset of cancer cells, a phenomenon often referred as ‘fractional

killing'. Cancer cells that survive chemo- or radiotherapy may then proliferate leading to relapse. Fractional killing may occur because of uneven distribution of a drug within the tumour mass (Tannock et al., 2002) and because of intra-tumour heterogeneity (Caiado et al., 2016).

Role of intra-tumour heterogeneity in cancer treatment

Genetic heterogeneity within a tumour is a major cause of drug resistance (Fig. 3.1; Caiado et al., 2016) and is caused either by pre-existing mutant cells that are, by chance, already resistant or by tumour cells that escape cell death by chance or by mechanisms of drug tolerance and then acquire additional mutations during therapy (Greaves and Maley, 2012; Reya et al., 2001). Frequently, mutations alter drug uptake and efflux mechanisms, binding sites of the drug on the target or other sites leading to reactivation of the target or its effectors. These mutations will, therefore, result in differential sensitivities to drug treatment of different mutant cells (Barranco et al., 1972). While genetic heterogeneity has been a focus of much research, recently, non-genetic heterogeneity between genetically identical cells has also been also identified as a key mechanism in the emergence of resistance in several cancers.

Non-genetic heterogeneity arises from four interrelated and non-mutually exclusive mechanisms: epigenetic regulation, cellular differentiation hierarchies, the influence of the tumour environment, and stochastic fluctuations in gene expression (Fig. 3.1; Caiado et al.,

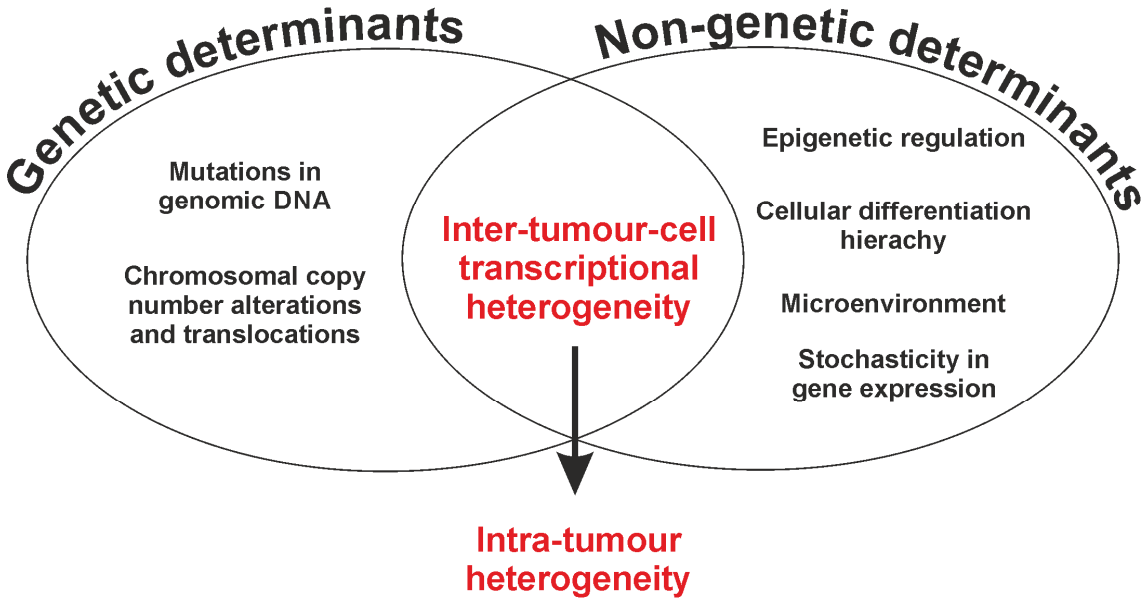

Figure 3.1 – **Sources of intra-tumour heterogeneity**

Intra-tumour heterogeneity arises from heterogeneity in the gene expression of individual tumour cells which is determined by genetic and non-genetic factors. Adapted from Caiado et al., 2016.

2016). Together, these processes cause heterogeneity in gene expression between tumour cells and can affect treatment sensitivity, just as genetic determinants do.

For example, in an isogenic model of 10 colorectal cancers, Kreso *et al*. found that genetically identical cells exhibited variation in proliferation, persistence and resistance after xenotransplantation and that chemotherapy selected for a subset of such cells (Kreso et al., 2013). Similarly, in melanoma, a subset of cells temporarily exhibits a slowdown in the cell cycle through chromatin changes. While the presence of this subset is required for sustained tumour growth and resistance to chemotherapy, the identity of these cells changes over time (Roesch et al., 2010). Similarly, Sharma and colleagues describe the presence of a subset of lung-cancer derived cells that showed resistance to drugs including Cisplatin and find that the resistant cell state is created transiently through epigenetic modification (Sharma et al., 2010).

Therefore, accumulating evidence implicates non-genetic heterogeneity as a fundamental, yet underappreciated, determinant of resistance and in the response to cancer therapies. However, the molecular mechanisms underlying such heterogeneity are largely unknown. In this chapter, I attempt to falsify the hypothesis that cell-to-cell variation in the dynamics of signalling networks underlies the heterogeneity in response to DNA damaging drugs. In the following paragraphs, I will, therefore, introduce the most pertinent literature on non-genetic heterogeneity in response to cell death stimuli to give an overview of the field to which this dissertation aims to contribute to.

Experimental evidence for non-genetic heterogeneity in response to cell death stimuli

Non-genetic heterogeneity in response to pro-apoptotic stimuli appears to be universal across many different cell lines and kind of stimulus (Spencer and Sorger, 2011). Early single-cell studies carried out with time-lapse microscopy and flow cytometry have demonstrated that both the onset and mode of cell death is highly variable in genetically identical populations of cells (Goldstein et al., 2000; Tyas et al., 2000). Building on this work in a seminal paper, Gascoigne and Taylor performed time-lapse imaging of 15 different cancer cell lines and observed extensive inter- and intra-line difference in response to the same anti-mitotic drugs (Gascoigne and Taylor, 2008). Using single-cell proteomics, Cohen *et al.* demonstrated heterogeneity in protein dynamics in response to the DNA damaging agent Camptothecin (Cohen, 2008). Similarly, heterogeneity in TRAIL (tumour necrosis factor-related apoptosis-inducing ligand)-induced extrinsic apoptosis has been extensively studied using a combination of time-lapse imaging and flow cytometry of caspase-8 and caspase-3 substrate cleavage sensors and computational models (Albeck et al., 2008a, 2008b). Importantly, this work from

Albeck and colleagues was the first comprehensive study of the dynamics of cleavage for two caspase substrates with sufficiently large sampling of cell populations to identify novel intermediate cell death states. Using the same model system and comparing identical sister cells, Spencer and Sorger showed that stochastic differences in protein expression can explain the fractional killing of TRAIL (Spencer et al., 2009). Later, Roux *et al.* found that the extent of caspase-8 activity in response to TRAIL relative to a threshold determines fractional killing and that the expression levels of c-FLIP and BCL-2 that vary between genetically identical cells, at least partially, set this threshold (Roux et al., 2015).

Most recently, Paek *et al.* demonstrated that cell-to-cell variation in p53 dynamics, measured using time-lapse imaging, leads to fractional killing in response to the DNA-inducing agent Cisplatin (Paek et al., 2016). They describe a threshold level for p53 at which cell death is initiated. While the importance of signal thresholds had already been described in other studies (Chen et al., 1996; Gascoigne and Taylor, 2008; Kracikova et al., 2013), the novelty of Paek's finding is that the threshold increases with time after Cisplatin treatment due to the induction of proapoptotic genes, predominantly from the family of Inhibitors of Apoptosis (IAPs). The presence of both heterogeneity in p53 dynamics as well as a dynamically moving threshold exemplifies the complexity of cell fate decisions and suggests novel approaches, such as treatment holidays, to address fractional killing in tumour therapy.

While the studies above have provided invaluable insights into the mechanisms of fractional killing in genetically identical populations, the number of factors they were able to study simultaneously was limited, and therefore essential information was likely missed. For example, Paek and colleagues observed p53 at the single-cell level, while IAP levels that set the threshold were only studied at a population level (Paek et al., 2016). As Paek and colleagues pointed out, studying both p53 and IAP dynamics over time simultaneously in the same cell might further help in the rational design of treatments aiming to maximize the number of cells that respond. Therefore, there is a strong need for tools that allow monitoring multiple signalling events and cell fate in single cells over time to sufficiently map the complexity of the signalling pathways involved. Consequently, we decided to use the novel tools for multiplexed imaging described in the second chapter of this dissertation to study the heterogeneity of cell death in response to Cisplatin-induced DNA-damage.

In the following sections, I will first introduce the mode of action of Cisplatin and the cellular response to DNA damage, followed by a description of the cell death pathways initiated by this response, with a focus on the role of caspases and their hierarchical activation.

3.1.2 Cisplatin-induced DNA damage response

Since its first approval in 1978, Cisplatin and its analogues Carboplatin and Oxaliplatin have become the first-line treatment for solid tumours including testicular, ovarian, cervical, head and neck and small-cell lung cancers (Basu and Krishnamurthy, 2010). Cisplatin is also used in combination with other anti-cancer agents as well as an adjuvant treatment after radiotherapy and surgery. However, the strong toxicity of Cisplatin on healthy tissue, especially in kidneys, and the frequent development of chemoresistance limit the effectiveness of Cisplatin.

Mechanism of Cisplatin-mediated DNA damage

Chemically, Cisplatin, or cis-diamminedichloroplatinum(II), is a neutral complex of divalent Pt with two chloride and two amine ligands (Kelland, 1993). It can cross the plasma membrane by passive or facilitated diffusion, as well as active transport, depending on the cellular context (Basu and Krishnamurthy, 2010). Once inside the cell, Cisplatin is aquated forming a potent electrophile that reacts with cellular nucleophiles, such as nucleic acids as well as thiol groups of proteins.

Non-DNA targets of Cisplatin are predominantly thiol-rich Glutathione and Metallothionein, which lead to its detoxification and contribute to resistance (Cepeda et al., 2007). Cisplatin also binds to lipids in the plasma membrane, which can cause membrane damage and induction of cell death pathways (Speelmans et al., 1997). While these mechanisms contribute to the cellular response to Cisplatin, binding and damaging DNA is considered the predominant cytotoxic mechanism (Basu and Krishnamurthy, 2010).

At the DNA, Cisplatin forms covalent bonds between the N^7 position of the purine bases creating 1,2- or 1,3-intrastrand crosslinks and to a lower extent inter-strand cross-links (Fuertes et al., 2003). These DNA lesions are considered a major cause for the cytotoxic effect of Cisplatin because they interfere with DNA replication as well as the transcription of essential genes. If the DNA damage at stalled replication forks is not repaired, the fork can collapse. This fork collapse leaves DNA unprotected, which often results in double-strand breaks that activate DDR and cell death pathways. Here, I will first discuss the DDR pathways in response to Cisplatin and later introduce cell death mechanisms.

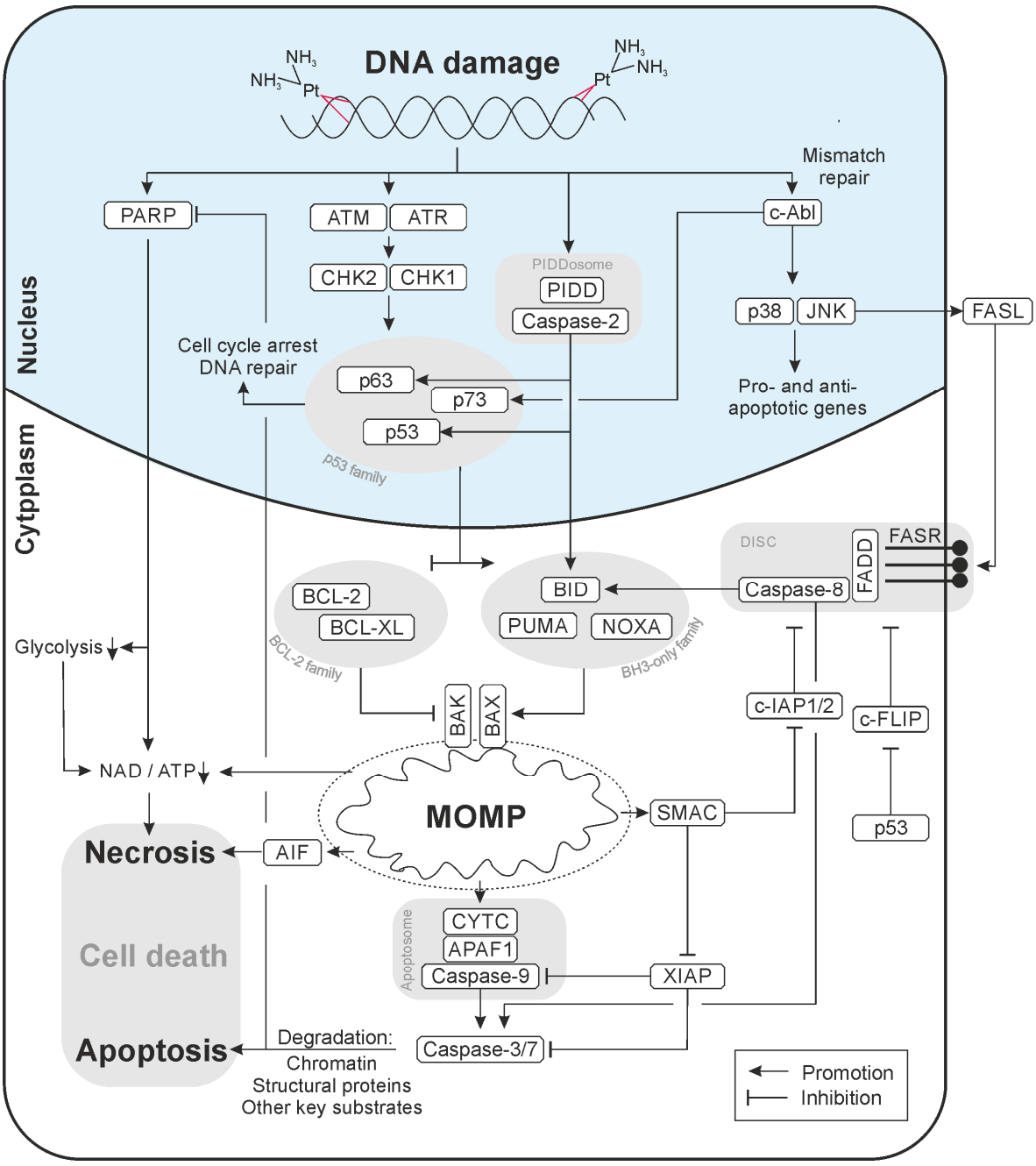

Figure 3.2 – **Cell death response to Cisplatin-induced DNA damage**

In response to DNA damage induced by Cisplatin, a network of proteins is activated that ultimately leads to necrotic or apoptotic cell death. A complete discussion and references for the shown connections are presented in the main text. Not all involved proteins are shown for clarity. In particular, caspase-3 also promotes caspase-2 and -9 activity by processing. Caspase-2 can also be activated by binding to DISC and in the absence of PIDD. More details on the events downstream of MOMP including all released outer membrane space proteins can be found in Fig. 3.3. Finally, pro-survival signalling that negatively regulates all shown cell death pathways at multiple points is omitted for clarity, but plays a crucial role in the cell death response as discussed in the main text. Layout based on Matt et. al, 2016, but strongly adapted. Abbreviations: PARP, Poly(ADP-Ribose) Polymerase; ATM, Ataxia Telangiectasia Mutated; ATR, Ataxia Telangiectasia And Rad3-Related Protein; CHK1/2, Checkpoint Kinase 1/2; PIDD, P53-Induced Death Domain Protein; JNK, C-Jun N-Terminal Kinase; p38, p38

mitogen-activated protein kinase; FASL, Fas Ligand; FASR, Fas receptor (CD95); BCL-2/-XL, B-Cell CLL/Lymphoma-2/-XL; BID, BH3 (BCL-2 homology 3) Interacting Domain Death Agonist; PUMA, P53 Up-Regulated Modulator Of Apoptosis; NOXA, Phorbol-12-Myristate-13-Acetate-Induced Protein; FADD, Fas Associated Via Death Domain; DISC, Death Inducing Signalling Complex c-IAP1/2, cellular Inhibitor of Apoptosis 1/2; c-FLIP, Cellular FLICE-Like Inhibitory Protein; BAX, BCL2 Associated X; BAK, BCL2 Antagonist/Killer 1; SMAC, Second Mitochondria-Derived Activator Of Caspase also known as DIABLO, Direct IAP-Binding Protein With Low PI; AIF, Apoptosis Inducing Factor; CYTC, cytochrome-c; APAF1, Apoptotic Peptidase Activating Factor 1; XIAP, X-Linked Inhibitor Of Apoptosis; NAD, Nicotinamide adenine dinucleotide; ATP, Adenosine triphosphate.

DDR pathways in response to Cisplatin

There are two well described Cisplatin-induced DDR pathways, one acting through the central tumour suppressor p53 and another through the tyrosine kinase c-ABL (Fig. 3.2).

p53, a transcription factor and potent tumour suppressor, is a central hub in stress cellular responses and critical element of the DDR (Vousden et al., 2009). Under normal conditions, p53 expression is maintained at very low levels by a negative feedback loop with the E3 ubiquitin ligase MDM2, a transcriptional target of p53. Upon DNA damage, the kinases CHK1 and CHK2 are activated by upstream DNA-damage sensing kinases ATM and ATR and in turn, phosphorylate p53 resulting in its stabilization. Stabilized p53 then induces expression of a multitude of genes involved in the DDR, such as P21 which causes cell cycle arrest until the damage is repaired, DNA repair genes such as GADD45, and finally genes that induce cell death such as BAX, BAK, NOXA and PUMA (De Laurenzi and Melino, 2000). Furthermore, p53 promotes cell death by binding and inhibiting anti-apoptotic protein BCL-XL (Kutuk et al., 2009) and inducing degradation of c-FLIP thereby activating a caspase-8-dependent cell death programme (Abedini et al., 2008). Although p53 plays a key role in Cisplatin-mediated cell death, p53-deficient cells still respond to Cisplatin, suggesting p53-independent mechanisms.

One such mechanism is the activation of c-ABL which in turn activates JNK as well as p38 MAPK (Kharbanda et al., 1995) in cells that are proficient for one of the major repair pathways for Cisplatin-crosslinks, mismatch repair. While JNK and p38 MAPK both regulate the expression of a wide range of pro- as well as anti-apoptotic genes, JNK also directly inhibits anti-apoptotic proteins BCL-2 and BCL-XL to induce apoptosis (Sui et al., 2014). Long-term activation of JNK and p38 MAPK also promotes caspase-8-dependent cell death by induction of the expression of FAS ligand, whose role is further discussed in section 3.1.4 (Brozovic et al., 2004). Finally, c-ABL directly stabilizes the p53 family member, P73, which can transactivate pro-apoptotic genes by binding to the p53 promoter (Wang et al., 1999).

Together, this description demonstrates the complexity of the DDR to Cisplatin. Arguably, not a single, but multiple mechanisms are active at the same time in the same cell or different cells in a population, determining their sensitivity to Cisplatin-induced cell death and

suggesting underlying mechanism for the observed heterogeneity, as exemplified by role of cell-to-cell variation of p53 dynamics discussed at length above (Paek et al., 2016).

As I will show next, the cell death pathways induced through DDR show a similar complexity and potential for heterogeneity.

3.1.3 Cisplatin induces two different types of cell death

Apoptosis and necrosis constitute the two major cell death pathways in response to any death stimulus. In the first instance, the morphology of apoptotic and necrotic cells as well as their underlying signalling networks are rather distinct (Degterev and Yuan, 2008).

Apoptosis is characterized by cell shrinkage, chromatin condensation and fragmentation, membrane blebbing and the formation of apoptotic bodies that contain cellular material. Because the membrane integrity is maintained and no intracellular components are exposed to the extracellular space, apoptosis is generally thought to produce no immune response (Degterev and Yuan, 2008). In contrast, necrosis is characterized by rounding of the cell, cytoplasmic swelling, dilation of organelles and the absence of chromatin condensation. Because the membrane integrity is not maintained, the release of intracellular material can trigger an immune response, which in turn can lead to local or systemic damage of tissue (Berghe et al., 2014). The effect of the immune response to necrosis is considered one important cause for cytotoxicity on healthy tissue that can lead to disruption of treatment (Crusz and Balkwill, 2015; Degterev and Yuan, 2008). Morphological classification has been the predominant way to identify cell death modalities. However, it is now established in the field that morphology is only of limited use and should only be used to inform biochemical investigation because different kind of cell death can exhibit similar phenotypes and a qualitative assessment of morphology is prone to misinterpretation (Galluzzi et al., 2012). Therefore, cell death modalities are defined by their biochemistry, rather than morphology.

In that regard, historically, apoptosis has been described as a “programmed cell death” that is controlled by cellular signalling and induced by specific intracellular and extracellular triggers. In contrast, necrosis was considered an “uncontrolled” form of cell death triggered by a general collapse of the cell, for example to damage to the lipid membranes by reactive oxygen species

and a depletion of cellular energy. However, it is increasingly accepted that necrosis is also tightly regulated by cellular signalling in response to many types of damage if not all (Berghe et al., 2014). Depending on the underlying biochemical mechanisms, many different forms of necrotic, non-apoptotic, cell death have been described, including Necroptosis, Parthanatos, Oxytosis, Ferroptosis, NETosis, Pyronecrosis and Pyroptosis (Galluzzi et al., 2012).

Cisplatin can cause apoptosis and necrosis in the same cell population

Cisplatin can give rise to apoptosis (Henkels and Turchi, 1997), necrosis (Guchelaar et al., 1998; Matsumoto et al., 1997; Pérez et al., 1999) or both (Montero et al., 2002; Pestell et al., 2000; Segal-Bendirdjian and Jacquemin-Sablon, 1995) in the same cell population.

It has been suggested that the energetic status of the cell determines whether a Cisplatin-treated cell dies from apoptosis or necrosis (Fuertes et al., 2004), because Cisplatin and other chemotherapeutic drugs lead to a depletion of ATP in a time-dependent manner (Zhou et al., 2002) and the level of ATP has been found to determine the cellular decision between apoptosis or necrosis (Eguchi et al., 1997; Leist et al., 1997). This is in line with the general definition of apoptosis as ATP-dependent and necrosis as an ATP-independent mechanism (Galluzzi et al., 2012).

The depletion of ATP has been connected to a hyperactivation of PARP (Poly-ADP-Ribose Polymerase) that is triggered in response to DNA damage and promotes DNA repair (Dulaney et al., 2017). PARP activity utilizes NAD whose depletion leads to a breakdown of the electron-transport chain and loss of ATP production. Additionally, PARP also inhibits Hexokinase, the first enzyme in Glycolysis, leading to a further interference with cellular metabolism and ATP depletion (Andrabi et al., 2014). PARP hyperactivation and ATP/NAD depletion are hallmarks of one kind of necrotic cells death, termed Parthanatos (Andrabi et al., 2008; Los et al., 2002). During Parthanatos, PARP not only depletes cellular energy, but directly causes the release of AIF (apoptosis-inducting-factor) from the mitochondria which induces large DNA fragmentation once it entered the nucleus, which was recently suggested to be the actual cause of cell death (Berghe et al., 2014; Fatokun et al., 2014; Fig. 3.3). Whether the necrotic cell death in response to Cisplatin is indeed Parthanatos remains to be experimentally validated.

Deficient caspase activation as a cause of necrotic cell death

However, there are indications that PARP plays a role in Cisplatin-induced cell death and that it is linked to caspase activation. During apoptosis, PARP is inactivated through caspase

cleavage, maintaining sufficiently high ATP levels to perform the ATP-dependent execution of apoptosis and preventing Parthanatos (Cepeda et al., 2007). This notion supports the hypothesis in which in response to Cisplatin, and possibly other pro-apoptotic stimuli, necrosis functions as a backup mechanism if apoptosis cannot be performed efficiently, and necrosis should be considered as “defective apoptosis”. The observation that caspase inhibition induces a switch from apoptosis to necrosis strongly supports this (Lemaire et al., 1998). Furthermore, Vakifahmetoglu *et al.* showed that Cisplatin induces necrotic cell death in a Cisplatin-resistant cell line in the absence of PARP processing and caspase activity, while in a different line, Cisplatin induces apoptotic cell death including the characteristic PARP processing by active caspases (Vakifahmetoglu et al., 2008). Notably, the cell line that died of a necrotic cell death is more resistant to Cisplatin than their apoptotic counterparts, suggesting that the induction of different cell death pathways is linked to fractional killing (a concept discussed in section 3.1.1). Further evidence that caspases play a crucial role in the response to Cisplatin comes from two studies that showed that a failure to activate caspase-9 results in a reduced sensitivity to Cisplatin in testicular germ cell cancer and ovarian cancer (Liu et al., 2002; Mueller et al., 2003).

Together, these studies put caspases in the focus of the investigation of Cisplatin-induced cell death heterogeneity, suggesting that deficiencies in caspase processing can lead to a defective apoptosis shifting cell death from apoptosis to necrosis and possibly giving rise to Cisplatin-resistance. However, whether cell-to-cell differences in caspase activation are the cause for the non-genetic heterogeneity observed in terms of fractional killing as well as the type of cell death in response to Cisplatin remains unknown.

Therefore, in the following section, I will formally introduce caspases as key mediators of apoptotic cell death and end with a discussion of their role in response to DNA-damage.

3.1.4 Caspase activation in apoptosis

Caspases (*c*ysteine-*asp*artic prote*ases*) are a family of proteolytic enzymes that have functions in inflammation (caspases-1, -4, -5, -11 and -12) as well as cell death (Shalini et al., 2014). Depending on the position in the proteolytical cascade, cell death caspases are classed as initiator caspases (caspase-2, 8, 9, 10) that are activated upstream closest to the stimulus and executioner caspases (caspase-3, 6, 7) that are activated by initiator caspases and are responsible for the dismantling of the cell (Galluzzi et al., 2012).

Caspases are expressed as inactive proenzymes consisting of a large and a small subunit (Shalini et al., 2014). In addition, initiator caspases contain an internal oligomerization domain, the death effector domain (DED) for caspase-8 and -10 and the caspase recruitment domain (CARD) for caspase-2 and -9. DED and CARD domains mediate homodimerization of caspases which is facilitated by the binding to macro-molecular scaffolding complexes such as the death-induced signalling complex (DISC; caspase-8, -10), the apoptosome (caspase-9) or the p53-induced death domain protein complex (PIDDosome, caspase-2). The dimerization is required and sufficient for their activation. However, cleavage of the inter-subunit linker and removal of the dimerization domains by other caspases or autocatalytic processing can further enhance their activity. In contrast, effector caspases are expressed as constitutive dimers which are fully activated when cleaved at the inter-subunit by initiator caspases (Julien and Wells, 2017). The special dual role of caspase-2 as initiator and executioner caspase will be discussed in section 3.1.5.

Caspases are also tightly regulated by several mechanisms, predominantly through post-translational modification as well as direct inhibition. For example, phosphorylation by Cyclin-dependent kinase 1 and other kinases (Andersen et al., 2009) inhibits caspase-2 activity. Caspase-9 is the target of a large number of kinases including ERK, CDK1, AKT and P38 MAPK, all capable of preventing caspase-9 activation (Li et al., 2017). Additionally, active caspase-9 can be directly inhibited by binding of p53 or XIAP (X-linked Inhibitor of Apoptosis). XIAP belongs to the Inhibitor of Apoptosis family (IAP) which also includes other anti-apoptotic members cellular IAPs 1 and 2 (cIAP1/2), melanoma-IAP (ML-IAP) and Survivin (Fulda and Vucic, 2012). Among those, only XIAP has been shown to directly bind and inhibit caspases (caspase-3, -7 and -9; Eckelman and Salvesen, 2006). The other anti-apoptotic IAPs affect caspases in indirect ways. For instance, cIAPs bind SMAC tightly preventing SMAC-dependent inhibition of XIAP; furthermore, cIAPs exhibit E3 ubiquitin ligase activities and regulate the stability of many proteins involved in cell death, including caspase-3, caspase-7 and other IAPs (Fulda and Vucic, 2012).

As already indicated, caspases are key initiators and effectors in apoptotic cell death, warranting a closer look into this key process. As such, apoptosis can be divided into intrinsic and extrinsic pathways depending on the origin of the apoptotic stimulus (Galluzzi et al., 2012).

Mechanisms of intrinsic apoptosis

In intrinsic apoptosis (Fig. 3.3), a variety of intracellular stressors such as DNA damage, oxidative stress or unfolded proteins results in the insertion and opening of pores consisting of

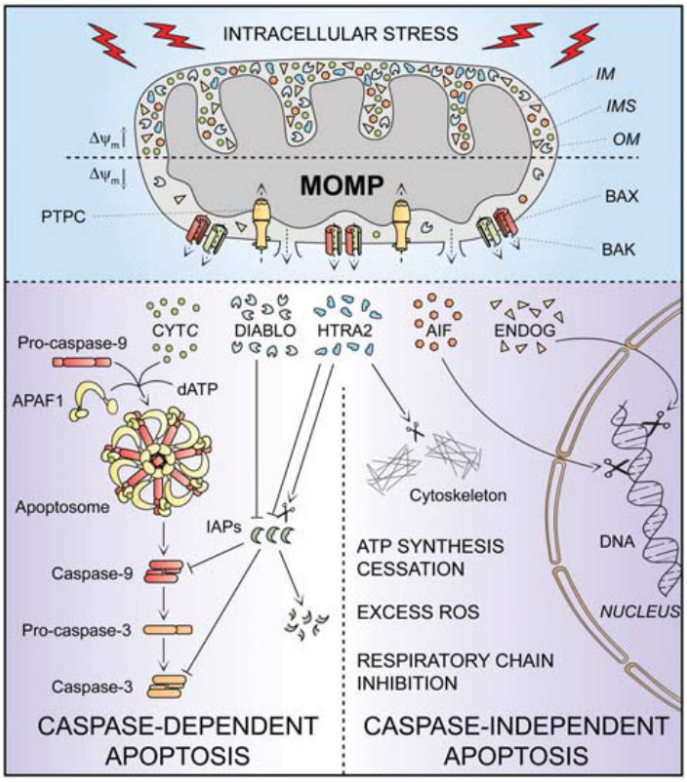

Figure 3.3 – **Caspase-dependent and caspase-independent intrinsic apoptosis**

Intracellular stresses, such as DNA damage, can lead to mitochondrial outer membrane permeabilization (MOMP) through the insertion of the pore proteins BAX and BAK. MOMP results in the loss of membrane potential ($\Delta\psi_m$) and release of intermembrane space (IMS) proteins CYTC, DIABLO, HTRA2, AIF and ENDOG which induce caspase-dependent or caspase-independent apoptosis. For further details see main text. The illustration is taken from Galluzzi et al., 2012. Abbreviations (that are not mentioned in Figure 3.2): IM, inner membrane; IMS, intramembrane space; OM, outer membrane; PTPC, permeability transition pore complex; HTRA2, high temperature requirement protein A2; ENDOG, endonuclease G; ROS, reactive oxygen species.

the proteins BAX and BAK that permeabilize the outer membrane (a process termed MOMP, mitochondrial outer membrane permeabilization). The insertion of BAX/BAK is tightly controlled by opposing classes of proteins, the anti-apoptotic BCL-2 family including BCL-2 and BCL-XL and the pro-apoptotic BH3-only protein family including BID, PUMA and NOXA (Matt and Hofmann, 2016; Fig. 3.2). BH3-only proteins are transcriptionally induced by key components of the DDR including p53, p63, p73 and JNK. MOMP is induced if the BH3-only proteins have reached sufficient levels to neutralize the inhibitory effect of the BCL-2 family proteins on BAX/BAK (Matt and Hofmann, 2016). Subsequently, MOMP leads to a) the release of a number of toxic proteins (CYTC, DIABLO, HTRA2, AIF, ENDOG) from the mitochondria to the cytoplasm; b) the dissipation of the mitochondrial potential $\Delta\psi_m$ which disrupts the $\Delta\psi_m$-dependent ATP synthesis, and c) the build-up of reactive oxygen species due to CYTC-loss-

induced failure of the respiratory chain. Together, these events result in the induction of cell death by two non-mutually-exclusive pathways, one caspase-dependent and the other caspase-independent whose occurrence depends on the physiological and experimental conditions (Fig. 3.2 and 3.3; Galluzzi et al., 2012).

Caspase-dependent intrinsic apoptosis is induced by the CYTC- and ATP-dependent assembly of the apoptosome. Binding of CYTC to the apoptosome induces the dimerization of caspase-9 which is sufficient to activate its protease function, leading to processing and activation of caspase-3 and caspase-7. Caspase-3 and -7 target a large number of substrates involved in cell cycle, DNA repair, cytoskeleton, signalling and other crucial processes whose cleavage ultimately results in the DNA fragmentation and dismantling of the cell. The activity of caspase-3, -7 and -9 is further enhanced by the inhibition of IAP family proteins by DIABLO (also known as SMAC) and HTRA2.

In caspase-independent intrinsic apoptosis, HTRA2 damages the cytoskeleton whereas AIF and ENDOG cause DNA fragmentation, which, together with the breakdown of the cellular metabolism, leads to cell death (Fig. 3.3).

Extrinsic apoptosis as alternative path leading to apoptotic cell death

Extrinsic apoptosis is induced by a plethora of extracellular ligands which bind to a family of death receptors, including FASR (binding FASL, or FAS ligand; also known as CD95), TNFR and TRAILR (Berghe et al., 2014). The ligands can hereby both originate from neighbouring cells as well as being expressed by the same cell (Fig. 3.2). In the most common case, ligand-binding to the receptor induces the assembly of the so-called “death-inducing signalling complex” (DISC) consisting of the adapter protein FADD bound to caspase-8 and the pro-survival proteins cIAP1/2 and c-FLIP, which can regulate caspase-8 activity and are themselves tightly regulated. Under conditions permissive for caspase-8 activation, caspase-8 can trigger apoptosis either by processing caspase-3 and caspase-7 directly or by cleaving Bid which will then induce MOMP thus activating the intrinsic pathway (Galluzzi et al., 2012).

Cisplatin can activate both the intrinsic as well as extrinsic apoptotic pathway

Cisplatin has been found to induce both the extrinsic and intrinsic apoptotic pathways in different cell lines (Basu and Krishnamurthy, 2010; Cepeda et al., 2007; Fig. 3.2). However, whether genetically identical cells can trigger both the extrinsic and intrinsic pathway remains a matter of active debate (Basu and Krishnamurthy, 2010). It is tempting to speculate that a possible co-occurrence of intrinsic as well as extrinsic apoptosis could be an underlying

mechanism for the heterogeneous response to Cisplatin within a clonal population. Therefore, to characterize the mechanisms underlying the heterogeneity in response to Cisplatin, it is necessary to monitor the activation of multiple caspases (covering both intrinsic and extrinsic pathway) and cell fate (apoptotic or necrotic) at the same time and the same cell for extended periods of time. With our novel imaging platform, we can overcome this limitation of state-of-the-art techniques and simultaneously observe the activation of at least three caspases and monitor cell fate.

This new capability will not only permit us to investigate the role of caspase dynamics in determining cell fate but also directly test two opposing and strongly debated hypotheses involving the role of caspase-2 and -9 in response to DNA damage.

3.1.5 Order of caspase-2 and -9 activation in response to DNA-damage

Whether caspase-2 is active upstream or downstream of caspase-9 in DNA damage has been the source of much discussion (Fava et al., 2012; Kumar, 2009; Miles et al., 2017; Olsson et al., 2014; Zhivotovsky and Orrenius, 2005). Among the caspases, caspase-2 is unique because, depending on the context, it can function both as initiator and executioner caspase (Fava et al., 2012). For instance, the CARD-dimerization-induced activation mechanism and the cleavage of Bid to induce MOMP are shared with initiators caspase-9 and -8, respectively. However, in support of a role as executioner, caspase-2 is not required for the processing of executioner caspases (Van de Craen et al., 1999), it is activated by caspase-3, -8, -6 and -7 and it cleaves cytoskeletal substrates such as PARP, golgin-160 and spectrin contributing to the ordered dismantling of the cell (Van de Craen et al., 1999; Fava et al., 2012; Vakifahmetoglu-Norberg et al., 2013). One context in which there is evidence for a role of caspase-2 both as an initiator, as well as executioner caspase, upstream or downstream of caspase-9 is DNA-damage induced apoptosis. Thus, in the following, I will introduce existing evidence for activation of caspase-2 and -9 specifically in response to DNA damage.

Caspase-2 as initiator caspase in the DNA damage response

Several mechanisms for caspase-2 as initiator caspase in response to DNA damage have been reported (see also Fig. 3.2). In the presence of CHK1 inhibition caspase-2 is activated via PIDD in p53-deficient HeLa cells in response to ionizing-radiation-induced DNA damage leading to a caspase-3, -8 and -9-independent apoptosis (Ando et al., 2012; Sidi et al., 2008).

Caspase-2 activation can also occur in the absence of PIDD (Manzl et al., 2009) as well as by binding to the DISC complex as part of the extrinsic apoptotic pathway (Olsson et al., 2009). Activated caspase-2 can then cleave MDM2 which leads to stabilization of p53 and augmentation of the DNA damage response and protection from cell death in U2OS and a number of lung cancer cell lines (Oliver et al., 2011). Alternatively, caspase-2 can process an inhibitory splice variant of p53-family member p63 which leads to the de-inhibition of the pro-apoptotic variant which in turn transactivate pro-apoptotic genes such as PUMA and NOXA in several cell lines (Jeon et al., 2012). Finally, caspase-2-deficient mouse embryonic fibroblasts show defects in the DNA damage response, increased resistance to treatment and accelerated tumorigenesis in a mouse model, suggesting a role as a tumour suppressor (Ho et al., 2009; Puccini et al., 2013a). Thus, caspase-2 has an important role in the DNA damage response, at least under certain conditions.

Caspase-9 as initiator caspase in the DNA damage response

In contrast to caspase-2, caspase-9 has been firmly characterized as an initiator caspase that is activated upon MOMP-induced apoptosome assembly and whose only reported substrates are caspase-3 and -7 (Yin et al., 2006). As mentioned earlier, caspase-9 has been shown to be crucial for efficient induction of apoptosis in response to DNA-damaging agents, including Cisplatin, in testicular germ cell cancer as well as ovarian cancer (Liu et al., 2002; Mueller et al., 2003). Both studies show that in Cisplatin-resistant cells, caspase-9 is neither activated nor processed. Mueller *et al.* further show that inhibition of caspase-9 in Cisplatin-sensitive cells leads to an increase in tolerance clearly pointing to caspase-9 as a key factor mediating chemoresistance. Importantly, Cisplatin still activates a caspase-2/-3-dependent apoptosis response upon pharmacological caspase-9 inhibition, but only at higher doses, corroborating caspase-9 as a factor in drug resistance. Finally, a role for caspase-9 in chemoresistance has also been described for head and neck cancer cells (Kuwahara et al., 2003) as well as other DNA damaging agents such as Cyclophosphamide (Schwartz and Waxman, 2001), Adriamycin, Etoposide and 5-Fluorouracil (Wu and Ding, 2002). In summary, caspase-9 has been attributed a key role in DNA-damage induced cell death and resistance.

Hierarchical activation of caspase-2 and -9 remains an open question

Different studies have identified either caspase-2 or caspase-9 as the apical initiator caspase. However, only a few studies have reported on direct measurements of the relative timing of caspase-2 and caspase-9 activation which is required to obtain direct evidence of their relative timing. Table 3.1 shows all studies we could identify that investigated both caspases in

response to DNA damage, classed by the apical caspase. It is notable that both classes cover a wide range of DNA damaging agents and cell lines, indicating that the underlying mechanisms are likely not specific for cell lines or agents. The two major methods used were the assessment of procaspase cleavage by Western Blot and fluorometric assays using caspase-specific peptide sequences. The combination of these methodologies is considered essential to study initiator caspases because processing is not required for the activity of initiator caspases, and both techniques were used to find apical caspase-2 and -9. For perturbation, genetic knockouts, siRNA-mediated knockdowns as well as caspase inhibitors were used, with no clear bias for one method for one apical caspase notable. Thus, comparison of the experimental conditions alone is not sufficient to explain the contradicting results in the order of caspase-2 and -9, warranting further investigation.

Finally, and most importantly, the time resolution of studies in Table 3.1 varied greatly from 1 hour to 24 hours with a wide range of time points. Considering that the time from MOMP to caspase-3 activation has been measured to be around 10 min (Tyas et al., 2000), even a 1-hour time resolution is insufficient to resolve fast caspase activation dynamics.

Conclusive remarks

In summary, the current literature on the order of caspase-2 and caspase-9 provides evidence that either may act as an apical caspase. However, it is severely limited by the low temporal resolution inherent to the techniques used. Furthermore, only bulk cell populations have been studied which, as described in sections 1.1 and 3.1.1, will mask non-genetic heterogeneity. It is conceivable that different experimental protocols studying caspase activation on population averages would classify the response of the same cell line treated with the same drug into an artificial class where either caspase-2 or -9 are the leading initiator caspases.

Insufficient experimental evidence based on live single-cell measurements is available to date to dissect cell death phenotypes and the related kinetics of biochemical events to address this issue. As introduced above, this is an important problem to study, not only for academic purposes. Genetic alterations or drug-induced perturbations of caspase networks are mechanistically linked to chemoresistance. Therefore, it is of fundamental importance to dissect if and how cell-to-cell variability in caspase networks (e.g., their kinetics, order and extent of activation) is linked to the heterogeneity of cell fate, which may result in transient populations of chemoresistant cells.

By applying our multiplexed biochemical imaging technique to the study of Cisplatin-induced cell death, we can overcome existing methodological limitations and directly characterize differences in caspase network dynamics that can lead to different type of cell death in genetically identical, but heterogeneous cell populations.

Table 3.1 - **Collection of studies of caspase activation hierarchy in response to DNA damage**. Only studies that assess caspase-2 and caspase-9 activation have been included. If not explicitly shown, MOMP has not been assessed in the particular study. C: caspase.

Reference	Pro-apoptotic stimulus	Cell line	Detection method	Time points	Experimental perturbation	Suggested hierarchy	Notes
Caspase-2 upstream							
Lassus, 2002	Etoposide, Cisplatin, UV	IMR90-E1A, A549, U2OS	Western Blot, Immunofluorescence	18 h	Caspase-2 and Apaf-1 knockdown	C2 → MOMP → C9	Caspase-9 not directly measured
Robertson, 2002	Etoposide	Jurkat	Fluorometry (VDVAD-, DEVD-, LEHD-AMC)	3, 4, 5, 6 h	Caspase-2 knockdown; Caspase inhibition (z-VDVAD/DEVD/LEHD-fmk)	C2 → MOMP→ C9 → C3	MOMP independent of enzyme activity of Caspase 2 (Robertson, 2004); knockdown incomplete, C2-dependency partial
Vakifahmetoglu, 2008	Cisplatin	Caov-4	Western Blot, Fluorometry (VDVAD-, DEVD-, LEHD-AMC)	8, 16, 24, 36, 48, 72 h (Fluorometry) 24, 48, 72 h (Western Blot)	Caspase-2 knockdown, Cisplatin-resistant cell line (Skov3)	C2 → MOMP → C3 → C9	C2 translocation to the cytoplasm precedes apoptosis
Olsson, 2009	5-Fluoruracil	HCT116	Western Blot	3, 5, 8, 10, 13, 16, 20, 24 h	Caspase-9 knockdown, Caspase-8 co-IP	C8 → C2 → MOMP → C9 → C3	

Reference	Pro-apoptotic stimulus	Cell line	Detection method	Time points	Experimental perturbation	Suggested hierarchy	Notes
Caspase-9 upstream							
Mueller, 2003	Cisplatin	2102EP, H12.1, 1411HP (human testicular germ cell cancer cell line)	Western Blot, Fluorometry (VDVAD-, DEVD-, LEHD-AMC)	24 h	Caspase-9 inhibition (Z-LEHD-FMK)	C9 → C3/C2	C9 is required in CP-sensitive cells, but not in CP-resistant cell line
Paroni, 2004	UV, C2 over-expression	MCF7+C3, IMR90-E1A	Western Blot, Immunofluorescence	15 h	C2 overexpression, Dominant-negative C9	UV: C9 → C3 → C2 C2-OE: C2 → C9	Upon C2 overexpression-induced cells death, C2 is upstream
Lakhani, 2006	UV	MEFs	Western Blot, FACS (for MOMP)	6, 9 h (FACS) 1, 2, 4 h (Western Blot)	$C3^{-/-}/C7^{-/-}$, $C9^{-/-}$ knockout cells	C3/C7 → C9 → MOMP	C2 processing not detected under tested conditions
Samraj, 2006	Etoposide, Staurosporine	Jurkat	Western Blot, Fluorometry (VDVAD-AMC)	1, 3, 6, 12, 18, 24 h	$C9^{-/-}$ knockout cells, complementation with C9	C9 → C2/C3	
Guerrero, 2008	IR, chemically-inducible C9	H9, Jurkat	Western Blot	3, 6, 9 h	Dominant-negative C9, Caspase knockdown	MOMP → C9 → C3 → C2	C2 not required for cell death
Inoue, 2009	Etoposide, Staurosporine	Jurkat, MCF7	Western Blot	16 h	C9 knockout and reconstitution, C3 deficient MCF7, C7 knockdown	C9 → C3/7 → C2	C7 processing of C2 dominates of C3 effect

3.2 Material and methods

Detailed information for all reagents used in this study can be found in Table S4.

3.2.1 Molecular cloning

The general description of the cloning strategy used to engineer caspase sensors is described in section 2.2.1 with oligonucleotides listed in Table S1.

Co-expression vectors expressing mTagBFP-VDTTD-sREACh (‘B’), mAmetrine-DEVDR-msCP576h (‘A’) and tdNirFP-LEHD-mKeima (‘K’) on one polyprotein were created by linking sensors with the two most efficient (Kim et al., 2011) self-cleaving viral P2A (porcine teschovirus-1 2A; ATNFSLLKQAGDVEENPGP) and T2A (*Thoseaasigna* virus 2A; EGRGSLLTCGDVEENPGP) linkers. The linkers were flanked upstream by a GSG peptide to further enhance cleavage efficiency (Szymczak et al., 2004). Nucleotide sequences that had been previously optimized to prevent recombination between 2A sites have been used (Tab. S1; Szymczak et al., 2004). Cloning was performed using the scarless SapI approach described for the creation of tdNirFP (section 2.2.1). In short, the single sensors described in Chapter 2 were amplified using PCR with primers carrying parts of the 2A site and SapI restriction sites. After ligation of the SapI-digested PCR products, the fusion was ligated into a fresh pcDNA3.1(-) backbone. First, vectors BA and BK were created with a single P2A site. To add the K sensor to BA, BA and K were PCR amplified with primers introducing the T2A sequence.

The caspase-8 FRET sensor was derived from the caspase-2 sensor by replacing the linker in mTagBFP-VDTTD-sREACh with the peptide AAALGGTGSGSIETDGGIETDGGT carrying two tandem copies of the IETD motif (Luo et al., 2003). Cloning was performed using restriction digest and linker ligation as described in section 2.2.1.

3.2.2 Creation of stable cell lines

HeLa cell lines stably expressing the caspase-2 sensors (B, see 3.2.1) or the BK and BAK co-expression systems were created as follows. 150,000 parental HeLa (see section 2.2.2 for origin and culture conditions) were plated on 3.5 cm dishes 24 hours prior to the transfection with 250 ng (B) or 750 ng (BK, BAK) plasmid DNA using JetPRIME (Polyplus) at ~50%

confluency and according to the manufacturer's instructions with medium replaced 6 hours after transfection. 24 hours after transfection, confluent cells were trypsinized and replated on 10 cm dishes; clones integrating the transgenes were selected by adding 800 ng/ml G418 (Invitrogen) to the medium. The selection medium was replaced every 3-4 days. After four weeks of continuous selection, polyclonal populations were sorted by FACS (Beckton Dickinson Influx cell sorter) for expression of two donor fluorophores (Filter sets: mTagBFP excitation 405 nm - emission 460/50 nm; mAmetrine excitation 405 nm – emission 520/35 nm). Sorted bulk populations were collected in 24-well plates and kept under 800 ng/ml G418 selection. To create monoclonal cell lines, single cells from the sorted polyclonal populations were FACS sorted as above but into 96-well plates and expanded to 6-well size (~4-weeks) under continuous selection. Poly- and monoclonal cell lines were then maintained under minimal selection (200 ng/ml G418). Expression of the sensors was validated by flow cytometry, Western Blot and microscopy.

3.2.3 Fluorescence emission spectra

Fluorescence emission spectra were acquired as described in section 2.2.4. To optimize the emission ratio of co-expressed donors, the two-photon laser wavelength was tuned to 840 nm, 860 nm and 880 nm.

3.2.4 Viability assay (SRB)

3,000 parental HeLa and 6,000 HeLa-BAK cells (numbers adjusted for the difference in growth rate) were plated in 50 µl full medium (DMEM with 10% FCS, Pen/Strep supplemented with 200 ng/ml G418 for HeLa-BAK) on 11 wells of a 96-well plate in triplicate. The first column was used as medium-only control. 50 µl full medium containing 2 µM LCL161 (LKT Laboratories) or equal amounts of DMSO were added to the wells 24 hours later resulting in a final concentration of 1 µM. After an additional 24 hours, Cisplatin (Sigma) was added to the cells in a 9-step two-fold serial dilution starting from 400 µM. For untreated and buffer-only control, the maximum concentration for 0.9% NaCl (1:5) or Cisplatin (400 µM) were used.

For titration of U0126 and Afuresertib (Fig. 3.28), 6,000 HeLa-BAK cells were plated in 100 µl and treated 48 hours later with a twofold serial dilution both drugs, starting at 5 µM and 10 µM respectively, as described for Cisplatin.

After 24 hours incubation with either Cisplatin or U0126/Afuresertib, the medium was removed and cells fixed with 50 µl of 1% trichloroacetic acid (Sigma) overnight at 4°C. To stain cellular protein, 50 µl of 0.057% Sulforhodamine B (SRB) in 1% acetic acid (Sigma) was added and incubated for 30 min at room temperature. SRB was removed and wells washed 3x with 1% acetic acid. After air-drying the plate at room temperature overnight, SRB was resuspended in 100 µl 10 mM Tris pH 8.0 (Sigma) and the absorbance at 510 nm recorded using a Tecan plate reader. The analysis was performed by subtraction of the buffer-only control absorbance from all samples followed by normalization to the untreated control in Microsoft Excel. Mean and standard deviation were calculated from the normalized values and plotted in GraphPad Prism version 5 (GraphWorks).

3.2.5 Flow cytometry and cell cycle profiling

To measure sensor co-expression by flow cytometry (Fig. 3.4D), 300,000 parental HeLa were plated on 6 cm dishes and transfected with a total of 1.5 µg plasmid DNA for controls, B/A equimolar co-transfection and BA co-expression plasmid using JetPRIME (Polyplus) according to the manufacturer's instructions. 24 hours after transfection, cells were harvested by trypsinization, pelleted by centrifugation (1000 rpm for 5 min at room temperature), washed once with PBS, and fixed by adding 2 ml 70% Ethanol drop-wise to the pellet while vortexing followed by incubation at 4°C overnight. After fixation, cells were pelleted and washed twice with ice-cold PBS, and resuspended in PBS for analysis. Flow cytometry was performed on an LSRFortessa (BD Biosciences; filter sets: mTagBFP: excitation 405 nm - emission 450/50 nm, mAmetrine: excitation 405 nm - emission 525/50 nm). Manual compensation was performed for the sensor co-expression using mTagBFP-sREACh and mAmetrine-msCP576 single transfections. Data were analysed using FACSDiva (BD Biosciences).

For validation of stable cell lines (Fig. 3.5E), ~ $1x10^6$ exponentially growing cells were harvested, processed and analysed as described above. To also measure mKeima fluorescence, an additional filter set (excitation 405 nm - emission 610/20 nm) was used on an LSRFortessa. Data were analysed using FlowJo X (version 10; FlowJo).

For cell cycle profiling (Fig. 3.5F), 400,000 parental HeLa cells and 600,000 HeLa-BAK cells were plated on 6 cm dishes in full medium containing 2 mM Thymidine (Sigma). After 16 hours, cells were washed twice with PBS and fresh medium was added. After 8 hours of release, 2 mM Thymidine was added directly to the dishes and removed 16 hours later. Cells were harvested for flow cytometry as described above for stable cell line validation. After the final

two PBS washes, DNA was stained by addition of 10 µM (1:500) DRAQ5 (Biolegend) in PBS for 15 min followed by analysis using an LSRFortessa (filter set: excitation 640 nm - emission 730/45 nm). The cell cycle phases were determined using the univariate Dean-Jett-Fox algorithm in FlowJo X.

3.2.6 Western Blot

For the Cisplatin time-lapse experiments (Fig. 3.6, 3.7, 3.26), 450,000 parental and 900,000 HeLa BAK cells were plated on 6 cm dishes. For Figure 3.26, fresh medium with 1 µM LCL161 or DMSO was added to half of the plates 20 hours after plating. After 20 hours of incubation, cells were washed once with PBS and fresh medium containing 1 µM LCL161 or DMSO and 100 µM Cisplatin or 0.9% NaCl added. At the indicated time points, cells were harvested by removing the supernatant followed by a single wash in PBS and incubation with Trypsin/EDTA for 5 min at 37°C. Detached cells were resuspended twice in full medium and combined with the supernatant prior to centrifugation at 1000 rpm for 5 min at 4°C. In the final wash step, 50 µl of the volume was saved for RNA extraction and the remainder pelleted and frozen at -80°C until processing.

For titration of LCL161, 300,000 parental HeLa and 600,000 HeLa-BAK cells were plated on 6-well plates and 24 hours later treated with a serial two-fold dilution of LCL161 prepared in fresh medium starting at 8 µM (Fig. 3.25D-E) or 1 µM (Fig. 3.25F-G; here, 12-well plates with 50% of cells were used). Cells were harvested 16 hours as described above.

To quantitate the effect of U0126 (Sigma) and Afuresertib (Stratech) on Erk and Akt levels by Western Blot (Fig. 3.28B), 300,000 HeLa-BAK cells were plated on 3.5 cm dishes and ~20 hours later treated with one or both inhibitors in full medium. The total DMSO concentration was kept constant for all samples. Cells were harvested after 2 hours as described above.

For all samples, cell lysis and Western Blotting was performed as described in section 2.2.5 using Licor Odyssey. Detailed information for primary and secondary antibodies used in this chapter can be found in Tab. S4. Quantification of the bands was performed in Image Studio version 5.25 (Licor) and analysed in Microsoft Excel. Graphs were plotted in GraphPad Prism.

3.2.7 RNA extraction, cDNA synthesis and quantitative PCR

For RNA extraction, parental HeLa and HeLa-BAK cells were grown and treated as described for Western Blot analysis of the Cisplatin time lapse (section 1.1.7). Cell pellets stored for RNA extraction were resuspended in 350 µl RLT buffer (Qiagen RNeasy Plus Mini Kit; cat. # 74134) supplemented with 1:100 β-Mercaptoethanol (Sigma). Lysis was performed by passing through a QIAshredder column (Qiagen, cat. # 79654). Lysates were then stored at -80°C until processing using the RNeasy Plus Mini Kit as per the manufacturer's instructions. In the final step, RNA was eluted twice with 30 µl H_2O and stored at -80°C.

cDNA synthesis was performed using the Cloned AMV First-Strand cDNA Synthesis Kit (Invitrogen, cat. # 12328040). First, 1 µg ng RNA was denatured at 65°C for 5 min in a 12 µl mix containing random hexamer primers (final concentration in 20 synthesis mix: 2.5 ng/ml), oligo $(dT)_{20}$ primers (2.5 µM) and dNTP (0.5 mM). Next, the cDNA synthesis mix was added containing DTT (5 mM), RNAseOUT (40 units) and Cloned AMV Reverse transcriptase (15 units). The synthesis was performed in a three-step reaction, 10 min at 25°C, 50 min at 50°C and 5 min at 85°C to terminate the reaction. cDNA was diluted to 50 µl in H_2O stored at -20°C until further use.

For quantitative PCR, for each primer pair a master mix containing Lightcycler 480 SYBR Green Master Mix (Roche Diagnostics, cat # 4887352001; final concentration: 1x) and 250 nM of each forward and reverse primer (Tab. S1) was prepared and 19 µl pre-laid into the wells of a white-walled LightCycler 480 Multiwell 96-well plate (Roche Diagnostics, cat. # 4729692001). 1 µl cDNA was added for each sample in triplicates and mixed by pipetting. The sealed plate was then spun down at 1,500 g for 1 min and the PCR performed on an LC480 Light Cycler (Roche Diagnostics). The PCR protocol was as follows:

Pre-incubation	95°C for 10 sec
Amplification	45 cycles of denaturation (95°C for 10 sec), annealing (60°C for 10 sec), elongation (72°C for 10 sec)
Melting curve	95°C for 5 sec followed by 65°C for 1 min

After PCR, the amplicon size and specificity of the reaction were confirmed by running the content of each well on a 2% Agarose gel stained with SYBR Safe (Invitrogen) at 135V for 30min. qPCR data were analysed in Microsoft Excel using the ΔΔCT-method with GAPDH (Glyceraldehyde 3-phosphate dehydrogenase) amplification as a control for all samples.

Triplicate ΔΔCT values were averaged and plotted along with upper (mean +standard deviation) and lower (mean –standard deviation) using GraphPad Prism.

3.2.8 Growth curves

60,000 HeLa parental and 60,000, 90,000 and 120,000 HeLa-BAK cells were plated in triplicates on a 12-well plate in full medium (supplemented with 200 ng/µl G418 for HeLa-BAK). Approximately 8 hours after plating, cells were transferred into an Incucyte™ (Essen Bioscience), an incubator equipped with an imaging system to measure confluency. Measurements were performed automatically every 2 hours for five days and confluency data analysed in Microsoft Excel. Mean and standard deviation were plotted using GraphPad Prism. Single images were exported from the Incucyte software to create figure 3.5H.

3.2.9 Annexin-V / 7-AAD / TMRM imaging assay

15,000 parental HeLa cells were plated on 8-well LabTek II chambered coverglass (Nunc, cat. # 155409). ~48 hours later the medium was removed, wells were washed twice with PBS and the staining solution added. The solution was prepared in Leibovitz (L-15) medium supplemented with 10% FCS and Pen/Strep and contained the indicated final concentrations of the following reagents: Cisplatin or 0.9% NaCl (100 µM), FITC-labelled Annexin-V (Biolegend; 1:200), 7-AAD (7-amino-actinomycin D; Biolegend; 1:200), $CaCl_2$ (2.5 mM; required for Annexin-V binding to phosphatidylserine) and TMRM (Tetramethylrhodamine, methyl ester; 20 nM). After addition of the staining solution, cells were transferred to the microscope and incubated at 37°C on stage for at least 30 min before starting imaging. Imaging was performed using a Nikon Ti wide field microscope equipped with an sCMOS camera (Andor Zyla). Images of four channels (bright field; FITC, TRITC for TMRM; Cy5 for 7-AAD) were acquired every 15 min for 16 hours at a resolution of 2560 x 2160 pixels with no binning using a Plan Fluor 40x Oil DIC objective (Nikon). Five fields of view were collected per sample. Image analysis was performed manually using Fiji (ImageJ, NIH) by drawing a region of interest around the whole cell for all three channels followed by export of data to Microsoft Excel. Single-cell traces for all channels were normalized to minimum and maximum. The difference between the FITC and 7-AAD signal (ΔAV-7AAD) at each time point was calculated from the normalized single-cell traces. Traces and maximum values were plotted in GraphPad Prism.

3.2.10 Cell cycle imaging (FUCCI)

15,000 parental HeLa cells were plated on 8-well LabTek II chambered coverglass (Nunc). 24 hours later, 18 µl of each of the two components (Geminin-emGFP and TagRFP-Cdt1) of the baculoviral Premo™ FUCCI Cell Cycle Sensor (BacMam 2.0; Invitrogen) were added directly to the wells containing 300 µl full medium. After an additional 24 hours, cells were washed twice with PBS and imaging medium (Leibovitz (L-15) with 10% FCS and Pen/Strep) added containing a final concentration of 100 µM Cisplatin or 0.9% NaCl. Imaging was performed as described in section 3.2.9 using the FITC and TRITC cube for emGFP and mTagRFP, respectively. Image analysis was performed in Fiji. Cells with a clear emGFP or TagRFP signal in the first frame were analysed for the occurrence of the first morphological sign of cell death (shrinking or blebbing) in the brightfield channel. Data were plotted in GraphPad Prism.

3.2.11 Sample preparation for time-lapse FLIM

For each time-lapse FLIM experiment, two 8-well LabTek II chambered coverglass slides (Nunc) were prepared. On the control slide, 15,000 parental HeLa cells were plated in all wells and 24 hours later transiently transfected using JetPRIME with DNA plasmids expressing donors, the uncleavable controls and two acceptors (sREACh, tdNirFP). The transfection medium was removed 4-6 hours later. 24 hours after transfection, control cells were washed twice and 300 µl imaging medium (Leibovitz (L-15) with 10% FCS and Pen/Strep) added to all wells followed by FLIM acquisition as described in the next section. For the sample used for time lapse, either 15,000 HeLa parental or 30,000 HeLa-BAK cells were plated. When required (Fig. 3.13, 3.16), transfection was performed as described for the control slide.

When used, inhibitors or corresponding solvent controls were added to the sample slide either 6 hours after transfection (caspase-Inhibitors at 25 µM each, LCL161 at 1 µM) or 2 hours before starting imaging (U0126 at 7.5 µM, Afuresertib at 5 µM) by adding 400 µl of fresh DMEM with 10% FCS, Pen/Strep and 200 µg/ml G418 prepared with the inhibitors at the indicated final concentrations. For details on all inhibitors, see Table S4. After imaging of the control slide, the slide utilized for time-lapse imaging was prepared by washing twice with PBS and adding 400 µl imaging medium containing Cisplatin at 100 µM, 0.9% NaCl and inhibitors at the same concentration used for pre-treatments.

For the double-thymidine block and release experiment shown in Figure 3.15, cells were prepared as above with the following additional steps. 2 mM Thymidine (Sigma) was added at the time of plating followed by two washes with PBS and addition of fresh medium 16 hours later. After another 8 hours, 2 mM Thymidine was added to the medium and removed as for the first block either after 16 hours (i.e. 7 hours before the start of imaging, for G2 cells) or 23 hours (i.e. at the time of starting imaging, for G1 cells). Directly prior to imaging, all samples were changed to imaging medium containing Cisplatin as described above.

U2OS cells (received from ECACC, cat. # 92022711) were used exactly as parental HeLa cells with the exception that 25,000 cells were plated and 200 ng of the BAK co-expression plasmid was transiently transfected using JetPRIME.

3.2.12 Multicolour fluorescence-lifetime imaging and data analysis

Samples were imaged at 37°C on a Leica SP5 confocal microscope (Leica Microsystems) equipped with a Chameleon Vision 2 Ti:Sapphire laser (Coherent) for two-photon excitation. Images were acquired with three parallel, hybrid photomultiplier tubes (HyD - two by Leica Microsystems and one additional by Becker & Hickl) with 256x256 pixel resolution using a 40x oil objective (Leica HCX PL APO CS 40.0x1.25 OIL UV). The detectors were mounted at a customized non-descanned port using a Leica Quad adapter to split the optical path for two HyD of Leica and an additional channel not supported by the Leica SP5. After a short pass 680 nm filter, the emission light was split by a 565 nm dichroic mirror. The transmitted light passes through a filter set for mKeima (624/40 nm) positioned in front of the Becker & Hickl detector. The reflected light was further split by a 506 nm dichroic onto the two remaining detectors with filter sets for mTagBFP and mAmetrine (mTagBFP: 483/30 nm, mAmetrine: 543/30 nm). The detectors were read-out by fast electronics based on multi-hit time-to-digital converters (Surface Concept) which were controlled by in-house developed MATLAB software (Mathworks).

For each field of view, a z-stack of 75 images spanning 25 µm was acquired within 48 seconds. For controls, a single z-stack for two fields of view per well was acquired. For the time-lapse samples, z-stacks of 12 fields of view were automatically acquired every 15 min for 16 hours. Videos S1, S5 and S7 were generated from the images acquired with the Leica LAS software for the detectors for mTagBFP and mAmetrine. Image processing was performed in Fiji by

creating maximum projections for every time point followed by the creation of a composite image from both channels.

FLIM data were analysed using an in-house developed data pipeline in MATLAB by Dr Kalina Haas and Dr Alessandro Esposito (see also Fig. 8C-E). In short, stored photon streams were processed to generate 3D image stacks and summed over the axial direction to create an 'extended focus' image. In the resulting FLIM movies, single cells were segmented (predominantly by the author) and tracked with semi-automatic algorithms and always manually curated. Unmixing of biosensors was achieved by transforming the fluorescence signals extracted from individual cells by multi-dimensional phasor-transforms (Digman et al., 2008; Esposito et al., 2013; Popleteeva et al., 2015). Utilizing the control measurements of single sensors and fluorophores this algorithm was used to unmix the contribution of individual molecular species (cleaved sensors, uncleaved sensors, residual sensitized emission and background autofluorescence). The relative enzymatic activity (REA) for each caspase and cell was computed as the fraction of cleaved substrates normalized to cleaved and uncleaved sensors. Using a threshold of 10% change in REA between the first and last three time-points for each caspase, cells were classified according to their caspase activation (Fig. 3.8D). Confidence intervals of the mean trajectories were calculated using bootstrapping. To obtain true caspase activation dynamics of a given population, single-cell REA trajectories were synchronized at the time point of 50% caspase-3 and traces clipped to included ~3 hours before and after that value. For the estimation of activation rate and maximum REA level, a sigmoid was fitted into the single-cell trajectories. Graphs were plotted in MATLAB by Drs Haas and Esposito and adapted for further analysis and presentation by the author. Figures were prepared using MATLAB and GraphPad Prism.

3.2.13 Morphological classification of death phenotypes

The morphological classification was performed manually for all experiments using FLIM movies showing tracked cells in MATLAB. For each cell, three parameters could be assigned, i) the first frame of cell shrinking (defined as continuous loss in cell size of more than ~10% and judged visually), ii) the last frame of cell shrinking and iii) the first frame of cell blebbing (defined as the appearance of a visually discernible and persistent membrane protrusions). If cells were completely detached and rounded to near-perfect spheres, the subsequent blebbing (i.e. formation of apoptotic bodies and/or secondary necrosis) was not recorded. Cells that only showed parameters i) and ii) were classified as 'shrunk', those that only showed iii) as 'bleb' and those that showed all three as 'shrunk-bleb'. Blind classification was performed

independently by three researchers. In the event of disagreement, a majority consensus determined the final assignment to phenotypic classes. The time of cell death was defined as the first frame of cell shrinking or blebbing, calculated as the average of the three scorers and plotted in GraphPad Prism.

3.3 Results

3.3.1 Validation of FRET sensors and cell lines for multiplexed caspase imaging

Development and characterization of the expression system

To study the activity of caspase-2, -3 and -9 simultaneously in single cells, the three optimized sensors developed in Chapter 2 (i.e. caspase-2: mTagBFP-VDTTD-sREACh; caspase-3: mAmetrine-DEVDR-msCP576h; caspase-9: tdNirFP-LEHD-mKeima; named henceforth B, A, K according to the respective donor) were sub-cloned into a co-expression vector separated with viral 2A sites that are autocatalytically cleaved post-translationally (Szymczak et al. 2004; Fig. 3.4A-C). The use of a multicistronic vector with self-splicing peptides ensures the equimolar expression of fluorescent proteins, in contrast to internal ribosomal entry sites (IRES) where levels of upstream and downstream genes differ more widely (Goedhart, 2011). The 2A peptides reduced the variation in expression of the blue and green sensors that are expressed at similar ratios across the population as shown in Fig. 3.4D. The emission spectra of the HeLa cells transfected with the “BAK” plasmid for the co-expression of three sensors confirm that the sensors are well expressed and at relative levels of brightness that we expected from their reported molecular brightness (Fig. 3.4E; Tab. 2.1) rather than because of uneven expression of the constructs.

Development and validation of stable cell lines

Next, monoclonal HeLa cell lines stably expressing single-sensor (HeLa-B) and as well as co-expression systems ‘BK’ and ‘BAK’ (HeLa-BK and HeLa-BAK) were derived to avoid the toxicity caused by transient transfections, variability in expression and, more in general, to simplify the experimental procedures. HeLa cells were chosen as cell line because, in early

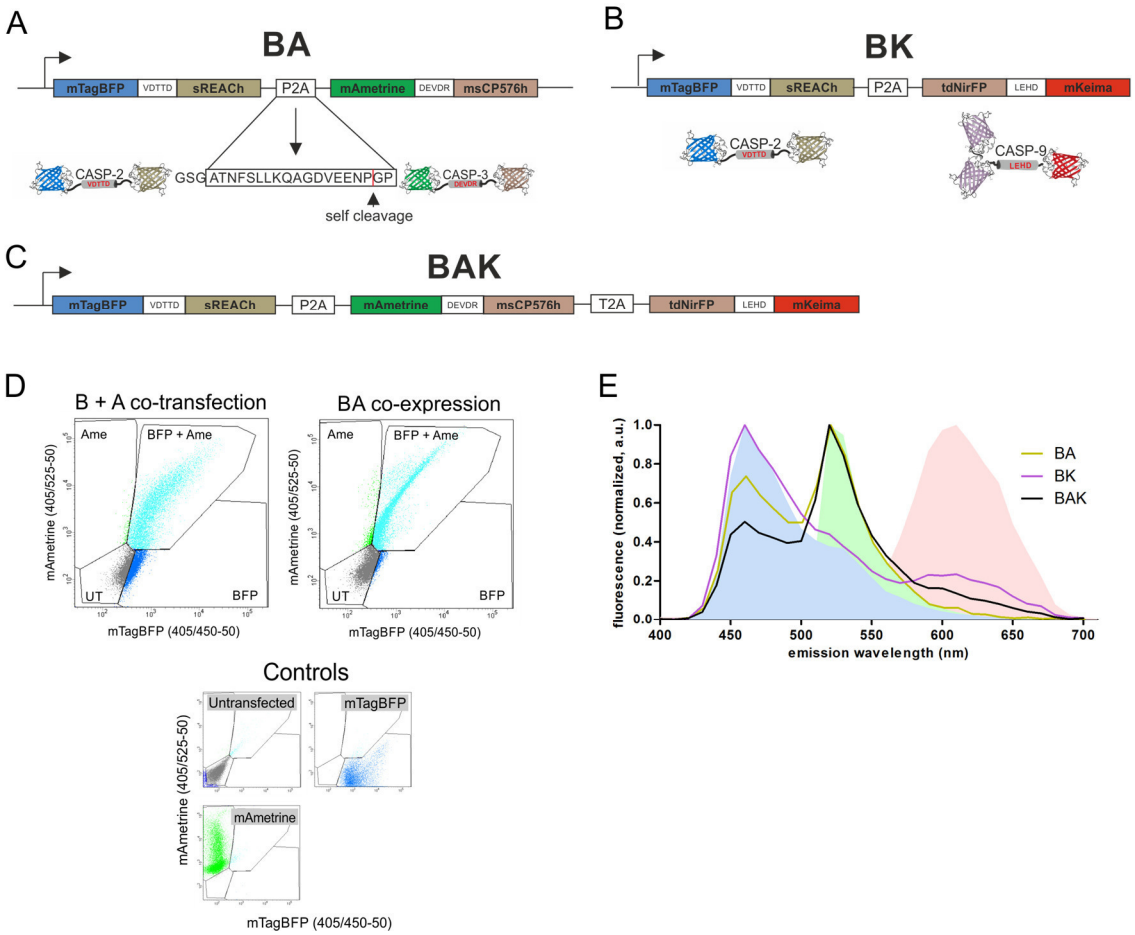

Figure 3.4 – **Co-expression systems for caspase sensors**

A-C: Schematics of co-expression systems. FRET-based biosensors for caspase-2 (mTagBFP-VDTTD-sREACh, 'B'), caspase-3 (mAmetrine-DEVDR-msCP576h, 'A') and caspase-9 (tdNirFP-LEHD-mKeima. 'K') are linked with self-cleaving P2A or T2A peptide linkers. The label above each construct indicates the sensors used. Molecular models of sensors in A-B courtesy of Alessandro Esposito.

D: Comparison of co-transfection of B and A sensor (top left) with the BA co-expression system shown in panel A (top right) and corresponding controls (bottom) by flow cytometry.

E: Fluorescence emission spectrum of co-expression systems shown in A-C with excitation at 840 nm for 2PE, sensors transiently expressed in HeLa cells. Emission spectra of single sensors shown as shaded areas in the background. Data is from a minimum of five cells per spectrum and from one experiment.

pilot experiments with transient transfection of the BK vector, HeLa exhibited marked differences between caspase-2 and -9 activation in response to Cisplatin (data not shown). Most importantly, HeLa cells have been used previously to study caspase-2, -3 and -9 dynamics in response to Cisplatin (Lin et al., 2006; Mueller et al., 2003; Vakifahmetoglu et al., 2008) and originate from a cervical tumour, for which Cisplatin is an important drug (Basu and Krishnamurthy, 2010).

Western Blotting, emission spectra and flow cytometry measurements confirmed sufficient expression in a number of clones (Fig. 3.5A-E). A possible complication using 2A peptides is partial cleavage resulting in a mix of fused and single proteins, which, in our experiments, could lead to intramolecular FRET and other artefacts. However, Western Blotting did not show high molecular weight bands when lysates of HeLa-BK and HeLa-BAK clone were probed with antibodies for fluorescent proteins, confirming the full cleavage of the 2A peptides we used (Fig. 3.5A).

For further experiments, HeLa-BAK clone #7 (subsequently referred to as HeLa-BAK) was chosen and further validated. Notably, only two clones of HeLa-BAK out of the seven picked initially proliferated and only one clone showed expression. This is in line with reports describing the difficulty of obtaining stable cell lines with high and maintained expression of multiple fluorescent proteins (Aoki et al., 2012). HeLa-BAK cells exhibited a slightly higher S/G2 population (Fig. 3.7F), proliferate at a slower rate (Fig. 3.7G) and appear to have decreased viability (see dead cells in Fig. 3.7H and increased sub-G1 peak in panel F), likely due to the high constitutive expression of the construct. However, these differences do not appear to be substantial and, most importantly, HeLa-BAK cells exhibit similar sensitivity to Cisplatin as well as similiar dynamics of procaspase processing compared to the parental cell line (Fig. 3.5I and Fig. 3.6). Also, Western Blot analysis of procaspase and PARP processing (Fig. 3.6A) reveals that HeLa-BAK might trigger apoptosis earlier than the parental cell line, but with no apparent changes in the dynamics (Fig. 3.6D). Moreover, in a number of experiments (Fig. 3.13, 3.17), parental HeLa cells transiently transfected with single- or co-expression caspase sensor plasmids as well as non-transfected cells have been used as controls. Consistently, we have never observed differences between transfected HeLa parental cells and HeLa-BAK stable cells in experiments described in the following figures. Together, these observations indicate that HeLa-BAK cells are a suitable model system to study caspase activation dynamics in response to Cisplatin.

Optimization of the excitation wavelength

We have observed that the three donor fluorophores exhibit different brightness. To identify the most suitable excitation wavelength to image HeLa-BAK cells, spectral imaging of HeLa-BAK cells was used to estimate the contribution of fluorescence emission of the different donors to the total emission. Increasing the excitation wavelength resulted in a net increase

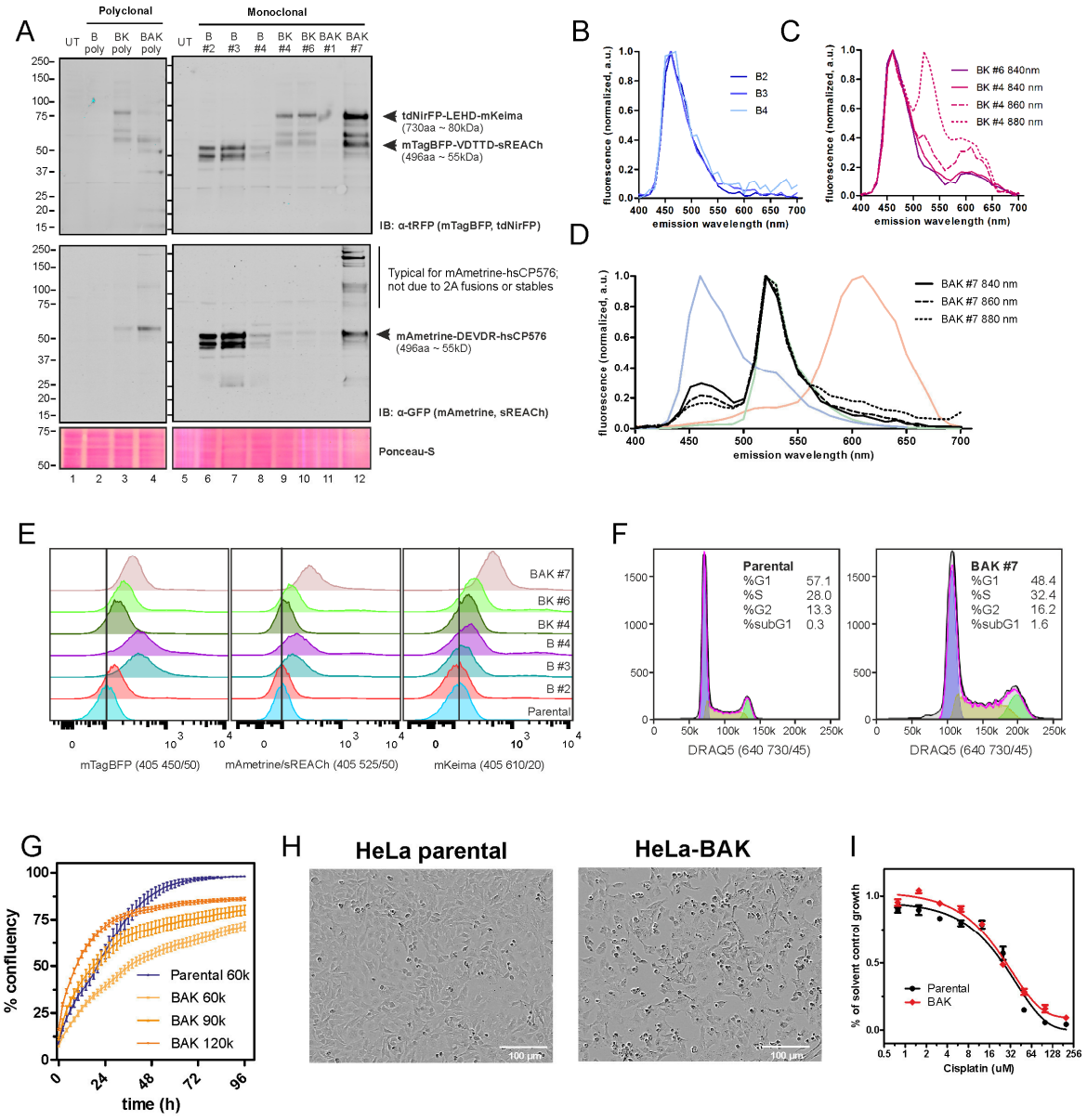

Figure 3.5 – **Validation of stable HeLa cell lines for caspase sensors**

A: Western Blot of lysates from HeLa cells stably expressing single sensor for caspase-2 and co-expression systems BK and BAK described in Figure 3.4. Untransfected (UT) cells were run as control. The tRFP antibody detects tdNirFP and mTagBFP and the GFP (JL-8) antibody mAmetrine and sREACh. Double-bands are due to cleavage during denaturation and high molecular weight bands observed for mAmetrine-msCP576 (both discussed in Chapter 2). The shift of the 2A fusions (lanes 3, 4, 9-12) compared to the single sensors (lanes 2, 6-8) is due to additional 22aa (~2.4kD) of the 2A linker.

B-D: Fluorescence emission spectra of stable monoclonal cell lines as in panel A were acquired at 840 nm (panel B) and 840, 860, 880 nm (panel C-D) for 2PE. In D, spectra of HeLa cells transiently expressing single sensors are plotted as coloured lines.

E: Flow cytometry measurement of donor fluorescence of fixed monoclonal cell lines from B-D and parental control cells. Vertical lines show peak fluorescence in parental controls as reference.

F: Cell cycle analysis of DRAQ5-stained BAK #7 monoclonal cell line compared to parental HeLa cells. Shaded area under the curve corresponds to G1, S and G2 populations derived using the Dean-Jett-Fox algorithm.

A-F: Data are from one experiment for each panel shown.

G-H: Cell growth of parental HeLa cells (plated at 60,000 cells per 12-well) and BAK #7 cells (plated at 60,000, 90,000 and 120,000 cells per 12-well) as measured by confluency in an Incucyte™ imaging system. Shown are mean and standard deviation of three wells per sample for one experiment. Panel H shows representative images of growth curves in panel G taken at 96 hours for parental cells and BAK cells (plated at 120,000 cells).

I: Viability of parental and HeLa BAK cells at increasing doses of Cisplatin measured using the SRB assay. Mean and standard deviation of three technical replicates for one experiment are shown. One-phase decay fitted using GraphPad, EC50: Parental, 26.5 µM; BAK, 23.08 µM (non-significant difference; 1-way ANOVA).

of the mKeima fluorescence, however, it also caused loss of mTagBFP signal and a sharp increase of the fluorescence emitted by sREACh in the BK construct; this indicates direct excitation of sREACh which would interfere with unmixing (Fig. 3.5C-D). Therefore, the excitation wavelength optimal for imaging the HeLa-BAK cells was set at 840 nm.

Initial observation of caspase dynamics from ensemble measurements

Studying the cell population by Western Blot to validate the sensors already provided us with some insight into the behaviour of key cell death factors in Cisplatin-treated HeLa cells (Fig. 3.6). First, caspases-2, -3, -9, -8 and PARP are all processed in response to 100 µM Cisplatin starting around 8 hours and showing a gradual response. The 100 µM concentration of Cisplatin was selected to guarantee the triggering of cell death in a majority of cells, corresponding to four times the EC50 values (or EC90; Fig. 3.5I). The apparent gradual response is the result of averaging the switch-like response of single cells that die at widely different points after treatment (Video S1; Tyas et al., 2000) as discussed in the introduction. Importantly, this response is mirrored by the processing of caspase sensors on Western Blot, confirming the appropriate response of the biosensors with an additional line of evidence (Fig. 3.7). Also, at the end of the experiment (~16 hours), a certain amount of procaspases, as well as of biosensors, remain unprocessed; this indicates that a subpopulation of cells does not activate caspases and/or does not die, as expected by the chosen Cisplatin concentration. The order of caspase activation cannot be established at a 4 hours time resolution, a resolution that is not uncommon for population studies of this kind (Tab. 3.1). The only striking difference is observed for caspase-8 which is processed later than the other three caspases in both cell lines, suggesting that under these conditions the caspase-8-mediated extrinsic pathway might be not activated initially (Fig. 3.6B-C). It is important to notice that, even though HeLa cells express human Papilloma Virus E6 protein that subdues p53 levels, p53 is both stabilized as well as phosphorylated on serine-15 (by CHK1 and CHK2) in response to Cisplatin (Fig. 3.6A).

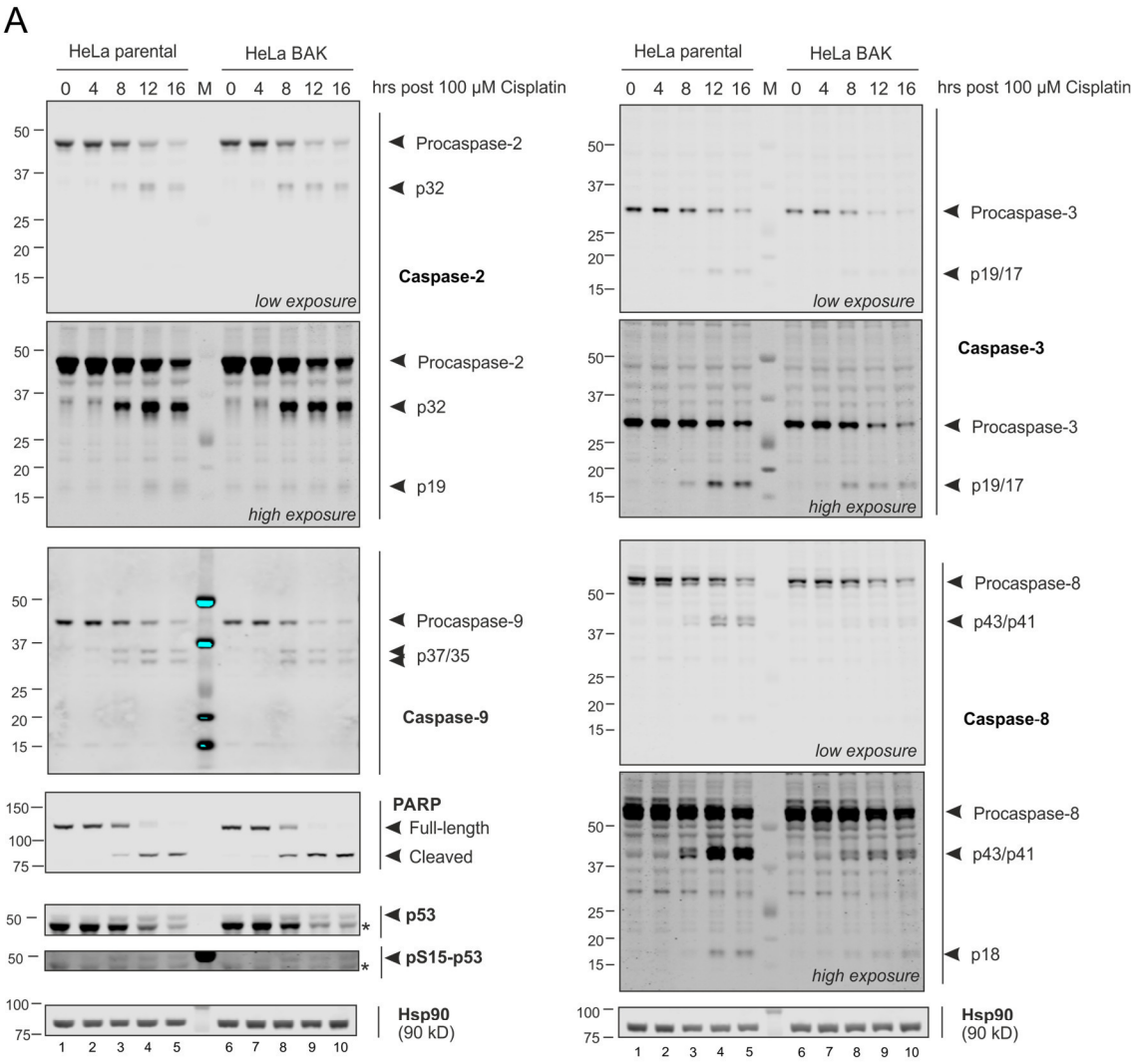
A
HeLa parental
HeLa BAK
0 4 8 12 16 M 0 4 8 12 16
hrs post 100 µM Cisplatin
Procaspase-2
p32
Caspase-2
low exposure
high exposure
p19
Procaspase-3
p19/17
Caspase-3
Procaspase-9
p37/35
Caspase-9
Procaspase-8
p43/41
Caspase-8
p18
PARP
Full-length
Cleaved
p53
pS15-p53
Hsp90
(90 kD)
1 2 3 4 5 6 7 8 9 10

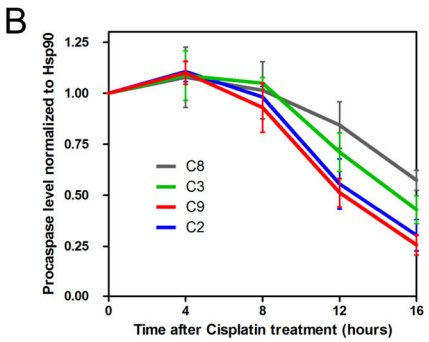
B
Procaspase level normalized to Hsp90
Time after Cisplatin treatment (hours)
C8
C3
C9
C2

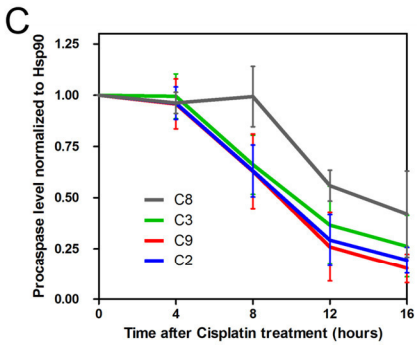
C
Procaspase level normalized to Hsp90
Time after Cisplatin treatment (hours)
C8
C3
C9
C2

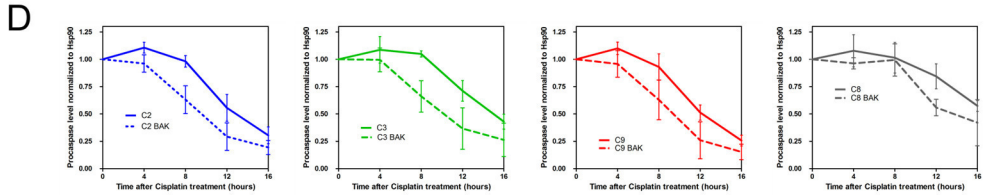
D
C2
C2 BAK
C3
C3 BAK
C9
C9 BAK
C8
C8 BAK
Time after Cisplatin treatment (hours)

Figure 3.6 – **Dynamic response of caspases, p53 and PARP after treatment with Cisplatin**

A: Representative Western Blot of lysates from parental HeLa cells and HeLa-BAK cell line treated with 100 µM Cisplatin and harvested at indicated time points. Asterisks for p53 blots indicate bands of caspase-2 and caspase-9 from a previous detection on the same membrane. For caspase-2, -3 and -9 high and low exposures are shown to visualize all bands.

B-C: Quantification of procaspase (C2/3/9: caspase-2/3/9) levels for parental HeLa (B) and HeLa-BAK cells (C) treated analysed as in A. Mean and standard deviation of four independent experiments are shown.

D: Comparison of dynamics of procaspase cleavage plotted B-C for HeLa parental (solid line) and HeLa BAK cells (dashed line).

This is in line with a previous report describing that in response to Cisplatin, p53 is stabilized in HeLa cells coinciding with the Cisplatin-mediated downregulation of E6 (Wesierska-Gadek et al., 2002). Therefore, in contrast to the majority of applications, HeLa cells can be considered p53-proficient in response to Cisplatin.

In summary, we successfully cloned and validated a monoclonal cell line expressing all three FRET sensors and confirmed the suitability for studying Cisplatin-induced cell death in a bulk population using Western Blot.

3.3.2 Deconvolution of single-cell caspase dynamics and non-genetic heterogeneity

Following their validation, we used HeLa-BAK cells on our multicolour FLIM platform to study caspase dynamics in single cells (Fig. 3.8A-B). Novel detection technologies and data analysis pipelines tailored to achieve biochemical multiplexing have been developed by co-workers Dr Kalina Haas and Dr Alessandro Esposito as part of a team effort to establish a live single-cell biochemistry methodology. Here, I will, therefore, provide only a brief overview of these developments to the extent required to interpret the presented data. Full details and materials will be available elsewhere (manuscripts in preparation).

Setup of the sensing platform

The platform consists of a two-photon laser scanning microscope combined with very efficient photon-counting hybrid photomultiplier tubes as detectors at the non-descanned port of a Leica SP5 microscope. Fast FLIM measurements in excess of one order of magnitude of commercial solutions available at the time of the engineering of the system were achieved by the development of fast electronics based on multi-hit time-to-digital converters (Fig. 3.8C).

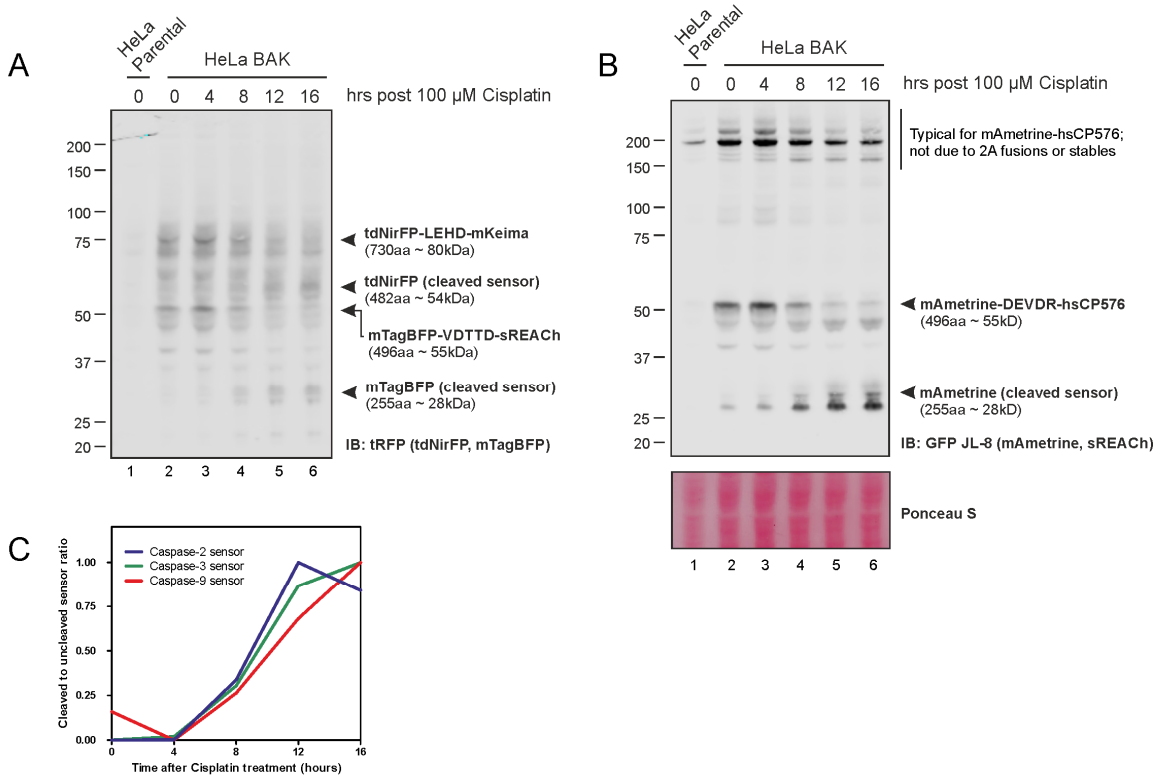

Figure 3.7 – **Dynamic response of the BAK sensor after treatment with Cisplatin as measured by Western Blot**

A-B: Western Blot of lysates from HeLa BAK cells treated with 100 µM Cisplatin and harvested at indicated time points and plotted for caspase sensors as indicated and as in 3.5A. Lysates from HeLa parental cells run as a control. The same membrane was simultaneously probed with tRFP (A) and GFP (B) antibodies. Ponceau S staining is shown to confirm equal loading.

C: Ratio of cleaved over uncleaved sensor quantified from Western Blot in panel A.

All data from a single experiment.

This configuration allows to image 75 optical slices covering 25 µM in 48 sec with very low excitation power (<1 mW at 840 nm) thus minimizing phototoxicity (Video S1). The imaging of a larger volume, rather than a single optical section, is necessary because dying cells detach from the surface and move away from the initial focal plane. Because of the fast acquisition and the low excitation power, we were able to acquire up to 12 fields of views sequentially in a fully automated mode with a 15 min time resolution and for a duration of at least 16 hours. Data were analysed using an in-house developed data pipeline. Briefly, stored streams of photons were processed to generate 3D image stacks, subsequently summed over the axial direction to form an ‘extended focus’ image that provides in focus 2D multicolour FLIM images with high signal. The FLIM movies were tracked and segmented with semi-automatic

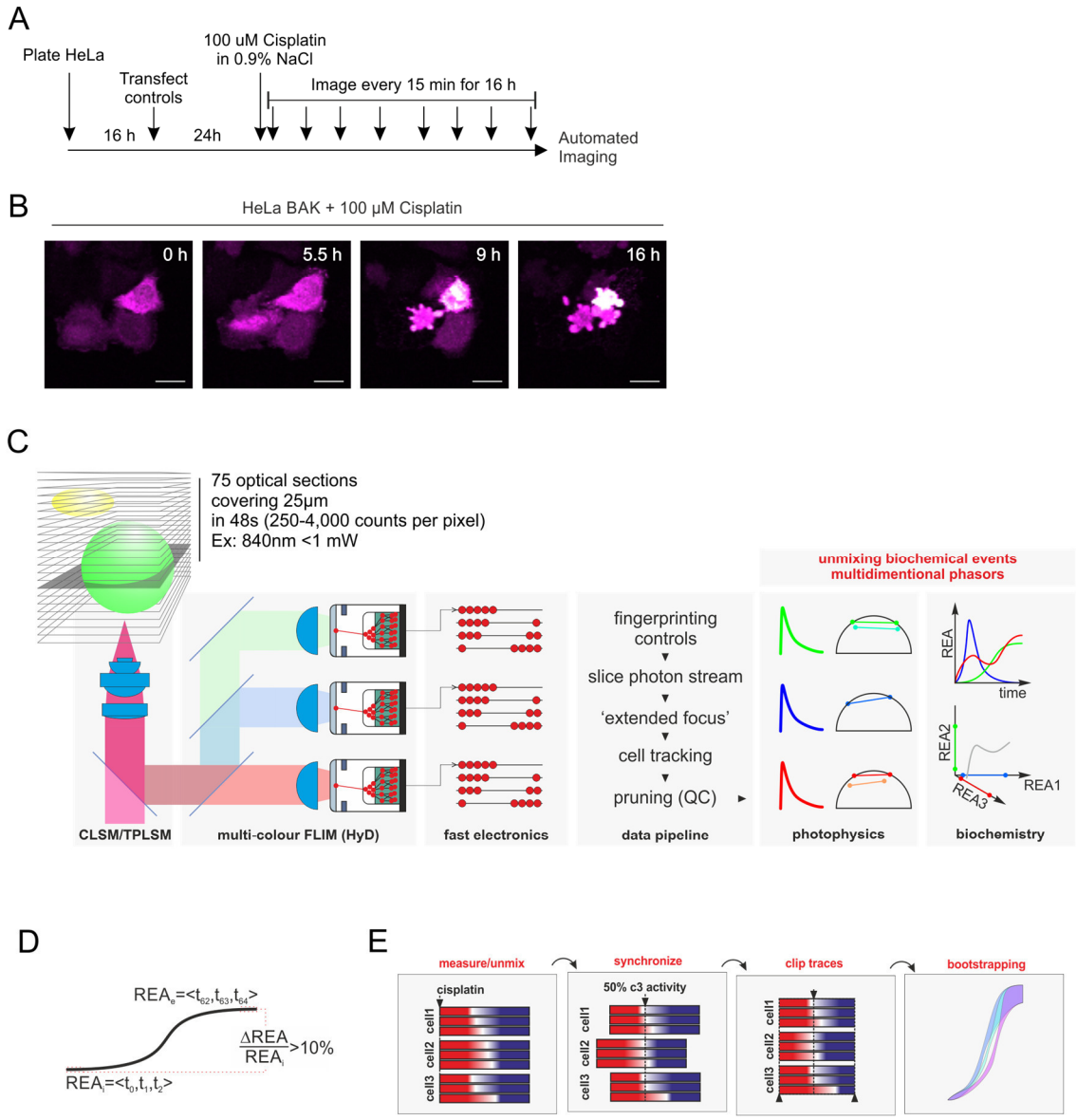

Figure 3.8 – **Experimental setup and data analysis for three-colour live-cell caspase imaging**

A: Schematic of experimental setup.

B: Representative images of HeLa-BAK cells treated as shown in panel A extracted from time-lapse movie (Video S1). Shown are composite images of maximum projections from the mTagBFP and mAmetrine channel.

C: Setup of the custom-built imaging platform for three-colour live-cell imaging. 75 optical slices are acquired using a two-photon laser scanning microscope (TPLSM), spectrally split onto three hybrid photomultiplier tubes which are read-out by fast bespoke electronics. Data is analysed using a pipeline developed in-house resulting in the calculating of relative enzymatic activities (REA) for three sensors. For further details see main text.

D: Illustration of the algorithm used to determine activation of caspases. A caspase is considered active if the difference between the average of REA at the first and last three time points is larger than 10% percent of the first three.

E: Illustration of the approach used to compute bootstrapped average caspase dynamics starting from asynchronous single-cell REA traces. C-E: Images courtesy of Dr Alessandro Esposito.

algorithms and always manually curated. Unmixing of biosensors was achieved by transforming the fluorescence signals extracted from individual cells by multi-dimensional phasor-transforms (Digman et al., 2008; Esposito et al., 2013; Popleteeva et al., 2015). Utilizing control measurements of single sensors and fluorophores, this bespoke algorithm permitted us to fingerprint the complex photophysical data we acquired and to unmix the contribution of individual molecular species (cleaved sensors, uncleaved sensors, residual sensitized emission and background autofluorescence). The relative enzymatic activity (REA) for each caspase and cell was computed as the fraction of cleaved substrates normalized to cleaved and uncleaved sensors (Video S2). Therefore, analysis of the photophysical properties of the samples is carried out in the background and the data pipeline provides only meaningful biochemical data. The trajectories of the three caspases for each cell can be then depicted as a function of time (Fig. 3.8C). This approach allows us to acquire and analyse both morphological (Fig. 3.8B) as well as biochemical information (Fig. 3.9, 3.10A; Video S2) of hundreds of single cells over 16 hours in a single experiment.

Heterogeneity in caspase activation

Caspase traces of 564 Cisplatin-treated HeLa-BAK cells from 12 independent experiments are depicted in Figure 3.10A. It confirms the large degree of heterogeneity in the time of caspase activation (Tyas et al., 2000; Video S1). However, this multiplexed single-cell analysis also revealed the previously unnoticed existence of at least three distinct subpopulations (Fig. 3.10C; video S2). These populations would not be visible with ensemble measurements as illustrated by the population average of all the single-cell traces that is akin to the dynamics observed by Western Blot (Fig. 3.10B) or without biochemical multiplexing. The lower maximum REA for caspase-9 recapitulates the results from Chapter 2, where, independently of the FRET pair, a maximum of 50% REA was observed for caspase-9, and 80-90% for caspase-2 and -3 (Fig. 2.9 and 2.13).

We observed a population of cells that activate all three caspases (‘c2/c3/c9 responsive’) and that on average trigger caspase-3 activity at around 8.8 hours as estimated from the half-maximum of the sigmoidal curves (Fig. 3.10E; video S2A). As shown in panel D, 50% of the cells belong to the population. There is also a population of cells that activate caspase-2

and -3, but not caspase-9 (Fig. 3.10A, C, and D; video S2B ‘c2/c3 responsive’). The classification into ‘responsive’/’non-responsive’ was performed by employing a 10% threshold on the individual traces of single cells, i.e. a caspase is considered activated if the difference between the averages of the first and last three time points is larger than 10% (Fig. 3.8D).

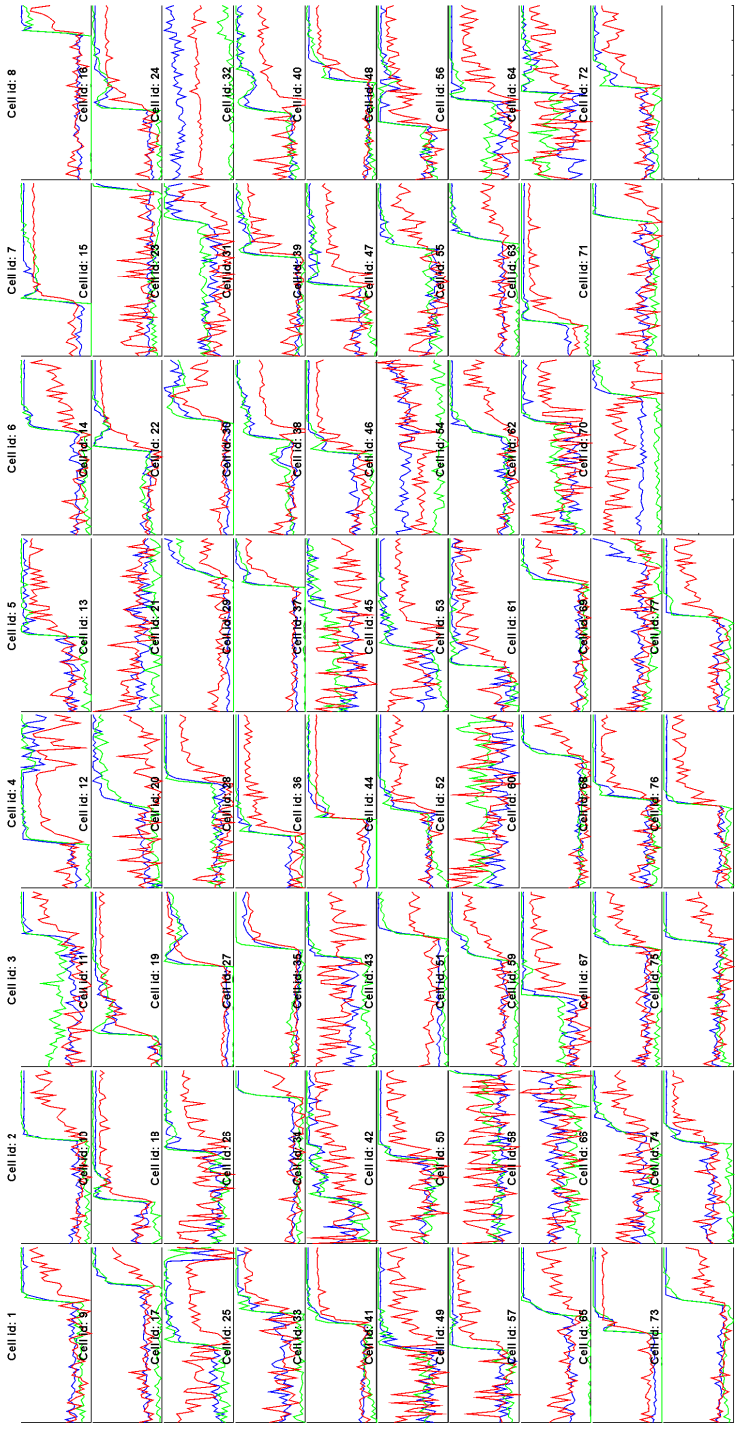

Figure 3.9 – **Raw data of three-colour caspase FLIM imaging**

REA trajectories of 77 HeLa-BAK cells treated with 100 µM Cisplatin and imaged for 16 hours as described in Fig. 3.8A and C. Blue, caspase-2; Green, caspase-3; Red, caspase-9. Shown are all cells from a single experiment.

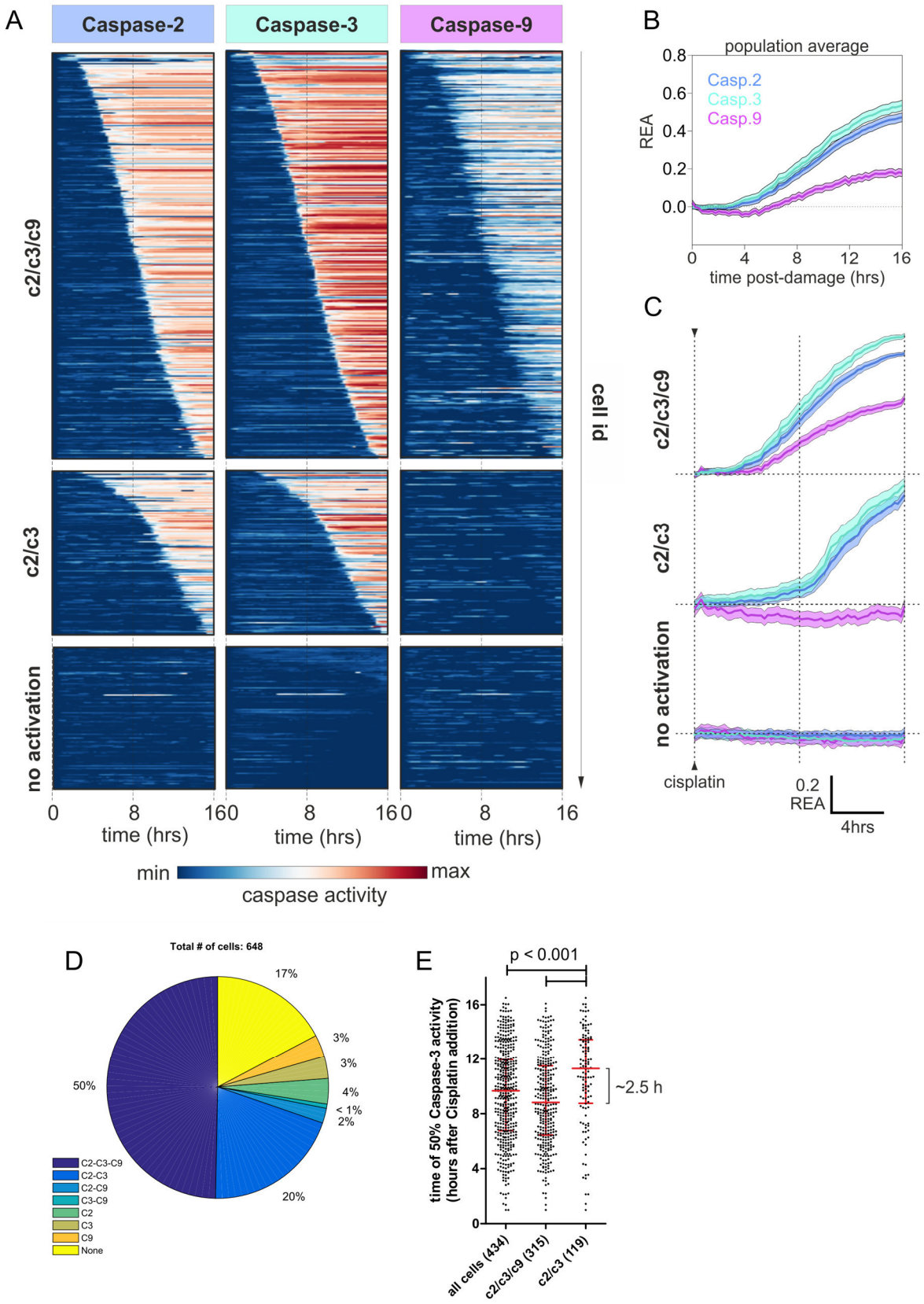
A
Caspase-2
Caspase-3
Caspase-9
c2/c3/c9
c2/c3
no activation
cell id
0
8
160
time (hrs)
min
max
caspase activity
B
population average
Casp.2
Casp.3
Casp.9
REA
0.8
0.6
0.4
0.2
0.0
0
4
8
12
16
time post-damage (hrs)
C
c2/c3/c9
c2/c3
no activation
cisplatin
0.2
REA
4hrs
D
Total # of cells: 648
17%
3%
3%
4%
< 1%
2%
20%
50%
C2-C3-C9
C2-C3
C2-C9
C3-C9
C2
C3
C9
None
E
p < 0.001
time of 50% Caspase-3 activity
(hours after Cisplatin addition)
16
12
8
4
0
~2.5 h
all cells (434)
c2/c3/c9 (315)
c2/c3 (119)

Figure 3.10 – **Deconvolution of heterogeneity in caspase activation in response to Cisplatin**

A: Relative enzymatic activity for caspase-2, -3 and -9 shown for 564 individual HeLa-BAK cells classed into three largest groups and sorted by time of caspase-3 activation after treatment with 100 µM Cisplatin. Data is from 12 independent experiments.

B: Average of REAs for caspase-2, -3, and -9 of all 648 HeLa BAK cells from 12 experiments. Bootstrapped averages with 95% confidence intervals are shown.

C: REA averages for classes shown in A and plotted as in B.

D: Prevalence of classes of HeLa BAK cells determined by caspase activation. 648 cells from 12 experiments are included.

E: Time after Cisplatin treatment at which caspase-3 activity reaches 50% for all cells and c2/c3/c9 and c2/c3 classes from 12 experiments. Number of cells shown in brackets. Median and interquartile range are overlaid in red. Significance was tested using the Kruskal-Wallis Test followed by the Dunn's Multiple Comparison Test.

A-C: Adapted from representation by Dr A Esposito.

Employing this threshold, the c2/c3-responsive population constitutes 20% of the total population (Fig. 3.10D). In this population, caspase-3 activation is triggered at around 11.3 hours, significantly later than in the c2/c3/c9 population (Fig. 3.10E). There is also a population of cells that do not activate any caspase within the duration of the experiment, constituting 17% of the total population (Fig. 3.10A, C, D). Of this population, 66% show no morphological signs of cell death and, therefore, we classify these cells as surviving (Fig. 3.11A). The cells that die without caspase activation exhibit morphological evidence (cell shrinking) of cell death at around 12.5 hours, significantly later than comparable cells that activate any number of monitored caspases (10.7 hours Fig. 3.11B). Finally, there are smaller populations of cells that show activation of single caspases as well as a combination of all (Fig. 3.10A, D), although at lower levels than the predominant populations (Fig. 3.12 C-E, discussed below).

Single-cell caspase dynamics

Because the time of caspase activation is heterogeneous across the population, the average dynamics shown in Figure 3.10 mask the true caspase dynamics of single cells. To avoid this artefact, we first synchronised the individual biochemical trajectories using the 50% of maximal activation for caspase-3 as a reference point. Synchronized REA values for the c2/c3/c9-responsive, c2/c3-responsive and asynchronous non-responsive traces were then used to estimate the bootstrapped average and confidence intervals (see also Fig. 3.8E).

Bootstrapped REA values are shown as a function of time relative to synchronization (Fig. 3.12A-E). Here, the sharp activation of caspases contrasts the shallow responses measurable on population averages, and the differences between the c2/3/9- and c2/3- populations are unambiguous. In the c2/3/9-responsive population, caspase-2 and -3 appeared to be activated

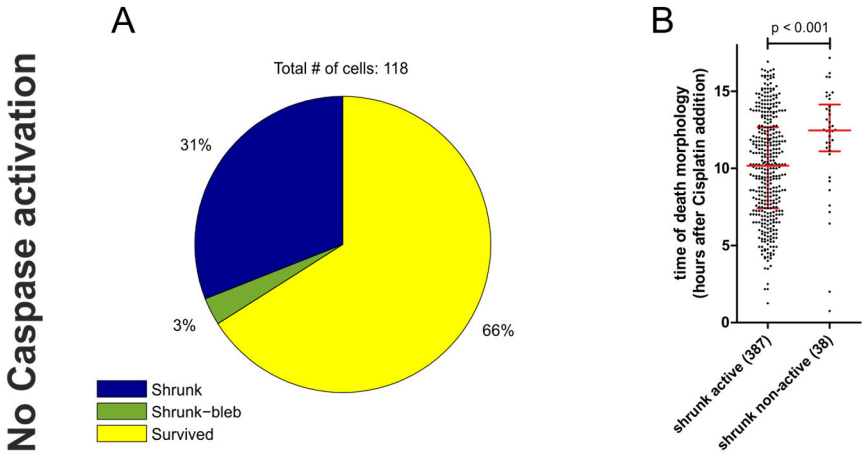

Figure 3.11 – **Characteristics of cells not activating any caspase**

A: Prevalence of cell fate phenotype for 118 HeLa-BAK cells that do not show caspase activation in response to 100 µM Cisplatin within 16 hours. Data from 12 independent experiments.

B: Time of appearance of the first morphological sign of cell death (cell shrinking) for all HeLa-BAK cells that activate either any or no caspase in response to 100 µM Cisplatin. Number of cells shown in brackets. Median and interquartile range are overlaid in red. Significance was tested using the Kruskal-Wallis Test followed by the Dunn's Multiple Comparison Test. Data from 12 independent experiments.

simultaneously, while the activation of caspase-9 is significantly delayed by ~ 20 min (Fig. 3.12A, H). In contrast, in the c2/c3-responsive population, caspase-2 activation is delayed by ~10 min relative to caspase-3 and the maximum REA level is reduced by 20% compared to the c2/c3/c9 population. We also observed that in the smaller populations, single caspase sensors are weakly, but significantly, activated in the absence of any response from the other sensors (Fig. 3.12 C-E). Not only does this demonstrate the power and sensitivity of this sensing approach to detect even small subpopulations with minimal activation of the sensors but it also addresses concerns about the specificity of the sensors directly. The measurement of cells that cleave individual sensors argues strongly in support of specificity of the chosen substrate cleavage motifs.

To further characterise the single-cell kinetics, we fitted a sigmoidal function to the single-cell traces to be able to accurately calculate the rate of caspase activation (Fig. 3.12F) and the maximum REA (Fig. 3.12G). In the c2/c3/c9 population, caspase-2 and-3 exhibited very

similar activation rates as well as maximum REA, while caspase-9 was clearly activated slower and to a lower maximum REA. In the c2/c3 population, the rate is reduced for both caspase-2 and -3 along with the maximum REA. Together, these observations suggest that caspase-2, -3 and -9 form a highly interdependent network in which activation of all caspases is required

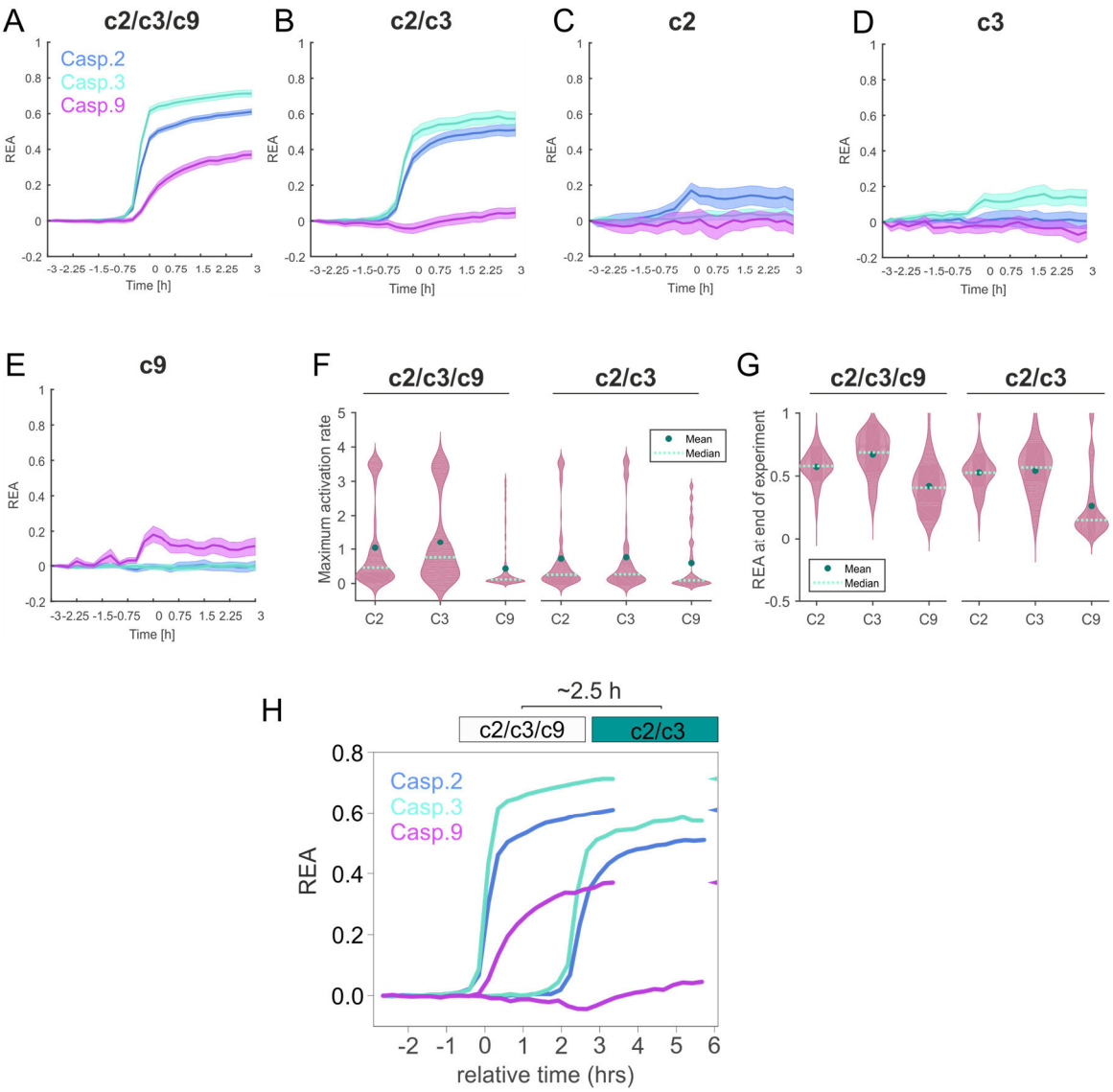

Figure 3.12 – **Single-cell caspase dynamics and subpopulations**

A-E: Relative enzymatic activity for caspase-2, -3 and -9 (blue/green/red) in indicated classes after synchronization of single-cell traces using 50% of caspase-3 activity as reference point. Shown are bootstrapped averages and confidence intervals. Number of cells per panel A-E: 315, 119, 24, 21, 21.

F-G: Distribution of maximum activation rate (F) and REA at the end of the experiment (G) calculated from sigmoidal fits for each caspase and classified into the two pre-dominant caspase response classes.

H: Summary of caspase dynamics (panels A-B) and relative timing (time of 50% caspase-3 activation shown in 3.10G) for c2/c3/c9 and c2/c3 populations.

All data is from 12 independent experiments.

for maximum activation rate, REA as well as the time of activation. In the absence of caspase-9 or multiple caspases, the network response is slowed and subdued, accompanied by a delay in the triggering of caspase activation (Fig. 3.12H).

3.3.3 Mechanism of caspase-9 inhibition and delay

Next, we further investigated possible mechanisms that could affect caspase-9 activation and therefore determine the prominent c2/c3 population.

Caspase-9 deficiency is independent of FRET sensor and HeLa cell line used

We first sought to rule out any technical explanations for the lack of caspase-9 activation. The caspase-9 sensor is unique within our suite of sensors, because of the presence of the tandem-dimer whose sterical effect on the linker required the extension of the linker to restore caspase cleavage (Fig. 2.13). To rule out that this difference in sensor architecture leads to a delay in cleavage of the linker, we transiently expressed the co-expression construct BA containing short caspase-2 and -9 linkers and thereby matching sensor designs. As shown in Figure 3.13A-D, we still detected a population that lacked caspase-9 activation and triggered caspase-2 later than the c2/c3-population (medians 7.8 hours vs 11.1 hours). This excluded any influence of the particular sensor architecture on caspase-9 activity. We also used the same dual-expression vector with linker for caspase-2 and caspase-3 and found as expected only one population of cells that activated both caspase-2 and caspase-3 (Fig. 3.13E-F). While all cells activated either caspase-2 and-3 or none at all, we found that the c2/c3 cells still clustered into two populations in regard to the time of caspase activation, suggesting the presence of a delayed population that, based on our earlier observations, does not activate caspase-9 (Fig. 3.13D).

The transient transfection of dual-caspase sensors permitted us to i) confirm the presence of a delayed c2/c3 population that is independent of the sensor used for caspase-9 monitoring and ii) demonstrate that the caspase-9 negative population is not an artefact specific to the HeLa-BAK clone #7, further validating both sensors and cell line.

Execution of MOMP does not determine c2/c3 population identity

The failure to sufficiently trigger MOMP has been described as a mechanism for delayed or completely abolished cell death (Tait et al., 2010). Thus, we hypothesized that the populations with reduced or completely abolished caspase activation could fail to induce MOMP resulting in the lack of caspase-9 activation (which is activated after MOMP). However, when staining

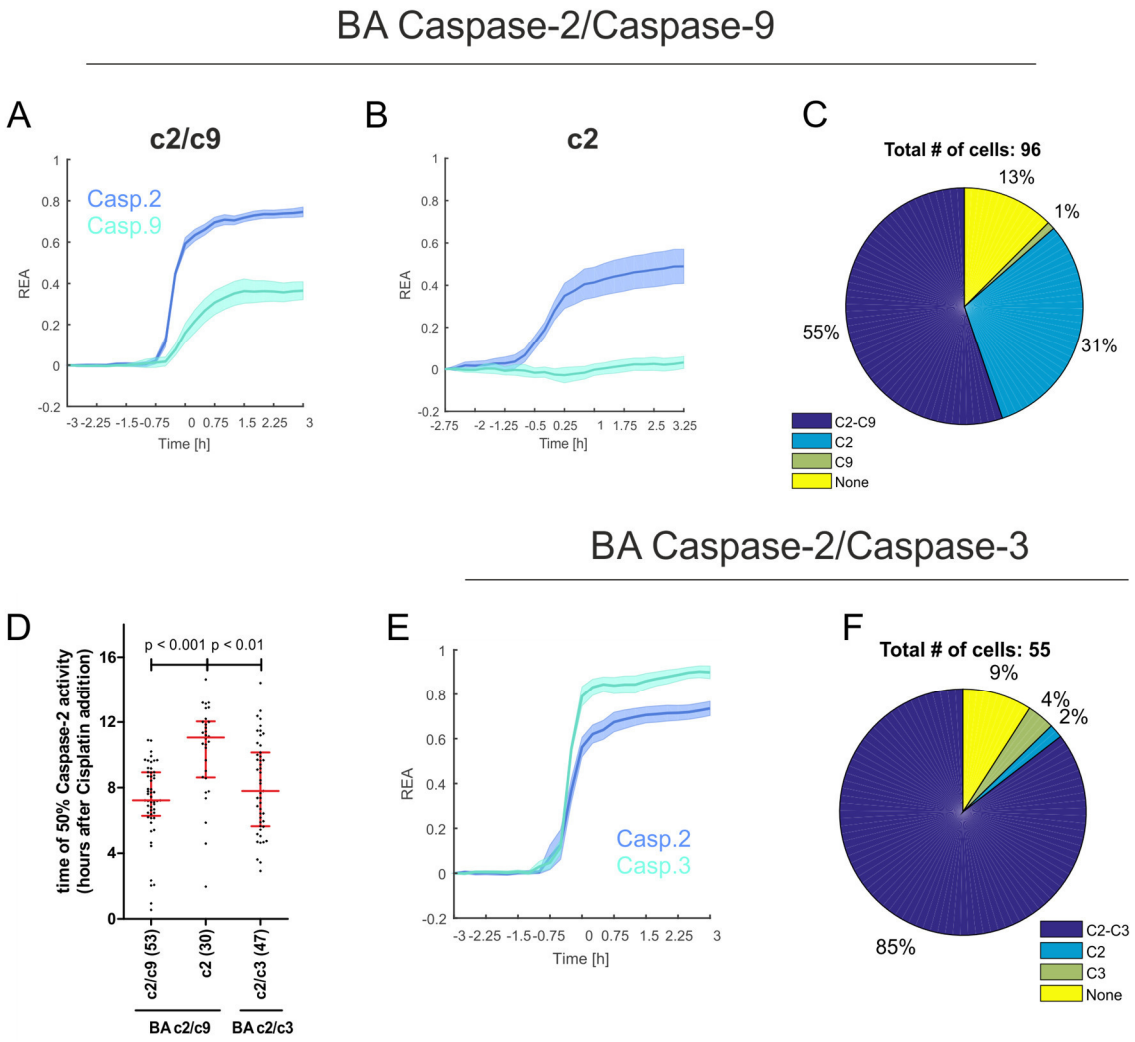

Figure 3.13 – **Confirmation of subpopulations and dynamics with two-colour sensors**

Parental HeLa cells were transiently transfected with caspase-2/-9 (A-C) and caspase-2/-3 (E-F) co-expression systems (mTagBFP-VDTTD-sREACh-P2A-mAmetrine-DEVDR/LEHD-msCP576h) and treated with 100 µM Cisplatin followed by multiplexed imaging. Data are from one experiment.

A-B: REA trajectories for caspase-2 (blue) and -3 (green) for c2/c9 and c2 population. Single-cell trajectories were synchronized using 50% caspase-2 activation. Bootstrapped averages and confidence intervals are shown.

C: Prevalence of detected caspase response classes for cells expressing the caspase-2/-9 sensor construct.

D: Time of 50% caspase-2 activity after Cisplatin treatment for both co-expression systems and classes shown in A-B and E. Number of cells shown in brackets. Median and interquartile range are overlaid in red. Significance was tested using the Kruskal-Wallis Test followed by the Dunn's Multiple Comparison Test.

E: REA trajectory for c2/c3-responsive cells for caspase-2/-3 sensor construct created as described in A-B.

F: Prevalence of detected caspase response classes for cells expressing the caspase-2/-3 sensor construct.

intact mitochondria with TMRM (Tetramethylrhodamine) in parental HeLa cells that undergo Cisplatin-induced cell death, we found that all cells that showed clear death morphology showed a complete and rapid loss of TMRM corresponding to a complete MOMP (Fig. 3.14A-B; Video S3). This was also confirmed using the HeLa-BAK cell line (Video S4). We found that on average MOMP precedes the appearance of cell death signs by ~17 min (Fig. 3.14C). Considering the time resolution of 15 min, this value is likely overestimated, because shorter time intervals than 15 min will all be counted as 15 min. Together, these results suggest that the lack of caspase-9 activation in the c2/c3 population is not due to a failure to execute MOMP.

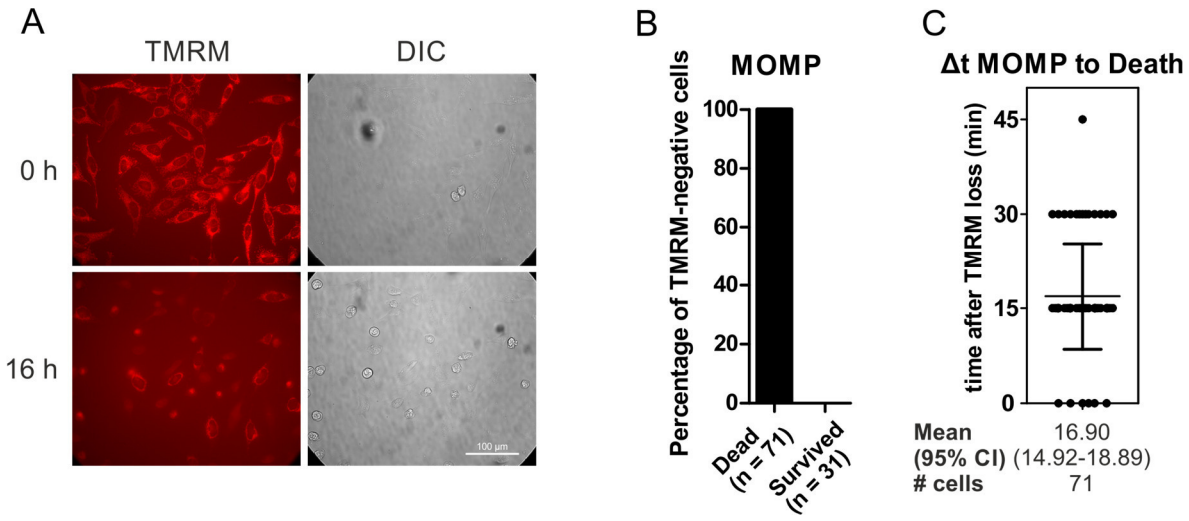

Figure 3.14 – **Measurement of mitochondrial outer membrane permeabilization**

A: Representative fluorescence and DIC images of the same field of view before and after treatment of TMRM-stained HeLa parental cells with 100 µM Cisplatin for 16 hours. Cells were imaged every 15 min.

B: Quantification of the fraction of TMRM-negative (i.e. MOMP-positive) cells treated as in A. Number of cells from a total of three fields of view and one experiment shown in brackets.

C: Time difference between the loss of TMRM staining and the first appearance of a morphological sign of cell death (shrinking or blebbing) for TMRM-negative cells shown in B. CI, confidence interval.

The cell cycle phase does not influence caspase-9 activation

Caspase-9 activity is known to be modulated by a number of factors whose activity is cell cycle-dependent, including CyclinB1/Cdk1 (Allan and Clarke, 2007) and p53 (Chee et al., 2013). This suggests that the position in the cell cycle at the time of Cisplatin addition could affect caspase-9 activity and, therefore, it could cause the emergence of the c2/3/9 and c2/3 populations.

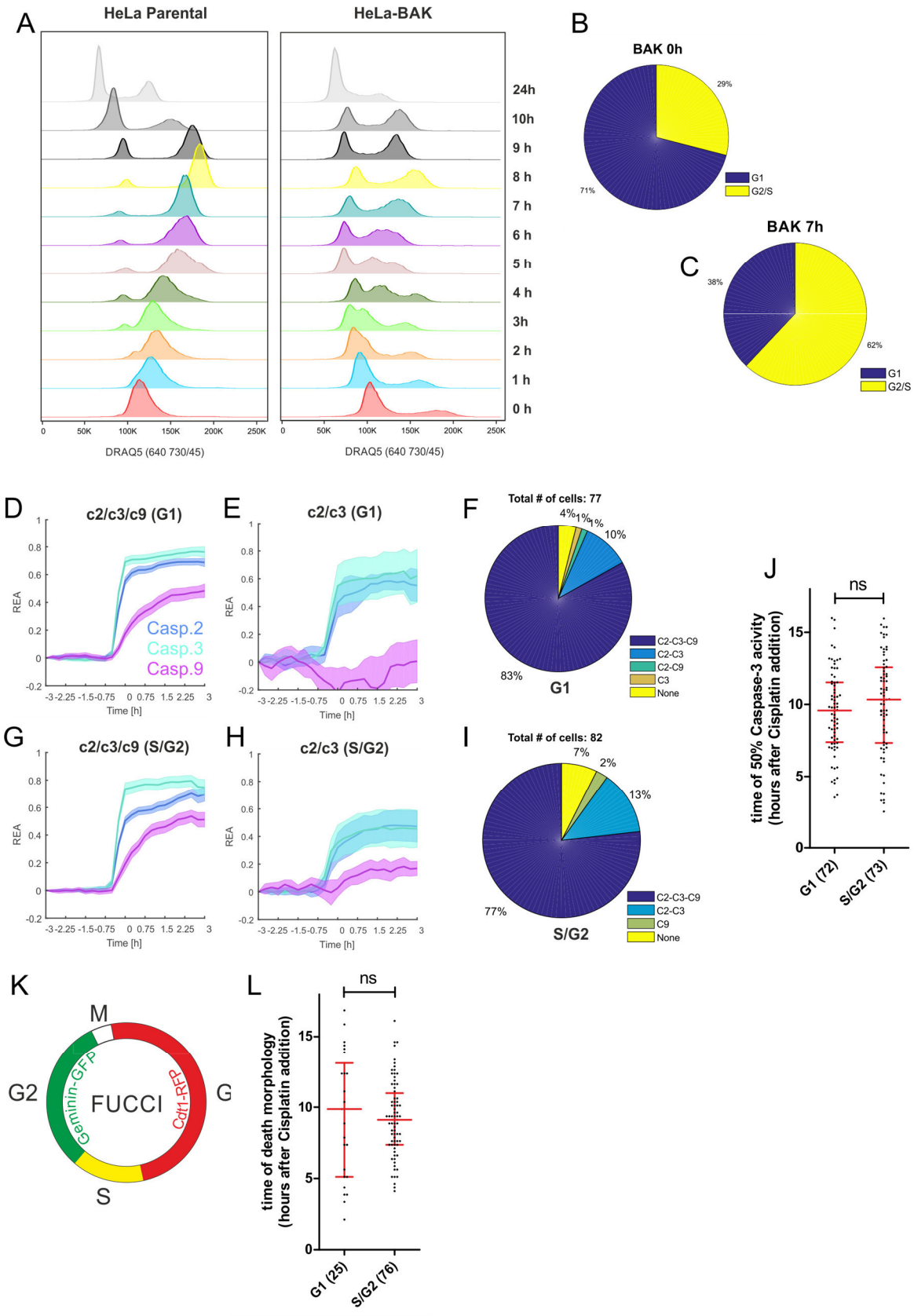
A
HeLa Parental
HeLa-BAK
24h
10h
9 h
8 h
7 h
6 h
5 h
4 h
3h
2 h
1 h
0 h
0 50K 100K 150K 200K 250K
DRAQ5 (640 730/45)
B
BAK 0h
29%
71%
G1
G2/S
C
BAK 7h
38%
62%
G1
G2/S
D
c2/c3/c9 (G1)
REA
Casp.2
Casp.3
Casp.9
Time [h]
E
c2/c3 (G1)
REA
Time [h]
F
Total # of cells: 77
4%
1%
1%
10%
83%
G1
C2-C3-C9
C2-C3
C2-C9
C3
None
G
c2/c3/c9 (S/G2)
REA
Time [h]
H
c2/c3 (S/G2)
REA
Time [h]
I
Total # of cells: 82
7%
2%
13%
77%
S/G2
C2-C3-C9
C2-C3
C9
None
J
ns
time of 50% Caspase-3 acivity (hours after Cisplatin addition)
G1 (72)
S/G2 (73)
K
M
G2
G
S
FUCCI
Geminin-GFP
Cdt1-RFP
L
ns
time of death morphology (hours after Cisplatin addition)
G1 (25)
S/G2 (76)

Figure 3.15 – **Prevalence of caspase populations is independent of the cell cycle phase at the time of treatment**

A: Cell cycle profiles of DRAQ5-stained HeLa parental and HeLa-BAK cells at indicated times after release from a double-thymidine block.

B-C: Proportion of cells in G1 and G2/S phases at 0 hours (B) and 7 hours (C) after release based on profiles in panel A.

D-E, G-H: caspase-2/-3/-9 dynamics of HeLa-BAK cell treated with 100 µM Cisplatin at 0 hours (D-E) or 7 hours (G-H) after release from a double-thymidine block. Synchronized, bootstrapped averages and confidence intervals for two classes are shown.

F, I: Prevalence of detected caspase response classes for cells treated at 0 hours (F) or 7 hours (I) after release from a double-thymidine block.

J: Time of 50% caspase-3 activity after treated with 100 µM Cisplatin for all cells shown in F (G1) and I (S/G2). Number of cells shown in brackets. Median and interquartile range are overlaid. Significance was tested using the Kruskal-Wallis Test followed by the Dunn's Multiple Comparison Test.

K: Schematic of the FUCCI system used to identify the cell cycle phase.

L: Time to the first appearance of death morphology (shrinking or blebbing) of parental HeLa cells expressing the FUCCI system treated with 100 µM Cisplatin. Cells showing only red fluorescence in the first frame were counted as G1, and cells showing green fluorescence as S/G2. Number of cells shown in brackets. Median and interquartile range are overlaid. Significance was tested using the Kruskal-Wallis Test followed by the Dunn's Multiple Comparison Test.

All data are from single experiments each for A-C, D-J and L, respectively.

Therefore, HeLa-BAK were synchronized in G1 using a double-thymidine block and cell cycle analysis performed to determine the time after release at which the majority of the cells was either in G1 or S/G2 phase (Fig. 3.15A-C). We then treated HeLa-BAK at those times with Cisplatin and performed multiplexed imaging of caspase-2, -3 and -9 as usual. We observed no difference between G1- and S/G2-treated cells in any of the parameters assessed (Fig. 3.15, D-J), suggesting that the cell cycle phase at the time of treatment does not influence caspase-9 activity nor the time of cell death.

We noticed that the double-thymidine block was less efficient in HeLa-BAK cells compared to HeLa parental cells, in agreement with the reduced proliferation rate discussed earlier (Fig. 3.15A). Thus, at the time of treatment, ~30% of the cells are in the 'undesired' cell cycle phase which could mask potential differences (Fig. 3.15B-C). Therefore, to avoid synchronization, we treated asynchronously growing HeLa parental cells expressing the FUCCI cell cycle marker (Fig. 3.15K) with Cisplatin and recorded the time of the appearance of any death morphology (Fig. 3.15L). Again, there was no clear difference between cells that expressed the G1 or the S/G2 marker at the time of treatment. However, as the number of cells that were treated in G1 is small, this conclusion ought to be confirmed with further repeats of this assay.

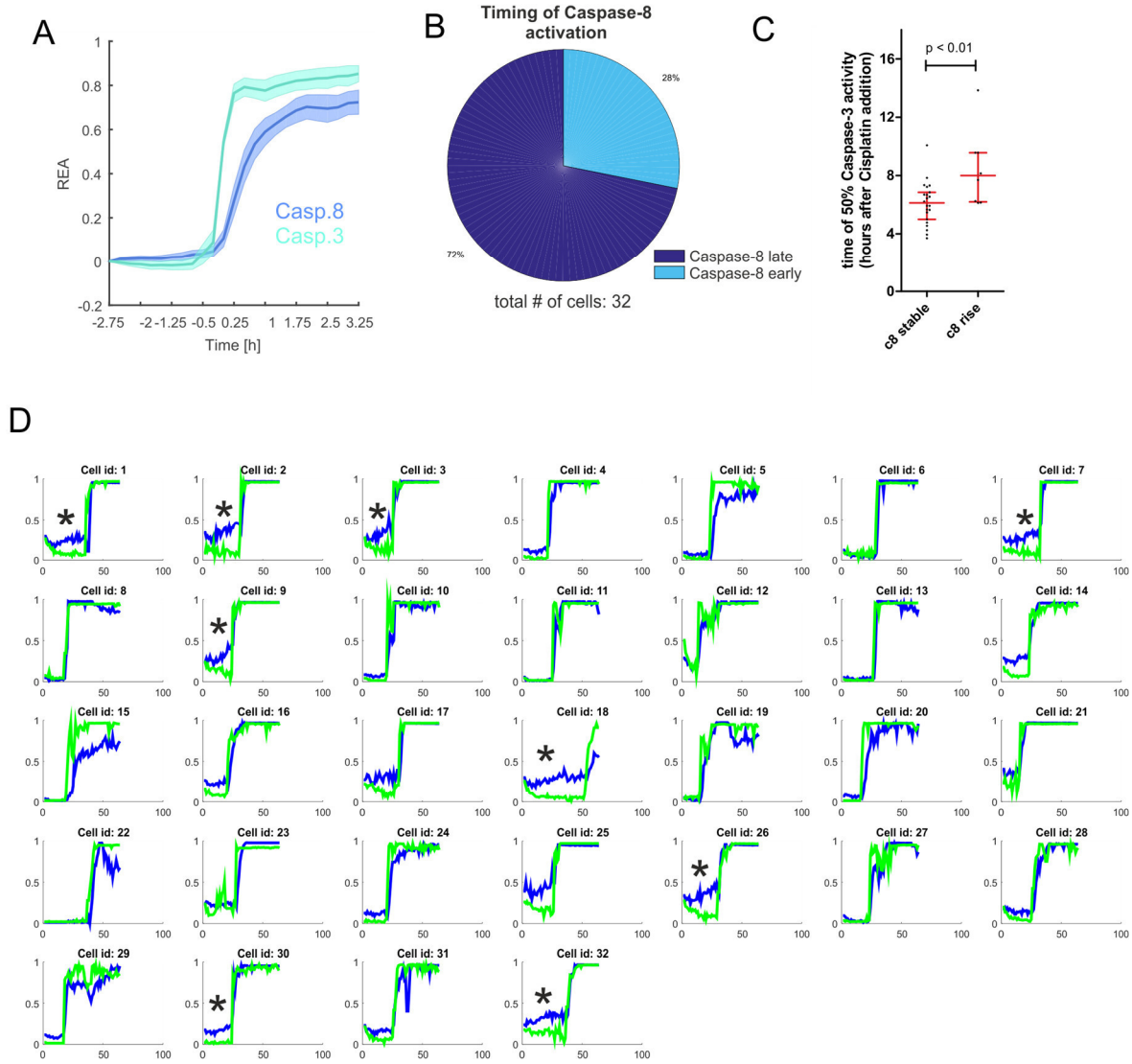

Figure 3.16 – **Caspase-8 dynamics and its implication in cell fate determination**

A: Dynamics of caspase-3 (green) and caspase-8 (blue) activation for parental HeLa cells treated with 100 µM Cisplatin treatment. Synchronized, bootstrapped averages and confidence intervals are shown.

B: Prevalence of cells that show an early activation in caspase-8 activity that precedes caspase-3 activation (marked with an asterisk in D).

C: Time of 50% caspase-3 activity for cells depending on the appearance of an early activation in caspase-8 activity. Median and interquartile range are overlaid in red.

D: Single-cell traces of cells averaged in A. Cells showing an early activation in caspase-8 are marked with an asterisk.

All data from a single experiment.

In summary, using two independent methods, we could show that caspase-9 activity in response to Cisplatin is independent of the cell-cycle state at the time of treatment.

Caspase-8 as a candidate to set caspase-9 activation

As depicted in Figure 3.2, Cisplatin-induced DNA damage can lead to the activation of caspase-8 via JNK and p38, which can induce cell death both by triggering MOMP and caspase-9 activation, as well as direct activation of caspase-3 bypassing MOMP.

Combining sensors for caspase-3 and -8, we observed early activation of caspase-8 preceding caspase-3 activity (manifested as a slow 'rise' reported by Albeck et al., 2008) in 28% of the cells (Fig. 3.16A-C). The full activation occurs ~20 min after caspase-3, indicating activation of the known feedback loop between caspase-3 and -8, and is likely corresponding to the late caspase-8 processing observed on Western Blot (Fig. 3.6). The proportion of cells with early caspase-8 activity is similar to the proportion of c2/c3 cells observed in other experiments (Fig. 3.16B, D). Moreover, such cells also show a ~2 hours delay in the onset of caspase-3 activation, reminiscent of the c2/c3 cells (Fig. 3.16C), suggesting that caspase-8 activity does indeed determine this population. However, to fully validate this hypothesis, caspase-8 and caspase-9 activity needs to be monitored simultaneously, an experiment that is currently being performed.

In summary, we confirmed that the delay of caspase-9 activation and lack of activation in a population of cells is independent of the HeLa cell line used, the sensor architecture, cell cycle state, and are currently investigating a potential role of caspase-8. Next, we used the full depth of information obtained with the sensing approach to connect caspase activation dynamics with cell fate.

3.3.4 A continuum of Cisplatin-induced apoptotic and necrotic cell death

When studying the intensity images derived from the biochemical trajectories, we observed the presence of different cell death phenotypes (Fig. 3.17A-B; Video S5). The large majority of cells (72%) exhibited rapid (usually completed within 15 min) cell shrinkage, detachment from the culture surface and subsequent appearance of membrane blebbing and apoptotic bodies ('shrunk' phenotype). A small population of the cells (4%) instead showed no apparent shrinking, but pronounced membrane blebbing while remaining attached to the surface ('bleb' phenotype). Another group of cells was characterized by an initial shrinking that remained

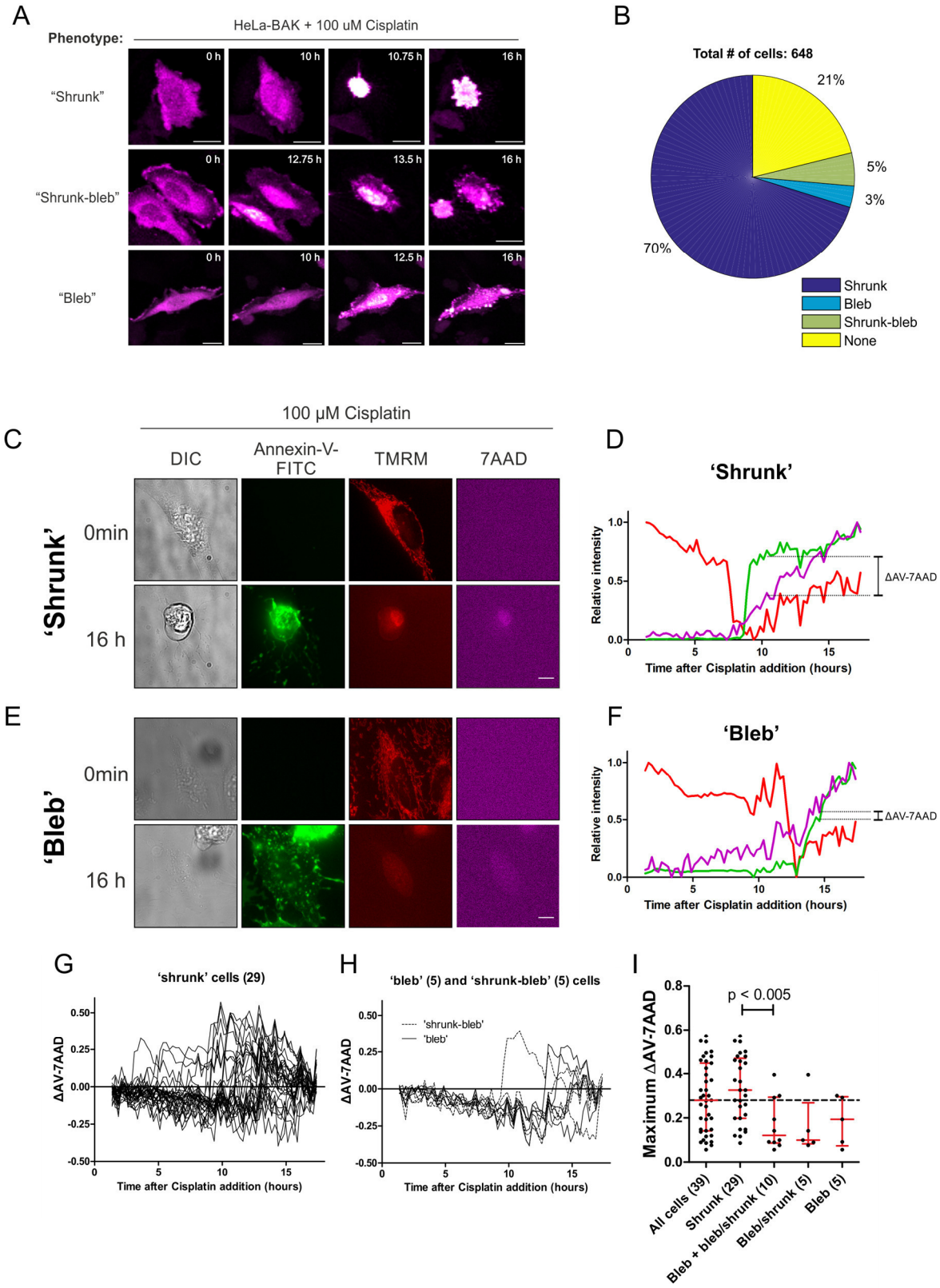
A
Phenotype:
HeLa-BAK + 100 uM Cisplatin
"Shrunk"
"Shrunk-bleb"
"Bleb"
0 h
10 h
10.75 h
16 h
12.75 h
13.5 h
12.5 h
B
Total # of cells: 648
21%
5%
3%
70%
Shrunk
Bleb
Shrunk-bleb
None
C
100 µM Cisplatin
DIC
Annexin-V-FITC
TMRM
7AAD
'Shrunk'
0min
16 h
D
'Shrunk'
Relative intensity
ΔAV-7AAD
Time after Cisplatin addition (hours)
E
'Bleb'
0min
16 h
F
'Bleb'
Relative intensity
ΔAV-7AAD
Time after Cisplatin addition (hours)
G
'shrunk' cells (29)
ΔAV-7AAD
Time after Cisplatin addition (hours)
H
'bleb' (5) and 'shrunk-bleb' (5) cells
'shrunk-bleb'
'bleb'
ΔAV-7AAD
Time after Cisplatin addition (hours)
I
p < 0.005
Maximum ΔAV-7AAD
All cells (39)
Shrunk (29)
Bleb + bleb/shrunk (10)
Bleb/shrunk (5)
Bleb (5)

Figure 3.17 – **Heterogeneity of cell death morphology in response to Cisplatin**

A: Representative images of HeLa-BAK cells showing distinct morphologies when undergoing cell death in response to 100 µM Cisplatin based on 12 independent experiments. Note that for 'shrunk-bleb' cells, the field of view includes a 'shrunk' cells (lower cell) for direct comparison. Scale bars are 10 µM.

B: Prevalence of cell death morphologies defined in A for HeLa-BAK cells undergoing Cisplatin-induced cell death in 12 independent experiments.

C, E: Representative images of parental HeLa cells stained with Annexin-V-FITC, TMRM and 7-AAD before at after treatment with 100 µM Cisplatin undergoing the 'shrunk' (C) or 'bleb' (E) cell death phenotype.

D, F: Quantification of normalized fluorescence in three channels for single cells shown in C, E.

G-H: Difference in fluorescence intensity between Annexin-V-FITC and 7-AAD signal at each time point after Cisplatin addition. Cells from three fields of view and one experiment are shown; number of cells in brackets. Curves are shown as classified accordingly to the phenotypes defined in panel A.

I: Maximum of curves in G-H classified by phenotype. Number of cells in brackets. Mean and standard deviation are overlaid. Horizontal dashed line indicates median of all cells. Significance was tested using the Mann-Whitney test.

C-I: Data from one experiment with three fields of view.

incomplete (i.e. cells did not round up perfect spheres; see Fig. 3.17A central panels for direct comparison of 'shrunk' and 'shrunk-bleb') followed by the appearance of membrane blebbing, thus, exhibiting characteristics of both 'bleb' and 'shrunk' phenotypes ('shrunk-bleb' phenotype). Finally, 20% of the cells did not show any discernible death phenotype. While the assignment of the 'shrunk' phenotype was usually unambiguous, an apparent continuum between the remaining phenotypes complicated the phenotypic assignment. Therefore, all cells were scored blindly by three researchers and the final assignment determined by majority consensus (see Material and Methods for details on scoring and criteria).

The 'shrunk' phenotype constitutes all key morphological determinants for apoptosis (cell shrinkage, detachment and blebbing), while the 'bleb' phenotype is more reminiscent of necrotic cell death (blebbing in the absence of shrinkage; Berghe et al., 2014; Degterev and Yuan, 2008; Galluzzi et al., 2012). To determine the mode of cell death, we performed an Annexin-V/7-AAD (7-amino-actinomycin D) co-staining assay on parental HeLa cells, considered the gold standard for distinguishing apoptotic from necrotic cell death (Vermes et al., 1995). Fluorescently-labelled Annexin-V (AV) binds to exposed phosphatidylserine (PS) in the plasma-membrane, whereas 7-AAD stains DNA, but can only enter if the membrane integrity is lost. In apoptotic cells, PS exposure precedes loss of membrane integrity, whereas in the necrotic cells initial loss of membrane integrity means that both events co-occur. We also co-stained the same cells with TMRM to determine the timing relative to MOMP (quantified earlier in Fig. 3.14).

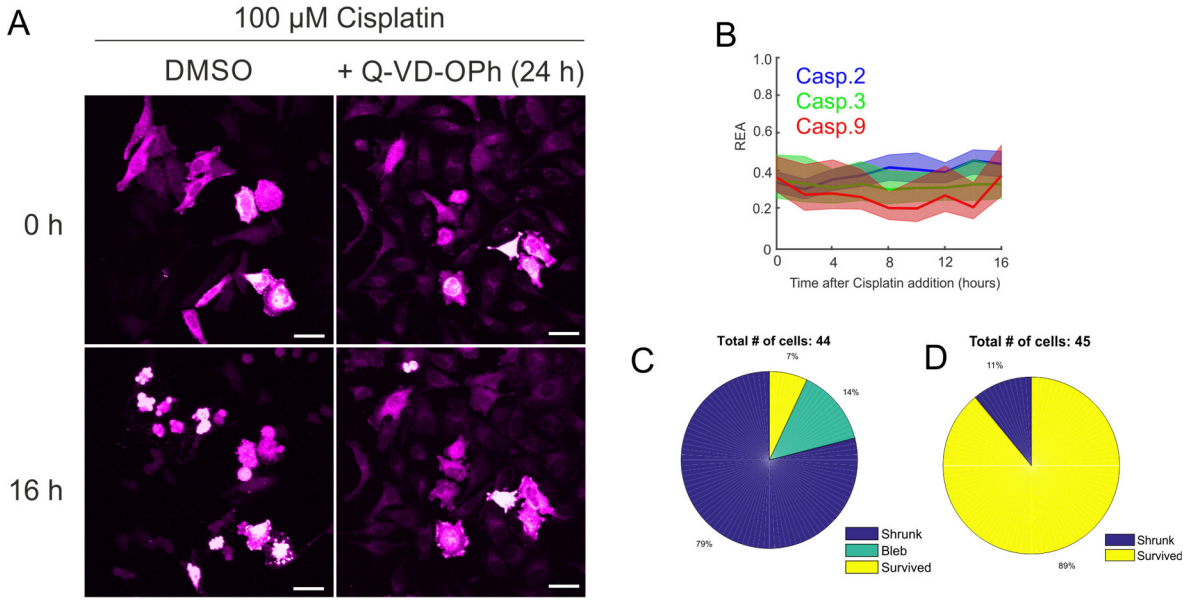

Figure 3.18 – **Cell death in response to Cisplatin is caspase-dependent**

A: Representative images of HeLa-BAK cells pre-treated for 24 hours in presence or absence of 25 µM pan-caspase inhibitor Q-VD-OPh, before and after treatment with 100 µM Cisplatin.

B: REA trajectories for caspase-2/-3/-9 (Blue, green, red) shown as bootstrapped averages with confidence intervals for cells pre-treated with Q-VD-OPh as in A.

C-D: Prevalence of cell death phenotypes after 16 hours treatment with 100 µM Cisplatin in the absence (C) or presence (D) of Q-VD-OPh.

Data from three field of views each in one experiment.

As shown in Figure 3.17C-F, AV precedes 7-AAD staining in ‘shrunk’ cells, while it co-occurs in ‘bleb’ cells. MOMP occurs in all cells that exhibit any cell death phenotype and precedes AV staining (see also Fig. 3.14). Quantifying the time delay between AV and 7-ADD for multiple cells confirmed that ‘shrunk’ exhibit a significantly longer delay than ‘bleb’ cells (Fig. 3.17G-I), suggesting that ‘shrunk’ cells are mostly apoptotic cells (62% above median delay of all cells), whereas ‘bleb’ cells are predominantly necrotic (40% above median delay of all cells). ‘Shrunk-bleb’ cells showed a delay similar to bleb cells, suggesting there are closer to necrotic cell death (20% above median delay of all cells). However, we expect that with more numbers of ‘bleb’ and ‘shrunk-bleb’ cells analysed the two populations could diverge more clearly. Aiming to further delineate the identity of the necrotic cell death, we treated HeLa with the potent pan-caspase inhibitor Q-VD-OPh (Fig. 3.18). Pan-caspase-inhibition protected the vast majority of cells from Cisplatin-induced apoptotic as well as necrotic cell death, indicating the caspases are required for both cell death pathways in our experimental model.

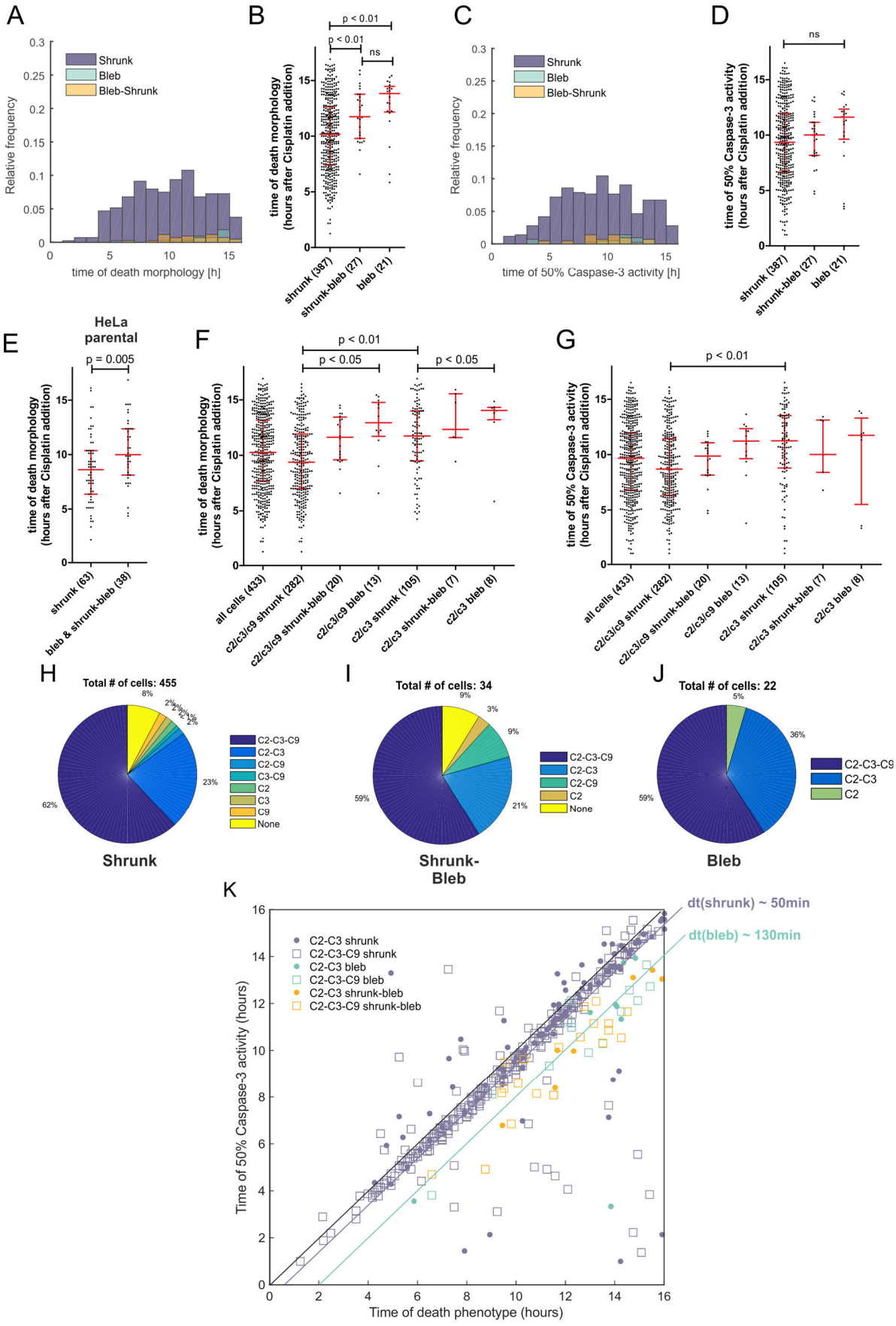
A
Relative frequency
Shrunk
Bleb
Bleb-Shrunk
time of death morphology [h]
B
time of death morphology (hours after Cisplatin addition)
p < 0.01
p < 0.01
ns
shrunk (387)
shrunk-bleb (27)
bleb (21)
C
Relative frequency
Shrunk
Bleb
Bleb-Shrunk
time of 50% Caspase-3 activity [h]
D
time of 50% Caspase-3 activity (hours after Cisplatin addition)
ns
shrunk (387)
shrunk-bleb (27)
bleb (21)
E
HeLa parental
p = 0.005
time of death morphology (hours after Cisplatin addition)
shrunk (63)
bleb & shrunk-bleb (38)
F
p < 0.01
p < 0.05
p < 0.05
time of death morphology (hours after Cisplatin addition)
all cells (433)
c2/c3/c9 shrunk (282)
c2/c3/c9 shrunk-bleb (20)
c2/c3/c9 bleb (13)
c2/c3 shrunk (105)
c2/c3 shrunk-bleb (7)
c2/c3 bleb (8)
G
p < 0.01
time of 50% Caspase-3 activity (hours after Cisplatin addition)
all cells (433)
c2/c3/c9 shrunk (282)
c2/c3/c9 shrunk-bleb (20)
c2/c3/c9 bleb (13)
c2/c3 shrunk (105)
c2/c3 shrunk-bleb (7)
c2/c3 bleb (8)
H
Total # of cells: 455
8%
2%
2%
2%
2%
23%
62%
C2-C3-C9
C2-C3
C2-C9
C3-C9
C2
C3
C9
None
Shrunk
I
Total # of cells: 34
9%
3%
9%
59%
21%
C2-C3-C9
C2-C3
C2-C9
C2
None
Shrunk-Bleb
J
Total # of cells: 22
5%
36%
59%
C2-C3-C9
C2-C3
C2
Bleb
K
dt(shrunk) ~ 50min
dt(bleb) ~ 130min
C2-C3 shrunk
C2-C3-C9 shrunk
C2-C3 bleb
C2-C3-C9 bleb
C2-C3 shrunk-bleb
C2-C3-C9 shrunk-bleb
Time of 50% Caspase-3 activity (hours)
Time of death phenotype (hours)

Figure 3.19 – **Correlation between cell death timing, phenotype and caspase activation**

A: Frequency distribution of the time of appearance of different cell death phenotypes of HeLa-BAK cells treated with 100 µM Cisplatin for 16 hours.

B: Data as in panel A but shown for single cells. Number of cells indicated in brackets. Median and interquartile range are overlaid in red. Significance was tested using the Kruskal-Wallis Test followed by a Dunn's Multiple Comparison Test.

C: Frequency distribution of time for 50% caspase-3 activity by cell death phenotype.

D: Data as in panel C but shown for single cells. Number of cells indicated in brackets. Median and interquartile range are overlaid in red. Significance was tested using the Kruskal-Wallis Test followed by a Dunn's Multiple Comparison Test.

E: Time of appearance of cell death phenotypes for parental HeLa cells treated with 100 µM Cisplatin for 16 hours. Median and interquartile range are overlaid in red. Significance was tested using the Mann-Whitney test.

F-G: Time of cell death morphology (F) and time to 50% caspase-3 activity (G) for cells in B and D shown by caspase response class (c2/c3/c9 or c2/c3). Median and interquartile range are overlaid in red.

H-J: Prevalence of caspase response classes for different death phenotypes.

K: Correlation between the time of 50% caspase-3 activity and time of appearance of the death phenotype after Cisplatin treated shown for single cells and classified by death phenotype and caspase response class (data as in F/G). Lines are approximations to aid illustration.

All data from 12 independent experiments.

Comparing timing and dynamics of caspase activation with cell death phenotypes

Analysing the timing of the appearance of the cell death phenotype (i.e. the first frame in which a cell shows either shrinking or blebbing, referred to as 'time of death') as well as the time of 50% caspase-3 activation (measured from the single-cell REA trajectories) for each phenotype, we found that 'bleb' cells are delayed by 2.5 to 3.5 hours compared to 'shrunk' cells, respectively (Time of death median 10.2 hours vs 13.8 hours; 50% c3 median 9.4 hours vs 11.6 hours; Fig. 3.19A-D). 'Shrunk-bleb' cells exhibit an intermediate timing both for the time of cell death and time of caspase-3 activation (medians 11.8 hours and 10.0 hours, respectively). We also confirmed the presence of 'shrunk' and 'bleb' phenotypes and a similar delay between them in parental HeLa cells (Fig. 3.19E).

We noted that there was a consistent difference between the two time-metrics (time of death and time of 50% caspase-3 activation) across all twelve experiments analysed in this set, with caspase-3 activation preceding the occurrence of any cell death morphology. The time difference increased from ~50 min for 'shrunk' cells to ~130 min for 'bleb' cells, suggesting a slower execution of cell death in bleb cells which could be biologically important (Fig. 3.19K). However, while determining the exact time of the appearance of the first morphological sign of death was usually unambiguous for cell shrinking, determining the first occurrence of

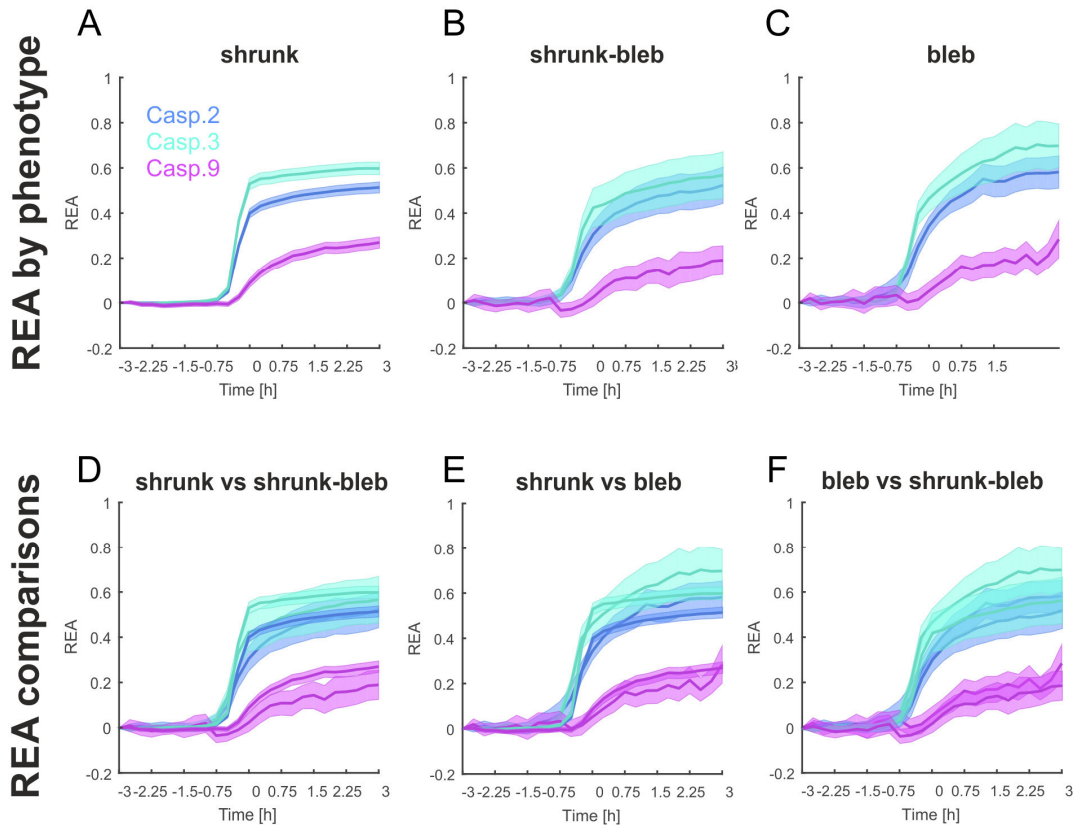

Figure 3.20 – **Comparison of caspase dynamics of cell death phenotypes**

A-C: Relative enzymatic activity for caspase-2, -3 and -9 of indicated cell death phenotypes. Single-cell traces were synchronized to 50% caspase-3 activity. Bootstrapped averages and confidence intervals from 12 independent experiments are shown.

D-F: Pair-wise overlays of graphs shown in A-C.

membrane blebbing was difficult and is likely prone to a large error. Therefore, we decided to show both time metrics in all further experiments.

Next, because the time difference between the c2/c3/c9 and c2/c3 populations was similar to the difference between ‘shrunk’ and ‘bleb’ cells, we hypothesized that they corresponded to the same population. However, when both time of death, as well as caspase-3 activation, was sub-divided into phenotypes and caspase responsiveness, we observed both the c2/c3/c9 and c2/c3 populations exhibit all phenotypes at approximately equal proportions, arguing against an overlap between caspase responsiveness and death phenotype (Fig. 3.19F-G). When we analysed the cells belonging to each phenotype regarding the prevalence of different caspase responsiveness, no clear difference could be observed, again suggesting a limited overlap between caspase responsiveness and death phenotype (Fig. 3.19H-J). We also computed

boot-strapped caspase trajectories for the three caspases, but, despite a markedly lower caspase-9 activation in ‘bleb’ and ‘shrunk-bleb’ cells, we could not unambiguously identify a difference in caspase activation between the different phenotypes (Fig. 3.20).

Taken together, these results suggest that a subdued caspase response is at least partially connected with a change in the cell death phenotype toward necrosis. In the next section (3.3.5), we will assess this connection further using targeted perturbation of the network.

U2OS osteosarcoma cells show heterogeneity in caspase activation and cell death phenotype

Next, we asked whether the large extent of non-genetic heterogeneity in caspase activation and cell death modes is a more general feature in the response to Cisplatin-induced cell death by using a different cell line. Thus, we used the osteosarcoma cell line U2OS transiently expressing the caspase-2/3/9 co-expression system that was used to create the HeLa-BAK cell line for multiplexed caspase imaging.

In response to Cisplatin, the majority (57%) of the U2OS cells did not activate caspases (Fig. 2.21A-B), of which 95% show no cell death phenotype. Of those cells that show caspase activation, c2/c3/c3 cells are the largest population (31% of total). The remainder activates either c2/c3 or c3 and c9 alone (4%, 3%, 6%, respectively), but considering the low number of cells, this classification remains uncertain. As for HeLa cells, we observed a high degree of heterogeneity in the time at which caspases are triggered (Fig. 3.21A; video S7). U2OS also showed a similar order of caspase activation with caspase-3 activated first, followed closely by caspase-2 (Fig. 3.21C). Caspase-9 was delayed by ~15 min relative to caspase-3. Moreover, the heterogeneity in cell death was recapitulated, too, with the ‘bleb’ phenotype

constituting the largest group (Fig. 3.21D). Also, ‘bleb’ cells showed a ~2-hour delay in caspase-3 activation and a ~2.5h delay in the appearance of the death phenotype (Fig. 3.21E-F), in concordance with results obtained in HeLa cells. Interestingly when comparing phenotype and caspase responsiveness, we found that ‘bleb’ cells were twice as likely to die in the absence of any caspase activation as ‘shrunk’ cells (Fig. 3.21G-H), suggesting that, at least in U2OS, failure to sufficiently activate the caspase network is a cause for a switch to a necrotic cell death. In HeLa cells, such a clear difference between caspase responsiveness and phenotype could not be observed in response to Cisplatin.

In summary, we could not only show that the pronounced non-genetic heterogeneity in cell death dynamics and death phenotypes is not limited to one cell line, but also demonstrate that there is considerable heterogeneity between genetically different cell lines.

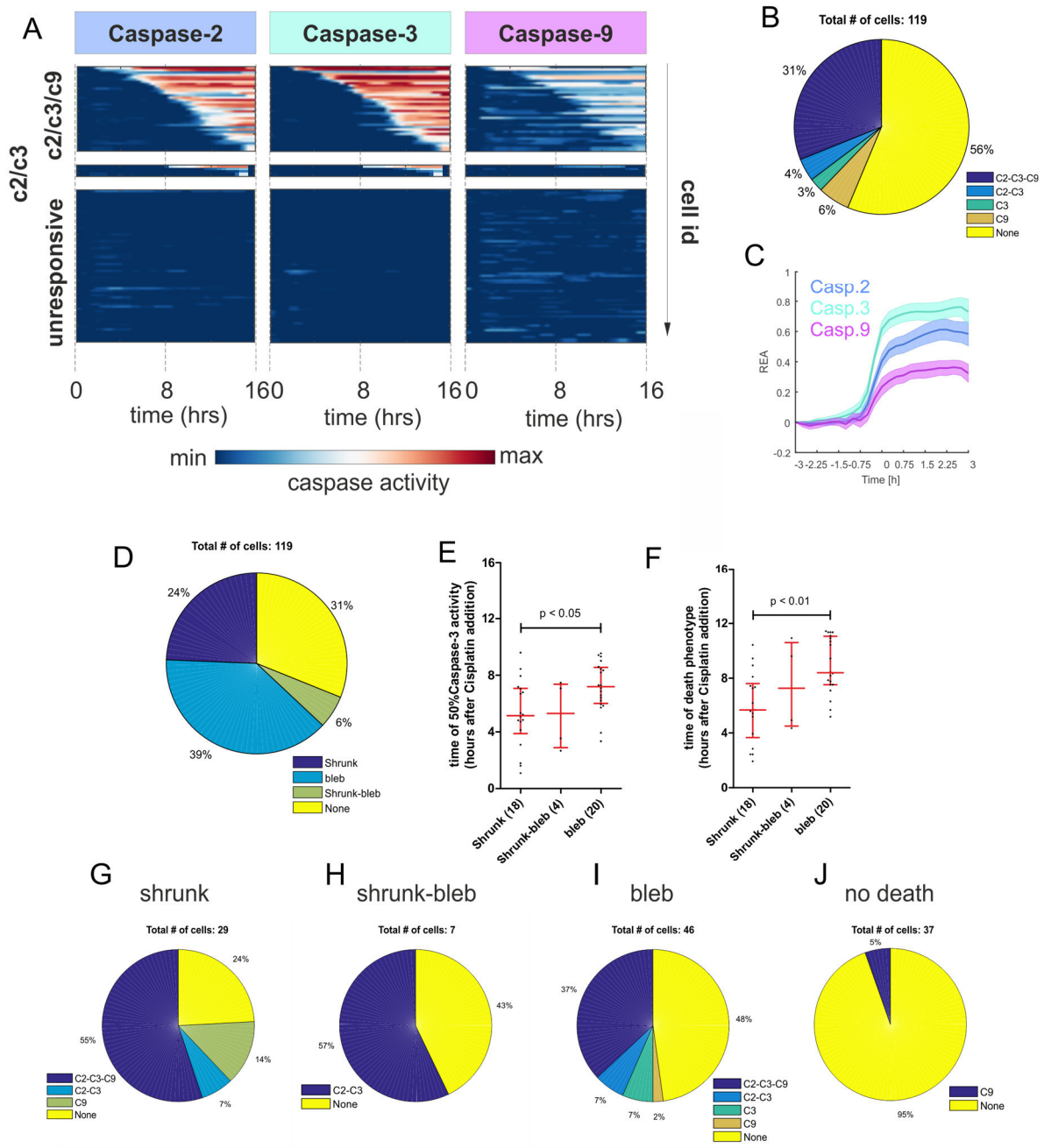

Figure 3.21 – **U2OS cells show heterogeneity in caspase activation and cell death phenotype**

A: Relative enzymatic activity for caspase-2, -3 and -9 shown for individual U2OS cells transiently transfected with the BAK co-expression system and treated with 100 µM Cisplatin. Three caspase response classes are shown and cells within each class sorted by time of caspase-3 activation after treatment.

B: Prevalence of caspase response classes.

C: Caspase-2/-3/-9 activation dynamics for the c2/c3/c9-responsive cells. Bootstrapped averages synchronized to 50% caspase-3 activity and confidence intervals are shown. Panels A and C adapted from Dr A Esposito.

D: Prevalence of cell death phenotypes.

E-F: Time of 50% caspase-3 activity (E) or appearance of cell death (F) for different cell death phenotypes. Median and interquartile range are overlaid in red. Number of cells shown in brackets. Significance was tested using the Kruskal-Wallis Test followed by a Dunn's Multiple Comparison Test.

G-J: caspase response classes of Cisplatin-treated U2OS cells shown for each death phenotype.

All data are from one experiment with a total of 119 cells.

3.3.5 Perturbation of the caspase network

Next, we used different small molecule inhibitors to gain further insight into the caspase dynamics and the role it plays in the determining cell fate in the Cisplatin-induced DNA damage response in HeLa cells.

Caspase inhibitors interfere with caspase dynamics and cell fate

First, we monitored caspase-2, -3, and -9 dynamics and death morphology in HeLa-BAK cells in the presence of irreversible peptidomimetic inhibitors against individual caspases (Fig. 3.22-24; also see chapter 2 for the use of these inhibitors for sensor validation).

In the presence of the caspase-2 inhibitor Z-VDVAD-FMK (Fig. 3.22C-D, J), we observed fewer cells that responded with all three caspases, while the frequency of c2/3-only cells remained unaltered. However, in these cells, caspase-2 exhibited slower kinetics compared to the other caspases and matched controls. Crucially, we observed a significant increase of cells (from ~2% to 17% of the total) that only cleaved the caspase-2 substrate sensor and cells that processed both the caspase-2 and -9, but not caspase-3 sensors (2% to 7%; Fig. 3.22F). In both cell populations, caspase activity reached only very low maximal levels of cleavage, suggesting that low activation of caspase-2 is insufficient to trigger a complete response of the caspase network (Fig. 3.23A-B).

This coincided with an increase of necrotic phenotypes to 15% compared to 8% in matched controls but no significant change in the time of cell death or caspase-3 activation, although we noticed a trend to earlier caspase-3 activation (median difference ~105 min) and cell death (median difference ~60 min) in particular in 'shrunk' cells and is similar in all other inhibitors (Fig. 3.24E-H). This coincided with a delay of the occurrence of 'bleb' and 'shrunk-bleb' cells for all inhibitors relative to the control by 1-2 hours (median time to bleb: ctrl: 11.7 hours, iC2:

12.3 hours; 13.3 hours; iC9: 12.6 hours). Due to the limited number of cells and experiments, the significance of these trends remains to be confirmed.

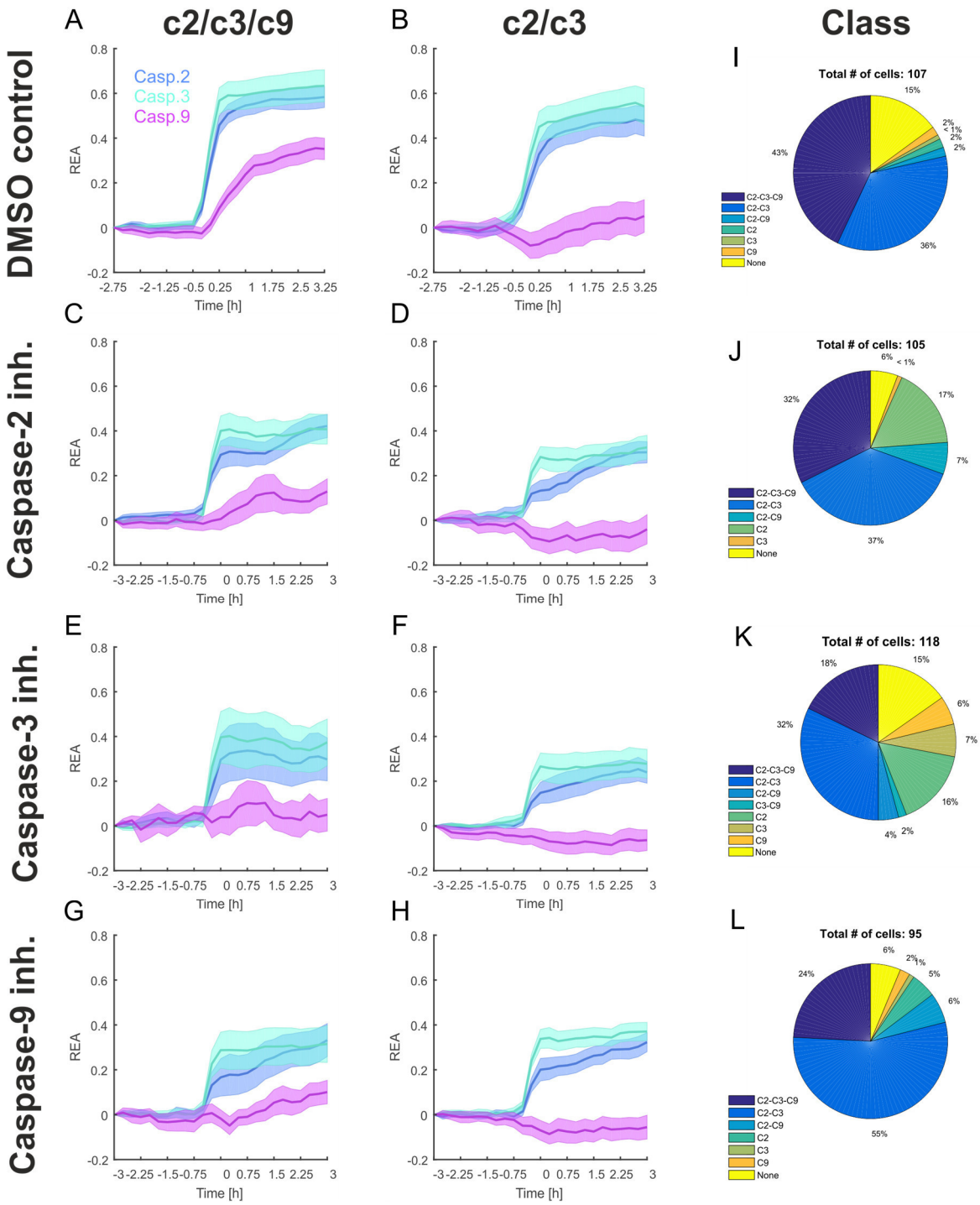

Figure 3.22 – **Caspase inhibition affects caspase dynamics and topology**

A-H: Relative enzymatic activity of caspase-2, -3 and -9 in HeLa-BAK cells treated with 100 µM Cisplatin. Cells were pre-treated for ~20 hours with 25 µM of caspase inhibitors (iC2: Z-VDVAD-FMK, iC3: Z-DEVD-FMK, iC9:

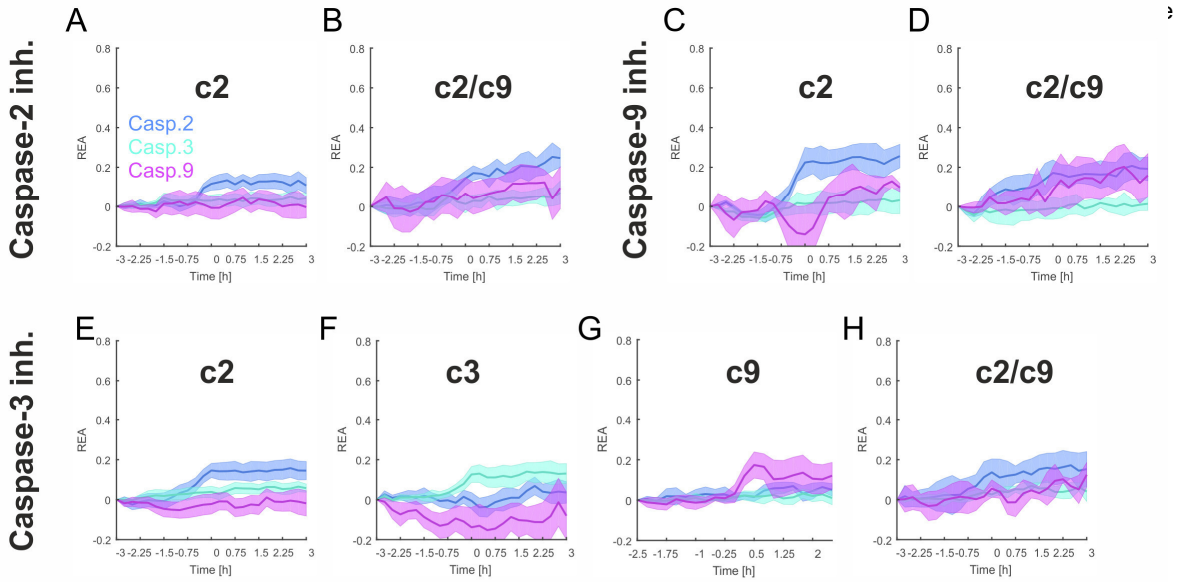

Figure 3.23 – **Dynamics of minor caspase response classes upon caspase inhibition**

The relative enzymatic activity of caspase-2, -3 and -9 in HeLa-BAK in indicated caspase response classes not shown in Fig. 3.22. Shown are synchronized, bootstrapped averages and confidence intervals for caspase response classes that contain ≥ 5% of cells. Number of cells per panel: 18, 7, 5, 6, 19, 8, 7, 5. Data from two independent experiments.

The caspase-3 inhibitor Z-DEVD-FMK led to an even stronger decrease in the prevalence of the c2/3/9-responsive phenotype (from 43% to 18%) and resulted in an increase in cells activating two or one caspases (Fig. 3.22E, F, K, 3.23E-F). Z-DEVD-FMK strongly increased the proportion of cells with a necrotic phenotype (8% to 29%) and is the only inhibitor that clearly increased the number of cells that do not show any death phenotype (5% to 10%; Fig. 3.24C).

The most prominent effects of caspase-9 inhibition with Z-LEHD-FMK is a pronounced shift from the c2/3/9-responsive population (43% to 24%) to the c2/9-only population (from 36% to 55%; Fig. 3.22J-L). It also increased the prevalence of cells that activate only caspase-2 or caspase-2 and -9 (Fig. 3.22G, H, L, 3.23C, D). Furthermore, the caspase-9 inhibitor increased the proportion of cells that die from a necrotic phenotype (8% to 25% of the total; Fig. 3.24D).

In summary, all caspase inhibitors resulted in a net decrease of all caspase activities in all populations (Fig. 3.22, 3.23) and increased the prevalence of populations that are rare or nonexistent in the unperturbed caspase network response (Fig. 3.24). Therefore, perturbation of a single caspase prevents efficient activation of the whole network. Moreover, all inhibitors

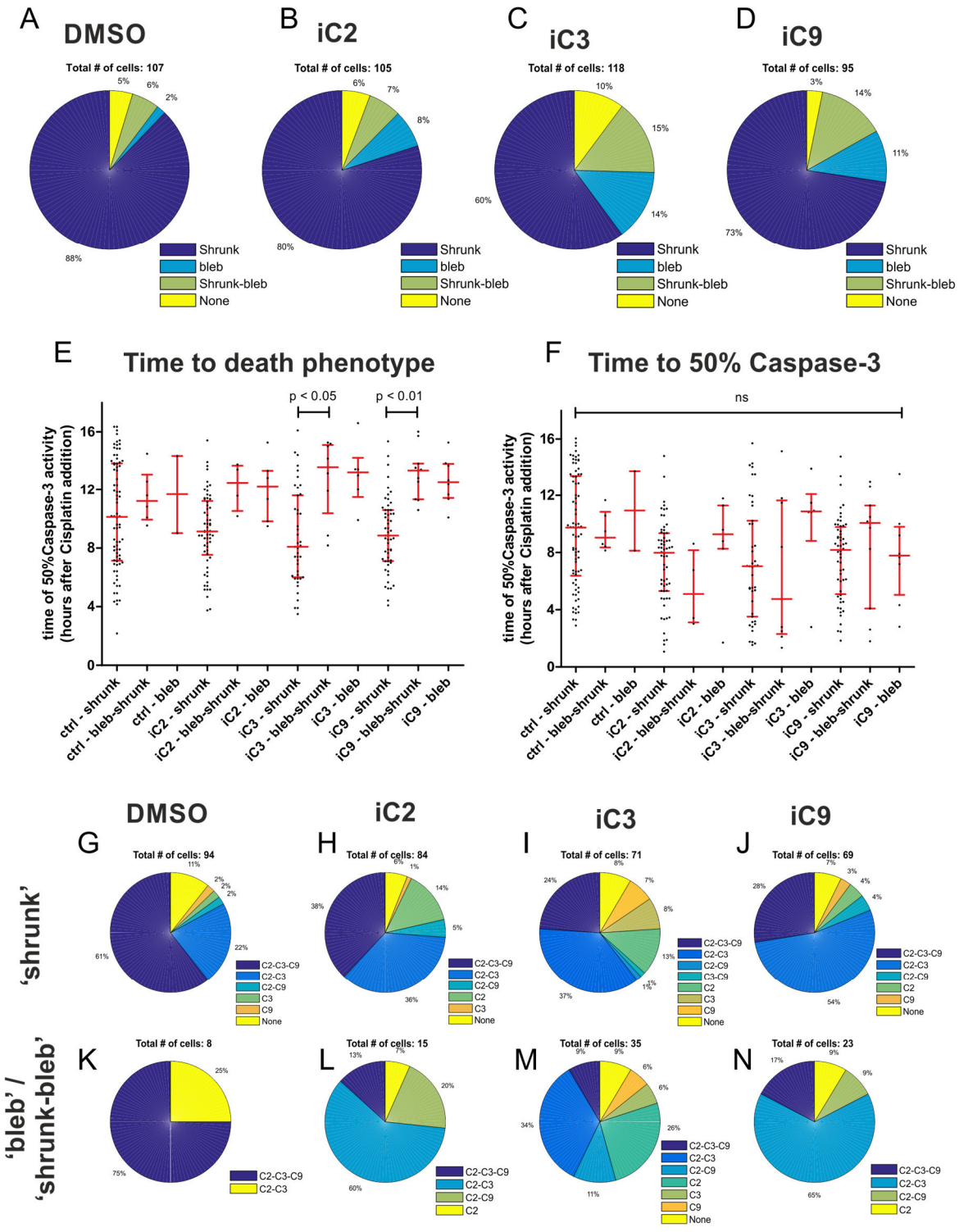

Figure 3.24 – **Effect of caspase inhibition on cell death timing and phenotype**

A-D: Prevalence of cell death phenotypes of HeLa-BAK cells treated with 100 µM Cisplatin and indicated caspase inhibitors as described in Fig. 3.22.

E-F: Time of the appearance of a death phenotype (E) or 50% caspase-3 activity (F) shown as a function of caspase inhibitors and classified by cell death phenotype. Shown are single cells and median and interquartile range are shown overlaid in red. Significance was tested using the Kruskal-Wallis Test followed by a Dunn's Multiple Comparison Test.

G-N: Prevalence of caspase response classes by death phenotypes and caspase inhibitors used.

Data is from the two independent experiments shown in Fig. 3.23.

showed a shift from apoptotic to necrotic cell death phenotypes (Fig. 3.24A-D). Compared to Cisplatin alone, caspase inhibition also strongly increased the proportion of cells not activating all three caspases in the population undergoing a necrotic cell death, whereas the effect among the apoptotic phenotypes was less pronounced (Fig. 3.24G-N). Collectively, these results confirm the existence of positive feedbacks, either direct or indirect, between caspases. When individual caspases are inhibited the resulting perturbed network is unable to trigger cell death efficiently resulting in a shift to necrotic forms of cell death.

Perturbation of caspase networks with clinically relevant inhibitors

If confirmed, the observation that changes in the caspase activation dynamics lead to a shift between different cell death types in a heterogeneous population could have profound implications for the treatment of cancer, where a rapid, apoptotic, inflammation-free cell death of all tumour cells is often considered beneficial (Crusz and Balkwill, 2015). We, therefore, used two sets of clinically relevant inhibitors to understand whether perturbation of the caspase dynamics allows us to shift cell death types.

Inhibition of IAP family proteins using LCL161

IAP family proteins (introduced in section 3.1.4) play a key role in controlling both extrinsic and intrinsic pathways of apoptosis by restraining the activity of key caspases either through direct inhibition of caspase-3, -7 and -9 (XIAP) or indirectly by affecting the stability of key factors in the pathway, including Smac/Diablo and caspase-3/-7 (Fulda and Vucic, 2012; Kocab and Duckett, 2016). IAPs are frequently overexpressed in human tumours and have been associated with the development of resistant and poor survival (Lopes et al., 2007; Nakagawa et al., 2006). To target IAPs for cancer treatment, a number of drugs are currently undergoing clinical trials alone and in combination with other agents including DNA damaging agents such as Cisplatin (Fulda, 2015). In response to Cisplatin and other DNA damaging drugs, expression of IAP family members cIAP1, cIAP2, XIAP and ML-IAP has been shown to be induced

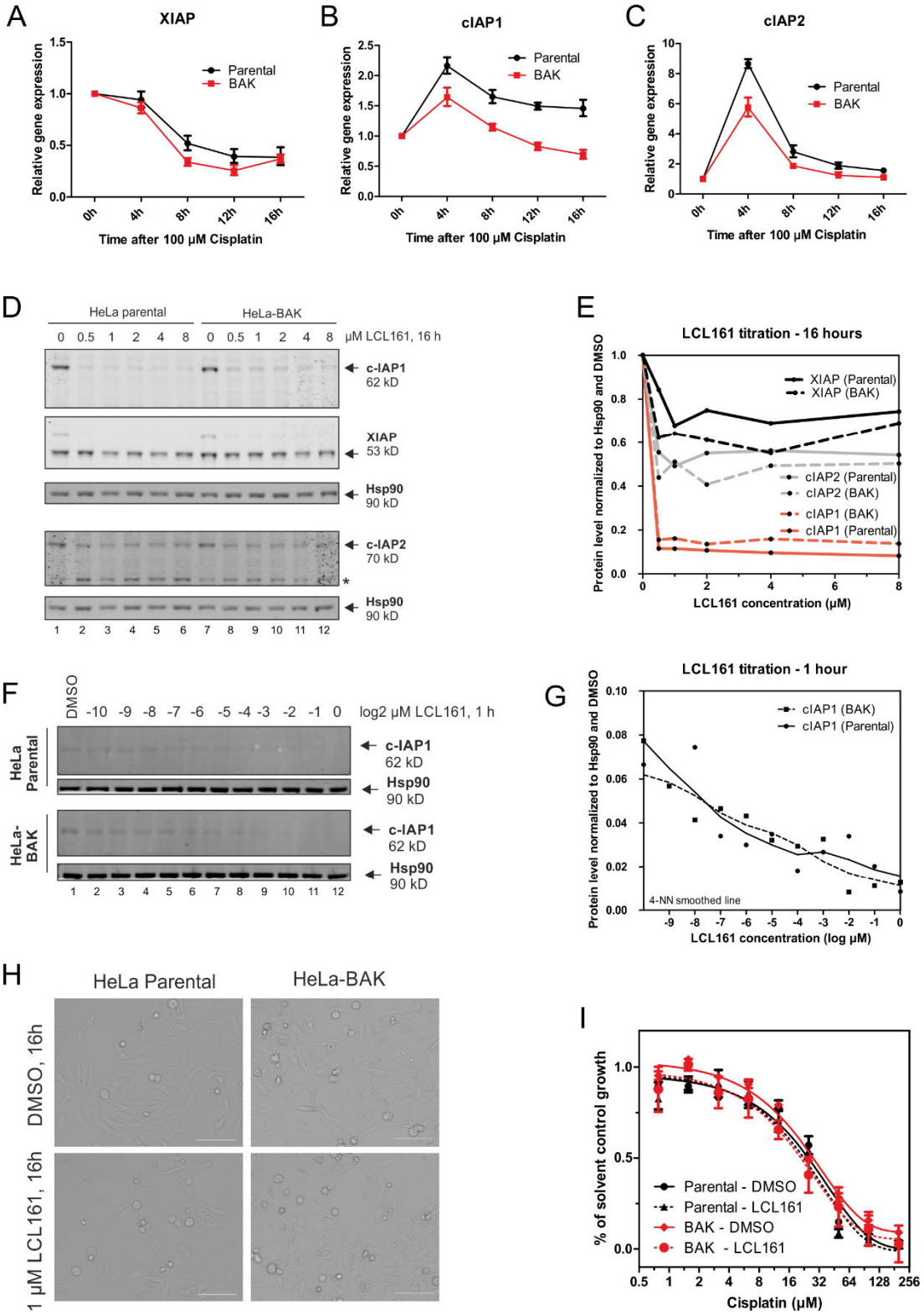
A
XIAP
Relative gene expression
Parental
BAK
Time after 100 µM Cisplatin
B
cIAP1
C
cIAP2
D
HeLa parental
HeLa-BAK
µM LCL161, 16 h
c-IAP1
62 kD
XIAP
53 kD
Hsp90
90 kD
c-IAP2
70 kD
E
LCL161 titration - 16 hours
Protein level normalized to Hsp90 and DMSO
XIAP (Parental)
XIAP (BAK)
cIAP2 (Parental)
cIAP2 (BAK)
cIAP1 (BAK)
cIAP1 (Parental)
LCL161 concentration (µM)
F
DMSO
log2 µM LCL161, 1 h
HeLa Parental
HeLa-BAK
G
LCL161 titration - 1 hour
4-NN smoothed line
LCL161 concentration (log µM)
H
HeLa Parental
HeLa-BAK
DMSO, 16h
1 µM LCL161, 16h
I
% of solvent control growth
Parental - DMSO
Parental - LCL161
BAK - DMSO
BAK - LCL161
Cisplatin (µM)

Figure 3.25 – **Validation of LCL161, a small molecule inhibitor of inhibitor of apoptosis (IAP) family proteins**

A-C: mRNA levels normalized to GAPDH of three IAP family proteins in response to treatment with 100 µM Cisplatin shown for parental HeLa and HeLa-BAK cells. Shown are mean with upper and lower limits of four independent experiments.

D, F: Parental HeLa and HeLa BAK were treated with indicated doses of LCL161 for 16 hours (D) or 1 hour (F) and lysates used for Western Blot. The asterisk indicates a reported non-specific band of unknown origin for c-IAP2 (Varfolomeev et al., 2007 and antibody data sheet).

E, G: Quantification of Western Blot in D and F.

H: Representative DIC images acquired with a BIO-RAD Zoe^{TM} imager for HeLa parental cells treated with 1 µM LCL161 or DMSO as solvent control for 16 hours.

I: Viability of parental HeLa and HeLa-BAK cells in response a 24-hour treatment with increasing doses of Cisplatin. Cells were pre-treated with 1 µM LCL161 or DMSO for 16 hours prior to addition of Cisplatin. DMSO samples are from same data as shown in Fig. 3.6I. Mean and standard deviation for technical replicates of one experiment are shown.

D-I: Data from a single experiment each for panels D-E, F-G, H and I.

(Altena et al., 2015; Duale et al., 2007; Hussner et al., 2012), suggesting a biological function to delay caspase activation to allow time for DNA repair and the integration of pro-survival signals. Accordingly, using one clinical IAP inhibitor, LCL161, Paek *et al*. showed that inhibition of IAPs lowers the apoptotic threshold permitting cells with lower p53 induction to die earlier (Paek et al., 2016). However, whether IAP inhibition affects caspase dynamics and the prevalence of different cell death types in combination with Cisplatin remains an open question.

We found that in parental HeLa cells and HeLa-BAK cells cIAP1 and cIAP2 transcription levels were upregulated transiently at 4 hours after Cisplatin addition (Fig. 3.25A-C), followed by a decrease of protein levels of cIAP1/2 and XIAP after 8 hours of Cisplatin treatment (Fig. 3.26A-D) confirming observations by Paek *et al* and others. Next, we determined the lowest – non-

lethal – effective dose of LCL161 that resulted in maximum degradation of cIAP1 and cIAP2, used previously as a marker for LCL161 effectiveness (Ramakrishnan et al., 2014) (Fig. 3.25D-H). By using such a low dose (1 µM), we could ensure that any change in cell death is due to the combination with Cisplatin, not LCL161 treatment alone. With Western Blot analyses, we showed that LCL161 substantially decreases cIAP1 and cIAP2 levels but – at the same time – LCL161 did not change the time course of IAP degradation and procaspase processing (Fig. 3.26). SRB viability assays also showed that LCL161 does not sensitize HeLa cells to Cisplatin at the chosen dose of 1µM (Fig. 3.25I). In summary, on a population-based level, low-dose IAP treatment appeared to have no discernible effect. We, therefore, asked next whether an effect could be visible at the single-cell level.

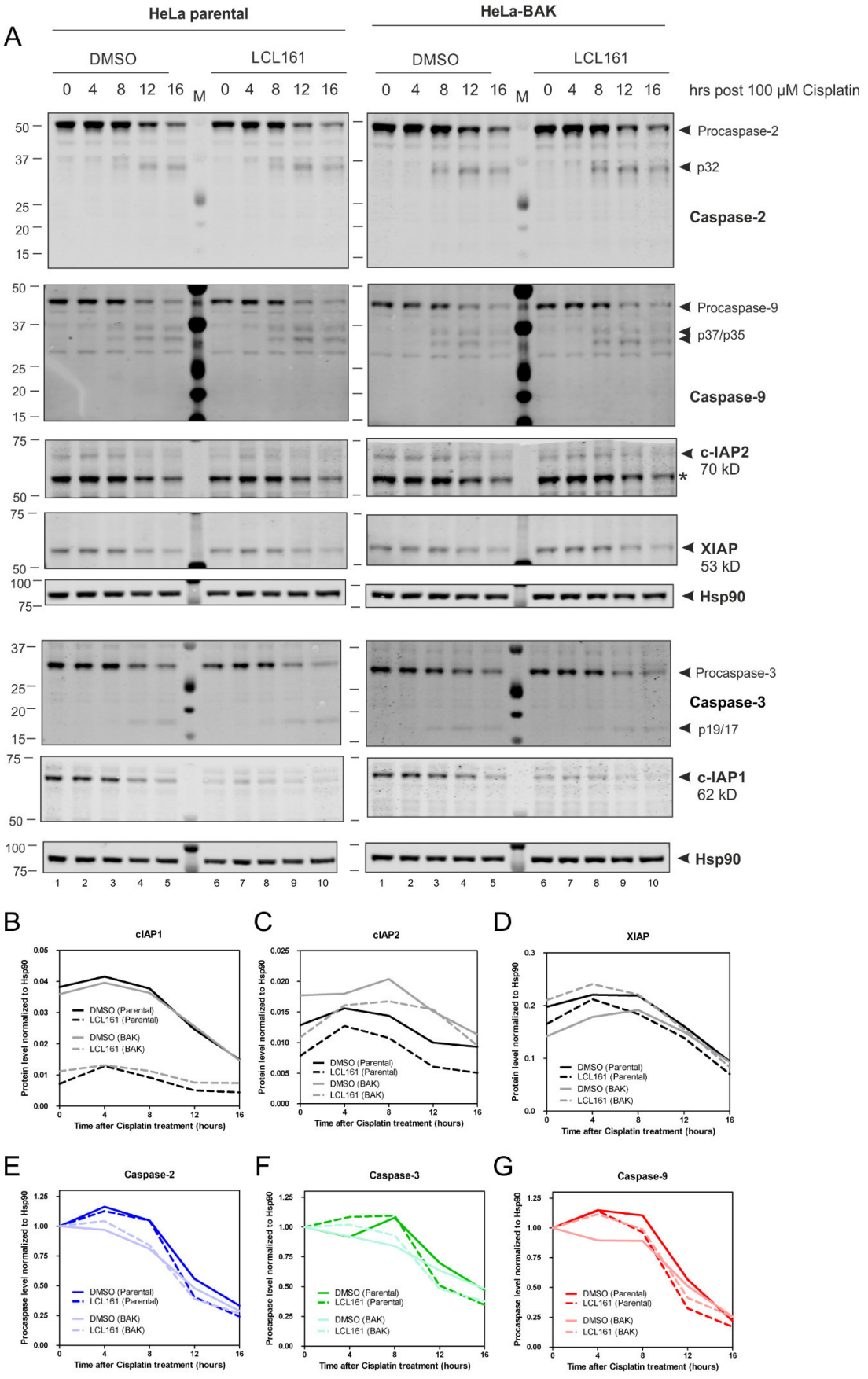
A
HeLa parental
HeLa-BAK
DMSO
LCL161
0 4 8 12 16 M 0 4 8 12 16
hrs post 100 µM Cisplatin
Procaspase-2
p32
Caspase-2
Procaspase-9
p37/p35
Caspase-9
c-IAP2
70 kD
XIAP
53 kD
Hsp90
Procaspase-3
Caspase-3
p19/17
c-IAP1
62 kD
Hsp90
1 2 3 4 5 6 7 8 9 10
B
cIAP1
C
cIAP2
D
XIAP
Protein level normalized to Hsp90
DMSO (Parental)
LCL161 (Parental)
DMSO (BAK)
LCL161 (BAK)
Time after Cisplatin treatment (hours)
E
Caspase-2
F
Caspase-3
G
Caspase-9
Procaspase level normalized to Hsp90

Figure 3.26 – **Effects of LCL161 on procaspase processing and IAP dynamics**

A: Western Blot of lysates from parental HeLa and HeLa-BAK cells treated with 100 µM Cisplatin and harvested at indicated time points. Cells were pre-treated with 1 µM LCL161 for 16 hours prior to Cisplatin addition. The asterisk indicates a reported non-specific band of unknown origin for c-IAP2 (Varfolomeev et al., 2007 and antibody data sheet).

B-G: Quantification of Western Blot in A for IAP (B-D) and procaspase (E-G) levels.

All data from a single experiment.

Thus, we performed multiplexed caspase-2/-3/-9 imaging using HeLa-BAK cells. Cells were pre-treated with LCL161 for 16 hours and we confirmed that prolonged exposure to LCL161 and time-lapse imaging in the absence of Cisplatin did not affect cell viability (Fig. 3.27A). At the single-cell level, low-dose LCL161 caused a decrease in the activation rate of caspase-2 and caspase-3 and the maximum REA (Fig. 3.27B, E and quantified in panel H-I). Additionally, the prevalence of the c2/3 population increased from a 19% found in matched controls to 29%

upon LCL161 treatment, an increase that is matched by a drop of the c2/c3/c9 population (Fig. 3.27D, G). These changes were also accompanied by a significant delay in the time of cell death (median time to death: 10.8 hours to 12.9 hours; Fig. 3.27J). The same trend was observed in the time of caspase-3 activation (Fig. 3.27K). This delay coincides with an increase in the prevalence of necrotic phenotypes (from <2% to 18%; Fig. 3.27L-M). However, when analysing the caspase response by phenotype in LCL161-treated cells, necrotic cells show no enrichment in non-c2/c3/c9 responses (Fig. 3.27N-O).

Taken together, these results suggest that the subtle caspase network perturbation by low, nontoxic doses of clinically relevant inhibitor results in a shift in cell fate from apoptosis to necrosis; these differences are invisible to population measurements, but are important, because the type of cell death can have a strong influence on treatment efficiency *in vivo*, by promoting or avoiding an inflammatory response (Crusz and Balkwill, 2015).

Since we could not demonstrate that the c2/c3 population is identical to the necrotic cells (Fig. 3.19) and necrotic cells were not always over-represented in non-c2/c3/c9 populations (Fig. 3.27N-O), we hypothesized that caspase-9 is dispensable for the execution of either death cell fate (apoptosis or necrosis) in HeLa cells; however, caspase-9 is required for a fast execution of cell death that in turn favour apoptosis over necrosis. When caspase-9 activity is reduced naturally in a population of cells or by perturbation of the caspase network through direct inhibition with caspase inhibitors (Fig. 3.23-25) or indirectly by inhibition of IAPs (Fig. 3.27), cells execute cell death slower and are thus more likely to die from necrosis.

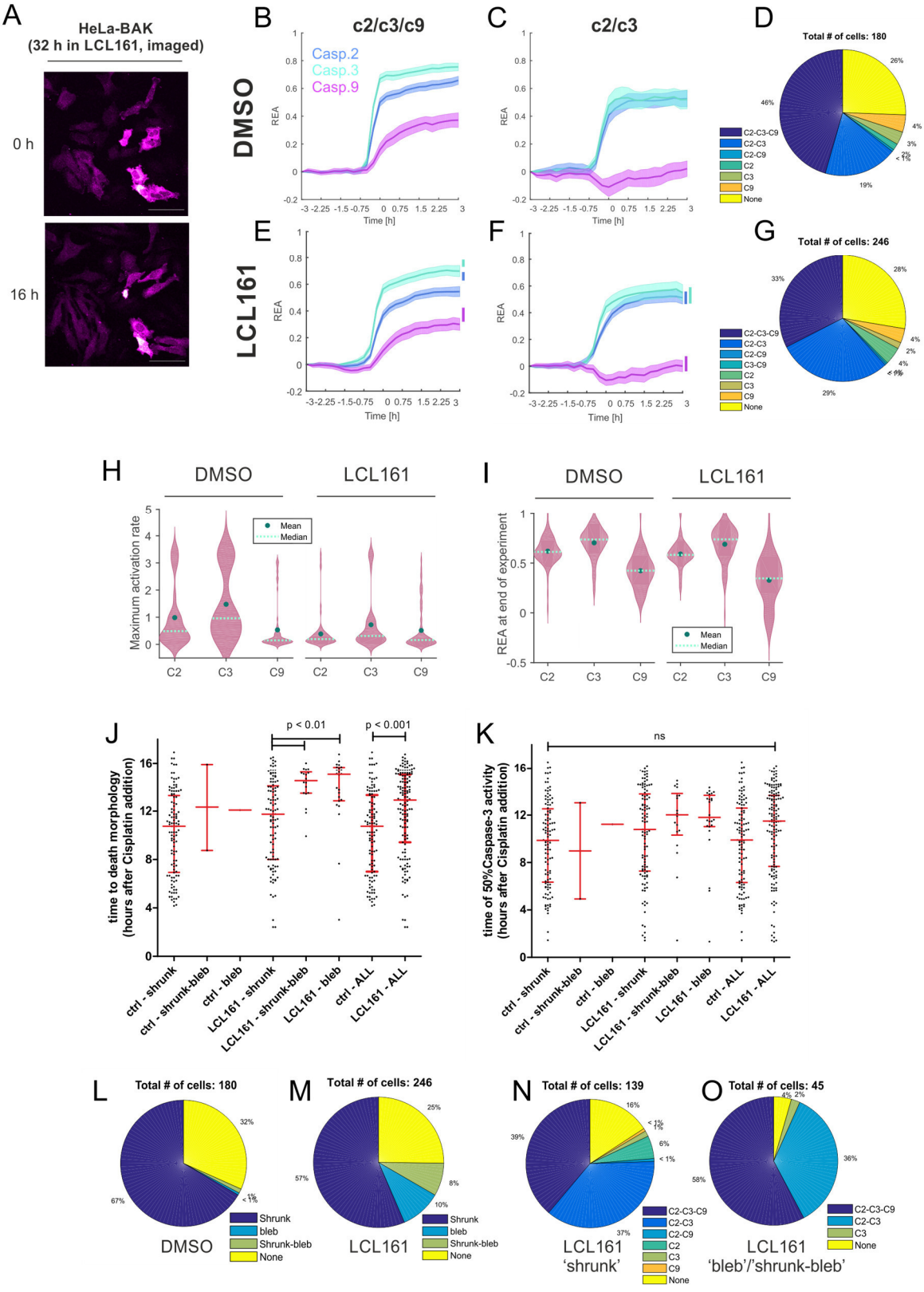
A
HeLa-BAK
(32 h in LCL161, imaged)
0 h
16 h
B
c2/c3/c9
DMSO
Casp.2
Casp.3
Casp.9
REA
Time [h]
C
c2/c3
D
Total # of cells: 180
C2-C3-C9
C2-C3
C2-C9
C2
C3
C9
None
E
LCL161
F
G
Total # of cells: 246
C3-C9
H
DMSO
LCL161
Maximum activation rate
Mean
Median
C2
C3
C9
I
REA at end of experiment
J
time to death morphology
(hours after Cisplatin addition)
p < 0.01
p < 0.001
ctrl - shrunk
ctrl - shrunk-bleb
ctrl - bleb
LCL161 - shrunk
LCL161 - shrunk-bleb
LCL161 - bleb
ctrl - ALL
LCL161 - ALL
K
time of 50%Caspase-3 activity
(hours after Cisplatin addition)
ns
L
Total # of cells: 180
DMSO
Shrunk
bleb
Shrunk-bleb
None
M
Total # of cells: 246
LCL161
N
Total # of cells: 139
LCL161
'shrunk'
O
Total # of cells: 45
LCL161
'bleb'/'shrunk-bleb'

Figure 3.27 – **IAP inhibition alters caspase dynamics, time and frequency of type of cell death in response to Cisplatin**

A: Representative images of HeLa-BAK cells treated with 1 µM LCL161 for a total of 32 hours before and after 16 hours of imaging of caspase dynamics. Scale bar is 50 µm.

B-C, E-F: Relative enzymatic activity of caspase-2, -3 and -9 in HeLa-BAK cells treated with 100 µM Cisplatin. Cells were pre-treated for ~16 hours with 1 µM of LCL161 (E-G) or DMSO (B-D). Shown are synchronized, bootstrapped averages and confidence intervals for two caspase response classes. Vertical bars in E-F indicate maximum REA of matched DMSO control in B-C for direct comparison.

D, G: Prevalence of caspase response classes for cells treated as B-C and E-F, respectively.

H-I: Distribution of maximum activation rate (H) and REA at the end of the experiment (I) calculated from sigmoidal fits for each caspase in the c2/c3/c9 response class only.

J-K: Time of the appearance of a death phenotype (J) or 50% caspase-3 activity (K) with or without LC161 and classified by cell death phenotypes. Shown are single cells with median and interquartile range overlaid in red. Significance was tested using the Kruskal-Wallis Test followed by a Dunn's Multiple Comparison Test.

L-M: Prevalence of cell death phenotypes in the absence (L) and presence (M) of LCL161 treatment.

N-O: Caspase response classes in the presence of LCL161 shown for 'shrunk' (N) and combined 'bleb'/'shrunk-bleb' cells.

Data from four independent experiments.

Inhibition of MEK and AKT kinases affects caspase dynamics and cell fate

To test this hypothesis, we decided to use a perturbation that would enhance caspase activation. If our hypothesis was correct, a perturbation of the network that leads to faster and higher caspase activation should exacerbate the apoptotic phenotype in contrast to necrosis.

The activity of caspases is regulated by a number of post-translational modifications including phosphorylation (Parrish et al., 2013). Among others, caspase-9 is inhibited through phosphorylation by ERK at Thr125 (Allan et al., 2003) and AKT kinases at Ser196 (Cardone et al., 1998).

In a pilot experiment, we used U0126, a MEK inhibitor which prevents ERK activation (Akinleye et al., 2013), and Afuresertib, a clinical-grade Akt inhibitor (Spencer et al., 2014), to derepress caspase-9 and accelerate cell death induced by Cisplatin. As for LCL161, we used doses that in the absence of Cisplatin did not affect viability (Fig. 3.28A-C) to attribute any changes in fate to the drug combination. We found that use of the inhibitors, either alone or in combination, resulted in an increased activity of all caspases as judged by the maximal REA values of each caspase with the effect being most pronounced in the c2/c3/c9 population when both inhibitors are used in combination, suggesting a synergism (Fig. 3.28D-K). Indeed, the synergism is demonstrated in the time of cell death and caspase-3 activation, where the combination, but not the single treatments, resulted in earlier death and caspase activation (Fig. 3.28T-U). Importantly, in support of our hypothesis, acceleration of cell death did not increase the

prevalence of the necrotic phenotype (Fig. 3.28P-S). Finally, no striking difference in the prevalence of the c2/c3/c9- and c2/c3- populations could be observed, suggesting that phosphorylation of caspase-9 by ERK and AKT is not responsible for determining caspase-9 activity in these populations (Fig. 3.28L-O). We acknowledge that these results are

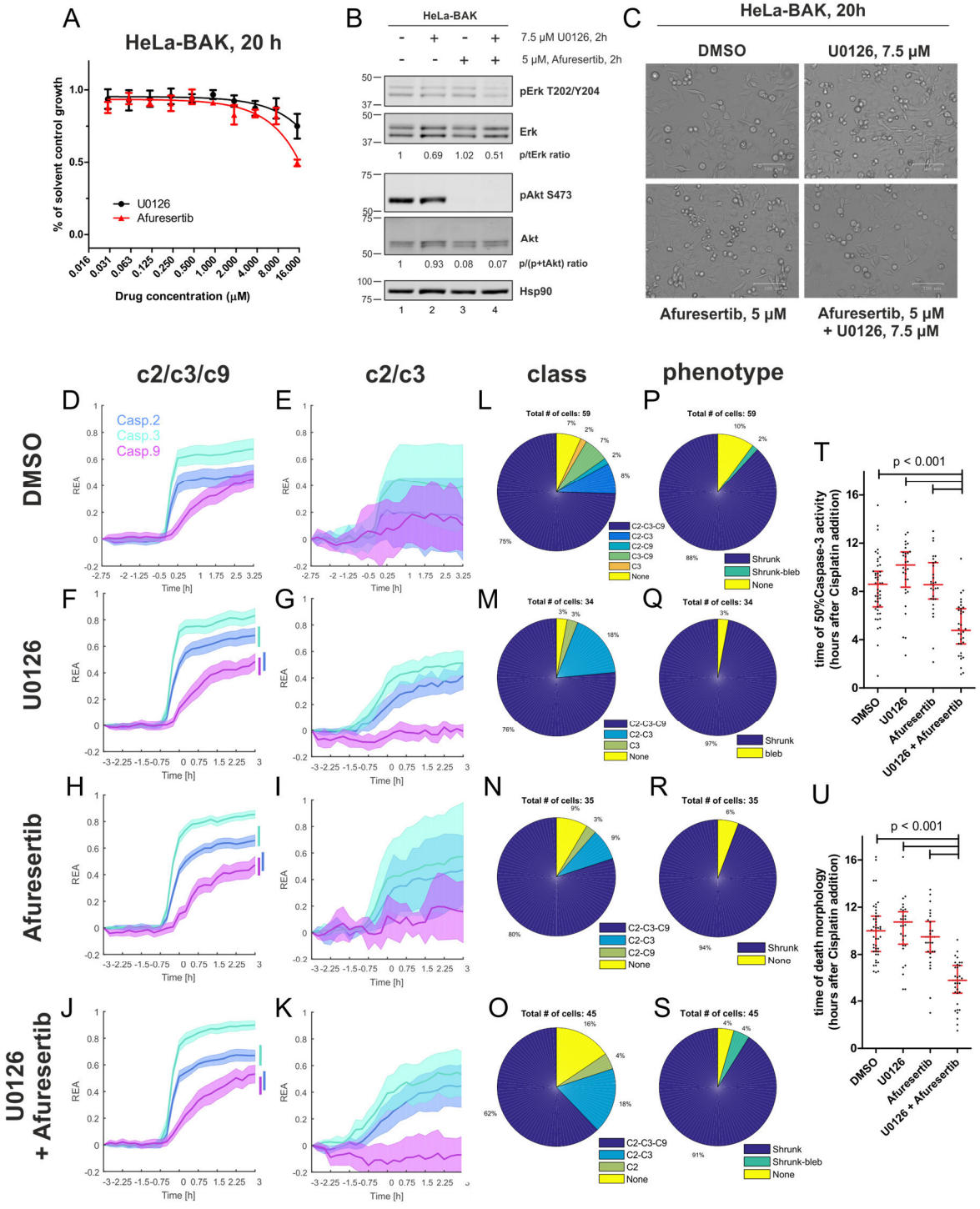

Figure 3.28 – **Inhibition of MEK and AKT kinases accelerates caspase dynamics and cell death**

A: Viability of HeLa-BAK cells treated for 20 hours with increasing doses of MEK inhibitor U0126 and AKT inhibitor Afuresertib.

B: Western Blot of lysates from HeLa-BAK cells treated with 7.5 µM U0126, 5 µM Afuresertib or both for 2 hours. The ratio between phosphorylated and unphosphorylated Erk and Akt is indicated relative to the vehicle control as a measure of pathway activation.

C: Representative DIC images of HeLa-BAK cells treated for 20 hours on the microscope stage with indicated inhibitors in the absence of Cisplatin. Images were acquired using a BIO-RAD Zoe^{TM} imager.

D-K: Relative enzymatic activity of caspase-2, -3 and -9 in HeLa-BAK cells treated with 100 µM Cisplatin. Cells were pre-treated for 2 hours with 7.5 µM U0126, 5 µM Afuresertib or both as indicated. For the c2/c3/c9 population, vertical bars indicate maximum REA of the matched DMSO control for direct comparison. Shown are synchronized, bootstrapped averages and confidence intervals for two caspase response classes.

L-O: Prevalence of caspase response classes for cells as treated in D-K.

P-S: Prevalence of cell death phenotypes for cells as treated in D-K.

T-U: Time of 50% caspase-3 activity (T) or the appearance of a death phenotype (U) for cells from all caspase response classes. Shown are single cells with median and interquartile range overlaid in red. Significance was tested using the Kruskal-Wallis Test followed by a Dunn's Multiple Comparison Test.

Data are from a single experiment each for panels A, B, C, and D-U.

preliminary and subject to high uncertainty owing to the small number of cells analysed, and require confirmation.

Still, if confirmed in further experiments, the effect of MEK and AKT inhibition supports the hypothesis that the dynamics of the caspase network is critical to determine a balance between apoptosis and necrosis. The activation of caspases is heterogeneous in time and typology. However, when caspases are activated, cell death will occur, but the longer a cell spends to trigger apoptosis, the more likely it will die from necrosis or survive. Clinical interventions should be therefore designed not just to trigger cell death, but to act on caspase network dynamics to unleash a prompt apoptotic response.

3.4 Discussion

Non-genetic heterogeneity of genetically identical tumour cells is an emerging concept underlying early oncogenesis, progression and treatment of cancers (Almendro et al., 2013; Caiado et al., 2016; Liang et al., 2014). In this work, we focussed on the role of non-genetic heterogeneity in response to the clinical DNA-damaging drug Cisplatin. In the first instance, non-genetic heterogeneity to Cisplatin treatment leads to so-called 'fractional killing', where only a fraction of cells are killed, an effect that can be determined by cell-to-cell variation in p53 dynamics (Berndtsson et al., 2007; Paek et al., 2016). Moreover, cells can trigger different

cell death programs such as apoptosis, necrosis and a plethora of different other death subtypes (Montero et al., 2002; Pestell et al., 2000; Segal-Bendirdjian and Jacquemin-Sablon, 1995) with implications for the overall effectiveness of treatment. Mechanistic insights into non-genetic heterogeneity in response to chemotherapeutic drugs are scant and better models describing cell fate choices are necessary. Better models will eventually permit to design chemical interventions in order to maximize the desired phenotypic output, including avoiding fractional killing and triggering more desirable cell death programmes, aiming to optimize the efficiency of treatment.

Caspases mediate the response to Cisplatin treatment

Studies comparing genetically distinct cell lines that are resistant or sensitive to Cisplatin have suggested caspases as key factors in the response to drug treatment. Resistant cells do not activate specific caspases or caspases in general in response to Cisplatin (Kuwahara et al., 2003; Liu et al., 2002; Mueller et al., 2003; Vakifahmetoglu et al., 2008) and show an increase in necrotic phenotype (Vakifahmetoglu et al., 2008). In genetically identical cells, heterogeneity with respect to timing and dynamics of individual caspases has been described (Spencer et al., 2009; Tyas et al., 2000) as well. However whether non-genetic heterogeneity in the dynamics of the network of caspases contributes to the response to Cisplatin is broadly uncharacterized because of lack of suitable single-cell assays, a limitation we have now overcome. Most previous work on caspases studied as an interconnected network of enzymes has been done by ensemble measurements and lacked the spatio-temporal resolution to study cell-to-cell variability.

Using our novel three-colour multiplexing platform, we could show for the first time that heterogeneity in the dynamics and network topology of caspase-2, -3 and -9 determines timing

and type of cell death in a clonal population. Cells with insufficient activation of the caspase network die later suggesting an increased tolerance to Cisplatin. Such cells also showed an increased prevalence of necrotic cell death. Crucially, targeted perturbation of the caspase network using low doses of clinical inhibitors of IAP proteins, MAPK pathway and AKT kinase permitted us to alter the timing and cell fate after Cisplatin treatment highlighting the importance of single-cell biochemical measurements in designing cancer treatments. The dynamics and heterogeneity of the biochemical networks driving the phenotypes that drugs are aimed to trigger or to target should be regarded as actionable targets in their own virtue.

3.4.1 Deconvolution of subpopulation in caspase dynamics

A key finding of this work is the existence of three major populations of cells with distinct caspase activation order, dynamics and time of cell death (Fig. 3.29A-B). One population activates all caspase-2, -3 and- 9 (‘c2/c3/c9-population’), and one lacks caspase-9 activation and triggers cell death on average 2.5 hours later (‘c2/c3-population’). We also found a population of cells that do not activate any caspase, of which one-third dies with a delay similar to the c2/c3-population. Two-thirds of the cells that do not activate caspases survive until the end of the 16-hour-experiment we performed, suggesting a significant presence of fractional killing as reported previously (Berndtsson et al., 2007; Paek et al., 2016).

Identification of a putative caspase-2 and caspase-3 feedback loop

The two populations that activate caspases have in common that caspase-3 activation appears to be upstream of MOMP as well as caspase-9 activation. In the c2/c3/c9 population, caspase-3 activation appears near simultaneous with caspase-2, while in the c2/c3 population, caspase-3 precedes caspase-2 activation by ~10 min (Fig. 3.12H). The large number of cells measured for both populations (315 and 119, respectively) and the high reproducibility across the 12 experiments analysed for this quantification provided high confidence about the relative timings of caspase-2 and -3.

Mechanistically, the near-simultaneous activation of caspase-2 and -3 suggests the existence of a positive feedback loop that increases the levels of active caspases rapidly, resulting in bistable dynamics. While a feedback from caspase-3 to caspase-2 has been previously shown *in vitro* and in cells (Van de Craen et al., 1999; Inoue et al., 2009), a caspase-2-mediated processing of caspase-3 has so far not been reported, although hinted to (Puccini et al., 2013b). However, caspase-2 cleaves substrates containing the IETD motif present in

procaspase-3 *in vitro* (Thornberry et al., 1997) and early unpublished studies have shown that caspase-2 exhibits procaspase-3 processing capabilities *in vitro* (Sharad Kumar, personal communication).

This possibility has been perhaps dismissed because of the limited specificity of the sensor constructs for the respective caspases. However, we observed a delayed caspase-2 response in c2/c3 cells and identify cells that only show activation of an individual caspase sensor, suggesting specificity (both in the absence (Fig. 3.12) and presence of caspase inhibitors (Fig. 3.23)). These observations are possible only by biochemical multiplexing in living cells;

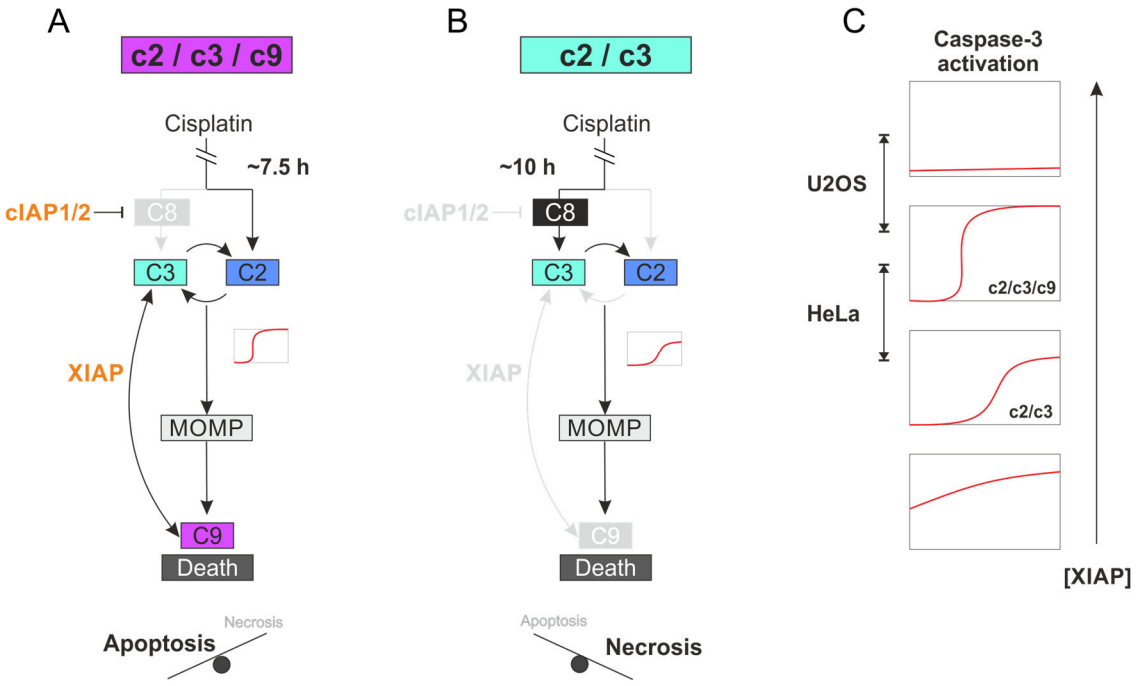

Figure 3.29 – **Hypothetical model of caspase dynamics and cell fate in response to Cisplatin**

A: In the c2/c3/c9 population caspase activation is predominantly triggered via activation of caspase-2 which activates caspase-3 thereby initiating a feedback loop. Both caspase-2 and -3 cleave BID to induce MOMP leading to initial caspase-9 activation. Caspase-3 can process caspase-9 from the lower to higher activity form which then enhances caspase-3 activity in a feedback loop. Caspase-9 activity is further enhanced by an implicit XIAP-mediated feedback loop where active caspase-3 sequesters XIAP away from caspase-9. Together, this results in a switch-like activation of caspase-3 (graph inset).

B: In c2/c3 cells, low levels of cIAP1/2 promote late caspase-3 activation via caspase-8, which subsequently activates caspase-2. This activation is insufficient to trigger the caspase-2/-3 feedback loop and results in sub-optimal activation of caspase-3 which is not sufficient to process caspase-9 into its high-activity form, thus, interrupting the caspase-9/-3 feedback loop. Additionally, XIAP levels are insufficient to effect caspase-9 activity through the caspase-3 to -9-arm of the feedback loop. Together, these changes result in a shift of caspase-3 activity to a more gradual and subdued response (graph inset).

C: Model of the effect of XIAP expression levels on caspase dynamics based on the models by Legewie et al. (2006) and Schmid et al. (2013). Very low levels lead to spontaneous caspase activation, while very high levels prevent caspase activation completely. High intermediate levels allow an efficient and fast activation of caspase-3, as observed in the c2/c3/c9 population, while at a lower level, the XIAP-mediated feedback loop is abrogated, resulting in shallower and less efficient caspase-3 activation. Based on our experimental results, the difference between HeLa and U2OS could be due to different XIAP expression levels as indicated.

therefore, it has not been possible to evaluate the specificity of substrates in the cell until now. Taken together, our data suggest that the optimized motifs, thoroughly discussed in Chapter 2 of this dissertation, have sufficient specificity to discern the activities of different caspases.

In c2/c3 cells (Fig. 3.29B), the delay between caspase-3 and -2 suggests that the putative feedback loop between caspase-2 and-3 is less efficient or inactive. Indeed, we observed a

decrease in maximal enzymatic activity and activation rate (Fig. 3.12) indicating a sub-optimal caspase-2 and -3 activation. Thus, the proposed feedback loop appears necessary for an optimal caspase activation. Two non-mutually exclusive mechanisms might explain the deregulation of a feedback loop in c2/c3 cells. First, we will discuss how a change in the upstream mechanism leading to triggering caspase-3 could affect the loop, and, second, investigate the role of caspase-9.

A switch from caspase-2- to caspase-8-induced network in c2/c3 cells could affect caspase dynamics and time of cell death

Processing and activation of caspase-3 depend on caspase-8 and caspase-9 activities (Van de Craen et al., 1999), or — as we suggest in this study — on the activity of caspase-2. A direct activation of caspase-3 in the absence of either of these three initiator caspases in response to DNA damage has not been observed so far. We therefore hypothesized that in c2/c3/c9 cells, caspase-2 is activated slightly before caspase-3, at a time difference below our time resolution, through mechanisms that have been shown to activate caspase-2 directly in response to DNA damage, including the formation of the PIDDosome (Ando et al., 2012) or PIDDosome-independent mechanisms (Manzl et al., 2009; Olsson et al., 2009, 2014; Vakifahmetoglu et al., 2006). Caspase-2 then activates caspase-3 through processing forming the suggested feedback loop leading to efficient, switch-like caspase activation. While the small time difference between caspase-2 and -3 argues for a direct mechanism, at this stage, we cannot exclude any indirect mechanisms involving additional proteins.

In contrast, in c2/c3 cells, caspase-2 is activated downstream of caspase-3. With caspase-9 not activated, caspase-8 remains the only candidate for caspase-3 activation in those cells. Indeed, we provided some preliminary support for a role of caspase-8 upstream of caspase-3 in a population of cells that trigger caspase-3 activity later (Fig. 3.16). The ~25 min delay of full caspase-8 activation relative to caspase-3 is in line with previous single-cell studies (Kawai et al., 2005) and likely due to the amplification loop between caspase-3 and -8 (Viswanath et al., 2001). Experiments to study caspase-8, -3 and -9 simultaneously are currently ongoing to confirm that the cells with early caspase-8 activation are identical to the c2/c3-population. If confirmed, a caspase-8-mediated pathway in c2/c3 cells could also explain the subdued caspase-3/-2 response, possibly because the described feedback loop is insufficiently induced when caspase-3 is triggered by caspase-8 and not by caspase-2. However, we are not aware of any experimental reports that directly compare the efficiency of the caspase-2 and caspase-8-mediated caspase response. Notably, caspase-8 has been shown to activate caspase-2 in

response to DNA damage using Western Blot (Olsson et al., 2009), but our data so far suggest that caspase-3 is the preferential target for caspase-8 processing. Imaging caspase-2, -3 and -8 together using our platform will allow us to address their relative timing at a single-cell level. The relevant experiments are currently in preparation. On a further note, the cause for a switch from caspase-2 to caspase-8-mediated caspase-3 activation remains an open question. In a later section, we will discuss how IAP family proteins could be involved in this mechanism.

Apart from being a possible explanation for the deregulation of the putative caspase-2/-3 feedback loop, the activation of caspase-3 via caspase-8 in c2/c3 cells could also explain the ~2.5 hours delay of caspase activation compared to c2/c3/c9 cells. Caspase-8 activation requires *de novo* expression of FAS ligand to induce the formation of the caspase-8-activating DISC complex which requires at least several hours (Brozovic et al., 2004; Micheau et al., 1997; Müller et al., 1998). In contrast, factors crucial for caspase-2 activation including the PIDDosome are generally considered to be constitutively expressed and quickly activated in response to DNA damage (Ando et al., 2012). Inhibition of *de novo* protein synthesis with Cycloheximide would allow testing this hypothesis experimentally.

In summary, we showed evidence that caspase-2 and -3 are activated upstream of caspase-9 activation in Cisplatin-treated HeLa cells and suggest a positive feedback loop that is required for complete and fast caspase activation. In a population of cells, characterized by the absence of caspase-9 activation, cell death is delayed by ~2.5 hours possibly because of a caspase-8-dependent activation. Next, I will discuss the role of caspase-9.

Caspase-9 could promote caspase-3 activation in a second feedback loop

The c2/c3/c9 and c2/c3 populations are not only characterized by the differences in caspase-2/-3 dynamics but crucially by the presence or absence of caspase-9 activation (Fig. 3.29A-B). In the former population, caspase-9 is consistently activated ~25 min after caspase-2 and -3. Notably, the delay between caspase-3 activation and the occurrence of a death phenotype is about 22 minutes. In independent experiments, we estimated the delay between cell shrinkage and MOMP to about 17 minutes. These measurements and the canonical model for caspase-9 activation suggest that caspase-9 acts downstream of MOMP and slightly precedes the dramatic morphological changes occurring during apoptosis (Fig. 3.29A). Caspase-9 is activated by CYTC aiding apoptosome assembly (Rodriguez and Lazebnik, 1999) when, after MOMP, CYTC translocates to the cytoplasm. The primary role of caspase-

9 is thought to activate caspase-3 (Galluzzi et al., 2012); however, our data suggest that caspase-3 is active before caspase-9, probably even before the occurrence of MOMP. Therefore, caspase-9 seems to be dispensable for caspase-3 activation. However, those cells that robustly trigger caspase-9 activated caspase-3 early and at higher rates, suggesting that the known caspase-3 – caspase-9 feedback loop (Blanc et al., 2000; Lakhani et al., 2006; Wu et al., 2016) is dispensable during Cisplatin response in HeLa cells, but is crucial for a fast response. This notion is supported by the observation that caspase-9 activation occurs at a time before caspase-3 reaches its maximum activity, suggesting that caspase-9 activity is required for full caspase-3 activation (Fig. 3.12A), which in turn could be required for the caspase-2/-3 loop discussed earlier.

Importantly, a loop between caspase-3 and caspase-9 could also explain the apparent lack of caspase-9 activation in the c2/c3 population. Caspase-9 exhibits two activity states *in vitro*, an early moderate activation followed by a later high activity state promoted by caspase-3 cleavage (Wu et al., 2016). Thus, for full activation caspase-9 requires caspase-3 processing. In c2/c3 cells, the reduced caspase-3 activation could be insufficient to process caspase-9, which therefore remains in the moderate activity form. This lower activity could be below the detection limit of the caspase-9 sensor in analogy to what we and others have observed for caspase-8 (Fig. 3.16; Albeck et al., 2008), leading to an apparent lack of caspase-9 activation in this population. Clearly, this poses the question what comes first, the insufficient activation of caspase-3 that leads to a low caspase-9 activity, or a low caspase-9 activity that leads to insufficient caspase-3 activation. We are carrying out experiments addressing this question using a caspase-9 sensor with a double substrate as for the caspase-8 experiments.

However, whether caspase-9 is working upstream of caspase-3 or not, our data incontrovertibly demonstrate the existence of non-genetic heterogeneity in caspase-9 activation. In some cells, caspase-9 contribute to a prompt apoptotic response, in others, the caspase-9 is not prominent and the activation of all caspases is reduced.

Lack of caspase-9 has no clear effect on time from caspase-3 activation to cell death

Interestingly, the reduction of caspase-2 and -3 activities in c2/c3 cells relative to the c2/c3/c9 population seems to have limited effect on the lag-time between caspase-3 activation and the onset of cell shrinkage. This surrogate measure for the speed of the execution of cell death was estimated at ~25 min in both populations (Fig. 3.19K). This suggests that once caspase-3 is activated apoptosis is executed efficiently and independently of caspase-9.

This observation also raises the more general question whether the lack of caspase-9 is the cause for the characteristic delay of the c2/c3 population. While the lack of caspase-9 activation is a striking marker of the c2/c3 population and possibly affects the efficiency of caspase activity in a feedback loop, its activation after caspase-2 and -3 argues that it cannot be a causal mechanism for the delay of the initial caspase induction and cell death. Also, the shift from caspase-2 to caspase-8 discussed above appears to be a good explanation for the delay in cell death. Together, this suggests that both the lack of caspase-9 activation as well as the shift to a delayed, caspase-8 mediated caspase network, could be the result of a common mechanism. Therefore, caspase-9 could, in our experiments, function as a marker for the identification of this mechanism, whose discovery could aid rational design of treatments to alter cell fate in response to DNA-damage.

3.4.2 IAP family proteins as a common mechanism for caspase-9 inhibition and delay in cell death

Therefore, we studied several candidates for the mechanism of caspase-9 inhibition. As we have established a new, formerly untested, technique, we also invested significant time in excluding possible sources of artefacts. However, different FRET pairs (Fig. 3.13) and cell lines (HeLa parental with transient transfection (Fig. 3.13), HeLa-BAK (Fig. 3.12) and U2OS (Fig. 3.21)) all confirmed the delay between caspase-3 and caspase-9 upon treatment with Cisplatin. Interestingly, in U2OS the c2/c3 population was negligible suggesting inter-cell line variability in the underlying mechanism as we will discuss below.

Next, we tested the hypothesis that inhibition of caspase-9 activation is dependent on cell cycle as CDK-dependent mechanisms of caspase inhibitions are known and cell cycle is a common source of non-genetic heterogeneity. We show that there is no cell cycle dependency in the phenotypes observed (Fig. 3.15). We also tested the possibility that partial MOMP (Ichim et al., 2015) in a subpopulation of cells could cause the observed heterogeneity. However, all dying cells execute MOMP efficiently (Fig. 3.14).

We also used two inhibitors against MEK and AKT, kinases that are known to inhibit caspase-9. Interestingly, MEK and AKT inhibitors combined do increase caspase-9 activity significantly resulting in a faster apoptotic response. However, these inhibitors failed to abrogate the c2/c3 population, suggesting that MAPK and PI3K pathway activities do not cause the heterogeneity in caspase-9 activation we have observed (Fig. 3.28).

IAP family proteins as key candidates to set caspase dynamics and cell fate

However, when using LCL161 to inhibit IAPs, the prevalence of the c2/c3-population increased significantly. The corollary to this observation is that, paradoxically, the inhibitory IAPs promote caspase-9 activation in untreated HeLa cells. At the same time, the activation rate and maximum activity were reduced for all caspases when IAPs are inhibited (Fig. 3.27) also in the c2/3/9 population. This apparently paradoxical observation is in agreement with a model for XIAP-mediated feedback loop with caspase-3 proposed by Legewie and colleagues (Legewie et al., 2006; Schmid et al., 2012). When XIAP expression is very low, caspase-3 activation occurs spontaneously in the absence of a pro-apoptotic stimulus, a phenomenon we did not observe (Legewie et al., 2006; Fig. 3.29C). However, intermediate levels of XIAPs interfere with caspase-3/-9 positive feedback loop resulting in a shallower, less efficient, response of the proteases. With increasing XIAP levels, the activation of caspase-3 becomes sharper and more efficient up to a point where all caspase activity is inhibited (Fig. 3.29C). Our experimental results are coherent with these predictions. Therefore, this model would also predict that cell-to-cell variability in XIAP expression or activity would alter caspase-9 activity and the overall dynamics of the caspase network.

Moreover, variation in the expression or activity of two other IAPs might play a similar role in the time of onset of caspase activation and subsequent cell death. cIAP1 and 2 inhibit the formation of a version of the caspase-8 activating DISC complex (Petersen et al., 2007; Varfolomeev et al., 2007b; Vince et al., 2007). Accordingly, in recent studies, LCL161 treatment was shown to promote caspase-8-mediated cell death (Qin et al., 2014; Yang et al., 2016). Pending confirmation of our preliminary results that identify caspase-8 as the apical caspase in the c2/c3 population, LCL161 would increase this caspase-9-negative population as observed here.

Interestingly, a recent study suggested a differential role for IAPs in caspase-8-dependent or independent apoptosis in response to Cisplatin (Paek et al., 2016). In HCT116 treated with Cisplatin, cIAP1/2 inhibit caspase-8 dependent apoptosis, whereas XIAP and MLIAP inhibit caspase-8 independent apoptosis, and together they appear to set a threshold for p53 activation to induce the respective type of apoptosis. This study was limited to the imaging of p53 dynamics of single cells and did not provide single-cell information about caspase network or IAPs dynamics; however, this work suggests that the complex interactions of the IAPs with the apoptotic machinery can have a profound effect on cell fate choices in response to DNA damage. In support of a differential role for IAPs in fine-tuning the caspase response, we

observed that cIAP1/2, but not XIAP, are induced transcriptionally at an early time point (Fig. 3.25). This difference in the IAPs dynamics could delay the caspase-8 dependent pathway facilitating early apoptosis by caspase-8-independent mechanisms in the absence of LCL161.

In summary, we can speculate that the c2/c3 population might be characterized by low levels of IAPs, where low XIAP results in a less efficient caspase-9/-3 activation feedback loop and a subdued caspase response, while low levels of cIAP1/2 might promote caspase-8 dependent apoptosis with a lag-time relative to the c2/c3/c9-population (Fig. 3.29).

Monitoring and modulating IAP levels could elucidate their role at a single-cell level

The direct experimental falsification of the hypothesis that cell-to-cell variability in IAPs causes the heterogeneity in caspase dynamics and cell death timing we observed would require single-cell measurements of IAP expression. As the level of multiplexing we have achieved was already unprecedented, we could not directly test this hypothesis with fluorescence-based assays run simultaneously with the multiplexing of caspase activities. Furthermore, IAP measurements in live cells would ideally be done by labelling IAPs at the endogenous gene locus using gene editing such as CRISPR/Cas9 in order to not inhibit caspases with ectopic expression of IAPs.

Finally, U2OS cells did not exhibit a substantial c2/c3 population. We are therefore evaluating XIAP expression levels of the two cell lines and its heterogeneity in expression with flow cytometry to test if XIAP heterogeneity alone could explain the different phenotypes we observed. If our model was of more general validity, siRNA-mediated knockdown of XIAP or treatment with LCL161 should shift U2OS cells to a more HeLa-like phenotype, including an increase in the c2/c3 population and a decrease in the caspase dynamics (Fig. 3.29C).

In summary, simultaneous monitoring of three caspases in response to Cisplatin allowed us to identify two populations with distinct caspase dynamics and time of cell death. Direct single-cell measurements of cascades of caspases suggest a shift from caspase-2 to caspase-8-mediated induction of the caspase network plausibly determined by differential activities of IAP family proteins. Furthermore, caspase-2 or caspase-9 have been both described as apical caspases in response to DNA damage (Tab. 3.1), but our results clearly suggest a role for caspase-2 upstream of caspase-9 in Cisplatin-treated HeLa cells (in line with Lassus et al., 2002; Olsson et al., 2009; Robertson et al., 2002; Vakifahmetoglu et al., 2008). Next, we aimed to understand whether the observed differences in caspase dynamics not only determine the

time of cell death but also the type of programmed cell death (e.g., apoptosis or necrosis) triggered.

3.4.3 Heterogeneity in the type of cell death

Cisplatin-treated HeLa cells show a continuum of apoptotic and necrotic cell death

We confirmed that genetically identical cells can trigger both apoptotic and necrotic cell death in response to Cisplatin as observed by others (Montero et al., 2002; Pestell et al., 2000; Segal-Bendirdjian and Jacquemin-Sablon, 1995). For simplicity, we classified three phenotypes, ‘shrunk’, ‘bleb’ and ‘shrunk-bleb’ that exhibited classical morphological characteristics of apoptosis, necrosis or both, respectively (Fig. 3.17). However, the classification was not unambiguous and required blind marking from different scientists. The presence of intermediate phenotypes suggests a continuum of cell death phenotypes, rather than the existence of very precise cell categories. With Annexin-V/7AAD co-staining we confirmed the coincidence between the ‘shrunk’ and ‘bleb’ scored cells as apoptotic and necrotic, respectively (Fig. 3.17), and with ‘shrunk-bleb’ cells potentially being necrotic. Nonetheless, we note that there is likely overlap between the classes and in particular regarding the ‘shrunk-bleb’ phenotype that consistently shows intermediate characteristics.

Identification of the type of necrotic cell death in response to Cisplatin

A large number of different types of necrotic cell death types have been described in the literature (Berghe et al., 2014; Galluzzi et al., 2012). One form of regulated necrosis, termed ‘necroptosis’ has received considerable attention in recent years (Wallach et al., 2016). Experimentally, necroptosis is usually induced by combining pan-caspase inhibition, IAP inhibition and induction of the extrinsic pathway using TNFα (Feoktistova et al., 2011; Tenev et al., 2011). These conditions are reminiscent of those linked to the mechanism we hypothesized for c2/c3 cells that exhibit lower caspase activation, IAP inhibition and shift to the extrinsic pathway. Moreover, necroptotic cells are reported to resemble our ‘bleb’ phenotype defined by the occurrence of membrane blebbing in the absence of cell shrinkage (Gong et al., 2017). However, the co-occurrence of Annexin-V and 7-AAD excludes necroptosis as a mechanism for the necrotic phenotypes observed in our study, because in contrast to other necrotic pathways, in necroptosis, PS externalization precedes loss of membrane in integrity

(Gong et al., 2017). Furthermore, since ‘bleb’ cells still activate caspases, contrary to the definition of necroptosis, and HeLa cells do not express RIPK3, necroptosis is likely not the type of necrosis we observed.

Parthanatos, a form of necrotic cell death characterized by hyperactivation of PARP and ATP/NAD+ depletion, is an alternative identity for the necrotic cell death observed in our experiments (Fatokun et al., 2014). As introduced in section 3.1.3, Cisplatin has been shown to result in a depletion of ATP in a time-dependent manner (Zhou et al., 2002) and the level of ATP has been found to determine the cellular decision between apoptosis or necrosis (Eguchi et al., 1997; Leist et al., 1997). Therefore, the delay of cell death observed for necrotic phenotypes in our experiments fits with death by Parthanatos, because at this later time point ATP could be sufficiently depleted to shift the cell fate away from apoptosis. Furthermore, the occurrence of MOMP in all dying cells regardless of the phenotype argues for Parthanatos since the presence of MOMP distinguishes it from other necrotic cell deaths (Fatokun et al., 2014). However, one key feature of Parthanatos is not observed in our work, which is that its induction is considered independent of caspase activity. When using a pan-caspase inhibitor we observed that ~90% of the cells survived, and, of the ones that still died in the absence of caspase activation, none showed a necrotic phenotype, arguing that the necrotic phenotype we observed is caspase-dependent (Fig. 3.18). It should be noted, that in this experiment we analysed only 45 cells in total, therefore requiring repetition to further strengthen this conclusion.

In summary, necrotic cells observed here in response to Cisplatin show some key features of Parthanatos, but direct experimental validation is required to confirm this association. One approach could be to measure ATP levels in cells treated with Cisplatin using the available FRET-based biosensors (Imamura et al., 2009; Tantama et al., 2013) replacing one caspase sensor in our platform or extending it with additional FRET pairs currently under development. Measurement of PARP levels in single cells by labelling of the endogenous locus using gene editing is a further possibility to confirm Parthanatos as cell death mechanism.

Connection of cell death phenotype with caspase dynamics

In apoptotic cells, caspase-3 inhibits PARP by cleavage preventing further ATP depletion required for the execution of apoptosis (Galluzzi et al., 2012), and thus, mechanistically linking caspase activity with cellular energy levels and the propensity to die from a necrotic cell death.

The connection between the mode of cell death and caspase activity in response to Cisplatin has been studied by a number of groups which collectively converged on a model where the shift from apoptotic to necrotic cell death functions as a backup mechanism when apoptosis is not executed efficiently. Lacking or insufficient activation of caspases has been suggested as one reason for such a 'defective apoptosis' (Cepeda et al., 2007; Gonzalez et al., 2001; Lemaire et al., 1998; Segal-Bendirdjian and Jacquemin-Sablon, 1995; Vakifahmetoglu et al., 2008). We, therefore, hypothesized that the disruption of the caspase network observed in the c2/c3 population of cells and in response to chemical perturbation is the cause for a shift from apoptotic to necrotic cell death. Indeed, we observed an increased lag time between caspase-3 activation and the first occurrence of blebs (Fig. 3.19K), suggesting that in late-dying 'bleb' cells, cell death is indeed less efficiently activated, or 'defective' (Segal-Bendirdjian and Jacquemin-Sablon, 1995). We also observed a trend for necrotic cells to exhibit lower caspase-9 activity (Fig. 3.20)

Although the data is suggestive of a correlation between the late-dying c2/c3 and the necrotic phenotype, we could not establish an identity between c2/3 cells and c2/c3/c9 cell with necrotic and apoptotic cells, respectively (Fig. 3.19). However, we did observe an increased likelihood for c2/c3/c9 cells to die early, for c2/c3 cells to die later and—at the same time—for necrotic and apoptotic cells to die later and early, respectively. Analysis of caspase-9 activities in relation to the onset of caspase-3 activation demonstrates a strong anti-correlation (Spearman coefficient of -0.4, $p<<0.001$; data not shown) suggesting that not only we are observing a continuum of cell death phenotypes, but also a continuum of caspase network activation patterns.

Therefore, we hypothesised that the role of different mechanisms for cell death is to ensure death in the presence of high acute levels of DNA damage. However, different mechanisms result in different timing of death onset, with longer lag-times before cell death more likely resulting in necrosis. We speculate that the mechanism underlying cell-to-cell variability relates to IAPs heterogeneity and that the shift of phenotype may relate to ATP depleting as in Parthanatos.

3.4.4 Targeted perturbation of caspase dynamics allows fine-tuning of cell fate

In the attempt of falsifying the hypothesis that timing of cell death could be the link between the dynamics of caspase network and death phenotypes, we perturbed the caspase network

using caspase inhibitors (Fig. 3.22). We found that the decrease in c2/c3/c9 cells coincided with the increase of necrotic cell death for all caspase inhibitors. In contrast to Cisplatin treatment alone, cells not activating all three caspases were over-represented among cells undergoing a necrotic phenotype (Fig. 3.24). Contrary to our expectations, we did not observe a significant delay in cell death or caspase activation for any caspase inhibitor, suggesting that under these conditions the increase in necrotic cells is independent of the time of cell death with the caveat that the number of cells triggering a necrotic phenotypes is small (53 cells) and further data may be needed to confirm this observation. Together, the caspase inhibitor data suggest that a strong perturbation of the caspase network is sufficient to shift cells from apoptotic to necrotic cell death.

With a more subtle perturbation of the caspase network using a low, non-toxic dose of the IAP inhibitor LCL161, the prevalence of the c2/c3-population increased and the onset of cell death occurred at a later time; at the same time, the frequency of necrosis increased significantly (Fig. 3.27). However, in contrast to the caspase inhibitor experiment, cells not activating all caspases were not overrepresented among necrotic cells compared to apoptotic cells. One possible reason for this result is that while still activating all caspases above the threshold, the rate of activation and maximum activity is also reduced in c2/c3/c9 cells which could explain the increase in necrotic cells across all populations. This supports the hypothesis that a perturbation of caspase signalling, which can manifest as an increase in the c2/c3 population as well as a subduction of activation in all caspases in c2/c3/c9, leads to increased necrotic cell death.

Unleashing caspases by MEK and AKT inhibition accelerates cell death and may decrease the prevalence of necrotic cell death

Finally, to test if a faster caspase activation would decrease the frequency of necrosis, we used inhibitors of the pro-survival kinases MEK and AKT. These inhibitors resulted in an increase of the activity of all caspases (Fig. 3.28). We could confirm a faster apoptotic process and no necrosis, opposite to the LCL161 experiments. We notice, however, that in the matched solvent-control we detected only 2 necrotic cells. Therefore, further data is currently acquired to confirm this observation. If confirmed, these results are of key importance, because they are not only confirming the link between caspase dynamics and cell fate but also suggest that by removing the inhibition on caspases cell fate can be shifted from necrosis to an early apoptotic cell death. Moreover, MEK and AKT seem to act in synergy. While low-dose single treatment is sufficient to alter network dynamics and prevent necrotic cell death, the acceleration of cell

death is only observed when cells are treated with both inhibitors. Considering translation into cancer treatment, such a synergistic effect and use of low non-toxic doses are key to minimize toxicity, and could even allow reducing the Cisplatin dose without losing efficacy in a combination treatment.

In summary, we provided evidence to support the hypothesis that a 'defective' caspase signalling network, present in a population of cells both prior to chemical network perturbation and exacerbated by it, can lead to a continuum of necrotic and apoptotic cell death at the population level. While the absence of caspase-9 activation in c2/c3 cells alone is not sufficient to induce necrotic cell death, cells with a low caspase activity, including that of caspase-9, are more likely to die from a necrotic cell death, possibly because of a delay of cell death under certain conditions. In contrast, accelerating cell death and increasing caspase activity shifts cell fate towards apoptosis.

Targeted perturbation of the caspase network could allow modulating cell death phenotype *in vivo* to balance pro- and anti-inflammatory response

A key feature of necrotic cell death is the inflammation and immune response that it entails, in contrast to apoptosis which is considered to be anti-inflammatory (Berghe et al., 2014; Crusz and Balkwill, 2015). Conventionally, a reduction of inflammation by promoting apoptosis is considered ideal in tumour treatment, but with advances in the understanding of the tumour microenvironment and the role of adaptive immunity, it becomes clear that at least some local inflammation that promotes antitumour immunity can be beneficial. For example, LCL161, which increased necrosis in our assays, has both been shown to promote local anti-tumour immunity in melanoma (Chesi et al., 2016), while at the same time reducing viability in a mouse model of lymphoma by inducing a detrimental systemic inflammatory response (West et al., 2016). This dual role strongly argues that pro-inflammatory necrosis and anti-inflammatory apoptosis need to be finely balanced to maximize the effectiveness of anti-tumour treatments. By investigating cell-to-cell variability that seems key in setting a balance between necrosis and apoptosis, we provided mechanistic insights into these cell death choices and underlying dynamics in the caspase network. Using this knowledge, we identified strategies to perturb network dynamics to shift phenotypes and, thus, demonstrate a powerful proof-of-concept on how to develop strategies to achieve the balance between phenotypes.

Concluding remarks

Targeting of network dynamics to elicit specific responses is an emerging concept in pharmacology (Behar et al., 2013; Jørgensen and Linding, 2010; Pawson and Linding, 2008). Our novel multiplexing platform allowed us to identify heterogeneity in dynamics of multiple caspases at the single-cell-level and, thus, recommending this network as a valuable target to tune responses to Cisplatin and likely other chemotherapeutic drugs to increase their efficiency both by directly sensitizing cancer cells and harnessing anti-tumour immunity.

Chapter 4 Overall conclusion and outlook

We set out to develop an imaging platform that would allow multiplexing of at least three FRET sensors in single living cells to measure dynamics of intricate signalling networks and connecting them with the cell fate that they encode.

Going through an intensive phase of rationally designing and improving FRET pairs for three-colour FLIM, we were successful in creating a suite of three spectrally separated pairs by combining bright blue, green and fluorescent donors excitable at a single two-photon excitation wavelength with non-fluorescent chromoproteins as acceptors.

Next, we applied this sensor suite to study the activity of caspase-2, -3 and -9 in response to DNA damage. Unexpectedly, we did not only find broad heterogeneity in the timing of caspase activation, but we also identified a previously unnoticed heterogeneity in patterns of caspase activation with a cell population lacking a robust caspase-9 response and exhibiting delayed cell death. The concurrent analysis of signalling dynamics at a single-cell level and cell fate permitted to establish a connection between cells that exhibit reduced caspase dynamics and those that are more likely to die from a necrotic form of cell death. Our results further suggested that cell-to-cell variation of the levels of IAP family proteins could be the underlying cause for differences in network topology and dynamics. These novel insights into caspase dynamics permitted us to design and test targeted perturbation strategies using clinically relevant inhibitors against IAPs as well as pro-survival kinases MEK and AKT to fine-tune caspase dynamics and with it delaying cell death and shifting the fate from apoptotic to necrotic cell death. In light of the emerging role of inflammation as pro- as well as antitumour mechanism, the ability to control the prevalence of pro-inflammatory necrotic cell death could be key to maximize treatment efficiency and overcome resistance.

To further increase the capabilities of the multiplexing platform presented in this dissertation, several avenues for future development could be considered. While the simultaneous imaging of three-nodes of a network has yielded important insights into its dynamics and heterogeneity,

the platform has been designed to be amenable to extension, for example by adding additional FRET sensors or complementing it with non-FRET based fluorescent sensors. Moreover, work is ongoing to develop light-controlled, optogenetic tools to be able to perform targeted and quantitative network perturbation on a subcellular level. The combination of biochemical multiplexing and optogenetics will permit us to perform all-optical analysis of biochemical networks at the single-cell level. This could enable the generation of mathematical models describing biochemical networks at a single-cell level with dynamic information, creating the foundations for single-cell systems biology of cell fate.

Furthermore, the multiplexing platform developed in this work could be used to study a wide-range of different signalling pathways exploiting the plethora of FRET sensors available to date. Indeed, we are currently adapting the sensors to study dynamics of RAS-dependent signal transduction pathways. Moreover, while two-dimensional cultures used in this and many other studies have given valuable insight into biological questions, three-dimensional cultures are emerging as a better model for the situation *in vivo*. Thus, the increased penetration depth of two-photon microscopy could be harnessed to perform multiplexed imaging in three dimensions, for example by using tumour spheroids or whole tissues either with a system as described in this work or through adaptation of light sheet microscopy. For instance, Baek *et al.* recently showed intra- and inter-cell line heterogeneity of 3D spheroids in response to Cisplatin (Baek et al., 2016). We have started to grow spheroid from HeLa-BAK cells and will continue to move the multiplexing platform to 3D.

In summary, the successful development and application of three-colour FRET imaging have permitted us to study network dynamics at an unprecedented detail uncovering pronounced non-genetic heterogeneity, which we exploited to design novel strategies for modulating cell fate in response to DNA damage. As the multiplexing platform is easily adaptable to study a wide-range of biological networks, this work could represent the start of a number of in-depth investigations into key biological questions whose answers have so far been in hidden in inaccessible heterogeneous cell populations.

Supplement 1 | Videos

All videos are supplied on a CD attached to this work.

Video S1 - **HeLa-BAK cells undergoing Cisplatin induced cell death**

Representative videos of cells treated with 100 µM Cisplatin (right) or 0.9% NaCl (left) as control and imaged every 15 min for 16 hours on the multiplexing platform. Composite image of maximum projections from mTagBFP and mAmetrine channels are shown.

Video S2 - **Dynamics for caspase-2, -3 and-9 activation in HeLa-BAK cells**

Representative animations of cells treated with 100 µM Cisplatin and imaged every 15 min for 16 hours. Shown are REA of caspase-2 (blue), -3 (green) and -9 (magenta) in a 3D blot relative to the uncleavable (unc) controls (upper left) and as trajectory over time (lower left). The fractional contribution of cleaved (solid lines) and uncleaved (dashed lines) forms of sensors used to calculate REA are shown as a function of time (upper right). Maximum projections of images from the three channels are depicted (lower right).

A: Cell from the c2/c3/c9 population that exhibits a ‘shrunk’ death phenotype.

B: Cell from the c2/c3 population that exhibits a ‘bleb’ death phenotype.

Video S3 - **HeLa parental stained with TMRM undergoing Cisplatin-induced cell death**

Representative field of view of HeLa Parental cells stained with 20 nM TMRM for 15 min and treated with 100 µM Cisplatin imaged every 15 min for 16 hours on a Nikon Ti Widefield microscope. Shown are DIC (grey) and TRITC (red) channels

Video S4 - **HeLa-BAK cells stained with TMRM undergoing Cisplatin-induced cell death**

Representative field of view of HeLa Parental cells stained with 20 nM TMRM for 15 min and treated with 100 µM Cisplatin imaged every 15min for 16 hours on Leica SP5 confocal laser scanning microscope using a 594 nm Argon for excitation of TMRM. Shown are bright field (left) and TMRM (right) channels.

Video S5 - **HeLa-BAK cells show a continuum of death phenotypes in response to Cisplatin**

Representative movies of HeLa-BAK cells undergoing different death phenotypes (as defined in Figure 3.17) in response to 100 µM Cisplatin. Left: ‘shrunk’, middle: ‘shrunk-bleb’, right: ‘bleb’. Not that the middle image also contains a ‘shrunk’ cells (lower cell). Imaging was performed on the multiplexing platform. Composite image of maximum projections from mTagBFP and mAmetrine channels are shown.

Video S6 - **Parental HeLa cells co-stained with TMRM, Annexin-V and 7-AAD undergoing Cisplatin-induced cell death**

Representative field of view of parental HeLa cells that were stained with TMRM (top right), FITC Annexin-V (lower left) and 7-AAD lower right prior to being treated with 100 µM Cisplatin. Imaging was performed on a Nikon Ti wide field microscope every 15 min for 16 hours.

Video S7 - **U2OS cells expressing the BAK caspase-2/-3/-9 sensor suite undergoing Cisplatin induced cell death**

U2OS cells transiently transfected with the BAK sensor for caspase-2, -3 and -9 were treated with 100 µM Cisplatin and imaged every 15 min for 16 hours on the multiplexing platform. Composite image of maximum projections from mTagBFP and mAmetrine channels are shown.

Supplement 2 | Materials

Table S1 – **Oligonucleotides used in this study.** All oligonucleotides were obtained from Sigma Aldrich. Sequences are shown in 5’ to 3’ direction. Sorted by the date of purchase.

Name	Purpose	Sequence
Chapter 2		
BDF	PCR of mTagBFP	ACGTGCTAGCATGGTGTCTAAGGGCGGAGAGCTGATTAAGG
BDR		AATTGCGGCCGCATTAAGCTTGTGCCCCAGTTTGC
BA2F	PCR of sREACh	ACGTGGTACCATGGTGAGCAAGGGCGAGGAGCTGTTCAC
BA2R		ACGTGTTTAAACCTACAGCTCGTCCATGCCGAGAGTGATCCC
GDF	PCR of mAmetrine	ACGTGCTAGCATGGTGAGCAAGGGCGAGGAGC
GDR		AATTGCGGCCGCGAGAGTGATCCCGGCG
GA1F	PCR of msCP576	ACGTGGTAC CATGGTGAGTGTGATCGCTAAACAAATGACC
GA1R		ACGTGTTTAAACTCAACCGAGCAAAGAGTGGCGTGC
GA2F	PCR of mOrange	AATTGGTACCATGGTGAGCAAGGGCGAGGAGAATAACATGG
GA2R		ACGTGTTTAAACTTACTTGTACAGCTCGTCCATGCCGCC
RDF	PCR of mKeima	ACGTGCTAGCATGGTGAGCAAGGGCGAGGAGCTGTTCACC
RDR		AATTGCGGCCGCGAGAGTGATCCCGGCGGC
RAF	PCR of mNeptune	ACGTGGTACCATGGTGTCTAAGGGCGAAGAGC
RAR		ACGTGTTTAAACTTACTTGTACAGCTCGTCCATGCC
UCLF	Uncleavable linker (SASG)	GGCCGCCCTGGGAGGCACCGGATCCGGCAGCGGGTCCGCCAGCGGCGGAGGTAC
UCLR		CTCCGCCGCTGGCGGACCCGCTGCCGGATCCGGTGCCTCCCAGGGC
C2F	Caspase-2 linker (VDVAD)	GGCCGCCCTGGGAGGCACCGGATCCGGCAGCGTGGACGTGGCCGATGGAGGTAC
C2R		CTCCATCGGCCACGTCCACGCTGCCGGATCCGGTGCCTCCCAGGGC
C3F	Caspase-3 linker (DEVD)	GGCCGCCCTGGGAGGCACCGGATCCGGCAGCGGGGACGAGGTGGATGGAGGTAC
C3R		CTCCATCCACCTCGTCCCCGCTGCCGGATCCGGTGCCTCCCAGGGC
C9F	Caspase-9 linker (LEHD)	GGCCGCCCTGGGAGGCACCGGATCCGGCAGCGGGCTGGAGCACGACGGAGGTAC
C9R		CTCCGTCGTGCTCCAGCCCGCTGCCGGATCCGGTGCCTCCCAGGGC
MFO-78_C2_VDTTD_F	Caspase-2 linker (VDTTD)	GGCCGCCCTGGGAGGCACCGGATCCGGCAGCGTGGACACCACAGATGGAGGTAC
MFO-79_C2_VDTTD_R		CTCCATCTGTGGTGTCCACGCTGCCGGATCCGGTGCCTCCCAGGGC
MFO-58_C3F_DEVDR	Caspase-3 linker (DEVDR)	GGCCGCCCTGGGAGGCACCGGATCCGGCAGCGGGGACGAGGTGGATCGAGGAGGTAC
MFO-59_C3R_DEVDR		CTCCTCGATCCACCTCGTCCCCGCTGCCGGATCCGGTGCCTCCCAGGGC
C2PHR-fw	PCR of CRY2PHR	ACGTGGTACCATGAAGATGGACAAAAAGACTATAGTTTGG
C2PHR-rv		ACGTGTTTAAACTGCTCGTCCGATCATGATCTGTGC
C2PHR-Nd100	PCR of CRY2PHR (delta100aa from N-terminus)	ACGTGGTACCAACCACCTCTATGATCCTGTTTCGTTAG
C2PHR-Nd200	PCR of CRY2PHR (delta200aa from N-terminus)	ACGTGGTACCCCGAGCAATGCGTTGTTAACTAGAG
C2PHR-Nd300	PCR of CRY2PHR (delta300aa from N-terminus)	ACGTGGTACCTGTTTCAACTTCCCGTTTACTCACGAG
C2PHR-FADF	PCR of CRY2PHR, FAD-binding domain (delta212aa from N-terminus)	ACGTGGTACCCCAGGATGGAGCAATGCTGATAAGTTAC
C2PHR-Cd50	PCR of CRY2PHR (delta50aa from C-terminus)	ACGTGTTTAAACTGGATGATGGATCCATTCAGTTGGC
C2PHR-Cd100	PCR of CRY2PHR (delta100aa from C-terminus)	ACGTGTTTAAACCTGCCAGCCAAGGATGTCACATTC
C2PHR-FADR	PCR of CRY2PHR (delta10aa from C-terminus)	ACGTGTTTAAACGGTTCTTGAAATAGCTTTAGCTAGTAGC
MFO-161_GFPc1_F_KpnI	PCR of GFPc1	ACGTGGTACCATGCCCCTGCCCACCAC
MFO-162_GFPc1_R_PmeI		ACGTGTTTAAACTCATTTGTACAGCTCGTCCATTCCC

Name	Purpose	Sequence
MFO-66_hCP576_F_KpnI	PCR of humanized hsCP576	ACGTGGTACCATGGTGTCCGTGATCGCCAAGC
MFO-67_hCP576_R_PmeI		ACGTGTTTAAACTCATCCCAGCAGGCTGTGCC
cjB-fw	PCR of cjBlue	ACGTGGTACC ATGGCTTCCAAAATCAGCGACAATGTACG
cjB-rv		ACGTGTTTAAAC TTAATTGTGACCAAGTTTAGATGGGCATG
iRFP-fw	PCR of iRFP713	ACGTGGTACCATGGCTGAAGGATCCGTCGCCAG
iRFP-rv		ACGTGTTTAAACTCACTCTTCCATCACGCCGATCTG
NirFP_fwd	PCR of NirFP as C-terminal fusion (from Emma Richardson)	CAGGGTACCATGGGAGAGGATAGCGAGCTGATCTCC
NirFP_rev		CAGGTTTAAACTTAGCTGTGCCCCAGTTTGCTAGGCAG
NheI-NirFP_fwd	PCR of NirFP as N-terminal fusion (from Emma Richardson)	CACGCTAGCATGGGAGAGGATAGCGAGCTGATCT
NirFP-NotI_rev		GTGGCGGCCGCGCTGTGCCCCAGTTTGCTAGGCAGG
KpnI-mKeima_fwd	PCR of mKeima as C-terminal fusion (from Emma Richardson)	CACGGTACCATGGTGAGTGTGATCGCTAAACAAA
mKeima-PmeI_rev		GTGGTTTAAACTTAACCGAGCAAAGAGTGGCGTGCAATG
tdNirFP_fwd1	PCR of two copies of NirFP to created tdNirFP using SapI cloning	CACGCTAGCATGGGAGAGGATAGCGAGCTGATCT
tdNirFP_rev1		GTGGCTCTTCCGGTGCTGCCGGTGCCATGCCCGCTGTGCCCCAGTTTGCTAGGC
tdNirFP_fwd2		CACGCTCTTCCACCGGCAGCGGCAGCTCCGGCACCATGGGAGAGGATAGCGAGCTGATCT
tdNirFP_rev2		GTGGCGGCCGCGCTGTGCCCCAGTTTGCTAGGC
MFO-115_tdN_F_NheI	PCR to create pcDNA3(-)tdNirFP	GCTGGCTAGCATGGGAGAGG
MFO-116_tdN-Stop_R_NotI		AGCTGCGGCCGCTTAGCTGTGCCCCAGTTTGC
MFO-117_sREACh_F_EcoRI	PCR to create pcDNA3(-)sREACh	TGCAGAATTCACCATGGTGAGCAAGGGC
MFO-118_sREACh_R_BamHI		ACGTGGATCCCTACAGCTCGTCCATGCCG
MFO-119_hsCP576_F_EcoRI	PCR to create pcDNA3(-)msCP576h	TGCAGAATTCACCATGGTGTCCGTGATCG
MFO-120_hsCP576_R_BamHI		ACGTGGATCCTCATCCCAGCAGGCTGTG
MFO-165_Ultram_F_KpnI	PCR of Ultramarine	ACGTGGTACCATGTCCGTGATCGCCACCC
MFO-166_Ultram_R_PmeI		ACGTGTTTAAACTTAAGCCACCACGGGCTTCC
MFO-167_tdUltra_Hifi_F1	PCRs to create tdUltramarine	GGAGACCCAAGCTGGCTAGCATGTCCGTGATCGCCACCC
MFO-168_tdUltra_Hifi_R1		CCGGTGCCATGCCCAGCCACCACGGGCTTCCG
MFO-169_tdUltra_Hifi_F2		TGGTGGCTGGGCATGGCACCGGCAGCACCGGCAGCGGCAGCTCCGGCACCATGTCCGTGATCG CCACCC
MFO-170_tdUltra_Hifi_R2		ACTTCCGGGTGAGGCGGCCGCAGCCACCACGGGCTTCCG
MFO-171_tdiRFP_Hifi_F1	PCRs to create tdiRFP682	GAGACCCAAGCTGGCTAGCATGGCCGAGGGCAGCGTG
MFO-172_tdiRFP_Hifi_R1		CCGGTGCCATGCCCCTCTTCCATCACGCCGATCTGC
MFO-173_tdiRFP_Hifi_F2		TGGAAGAGGGGCATGGCACCGGCAGCACCGGCAGCGGCAGCTCCGGCACCATGGCCGAGGGC AGCGTG
MFO-174_tdiRFP_Hifi_R2		ACTTCCGGGTGAGGCGGCCGCCTCTTCCATCACGCCGATCTGC
MFO-175_iRFP682_F_NheI	PCR of iRFP682	ACGTGCTAGCATGGCCGAGGGCAGCGTG
MFO-176_iRFP682_R_NotI		AATTGCGGCCGCCTCTTCCATCACGCCGATCTGCC
MFO-181_tdUltra_KpnI	PCR to swap tdUltramarine to C-terminus	ACGTGGTACCATGTCCGTGATCGCCACCC
MFO-182_tdUltra_PmeI		ACGTGTTTAAACTTAAGCCACCACGGGCTTCCG
MFO-183_tdiRFP682_KpnI	PCR to swap tdiRFP682 to C-terminus	ACGTGGTACCATGGCCGAGGGCAGCGTG
MFO-184_tdiRFP682_PmeI		ACGTGTTTAAACTTATCTTCCATCACGCCGATCTGC

Name	Purpose	Sequence
MFO-200_ShG_KpnI_F	PCR of ShadowG for C-terminal fusion	ACGTGGTACCATGGTGTCCAAGG
MFO-201_ShG_PmeI_R		ACGTGTTTAAACTCAGAGCTCATCCATG
MFO-202_ShG_NheI_F	PCR of ShadowG for N-terminal fusion	ACGTGCTAGCATGGTGTCCAAGG
MFO-203_ShG_NotI-Stop_R		AATTGCGGCCGCTTATCAGAGCTCATCCATG
MFO-208_Garnet_F_KpnI	PCR of mGarnet for C-terminal fusion	ACGTGGTACCATGAACAGCCTGATCAAAGAAAAC
MFO-209_Garnet_R_PmeI		ACGTGTTTAAACTTATCCGCCTCCCAGTCCAGC
MFO-210_Garnet_F_NheI	PCR of mGarnet for N-terminal fusion	ACGTGCTAGCATGAACAGCCTGATCAAAGAAAAC
MFO-211_Garnet_R_NotI		AATTGCGGCCGCTTATCCGCCTCCCAGTCCAGC
MFO-25_C7F	Caspase-7 linker (QKDVK)	GGCCGCCCTGGGAGGCACCGGATCCGGCCAGAAGGACGTGAAGGACGGAGGTAC
MFO-26_C7R		CTCCGTCCTTCACGTCCTTCTGGCCGGATCCGGTGCCTCCCAGGGC
Chapter 3		
MFO-36_ BFP_F_NheI	PCRs to link mTagBFP-VDTTD-sREACh and mAmetrine-DEVDRmsCP576 with a P2A site using SapI cloning	ACGTGCTAGCATGGTGTCTAAGGGCGGAGAGC
MFO-37_ sREACh_R_P2A_SapI		ACGTGCTCTTCACTGCTTCAGCAGGCTGAAGTTAGTAGCTCCGCTTCCCAGCTCGTCCATGCCGAGAG
MFO-38_ Ame_F_P2A_SapI		ACGTGCTCTTCACAGGCTGGAGACGTGGAGGAGAACCCTGGACCTATGGTGAGCAAGGGCGAGGAG
MFO-39_ No.20_R_PmeI		ACGTGTTTAAACTCAACCGAGCAAAGAGTGGCGTG
MFO-106_mKeima_R_PmeI	PCRs to link mTagBFP-VDTTD-sREACh and tdNirFP with a P2A site using SapI cloning	ACGTGTTTAAACACCGAGCAAAGAGTGGCG
MFO-107_tdN_F_P2A_SapI		ACGTGCTCTTCACAGGCTGGAGACGTGGAGGAGAACCCTGGACCTATGGGAGAGGATAGCGAGCTG
MFO-104_ hsCP576_R_T2A_SapI	PCRs to link mTagBFP-VDTTD-sREACh-P2A-mAmetrine-DEVDRmsCP576 and tdNirFP-LEHD-mKeima with a T2A site using SapI cloning	ACGTGCTCTTCATGTTAGCAGACTTCCTCTGCCCTCTCCGCTTCCTCCCAGCAGGCTGTGCCG
MFO-105_tdN_F_T2A_SapI		ACGTGCTCTTCAACATGCGGTGACGTCGAGGAGAATCCTGGACCTATGGGAGAGGATAGCGAGCTG
MFO-106_mKeima_R_PmeI		ACGTGTTTAAACACCGAGCAAAGAGTGGCG
MFO-250_cIAP1_qPCR_F	qPCR for cIAP1 (sequence from Paek et al., 2016)	TTGAGGTGTTGGGAATCTGG
MFO-251_cIAP1_qPCR_R		GGCCTTTCATTCGTATCAAGAAC
MFO-252_cIAP2_qPCR_F	qPCR for cIAP2 (sequence from Paek et al., 2016)	AATGCTTTTGCTGTGATGGTG
MFO-253_cIAP2_qPCR_R		GCTTGAACTTGACGGATGAAC
MFO-254_XIAP_qPCR_F	qPCR for XIAP (sequence from Paek et al., 2016)	GCTCAGAAAGACAGTATGCAAG
MFO-255_XIAP_qPCR_R		CCACAAGGAACAAAAACGATAGC
MFO-294_qPCR_GAPDH_F	qPCR for GAPDH (sequence from Siddharth De)	TGAGCTTGACAAAGTGGTCG
MFO-295_qPCR_GAPDH_R		GTCAGTGGTGGACCTGACCT
MFO-300_tdIETD-linker_F	Caspase-8 tandem linker	GGCCGCCCTGGGAGGCACCGGATCCGGCAGCATCGAGACCGACGGCGGCATCGAGACCGACGGAGGTAC
MFO-301_tdIETD-linker_R		CTCCGTCGGTCTCGATGCCGCCGTCGGTCTCGATGCTGCCGGATCCGGTGCCTCCCAGGGC

Table S2 – **Origin of cDNA templates for molecular cloning**

Template for	Plasmid name	Origin
bfloGFPc1	GeneArt® Strings™ DNA Fragments used directly for cloning	Synthesized based on published sequence (Bomati et al., 2014)
cjBlue	pRSET-cjBlue	Received from Atsushi Miyawaki
Clover	pcDNA3.1-Clover-mRuby2	Purchased from Addgene #49089
CRY2PHR	pCRY2PHR-mCherryN1	Purchased from Addgene #26866
hmKeima8.5	pMx-hmKeima8.5	Synthesized based on published sequence (Guan et al., 2015)
IFP4.1	IFP1.4-C1	Purchased from Addgene #54782.
iRFP682	piRFP682-N1	Purchased from Addgene #45459
iRFP713	piRFP	Purchased from Addgene #31857
mAmetrine	pmAmetrine-DEVD-tdTomato	Purchased from Addgene #18879
mBeRFP	Unknown, used directly for PCR	Received from Yang Fei
mGarnet	GeneArt® Strings™ DNA Fragments used directly for cloning	Synthesized based on published sequence (Hense et al., 2015)
mKeima	pRSET-mKeima	Received from Atsushi Miyawaki
mNeptune	pcDNA3-mNeptune	Received from Michael Lin
mOrange	pmOrange	Purchased from Clontech, Cat. # 632529
mRuby2	pcDNA3.1-Clover-mRuby2	Purchased from Addgene #49089
msCP576	pRSET-msCP576	Received from Atsushi Miyawaki
mTagBFP	pTagBFP-C	Purchased Evrogen, Cat. #FP171
NirFP	peNirFP-N	Purchased from Evrogen, Cat. #FP743
ShadowG	GeneArt® Strings™ DNA Fragments used directly for cloning	Synthesized based on published sequence (Murakoshi et al., 2015)
sREACh	mGFP-10-sREAChN3	Purchased Addgene #21947
Ultramarine	GeneArt® Strings™ DNA Fragments used directly for cloning	Synthesized based on published sequence (Pettikiriarachchi et al., 2012)

Table S3 **– Antibodies used in this study**.

Epitope/name	Supplier	Catalog number	Species	Concentration used	Blocking solution
Primary antibodies					
Akt (pan)	Cell Signalling	2920	Mouse	1:2000	5% BSA in TBST
Akt pS473	Cell Signalling	4060	Rabbit	1:1000	5% BSA in TBST
beta-actin	Sigma	A5441	Mouse	1:10000	5% Milk in TBST
Caspase-2	Millipore	MAB3507	Rat	1:250	5% BSA in TBST
Caspase-3	Cell Signalling	9668	Mouse	1:250	5% BSA in TBST
Caspase-8	Cell Signalling	9746	Mouse	1:500	5% BSA in TBST
Caspase-9	Cell Signalling	9502	Rabbit	1:500	5% BSA in TBST
c-IAP1	Cell Signalling	7065	Rabbit	1:1000	5% BSA in TBST
c-IAP2	Cell Signalling	3130	Rabbit	1:1000	5% BSA in TBST
Erk	Cell Signalling	4695	Rabbit	1:1000	5% Milk in TBST
Erk pT202/Y204	Cell Signalling	9106	Mouse	1:1000	5% Milk in TBST
GFP (JL-8)	Clontech	632381	Mouse	1:1000	5% Milk in TBST
Hsp90	Cell Signalling	4877	Rabbit	1:1000	5% BSA in TBST
Keima-Red	MBL	M126-3	Mouse	1:1000	10% Milk in PBS
p53	Santa Cruz	sc-126	Mouse	1:500	5% Milk in TBST
p53 pS15	Cell Signalling	9284	Rabbit	1:1000	5% BSA in TBST
PARP	BD Biosciences	556362	Mouse	1:1000	5% Milk in TBST
tRFP	Evrogen	AB233	Rabbit	1:1000	5% Milk in TBST
XIAP	Cell Signalling	2045	Rabbit	1:1000	5% BSA in TBST
Secondary antibodies					
IRDye® 680RD anti-Rabbit	Licor	925-68071	Goat	1:5000	Odyssey Blocking Buffer (PBS; cat. #927-40000)
IRDye® 680RD anti-Mouse	Licor	925-68070	Goat	1:5000	
IRDye® 800CW anti-Mouse	Licor	926-32210	Goat	1:5000	
IRDye® 800CW anti-Rabbit	Licor	925-32211	Goat	1:5000	

Table S4 – **Reagents used for multiplexed caspase imaging and related assays**. All reagents were filtered sterile or kept sterile if received as solution.

Reagent	Supplier	Catalogue number	Stock solution
7-AAD (7-amino-actinomycin D)	Biolegend	420403	50 ug/ml in PBS
Afuresertib (GSK2110183)	Stratech	57521	10 mM in DMSO
Biliverdin	Sigma	30891	25 mM in DMSO
$CaCl_2$ dihydrate	Acros Organics	423525000	2.5M in H_2O
Caspase-2 Inhibitor I (Z-VDVAD-FMK)	Calbiochem	218744	12.5 mM in DMSO
Caspase-3 Inhibitor II (Z-DEVD-FMK)	Calbiochem	264155	12.5 mM in DMSO
Caspase-9 Inhibitor I (Z-LEHD-FMK)	Calbiochem	218761	12.5 mM in DMSO
Cisplatin (cis-Diammineplatinum(II) dichloride)	Sigma	P4394	2 mM in 0.9% NaCl in H_2O (Fresh every four weeks)
DMSO	Fisher Scientific	BP231-100	Pure
DRAQ5	Biolegend	424101	5 mM as supplied
Ethyl Acetate	Sigma	319902	Pure
Etoposide	Sigma	E1383	10 mM in DMSO
FITC Annexin V	Biolegend	640905	100 ug/ml in PBS
Formaldehyde	Agar Scientific	R1026	16% (wt/vol) in H_2O
G418 (Geneticin)	Gibco	11811023	100 mg/ml in H_2O
JetPRIME	Source Bioscience	114-01	Ready to use
LCL161	LKT Laboratories	L1044	4 mM in DMSO
Pan-Caspase Inhibitor (Q-VD-OPh)	Biovision	1170	12.5 mM in DMSO
Premo™ FUCCI Cell Cycle Sensor (BacMam 2.0)	Invitrogen	P36238	Ready to use
Staurosporine	Santa Cruz	sc-360258	100 ug/ml in Ethyl Acetate
Sulforhodamine B	Sigma	230162	0.057% (wt/vol) in 1% acetic actid (vol/vol)
Thymidine	Sigma	T1895	100 mM in PBS

References

Abedini, M.R., Muller, E.J., Brun, J., Bergeron, R., Gray, D.A., and Tsang, B.K. (2008). Cisplatin Induces p53-Dependent FLICE-Like Inhibitory Protein Ubiquitination in Ovarian Cancer Cells. Cancer Res. *68*.

Ai, H.W., Hazelwood, K.L., Davidson, M.W., and Campbell, R.E. (2008). Fluorescent protein FRET pairs for ratiometric imaging of dual biosensors. Nat Methods *5*, 401–403.

Akinleye, A., Furqan, M., Mukhi, N., Ravella, P., and Liu, D. (2013). MEK and the inhibitors: from bench to bedside. J. Hematol. Oncol. *6*, 27.

Albeck, J.G., Burke, J.M., Aldridge, B.B., Zhang, M., Lauffenburger, D.A., and Sorger, P.K. (2008a). Quantitative analysis of pathways controlling extrinsic apoptosis in single cells. Mol. Cell *30*, 11–25.

Albeck, J.G., Burke, J.M., Spencer, S.L., Lauffenburger, D.A., and Sorger, P.K. (2008b). Modeling a snap-action, variable-delay switch controlling extrinsic cell death. PLoS Biol. *6*, 2831–2852.

Alford, S.C., Ding, Y., Simmen, T., and Campbell, R.E. (2012a). Dimerization-Dependent Green and Yellow Fluorescent Proteins. ACS Synth. Biol. *1*, 569–575.

Alford, S.C., Abdelfattah, A.S., Ding, Y., and Campbell, R.E. (2012b). A Fluorogenic Red Fluorescent Protein Heterodimer. Chem. Biol. *19*, 353–360.

Allan, L. a, and Clarke, P.R. (2007). Phosphorylation of caspase-9 by CDK1/cyclin B1 protects mitotic cells against apoptosis. Mol. Cell *26*, 301–310.

Allan, L.A., Morrice, N., Brady, S., Magee, G., Pathak, S., and Clarke, P.R. (2003). Inhibition of caspase-9 through phosphorylation at Thr 125 by ERK MAPK. Nat. Cell Biol. *5*, 647–654.

Almendro, V., Marusyk, A., and Polyak, K. (2013). Cellular Heterogeneity and Molecular Evolution in Cancer. Annu. Rev. Pathol. Mech. Dis. *8*, 277–302.

Altena, R., Fehrmann, R.S.N., Boer, H., de Vries, E.G.E., Meijer, C., and Gietema, J.A. (2015). Growth Differentiation Factor 15 (GDF-15) Plasma Levels Increase during Bleomycin- and Cisplatin-Based Treatment of Testicular Cancer Patients and Relate to Endothelial Damage. PLoS One *10*, e0115372.

Andersen, J.L., Johnson, C.E., Freel, C.D., Parrish, A.B., Day, J.L., Buchakjian, M.R., Nutt, L.K., Thompson, J.W., Moseley, M.A., and Kornbluth, S. (2009). Restraint of apoptosis during mitosis through interdomain phosphorylation of caspase-2. EMBO J. *28*, 3216–3227.

Ando, K., Kernan, J.L.L., Liu, P.H.H., Sanda, T., Logette, E., Tschopp, J., Look, A.T.T., Wang, J., Bouchier-Hayes, L., and Sidi, S. (2012). PIDD Death-Domain Phosphorylation by ATM Controls Prodeath versus Prosurvival PIDDosome Signaling. Mol. Cell *47*, 681–693.

Andrabi, S.A., Dawson, T.M., and Dawson, V.L. (2008). Mitochondrial and nuclear cross talk in cell death: parthanatos. Ann. N. Y. Acad. Sci. *1147*, 233–241.

Andrabi, S.A., Umanah, G.K.E., Chang, C., Stevens, D.A., Karuppagounder, S.S., Gagné, J.-P., Poirier, G.G., Dawson, V.L., and Dawson, T.M. (2014). Poly(ADP-ribose) polymerase-dependent energy depletion occurs through inhibition of glycolysis. Proc. Natl. Acad. Sci. U. S. A. *111*, 10209–10214.

Aoki, K., Komatsu, N., Hirata, E., Kamioka, Y., and Matsuda, M. (2012). Stable expression of FRET biosensors: A new light in cancer research. Cancer Sci. *103*, 614–619.

Aye-Han, N.-N., Allen, M.D., Ni, Q., and Zhang, J. (2012). Parallel tracking of cAMP and PKA signaling dynamics in living cells with FRET-based fluorescent biosensors. Mol. Biosyst. *8*, 1435–1440.

Baek, N., Seo, O.W., Lee, J., Hulme, J., and An, S.S.A. (2016). Real-time monitoring of cisplatin cytotoxicity on three-dimensional spheroid tumor cells. Drug Des. Devel. Ther. *10*, 2155–2165.

Baird, G.S., Zacharias, D.A., and Tsien, R.Y. (1999). Circular permutation and receptor insertion within green

fluorescent proteins. Proc. Natl. Acad. Sci. U. S. A. *96*, 11241–11246.

Bajar, B., Wang, E., Zhang, S., Lin, M., and Chu, J. (2016a). A Guide to Fluorescent Protein FRET Pairs. Sensors *16*, 1488.

Bajar, B.T., Wang, E.S., Lam, A.J., Kim, B.B., Jacobs, C.L., Howe, E.S., Davidson, M.W., Lin, M.Z., and Chu, J. (2016b). Improving brightness and photostability of green and red fluorescent proteins for live cell imaging and FRET reporting. Sci. Rep. *6*, 20889.

Barranco, S.C., Ho, D.H., Drewinko, B., Romsdahl, M.M., and Humphrey, R.M. (1972). Differential sensitivites of human melanoma cells grown in vitro to arabinosylcytosine. Cancer Res. *32*, 2733–2736.

Bartkova, J., Horejsí, Z., Koed, K., Krämer, A., Tort, F., Zieger, K., Guldberg, P., Sehested, M., Nesland, J.M., Lukas, C., et al. (2005). DNA damage response as a candidate anti-cancer barrier in early human tumorigenesis. Nature *434*, 864–870.

Basu, A., and Krishnamurthy, S. (2010). Cellular Responses to Cisplatin-Induced DNA Damage. J. Nucleic Acids *2010*, 1–16.

Becker, W., Su, B., Holub, O., and weisshart, K. (2010). FLIM and FCS detection in laser-scanning microscopes: Increased efficiency by GaAsP hybrid detectors. Microsc. Res. Tech. *74*, n/a-n/a.

Behar, M., Barken, D., Werner, S.L., and Hoffmann, A. (2013). The Dynamics of Signaling as a Pharmacological Target. Cell *155*, 448–461.

Berger, A.B., Witte, M.D., Denault, J.-B., Sadaghiani, A.M., Sexton, K.M.B., Salvesen, G.S., and Bogyo, M. (2006). Identification of early intermediates of caspase activation using selective inhibitors and activity-based probes. Mol. Cell *23*, 509–521.

Berghe, T. Vanden, Linkermann, A., Jouan-Lanhouet, S., Walczak, H., and Vandenabeele, P. (2014). Regulated necrosis: the expanding network of non-apoptotic cell death pathways. Nat. Rev. Mol. Cell Biol.

Berndtsson, M., Hägg, M., Panaretakis, T., Havelka, A.M., Shoshan, M.C., and Linder, S. (2007). Acute apoptosis by cisplatin requires induction of reactive oxygen species but is not associated with damage to nuclear DNA. Int. J. Cancer *120*, 175–180.

Bindels, D.S., Haarbosch, L., van Weeren, L., Postma, M., Wiese, K.E., Mastop, M., Aumonier, S., Gotthard, G., Royant, A., Hink, M.A., et al. (2017). mScarlet: a bright monomeric red fluorescent protein for cellular imaging. Nat. Methods *14*, 53–56.

Blanc, C., Deveraux, Q.L., Krajewski, S., Jänicke, R.U., Porter, A.G., Reed, J.C., Jaggi, R., and Marti, A. (2000). Caspase-3 is essential for procaspase-9 processing and cisplatin-induced apoptosis of MCF-7 breast cancer cells. Cancer Res. *60*, 4386–4390.

Bomati, E.K., Haley, J.E., Noel, J.P., and Deheyn, D.D. (2014). Spectral and structural comparison between bright and dim green fluorescent proteins in Amphioxus. Sci. Rep. *4*, 5469.

Brozovic, A., Fritz, G., Christmann, M., Zisowsky, J., Jaehde, U., Osmak, M., and Kaina, B. (2004). Long-term activation of SAPK/JNK, p38 kinase and fas-L expression by cisplatin is attenuated in human carcinoma cells that acquired drug resistance. Int. J. Cancer *112*, 974–985.

Bunt, G., and Wouters, F.S. (2017). FRET from single to multiplexed signaling events. Biophys. Rev. *9*, 119–129.

Caiado, F., Silva-Santos, B., and Norell, H. (2016). Intra-tumour heterogeneity - going beyond genetics. FEBS J.

Campbell, R.E., Tour, O., Palmer, A.E., Steinbach, P.A., Baird, G.S., Zacharias, D.A., and Tsien, R.Y. (2002). A monomeric red fluorescent protein. Proc Natl Acad Sci U S A *99*, 7877–7882.

Cardone, M.H., Roy, N., Stennicke, H.R., Salvesen, G.S., Franke, T.F., Stanbridge, E., Frisch, S., and Reed, J.C. (1998). Regulation of cell death protease caspase-9 by phosphorylation. Science *282*, 1318–1321.

Cepeda, V., Fuertes, M.A., Castilla, J., Alonso, C., Quevedo, C., and Pérez, J.M. (2007). Biochemical mechanisms of cisplatin cytotoxicity. Anticancer. Agents Med. Chem. *7*, 3–18.

Chae, H.J., Kang, J.S., Byun, J.O., Han, K.S., Kim, D.U., Oh, S.M., Kim, H.M., Chae, S.W., and Kim, H.R. (2000). Molecular mechanism of staurosporine-induced apoptosis in osteoblasts. Pharmacol. Res. *42*, 373–381.

Chan, M.C., Karasawa, S., Mizuno, H., Bosanac, I., Ho, D., Prive, G.G., Miyawaki, A., and Ikura, M. (2006). Structural characterization of a blue chromoprotein and its yellow mutant from the sea anemone Cnidopus japonicus. J Biol Chem *281*, 37813–37819.

Chee, J.L.Y., Saidin, S., Lane, D.P., Leong, S.M., Noll, J.E., Neilsen, P.M., Phua, Y.T., Gabra, H., and Lim, T.M. (2013). Wild-type and mutant p53 mediate cisplatin resistance through interaction and inhibition of active caspase-9. Cell Cycle *12*, 278–288.

Chen, X., Ko, L.J., Jayaraman, L., and Prives, C. (1996). p53 levels, functional domains, and DNA damage determine the extent of the apoptotic response of tumor cells. Genes Dev. *10*, 2438–2451.

Chesi, M., Mirza, N.N., Garbitt, V.M., Sharik, M.E., Dueck, A.C., Asmann, Y.W., Akhmetzyanova, I., Kosiorek, H.E., Calcinotto, A., Riggs, D.L., et al. (2016). IAP antagonists induce anti-tumor immunity in multiple myeloma. Nat. Med. *22*, 1411–1420.

Chiang, C.-Y., Lee, C.-C., Lo, S.-Y., Wang, A.H.-J., and Tsai, H.-J. (2015). Chromophore Deprotonation State Alters the Optical Properties of Blue Chromoprotein. PLoS One *10*, e0134108.

Chu, J., Haynes, R.D., Corbel, S.Y., Li, P., González-González, E., Burg, J.S., Ataie, N.J., Lam, A.J., Cranfill, P.J., Baird, M.A., et al. (2014). Non-invasive intravital imaging of cellular differentiation with a bright red-excitable fluorescent protein. Nat. Methods *11*, 572–578.

Costantini, L.M., Fossati, M., Francolini, M., and Snapp, E.L. (2012). Assessing the Tendency of Fluorescent Proteins to Oligomerize Under Physiologic Conditions. Traffic *13*, 643–649.

Van de Craen, M., Declercq, W., Van den brande, I., Fiers, W., and Vandenabeele, P. (1999). The proteolytic procaspase activation network: an in vitro analysis. Cell Death Differ. *6*, 1117–1124.

Cranfill, P.J., Sell, B.R., Baird, M.A., Allen, J.R., Lavagnino, Z., de Gruiter, H.M., Kremers, G.-J., Davidson, M.W., Ustione, A., and Piston, D.W. (2016). Quantitative assessment of fluorescent proteins. Nat. Methods *13*, 557–562.

Crusz, S.M., and Balkwill, F.R. (2015). Inflammation and cancer: advances and new agents. Nat. Rev. Clin. Oncol. *12*, 584–596.

Day, R.N., and Davidson, M.W. (2012). Fluorescent proteins for FRET microscopy: Monitoring protein interactions in living cells. BioEssays *34*, 341–350.

Degterev, A., and Yuan, J. (2008). Expansion and evolution of cell death programmes. Nat. Rev. Mol. Cell Biol. *9*, 378–390.

Delgado, M.E., Olsson, M., Lincoln, F.A., Zhivotovsky, B., and Rehm, M. (2013). Determining the contributions of caspase-2, caspase-8 and effector caspases to intracellular VDVADase activities during apoptosis initiation and execution. Biochim. Biophys. Acta *1833*, 2279–2292.

Demeautis, C., Sipieter, F., Roul, J., Chapuis, C., Padilla-Parra, S., Riquet, F.B., and Tramier, M. (2017). Multiplexing PKA and ERK1&2 kinases FRET biosensors in living cells using single excitation wavelength dual colour FLIM. Sci. Rep. *7*, 41026.

Digman, M.A., Caiolfa, V.R., Zamai, M., and Gratton, E. (2008). The phasor approach to fluorescence lifetime imaging analysis. Biophys. J. *94*, L14-6.

Ding, Y., Ai, H.W., Hoi, H., and Campbell, R.E. (2011). Forster resonance energy transfer-based biosensors for multiparameter ratiometric imaging of ca(2+) dynamics and caspase-3 activity in single cells. Anal Chem *83*, 9687–9693.

Ding, Y., Li, J., Enterina, J.R., Shen, Y., Zhang, I., Tewson, P.H., Mo, G.C.H., Zhang, J., Quinn, A.M., Hughes, T.E., et al. (2015). Ratiometric biosensors based on dimerization-dependent fluorescent protein exchange. Nat. Methods *12*, 195–198.

DiPilato, L.M., Cheng, X., and Zhang, J. (2004). Fluorescent indicators of cAMP and Epac activation reveal differential dynamics of cAMP signaling within discrete subcellular compartments. Proc. Natl. Acad. Sci. U. S. A.

101, 16513–16518.

Dobson, C.M. (2004). Principles of protein folding, misfolding and aggregation. Semin. Cell Dev. Biol. *15*, 3–16.

Dorstyn, L., Puccini, J., Wilson, C.H., Shalini, S., Nicola, M., Moore, S., and Kumar, S. (2012). Caspase-2 deficiency promotes aberrant DNA-damage response and genetic instability. Cell Death Differ. *19*, 1288–1298.

Duale, N., Lindeman, B., Komada, M., Olsen, A.-K., Andreassen, A., Soderlund, E.J., and Brunborg, G. (2007). Molecular portrait of cisplatin induced response in human testis cancer cell lines based on gene expression profiles. Mol. Cancer *6*, 53.

Dulaney, C., Marcrom, S., Stanley, J., and Yang, E.S. (2017). Poly(ADP-ribose) polymerase activity and inhibition in cancer. Semin. Cell Dev. Biol. *63*, 144–153.

Eckelman, B.P., and Salvesen, G.S. (2006). The Human Anti-apoptotic Proteins cIAP1 and cIAP2 Bind but Do Not Inhibit Caspases. J. Biol. Chem. *281*, 3254–3260.

Edgington, L.E., Berger, A.B., Blum, G., Albrow, V.E., Paulick, M.G., Lineberry, N., and Bogyo, M. (2009). Noninvasive optical imaging of apoptosis by caspase-targeted activity-based probes. Nat. Med. *15*, 967–973.

Edgington, L.E., van Raam, B.J., Verdoes, M., Wierschem, C., Salvesen, G.S., and Bogyo, M. (2012). An optimized activity-based probe for the study of caspase-6 activation. Chem. Biol. *19*, 340–352.

Eguchi, Y., Shimizu, S., and Tsujimoto, Y. (1997). Intracellular ATP levels determine cell death fate by apoptosis or necrosis. Cancer Res. *57*, 1835–1840.

Esposito, A., Oggier, T., Gerritsen, H., Lustenberger, F., and Wouters, F. (2005). All-solid-state lock-in imaging for wide-field fluorescence lifetime sensing. Opt. Express *13*, 9812–9821.

Esposito, A., Popleteeva, M., and Venkitaraman, A.R. (2013). Maximizing the biochemical resolving power of fluorescence microscopy. PLoS One *8*, e77392.

Evers, T.H., van Dongen, E.M.W.M., Faesen, A.C., Meijer, E.W., and Merkx, M. (2006). Quantitative Understanding of the Energy Transfer between Fluorescent Proteins Connected via Flexible Peptide Linkers. Biochemistry *45*, 13183–13192.

Fatokun, A.A., Dawson, V.L., and Dawson, T.M. (2014). Parthanatos: mitochondrial-linked mechanisms and therapeutic opportunities. Br. J. Pharmacol. *171*, 2000–2016.

Fava, L.L., Bock, F.J., Geley, S., and Villunger, A. (2012). Caspase-2 at a glance. J. Cell Sci. *125*, 5911–5915.

Feoktistova, M., Geserick, P., Kellert, B., Dimitrova, D.P., Langlais, C., Hupe, M., Cain, K., MacFarlane, M., Häcker, G., and Leverkus, M. (2011). cIAPs block Ripoptosome formation, a RIP1/caspase-8 containing intracellular cell death complex differentially regulated by cFLIP isoforms. Mol. Cell *43*, 449–463.

Filonov, G.S., Piatkevich, K.D., Ting, L.-M., Zhang, J., Kim, K., and Verkhusha, V. V (2011). Bright and stable near-infrared fluorescent protein for in vivo imaging. Nat. Biotechnol. *29*, 757–761.

Förster, T. (1948). Zwischenmolekulare Energiewanderung und Fluoreszenz. Ann. Phys. *437*, 55–75.

Fradkov, A.F., Verkhusha, V. V, Staroverov, D.B., Bulina, M.E., Yanushevich, Y.G., Martynov, V.I., Lukyanov, S., and Lukyanov, K.A. (2002). Far-red fluorescent tag for protein labelling. Biochem. J. *368*, 17–21.

Fuertes, M., Castilla, J., Nguewa, P., Alonso, C., and Perez, J. (2004). Novel Concepts in the Development of Platinum Antitumour Drugs: An Update. Med. Chem. Rev. - Online *1*, 187–198.

Fuertes, M.A., Castilla, J., Alonso, C., and Pérez, J.M. (2003). Cisplatin biochemical mechanism of action: from cytotoxicity to induction of cell death through interconnections between apoptotic and necrotic pathways. Curr. Med. Chem. *10*, 257–266.

Fulda, S. (2015). Promises and Challenges of Smac Mimetics as Cancer Therapeutics. Clin. Cancer Res. *21*, 5030–5036.

Fulda, S., and Vucic, D. (2012). Targeting IAP proteins for therapeutic intervention in cancer. Nat. Rev. Drug Discov.

11, 109–124.

Galluzzi, L., Vitale, I., Abrams, J.M., Alnemri, E.S., Baehrecke, E.H., Blagosklonny, M. V, Dawson, T.M., Dawson, V.L., El-Deiry, W.S., Fulda, S., et al. (2012). Molecular definitions of cell death subroutines: recommendations of the Nomenclature Committee on Cell Death 2012. Cell Death Differ. *19*, 107–120.

Galperin, E., Verkhusha, V. V, and Sorkin, A. (2004). Three-chromophore FRET microscopy to analyze multiprotein interactions in living cells. Nat. Methods *1*, 209–217.

Ganesan, S., Ameer-Beg, S.M., Ng, T.T., Vojnovic, B., and Wouters, F.S. (2006). A dark yellow fluorescent protein (YFP)-based Resonance Energy-Accepting Chromoprotein (REACh) for Forster resonance energy transfer with GFP. Proc Natl Acad Sci U S A *103*, 4089–4094.

Garcia-Calvo, M., Peterson, E.P., Rasper, D.M., Vaillancourt, J.P., Zamboni, R., Nicholson, D.W., and Thornberry, N.A. (1999). Purification and catalytic properties of human caspase family members. Cell Death Differ. *6*, 362–369.

Gascoigne, K.E., and Taylor, S.S. (2008). Cancer cells display profound intra- and interline variation following prolonged exposure to antimitotic drugs. Cancer Cell *14*, 111–122.

Goldstein, J.C., Kluck, R.M., and Green, D.R. (2000). A single cell analysis of apoptosis. Ordering the apoptotic phenotype. Ann. N. Y. Acad. Sci. *926*, 132–141.

Gong, Y.-N., Guy, C., Olauson, H., Becker, J.U., Yang, M., Fitzgerald, P., Linkermann, A., and Green, D.R. (2017). ESCRT-III Acts Downstream of MLKL to Regulate Necroptotic Cell Death and Its Consequences. Cell *169*, 286–300.e16.

Gonzalez, V.M., Fuertes, M.A., Alonso, C., and Perez, J.M. (2001). Is cisplatin-induced cell death always produced by apoptosis? Mol. Pharmacol. *59*, 657–663.

Gorgoulis, V.G., Vassiliou, L.-V.F., Karakaidos, P., Zacharatos, P., Kotsinas, A., Liloglou, T., Venere, M., Ditullio, R.A., Kastrinakis, N.G., Levy, B., et al. (2005). Activation of the DNA damage checkpoint and genomic instability in human precancerous lesions. Nature *434*, 907–913.

Grant, D.M., Zhang, W., McGhee, E.J., Bunney, T.D., Talbot, C.B., Kumar, S., Munro, I., Dunsby, C., Neil, M.A.A., Katan, M., et al. (2008). Multiplexed FRET to Image Multiple Signaling Events in Live Cells. Biophys. J. *95*, L69–L71.

Greaves, M., and Maley, C.C. (2012). Clonal evolution in cancer. Nature *481*, 306–313.

Grecco, H.E., Imtiaz, S., and Zamir, E. (2016). Multiplexed imaging of intracellular protein networks. Cytom. Part A *89*, 761–775.

Grünberg, R., Burnier, J. V, Ferrar, T., Beltran-Sastre, V., Stricher, F., van der Sloot, A.M., Garcia-Olivas, R., Mallabiabarrena, A., Sanjuan, X., Zimmermann, T., et al. (2013). Engineering of weak helper interactions for high-efficiency FRET probes. Nat. Methods *10*, 1021–1027.

Guan, Y., Meurer, M., Raghavan, S., Rebane, A., Lindquist, J.R., Santos, S., Kats, I., Davidson, M.W., Mazitschek, R., Hughes, T.E., et al. (2015). Live Cell Multi-Photon Fluorescence Correlation Spectroscopy with an Improved Large Stokes Shift Fluorescent Protein. Mol. Biol. Cell.

Guchelaar, H.J., Vermes, I., Koopmans, R.P., Reutelingsperger, C.P., and Haanen, C. (1998). Apoptosis- and necrosis-inducing potential of cladribine, cytarabine, cisplatin, and 5-fluorouracil in vitro: a quantitative pharmacodynamic model. Cancer Chemother. Pharmacol. *42*, 77–83.

Halazonetis, T.D., Gorgoulis, V.G., and Bartek, J. (2008). An oncogene-induced DNA damage model for cancer development. Science *319*, 1352–1355.

Henkels, K.M., and Turchi, J.J. (1997). Induction of apoptosis in cisplatin-sensitive and -resistant human ovarian cancer cell lines. Cancer Res. *57*, 4488–4492.

Hense, A., Prunsche, B., Gao, P., Ishitsuka, Y., Nienhaus, K., and Ulrich Nienhaus, G. (2015). Monomeric Garnet, a far-red fluorescent protein for live-cell STED imaging. Sci. Rep. *5*, 18006.

Ho, L.H., Taylor, R., Dorstyn, L., Cakouros, D., Bouillet, P., and Kumar, S. (2009). A tumor suppressor function for

caspase-2. Proc. Natl. Acad. Sci. U. S. A. *106*, 5336–5341.

Holohan, C., Van Schaeybroeck, S., Longley, D.B., and Johnston, P.G. (2013). Cancer drug resistance: an evolving paradigm. Nat. Rev. Cancer *13*, 714–726.

Huang, S. (2013). Genetic and non-genetic instability in tumor progression: link between the fitness landscape and the epigenetic landscape of cancer cells. Cancer Metastasis Rev.

Hussner, J., Ameling, S., Hammer, E., Herzog, S., Steil, L., Schwebe, M., Niessen, J., Schroeder, H.W.S., Kroemer, H.K., Ritter, C.A., et al. (2012). Regulation of Interferon-Inducible Proteins by Doxorubicin via Interferon γ-Janus Tyrosine Kinase-Signal Transducer and Activator of Transcription Signaling in Tumor Cells. Mol. Pharmacol. *81*.

Ichim, G., Lopez, J., Ahmed, S.U.U., Muthalagu, N., Giampazolias, E., Delgado, M.E.E., Haller, M., Riley, J.S.S., Mason, S.M.M., Athineos, D., et al. (2015). Limited Mitochondrial Permeabilization Causes DNA Damage and Genomic Instability in the Absence of Cell Death. Mol. Cell *57*, 860–872.

Imamura, H., Nhat, K.P.H., Togawa, H., Saito, K., Iino, R., Kato-Yamada, Y., Nagai, T., and Noji, H. (2009). Visualization of ATP levels inside single living cells with fluorescence resonance energy transfer-based genetically encoded indicators. Proc. Natl. Acad. Sci. U. S. A. *106*, 15651–15656.

Inoue, S., Browne, G., Melino, G., and Cohen, G.M. (2009). Ordering of caspases in cells undergoing apoptosis by the intrinsic pathway. Cell Death Differ. *16*, 1053–1061.

Jackson, S.P., and Bartek, J. (2009). The DNA-damage response in human biology and disease. Nature *461*, 1071–1078.

Jeon, Y.J., Jo, M.G., Yoo, H.M., Hong, S.-H., Park, J.-M., Ka, S.H., Oh, K.H., Seol, J.H., Jung, Y.K., and Chung, C.H. (2012). Chemosensitivity is controlled by p63 modification with ubiquitin-like protein ISG15. J. Clin. Invest. *122*, 2622–2636.

Jørgensen, C., and Linding, R. (2010). Simplistic pathways or complex networks? Curr. Opin. Genet. Dev. *20*, 15–22.

Julien, O., and Wells, J.A. (2017). Caspases and their substrates. Cell Death Differ.

Kandpal, R., Saviola, B., and Felton, J. (2009). The era of 'omics unlimited. Biotechniques *46*, 351–352, 354–355.

Katayama, H., Yamamoto, A., Mizushima, N., Yoshimori, T., and Miyawaki, A. (2008). GFP-like proteins stably accumulate in lysosomes. Cell Struct. Funct. *33*, 1–12.

Kawai, H., Suzuki, T., Kobayashi, T., Sakurai, H., Ohata, H., Honda, K., Momose, K., Namekata, I., Tanaka, H., Shigenobu, K., et al. (2005). Simultaneous real-time detection of initiator- and effector-caspase activation by double fluorescence resonance energy transfer analysis. J. Pharmacol. Sci. *97*, 361–368.

Kelland, L.R. (1993). New platinum antitumor complexes. Crit. Rev. Oncol. Hematol. *15*, 191–219.

Kennedy, M.J., Hughes, R.M., Peteya, L.A., Schwartz, J.W., Ehlers, M.D., and Tucker, C.L. (2010). Rapid blue-light-mediated induction of protein interactions in living cells. Nat Methods *7*, 973–975.

Kharbanda, S., Ren, R., Pandey, P., Shafman, T.D., Feller, S.M., Weichselbaum, R.R., and Kufe, D.W. (1995). Activation of the c-Abl tyrosine kinase in the stress response to DMA-damaging agents. Nature *376*, 785–788.

Kholodenko, B.N., Hancock, J.F., and Kolch, W. (2010). Signalling ballet in space and time. Nat. Rev. Mol. Cell Biol. *11*, 414–426.

Kim, J.H., Lee, S.-R., Li, L.-H., Park, H.-J., Park, J.-H., Lee, K.Y., Kim, M.-K., Shin, B.A., and Choi, S.-Y. (2011). High cleavage efficiency of a 2A peptide derived from porcine teschovirus-1 in human cell lines, zebrafish and mice. PLoS One *6*, e18556.

Kitevska, T., Roberts, S.J., Pantaki-Eimany, D., Boyd, S.E., Scott, F.L., and Hawkins, C.J. (2014). Analysis of the minimal specificity of caspase-2 and identification of Ac-VDTTD-AFC as a caspase-2-selective peptide substrate. Biosci. Rep.

Klarenbeek, J., Goedhart, J., van Batenburg, A., Groenewald, D., and Jalink, K. (2015). Fourth-generation epac-

based FRET sensors for cAMP feature exceptional brightness, photostability and dynamic range: characterization of dedicated sensors for FLIM, for ratiometry and with high affinity. PLoS One *10*, e0122513.

Kocab, A.J., and Duckett, C.S. (2016). Inhibitor of apoptosis proteins as intracellular signaling intermediates. FEBS J. *283*, 221–231.

Kogure, T., Karasawa, S., Araki, T., Saito, K., Kinjo, M., and Miyawaki, A. (2006). A fluorescent variant of a protein from the stony coral Montipora facilitates dual-color single-laser fluorescence cross-correlation spectroscopy. Nat. Biotechnol. *24*, 577–581.

Komatsu, N., Aoki, K., Yamada, M., Yukinaga, H., Fujita, Y., Kamioka, Y., and Matsuda, M. (2011). Development of an optimized backbone of FRET biosensors for kinases and GTPases. Mol. Biol. Cell *22*, 4647–4656.

Kracikova, M., Akiri, G., George, A., Sachidanandam, R., and Aaronson, S.A. (2013). A threshold mechanism mediates p53 cell fate decision between growth arrest and apoptosis. Cell Death Differ. *20*, 576–588.

Kremers, G.-J., Goedhart, J., van Munster, E.B., and Gadella, T.W.J. (2006). Cyan and yellow super fluorescent proteins with improved brightness, protein folding, and FRET Förster radius. Biochemistry *45*, 6570–6580.

Kreso, A., O'Brien, C.A., van Galen, P., Gan, O.I., Notta, F., Brown, A.M.K., Ng, K., Ma, J., Wienholds, E., Dunant, C., et al. (2013). Variable clonal repopulation dynamics influence chemotherapy response in colorectal cancer. Science *339*, 543–548.

van der Krogt, G.N.M., Ogink, J., Ponsioen, B., Jalink, K., and Gadella, T. (2008). A Comparison of Donor-Acceptor Pairs for Genetically Encoded FRET Sensors: Application to the Epac cAMP Sensor as an Example. PLoS One *3*, e1916.

Kumagai, Y., Kamioka, Y., Yagi, S., Matsuda, M., and Kiyokawa, E. (2011). A genetically encoded Forster resonance energy transfer biosensor for two-photon excitation microscopy. Anal Biochem *413*, 192–199.

Kumar, S. (2009). Caspase 2 in apoptosis, the DNA damage response and tumour suppression: enigma no more? Nat. Rev. Cancer *9*, 897–903.

Kunkel, M.T., Ni, Q., Tsien, R.Y., Zhang, J., and Newton, A.C. (2005). Spatio-temporal dynamics of protein kinase B/Akt signaling revealed by a genetically encoded fluorescent reporter. J. Biol. Chem. *280*, 5581–5587.

Kutuk, O., Arisan, E.D., Tezil, T., Shoshan, M.C., and Basaga, H. (2009). Cisplatin overcomes Bcl-2-mediated resistance to apoptosis via preferential engagement of Bak: critical role of Noxa-mediated lipid peroxidation. Carcinogenesis *30*, 1517–1527.

Kuwahara, D., Tsutsumi, K., Oyake, D., Ohta, T., Nishikawa, H., and Koizuka, I. (2003). Inhibition of caspase-9 activity and Apaf-1 expression in cisplatin-resistant head and neck squamous cell carcinoma cells. Auris. Nasus. Larynx *30 Suppl*, S85-8.

Lahav, G., Rosenfeld, N., Sigal, A., Geva-Zatorsky, N., Levine, A.J., Elowitz, M.B., and Alon, U. (2004). Dynamics of the p53-Mdm2 feedback loop in individual cells. Nat. Genet. *36*, 147–150.

Lakhani, S. a, Masud, A., Kuida, K., Porter, G. a, Booth, C.J., Mehal, W.Z., Inayat, I., and Flavell, R. a (2006). Caspases 3 and 7: key mediators of mitochondrial events of apoptosis. Science *311*, 847–851.

Lam, A.J., St-Pierre, F., Gong, Y., Marshall, J.D., Cranfill, P.J., Baird, M.A., McKeown, M.R., Wiedenmann, J., Davidson, M.W., Schnitzer, M.J., et al. (2012). Improving FRET dynamic range with bright green and red fluorescent proteins. Nat. Methods *9*, 1005–1012.

Lassus, P., Opitz-Araya, X., and Lazebnik, Y. (2002). Requirement for caspase-2 in stress-induced apoptosis before mitochondrial permeabilization. Science *297*, 1352–1354.

De Laurenzi, V., and Melino, G. (2000). Evolution of functions within the p53/p63/p73 family. Ann. N. Y. Acad. Sci. *926*, 90–100.

Laviv, T., Kim, B.B., Chu, J., Lam, A.J., Lin, M.Z., and Yasuda, R. (2016). Simultaneous dual-color fluorescence lifetime imaging with novel red-shifted fluorescent proteins. Nat. Methods *13*, 989–992.

Legewie, S., Blüthgen, N., and Herzel, H. (2006). Mathematical modeling identifies inhibitors of apoptosis as

mediators of positive feedback and bistability. PLoS Comput. Biol. *2*, e120.

Leist, M., Single, B., Castoldi, A.F., Kühnle, S., and Nicotera, P. (1997). Intracellular adenosine triphosphate (ATP) concentration: a switch in the decision between apoptosis and necrosis. J. Exp. Med. *185*, 1481–1486.

Lemaire, C., Andréau, K., Souvannavong, V., and Adam, A. (1998). Inhibition of caspase activity induces a switch from apoptosis to necrosis. FEBS Lett. *425*, 266–270.

Lev Bar-Or, R., Maya, R., Segel, L.A., Alon, U., Levine, A.J., and Oren, M. (2000). Generation of oscillations by the p53-Mdm2 feedback loop: a theoretical and experimental study. Proc. Natl. Acad. Sci. U. S. A. *97*, 11250–11255.

Li, D.-U., Arlt, J., Richardson, J., Walker, R., Buts, A., Stoppa, D., Charbon, E., and Henderson, R. (2010). Real-time fluorescence lifetime imaging system with a 32 x 32 0.13microm CMOS low dark-count single-photon avalanche diode array. Opt. Express *18*, 10257–10269.

Li, P., Zhou, L., Zhao, T., Liu, X., Zhang, P., Liu, Y., Zheng, X., and Li, Q. (2017). Caspase-9: structure, mechanisms and clinical application. Oncotarget.

Li, X., Zhang, G., Ngo, N., Zhao, X., Kain, S.R., and Huang, C.C. (1997). Deletions of the Aequorea victoria green fluorescent protein define the minimal domain required for fluorescence. J. Biol. Chem. *272*, 28545–28549.

Liang, H., Esposito, A., De, S., Ber, S., Collin, P., Surana, U., and Venkitaraman, A.R. (2014). Homeostatic control of polo-like kinase-1 engenders non-genetic heterogeneity in G2 checkpoint fidelity and timing. Nat. Commun. *5*, 4048.

Lin, J., Zhang, Z., Yang, J., Zeng, S., Liu, B.F., and Luo, Q. (2006). Real-time detection of caspase-2 activation in a single living HeLa cell during cisplatin-induced apoptosis. J Biomed Opt *11*, 24011.

Lin, M.Z., McKeown, M.R., Ng, H.-L., Aguilera, T.A., Shaner, N.C., Campbell, R.E., Adams, S.R., Gross, L.A., Ma, W., Alber, T., et al. (2009). Autofluorescent proteins with excitation in the optical window for intravital imaging in mammals. Chem. Biol. *16*, 1169–1179.

Lindenburg, L.H., Hessels, A.M., Ebberink, E.H.T.M., Arts, R., and Merkx, M. (2013). Robust Red FRET Sensors Using Self-Associating Fluorescent Domains. ACS Chem. Biol. *8*, 2133–2139.

Liu, J.R., Opipari, A.W., and Tan, L. (2002). Dysfunctional Apoptosome Activation in Ovarian Cancer : Implications for Chemoresistance Dysfunctional Apoptosome Activation in Ovarian Cancer : Implications. Cancer Res. *62*, 924–931.

Llopis, J., McCaffery, J.M., Miyawaki, A., Farquhar, M.G., and Tsien, R.Y. (1998). Measurement of cytosolic, mitochondrial, and Golgi pH in single living cells with green fluorescent proteins. Proc. Natl. Acad. Sci. U. S. A. *95*, 6803–6808.

Lopes, R.B., Gangeswaran, R., McNeish, I.A., Wang, Y., and Lemoine, N.R. (2007). Expression of the IAP protein family is dysregulated in pancreatic cancer cells and is important for resistance to chemotherapy. Int. J. Cancer *120*, 2344–2352.

Los, M., Mozoluk, M., Ferrari, D., Stepczynska, A., Stroh, C., Renz, A., Herceg, Z., Wang, Z.-Q., and Schulze-Osthoff, K. (2002). Activation and caspase-mediated inhibition of PARP: a molecular switch between fibroblast necrosis and apoptosis in death receptor signaling. Mol. Biol. Cell *13*, 978–988.

Luo, K.Q., Yu, V.C., Pu, Y., and Chang, D.C. (2003). Measuring dynamics of caspase-8 activation in a single living HeLa cell during TNFalpha-induced apoptosis. Biochem. Biophys. Res. Commun. *304*, 217–222.

Malladi, S., Challa-Malladi, M., Fearnhead, H.O., and Bratton, S.B. (2009). The Apaf-1*procaspase-9 apoptosome complex functions as a proteolytic-based molecular timer. EMBO J. *28*, 1916–1925.

Manzl, C., Krumschnabel, G., Bock, F., Sohm, B., Labi, V., Baumgartner, F., Logette, E., Tschopp, J., and Villunger, A. (2009). Caspase-2 activation in the absence of PIDDosome formation. J. Cell Biol. *185*, 291–303.

Matsumoto, M., Tsuchida, T., and Kawamoto, K. (1997). Cisplatin-induced cell death in human glioma. Int. J. Oncol. *11*, 1209–1212.

Matt, S., and Hofmann, T.G. (2016). The DNA damage-induced cell death response: a roadmap to kill cancer cells.

Cell. Mol. Life Sci. *73*, 2829–2850.

McStay, G.P., Salvesen, G.S., and Green, D.R. (2008). Overlapping cleavage motif selectivity of caspases: implications for analysis of apoptotic pathways. Cell Death Differ. *15*, 322–331.

Merzlyak, E.M., Goedhart, J., Shcherbo, D., Bulina, M.E., Shcheglov, A.S., Fradkov, A.F., Gaintzeva, A., Lukyanov, K.A., Lukyanov, S., Gadella, T.W.J., et al. (2007). Bright monomeric red fluorescent protein with an extended fluorescence lifetime. Nat. Methods *4*, 555–557.

Micheau, O., Solary, E., Hammann, A., Martin, F., and Dimanche-Boitrel, M.T. (1997). Sensitization of cancer cells treated with cytotoxic drugs to fas-mediated cytotoxicity. J. Natl. Cancer Inst. *89*, 783–789.

Miles, M.A., Kitevska-Ilioski, T., and Hawkins, C.J. (2017). Old and Novel Functions of Caspase-2. In International Review of Cell and Molecular Biology, pp. 155–212.

Miyamoto, A., Miyauchi, H., Kogure, T., Miyawaki, A., Michikawa, T., and Mikoshiba, K. (2015). Apoptosis induction-related cytosolic calcium responses revealed by the dual FRET imaging of calcium signals and caspase-3 activation in a single cell. Biochem. Biophys. Res. Commun. *460*, 82–87.

Miyawaki, A., Llopis, J., Heim, R., McCaffery, J.M., Adams, J.A., Ikura, M., and Tsien, R.Y. (1997). Fluorescent indicators for Ca2+ based on green fluorescent proteins and calmodulin. Nature *388*, 882–887.

Montero, E.I., Pérez, J.M., Schwartz, A., Fuertes, M.A., Malinge, J.M., Alonso, C., Leng, M., and Navarro-Ranninger, C. (2002). Apoptosis induction and DNA interstrand cross-link formation by cytotoxic trans-[PtCl2(NH(CH3)2)(NHCH(CH3)2) : cross-linking between d(G) and complementary d(C) within oligonucleotide duplexes. Chembiochem *3*, 61–67.

Mueller, T., Voigt, W., Simon, H., Fruehauf, A., Bulankin, A., Grothey, A., and Schmoll, H.-J. (2003). Failure of activation of caspase-9 induces a higher threshold for apoptosis and cisplatin resistance in testicular cancer. Cancer Res. *63*, 513–521.

Müller, M., Wilder, S., Bannasch, D., Israeli, D., Lehlbach, K., Li-Weber, M., Friedman, S.L., Galle, P.R., Stremmel, W., Oren, M., et al. (1998). p53 activates the CD95 (APO-1/Fas) gene in response to DNA damage by anticancer drugs. J. Exp. Med. *188*, 2033–2045.

Murakoshi, H., Lee, S.J., and Yasuda, R. (2008). Highly sensitive and quantitative FRET-FLIM imaging in single dendritic spines using improved non-radiative YFP. Brain Cell Biol *36*, 31–42.

Murakoshi, H., Shibata, A.C.E., Nakahata, Y., and Nabekura, J. (2015). A dark green fluorescent protein as an acceptor for measurement of Förster resonance energy transfer. Sci. Rep. *5*, 15334.

Nagai, T., Yamada, S., Tominaga, T., Ichikawa, M., and Miyawaki, A. (2004). Expanded dynamic range of fluorescent indicators for Ca(2+) by circularly permuted yellow fluorescent proteins. Proc. Natl. Acad. Sci. U. S. A. *101*, 10554–10559.

Nakagawa, Y., Abe, S., Kurata, M., Hasegawa, M., Yamamoto, K., Inoue, M., Takemura, T., Suzuki, K., and Kitagawa, M. (2006). IAP family protein expression correlates with poor outcome of multiple myeloma patients in association with chemotherapy-induced overexpression of multidrug resistance genes. Am. J. Hematol. *81*, 824–831.

Nakahata, Y., Nabekura, J., and Murakoshi, H. (2016). Dual observation of the ATP-evoked small GTPase activation and Ca2+ transient in astrocytes using a dark red fluorescent protein. Sci. Rep. *6*, 39564.

Newman, R.H., Fosbrink, M.D., and Zhang, J. (2011). Genetically encodable fluorescent biosensors for tracking signaling dynamics in living cells. Chem. Rev. *111*, 3614–3666.

Niino, Y., Hotta, K., and Oka, K. (2009). Simultaneous live cell imaging using dual FRET sensors with a single excitation light. PLoS One *4*, e6036.

Niino, Y., Hotta, K., and Oka, K. (2010). Blue fluorescent cGMP sensor for multiparameter fluorescence imaging. PLoS One *5*, e9164.

Oliver, T.G., Meylan, E., Chang, G.P., Xue, W., Burke, J.R., Humpton, T.J., Hubbard, D., Bhutkar, A., and Jacks, T. (2011). Caspase-2-mediated cleavage of Mdm2 creates a p53-induced positive feedback loop. Mol Cell *43*, 57–

71.

Olsson, M., Vakifahmetoglu, H., Abruzzo, P.M., Hogstrand, K., Grandien, A., and Zhivotovsky, B. (2009). DISC-mediated activation of caspase-2 in DNA damage-induced apoptosis. Oncogene *28*, 1949–1959.

Olsson, M., Forsberg, J., and Zhivotovsky, B. (2014). Caspase-2: the reinvented enzyme. Oncogene.

Ouyang, M., Huang, H., Shaner, N.C., Remacle, A.G., Shiryaev, S.A., Strongin, A.Y., Tsien, R.Y., and Wang, Y. (2010). Simultaneous visualization of protumorigenic Src and MT1-MMP activities with fluorescence resonance energy transfer. Cancer Res. *70*, 2204–2212.

Paek, A.L., Liu, J.C., Loewer, A., Forrester, W.C., and Lahav, G. (2016). Cell-to-Cell Variation in p53 Dynamics Leads to Fractional Killing. Cell.

Parrish, A.B., Freel, C.D., and Kornbluth, S. (2013). Cellular mechanisms controlling caspase activation and function. Cold Spring Harb. Perspect. Biol. *5*, a008672.

Pawson, T., and Linding, R. (2008). Network medicine. FEBS Lett. *582*, 1266–1270.

Pérez, J.M., Quiroga, A.G., Montero, E.I., Alonso, C., and Navarro-Ranninger, C. (1999). A cycloplatinated compound of p-isopropylbenzaldehyde thiosemicarbazone and its chloro-bridged derivative induce apoptosis in cis-DDP resistant cells which overexpress the H-ras oncogene. J. Inorg. Biochem. *73*, 235–243.

Pestell, K.E., Hobbs, S.M., Titley, J.C., Kelland, L.R., and Walton, M.I. (2000). Effect of p53 status on sensitivity to platinum complexes in a human ovarian cancer cell line. Mol. Pharmacol. *57*, 503–511.

Petersen, S.L., Wang, L., Yalcin-Chin, A., Li, L., Peyton, M., Minna, J., Harran, P., and Wang, X. (2007). Autocrine TNFalpha signaling renders human cancer cells susceptible to Smac-mimetic-induced apoptosis. Cancer Cell *12*, 445–456.

Pettikiriarachchi, A., Gong, L., Perugini, M.A., Devenish, R.J., and Prescott, M. (2012). Ultramarine, a chromoprotein acceptor for Förster resonance energy transfer. PLoS One *7*, e41028.

Peyker, A., Rocks, O., and Bastiaens, P.I.H. (2005). Imaging activation of two Ras isoforms simultaneously in a single cell. Chembiochem *6*, 78–85.

Piljic, A., and Schultz, C. (2008). Simultaneous recording of multiple cellular events by FRET. ACS Chem. Biol. *3*, 156–160.

Piston, D.W., and Kremers, G.-J. (2007). Fluorescent protein FRET: the good, the bad and the ugly. Trends Biochem. Sci. *32*, 407–414.

Popleteeva, M., Haas, K.T., Stoppa, D., Pancheri, L., Gasparini, L., Kaminski, C.F., Cassidy, L.D., Venkitaraman, A.R., and Esposito, A. (2015). Fast and simple spectral FLIM for biochemical and medical imaging. Opt. Express *23*, 23511–23525.

Puccini, J., Shalini, S., Voss, A.K., Gatei, M., Wilson, C.H., Hiwase, D.K., Lavin, M.F., Dorstyn, L., and Kumar, S. (2013a). Loss of caspase-2 augments lymphomagenesis and enhances genomic instability in Atm-deficient mice. Proc. Natl. Acad. Sci. U. S. A.

Puccini, J., Dorstyn, L., and Kumar, S. (2013b). Caspase-2 as a tumour suppressor. Cell Death Differ.

Purvis, J.E., and Lahav, G. (2013). Encoding and decoding cellular information through signaling dynamics. Cell *152*, 945–956.

Qin, Q., Zuo, Y., Yang, X., Lu, J., Zhan, L., Xu, L., Zhang, C., Zhu, H., Liu, J., Liu, Z., et al. (2014). Smac mimetic compound LCL161 sensitizes esophageal carcinoma cells to radiotherapy by inhibiting the expression of inhibitor of apoptosis protein. Tumour Biol. *35*, 2565–2574.

Ramakrishnan, V., Painuly, U., Kimlinger, T., Haug, J., Rajkumar, S. V, and Kumar, S. (2014). Inhibitor of apoptosis proteins as therapeutic targets in multiple myeloma. Leukemia *28*, 1519–1528.

Raspe, M., Kedziora, K.M., van den Broek, B., Zhao, Q., de Jong, S., Herz, J., Mastop, M., Goedhart, J., Gadella, T.W.J., Young, I.T., et al. (2016). siFLIM: single-image frequency-domain FLIM provides fast and photon-efficient

lifetime data. Nat. Methods *13*, 501–504.

Reya, T., Morrison, S.J., Clarke, M.F., and Weissman, I.L. (2001). Stem cells, cancer, and cancer stem cells. Nature *414*, 105–111.

Robertson, J.D., Enoksson, M., Suomela, M., Zhivotovsky, B., and Orrenius, S. (2002). Caspase-2 acts upstream of mitochondria to promote cytochrome c release during etoposide-induced apoptosis. J. Biol. Chem. *277*, 29803–29809.

Rodriguez, J., and Lazebnik, Y. (1999). Caspase-9 and APAF-1 form an active holoenzyme. Genes Dev. *13*, 3179–3184.

Rodriguez, E.A., Campbell, R.E., Lin, J.Y., Lin, M.Z., Miyawaki, A., Palmer, A.E., Shu, X., Zhang, J., and Tsien, R.Y. (2017). The Growing and Glowing Toolbox of Fluorescent and Photoactive Proteins. Trends Biochem. Sci. *42*, 111–129.

Roesch, A., Fukunaga-Kalabis, M., Schmidt, E.C., Zabierowski, S.E., Brafford, P.A., Vultur, A., Basu, D., Gimotty, P., Vogt, T., and Herlyn, M. (2010). A Temporarily Distinct Subpopulation of Slow-Cycling Melanoma Cells Is Required for Continuous Tumor Growth. Cell *141*, 583–594.

Roos, W.P., Thomas, A.D., and Kaina, B. (2015). DNA damage and the balance between survival and death in cancer biology. Nat. Rev. Cancer *16*, 20–33.

Roux, J., Hafner, M., Bandara, S., Sims, J.J., Hudson, H., Chai, D., and Sorger, P.K. (2015). Fractional killing arises from cell-to-cell variability in overcoming a caspase activity threshold. Mol. Syst. Biol.

Rusanov, A.L., Ivashina, T. V, Vinokurov, L.M., Fiks II, Orlova, A.G., Turchin, I. V, Meerovich, I.G., Zherdeva, V. V, and Savitsky, A.P. (2010). Lifetime imaging of FRET between red fluorescent proteins. J Biophotonics *3*, 774–783.

Ryu, H., Chung, M., Dobrzyński, M., Fey, D., Blum, Y., Lee, S.S., Peter, M., Kholodenko, B.N., Jeon, N.L., and Pertz, O. (2015). Frequency modulation of ERK activation dynamics rewires cell fate. Mol. Syst. Biol. *11*, 838.

Sample, V., Mehta, S., and Zhang, J. (2014). Genetically encoded molecular probes to visualize and perturb signaling dynamics in living biological systems. J. Cell Sci. *127*, 1151–1160.

Sanford, L., and Palmer, A. (2017). Recent Advances in Development of Genetically Encoded Fluorescent Sensors. In Methods in Enzymology, pp. 1–49.

Santos, S.D.M., Verveer, P.J., and Bastiaens, P.I.H. (2007). Growth factor-induced MAPK network topology shapes Erk response determining PC-12 cell fate. Nat. Cell Biol. *9*, 324–330.

Schmid, J., Dussmann, H., Boukes, G.J., Flanagan, L., Lindner, A.U., O'Connor, C.L., Rehm, M., Prehn, J.H.M., and Huber, H.J. (2012). Systems analysis of cancer cell heterogeneity in caspase-dependent apoptosis subsequent to mitochondrial outer membrane permeabilization. J. Biol. Chem. *287*, 41546–41559.

Schwartz, P.S., and Waxman, D.J. (2001). Cyclophosphamide induces caspase 9-dependent apoptosis in 9L tumor cells. Mol. Pharmacol. *60*, 1268–1279.

Segal-Bendirdjian, E., and Jacquemin-Sablon, A. (1995). Cisplatin resistance in a murine leukemia cell line is associated with a defective apoptotic process. Exp. Cell Res. *218*, 201–212.

Sergeeva, T.F., Shirmanova, M. V., Zlobovskaya, O.A., Gavrina, A.I., Dudenkova, V. V., Lukina, M.M., Lukyanov, K.A., and Zagaynova, E. V. (2017). Relationship between intracellular pH, metabolic co-factors and caspase-3 activation in cancer cells during apoptosis. Biochim. Biophys. Acta - Mol. Cell Res. *1864*, 604–611.

Shalini, S., Dorstyn, L., Dawar, S., and Kumar, S. (2014). Old, new and emerging functions of caspases. Cell Death Differ. 1–14.

Shaner, N.C., Campbell, R.E., Steinbach, P.A., Giepmans, B.N.G., Palmer, A.E., and Tsien, R.Y. (2004). Improved monomeric red, orange and yellow fluorescent proteins derived from Discosoma sp. red fluorescent protein. Nat. Biotechnol. *22*, 1567–1572.

Shaner, N.C., Steinbach, P.A., and Tsien, R.Y. (2005). A guide to choosing fluorescent proteins. Nat Methods *2*, 905–909.

Shankaran, H., Ippolito, D.L., Chrisler, W.B., Resat, H., Bollinger, N., Opresko, L.K., and Wiley, H.S. (2009). Rapid and sustained nuclear-cytoplasmic ERK oscillations induced by epidermal growth factor. Mol. Syst. Biol. *5*, 332.

Sharma, S. V, Lee, D.Y., Li, B., Quinlan, M.P., Takahashi, F., Maheswaran, S., McDermott, U., Azizian, N., Zou, L., Fischbach, M.A., et al. (2010). A Chromatin-Mediated Reversible Drug-Tolerant State in Cancer Cell Subpopulations. Cell *141*, 69–80.

Shcherbakova, D.M., and Verkhusha, V. V (2013). Near-infrared fluorescent proteins for multicolor in vivo imaging. Nat. Methods *10*, 751–754.

Shcherbakova, D.M., Hink, M. a, Joosen, L., Gadella, T.W.J., and Verkhusha, V. V (2012). An orange fluorescent protein with a large Stokes shift for single-excitation multicolor FCCS and FRET imaging. J. Am. Chem. Soc. *134*, 7913–7923.

Shcherbakova, D.M., Baloban, M., Emelyanov, A. V., Brenowitz, M., Guo, P., and Verkhusha, V. V. (2016). Bright monomeric near-infrared fluorescent proteins as tags and biosensors for multiscale imaging. Nat. Commun. *7*, 12405.

Shimozono, S., Hosoi, H., Mizuno, H., Fukano, T., Tahara, T., and Miyawaki, A. (2006). Concatenation of cyan and yellow fluorescent proteins for efficient resonance energy transfer. Biochemistry *45*, 6267–6271.

Shu, X., Royant, A., Lin, M.Z., Aguilera, T.A., Lev-Ram, V., Steinbach, P.A., and Tsien, R.Y. (2009). Mammalian expression of infrared fluorescent proteins engineered from a bacterial phytochrome. Science *324*, 804–807.

Sidi, S., Sanda, T., Kennedy, R.D., Hagen, A.T., Jette, C. a., Hoffmans, R., Pascual, J., Imamura, S., Kishi, S., Amatruda, J.F., et al. (2008). Chk1 suppresses a caspase-2 apoptotic response to DNA damage that bypasses p53, Bcl-2, and caspase-3. Cell *133*, 864–877.

Speelmans, G., Staffhorst, R.W., Versluis, K., Reedijk, J., and de Kruijff, B. (1997). Cisplatin complexes with phosphatidylserine in membranes. Biochemistry *36*, 10545–10550.

Spencer, S.L., and Sorger, P.K. (2011). Measuring and modeling apoptosis in single cells. Cell *144*, 926–939.

Spencer, A., Yoon, S.-S., Harrison, S.J., Morris, S.R., Smith, D.A., Brigandi, R.A., Gauvin, J., Kumar, R., Opalinska, J.B., and Chen, C. (2014). The novel AKT inhibitor afuresertib shows favorable safety, pharmacokinetics, and clinical activity in multiple myeloma. Blood *124*, 2190–2195.

Spencer, S.L., Gaudet, S., Albeck, J.G., Burke, J.M., and Sorger, P.K. (2009). Non-genetic origins of cell-to-cell variability in TRAIL-induced apoptosis. Nature *459*, 428–432.

Stennicke, H.R., Renatus, M., Meldal, M., and Salvesen, G.S. (2000). Internally quenched fluorescent peptide substrates disclose the subsite preferences of human caspases 1, 3, 6, 7 and 8. Biochem. J. *350 Pt 2*, 563–568.

Stepanenko, O. V, Bublikov, G.S., Stepanenko, O. V, Shcherbakova, D.M., Verkhusha, V. V, Turoverov, K.K., and Kuznetsova, I.M. (2014). A knot in the protein structure - probing the near-infrared fluorescent protein iRFP designed from a bacterial phytochrome. FEBS J. *281*, 2284–2298.

Stryer, L., and Haugland, R.P. (1967). Energy transfer: a spectroscopic ruler. Proc. Natl. Acad. Sci. U. S. A. *58*, 719–726.

Su, T., Pan, S., Luo, Q., and Zhang, Z. (2013). Monitoring of dual bio-molecular events using FRET biosensors based on mTagBFP/sfGFP and mVenus/mKOκ fluorescent protein pairs. Biosens. Bioelectron. *46*, 97–101.

Sui, X., Kong, N., Ye, L., Han, W., Zhou, J., Zhang, Q., He, C., and Pan, H. (2014). p38 and JNK MAPK pathways control the balance of apoptosis and autophagy in response to chemotherapeutic agents. Cancer Lett. *344*, 174–179.

Szymczak, A.L., Workman, C.J., Wang, Y., Vignali, K.M., Dilioglou, S., Vanin, E.F., and Vignali, D.A.A. (2004). Correction of multi-gene deficiency in vivo using a single “self-cleaving” 2A peptide-based retroviral vector. Nat. Biotechnol. *22*, 589–594.

Tait, S.W.G., Parsons, M.J., Llambi, F., Bouchier-Hayes, L., Connell, S., Muñoz-Pinedo, C., and Green, D.R. (2010). Resistance to caspase-independent cell death requires persistence of intact mitochondria. Dev. Cell *18*, 802–813.

Tannock, I.F., Lee, C.M., Tunggal, J.K., Cowan, D.S.M., and Egorin, M.J. (2002). Limited Penetration of Anticancer Drugs through Tumor Tissue. Clin. Cancer Res. *8*.

Tantama, M., Martínez-François, J.R., Mongeon, R., and Yellen, G. (2013). Imaging energy status in live cells with a fluorescent biosensor of the intracellular ATP-to-ADP ratio. Nat. Commun. *4*, 2550.

Tay, S., Hughey, J.J., Lee, T.K., Lipniacki, T., Quake, S.R., and Covert, M.W. (2010). Single-cell NF-kappaB dynamics reveal digital activation and analogue information processing. Nature *466*, 267–271.

Tenev, T., Bianchi, K., Darding, M., Broemer, M., Langlais, C., Wallberg, F., Zachariou, A., Lopez, J., MacFarlane, M., Cain, K., et al. (2011). The Ripoptosome, a signaling platform that assembles in response to genotoxic stress and loss of IAPs. Mol. Cell *43*, 432–448.

Terai, T., and Nagano, T. (2013). Small-molecule fluorophores and fluorescent probes for bioimaging. Pfl?gers Arch. - Eur. J. Physiol. *465*, 347–359.

Thornberry, N.A., Rano, T.A., Peterson, E.P., Rasper, D.M., Timkey, T., Garcia-Calvo, M., Houtzager, V.M., Nordstrom, P.A., Roy, S., Vaillancourt, J.P., et al. (1997). A combinatorial approach defines specificities of members of the caspase family and granzyme B. Functional relationships established for key mediators of apoptosis. J. Biol. Chem. *272*, 17907–17911.

To, T.-L., Schepis, A., Ruiz-González, R., Zhang, Q., Yu, D., Dong, Z., Coughlin, S.R., and Shu, X. (2016). Rational Design of a GFP-Based Fluorogenic Caspase Reporter for Imaging Apoptosis In Vivo. Cell Chem. Biol. *23*, 875–882.

Topell, S., Hennecke, J., and Glockshuber, R. (1999). Circularly permuted variants of the green fluorescent protein. FEBS Lett. *457*, 283–289.

Tsien, R.Y. (1998). The green fluorescent protein. Annu. Rev. Biochem. *67*, 509–544.

Tu, S., McStay, G.P., Boucher, L.-M., Mak, T., Beere, H.M., and Green, D.R. (2006). In situ trapping of activated initiator caspases reveals a role for caspase-2 in heat shock-induced apoptosis. Nat. Cell Biol. *8*, 72–77.

Tyas, L., Brophy, V.A., Pope, A., Rivett, A.J., and Tavaré, J.M. (2000). Rapid caspase-3 activation during apoptosis revealed using fluorescence-resonance energy transfer. EMBO Rep. *1*, 266–270.

Vakifahmetoglu, H., Olsson, M., Orrenius, S., and Zhivotovsky, B. (2006). Functional connection between p53 and caspase-2 is essential for apoptosis induced by DNA damage. Oncogene *25*, 5683–5692.

Vakifahmetoglu, H., Olsson, M., Tamm, C., Heidari, N., Orrenius, S., and Zhivotovsky, B. (2008). DNA damage induces two distinct modes of cell death in ovarian carcinomas. Cell Death Differ. *15*, 555–566.

Vakifahmetoglu-Norberg, H., Norberg, E., Perdomo, A.B., Olsson, M., Ciccosanti, F., Orrenius, S., Fimia, G.M., Piacentini, M., and Zhivotovsky, B. (2013). Caspase-2 promotes cytoskeleton protein degradation during apoptotic cell death. Cell Death Dis. *4*, e940.

Varfolomeev, E., Blankenship, J.W., Wayson, S.M., Fedorova, A. V, Kayagaki, N., Garg, P., Zobel, K., Dynek, J.N., Elliott, L.O., Wallweber, H.J.A., et al. (2007a). IAP antagonists induce autoubiquitination of c-IAPs, NF-kappaB activation, and TNFalpha-dependent apoptosis. Cell *131*, 669–681.

Varfolomeev, E., Blankenship, J.W., Wayson, S.M., Fedorova, A. V., Kayagaki, N., Garg, P., Zobel, K., Dynek, J.N., Elliott, L.O., Wallweber, H.J.A., et al. (2007b). IAP Antagonists Induce Autoubiquitination of c-IAPs, NF-κB Activation, and TNFα-Dependent Apoptosis. Cell *131*, 669–681.

Vermes, I., Haanen, C., Steffens-Nakken, H., and Reutelingsperger, C. (1995). A novel assay for apoptosis. Flow cytometric detection of phosphatidylserine expression on early apoptotic cells using fluorescein labelled Annexin V. J. Immunol. Methods *184*, 39–51.

Vince, J.E., Wong, W.W.-L., Khan, N., Feltham, R., Chau, D., Ahmed, A.U., Benetatos, C.A., Chunduru, S.K., Condon, S.M., McKinlay, M., et al. (2007). IAP Antagonists Target cIAP1 to Induce TNFα-Dependent Apoptosis. Cell *131*, 682–693.

Viswanath, V., Wu, Y., Boonplueang, R., Chen, S., Stevenson, F.F., Yantiri, F., Yang, L., Beal, M.F., and Andersen, J.K. (2001). Caspase-9 activation results in downstream caspase-8 activation and bid cleavage in 1-methyl-4-

phenyl-1,2,3,6-tetrahydropyridine-induced Parkinson's disease. J. Neurosci. *21*, 9519–9528.

Vousden, K.H., Prives, C., Yao, J., Patnaik, S., Wang, Q.E., El-Mahdy, M.A., Praetorius-Ibba, M., Wani, A.A., Weng, C., Klibanski, A., et al. (2009). Blinded by the Light: The Growing Complexity of p53. Cell *137*, 413–431.

Wallach, D., Kang, T.-B., Dillon, C.P., and Green, D.R. (2016). Programmed necrosis in inflammation: Toward identification of the effector molecules. Science (80-.). *352*.

Wang, J.Y.J., Gong, J., Costanzo, A., Yang, H.-Q., Melino, G., Kaelin, W.G., and Levrero, M. (1999). The tyrosine kinase c-Abl regulates p73 in apoptotic response to cisplatin-induced DNA damage. Nature *399*, 806–809.

Warren, S.C., Margineanu, A., Katan, M., Dunsby, C., and French, P.M.W. (2015). Homo-FRET Based Biosensors and Their Application to Multiplexed Imaging of Signalling Events in Live Cells. Int. J. Mol. Sci. *16*, 14695–14716.

Watrob, H.M., Pan, C.P., and Barkley, M.D. (2003). Two-step FRET as a structural tool. J. Am. Chem. Soc. *125*, 7336–7343.

Wesierska-Gadek, J., Schloffer, D., Kotala, V., and Horky, M. (2002). Escape of p53 protein from E6-mediated degradation in HeLa cells after cisplatin therapy. Int. J. Cancer *101*, 128–136.

West, A.C., Martin, B.P., Andrews, D.A., Hogg, S.J., Banerjee, A., Grigoriadis, G., Johnstone, R.W., and Shortt, J. (2016). The SMAC mimetic, LCL-161, reduces survival in aggressive MYC-driven lymphoma while promoting susceptibility to endotoxic shock. Oncogenesis *5*, e216.

Woehler, A. (2013). Simultaneous Quantitative Live Cell Imaging of Multiple FRET-Based Biosensors. PLoS One *8*, e61096.

Wu, G.S., and Ding, Z. (2002). Caspase 9 is required for p53-dependent apoptosis and chemosensitivity in a human ovarian cancer cell line. Oncogene *21*, 1–8.

Wu, C.-C., Lee, S., Malladi, S., Chen, M.-D., Mastrandrea, N.J., Zhang, Z., and Bratton, S.B. (2016). The Apaf-1 apoptosome induces formation of caspase-9 homo- and heterodimers with distinct activities. Nat. Commun. *7*, 13565.

Wu, X., Simone, J., Hewgill, D., Siegel, R., Lipsky, P.E., and He, L. (2006). Measurement of two caspase activities simultaneously in living cells by a novel dual FRET fluorescent indicator probe. Cytom. A *69*, 477–486.

Xia, T., Li, N., and Fang, X. (2013). Single-Molecule Fluorescence Imaging in Living Cells. Annu. Rev. Phys. Chem. *64*, 459–480.

Yang, C., Wang, H., Zhang, B., Chen, Y., Zhang, Y., Sun, X., Xiao, G., Nan, K., Ren, H., and Qin, S. (2016). LCL161 increases paclitaxel-induced apoptosis by degrading cIAP1 and cIAP2 in NSCLC. J. Exp. Clin. Cancer Res. *35*, 158.

Yang, J., Wang, L., Yang, F., Luo, H., Xu, L., Lu, J., Zeng, S., and Zhang, Z. (2013). mBeRFP, an Improved Large Stokes Shift Red Fluorescent Protein. PLoS One *8*, e64849.

Yin, Q., Park, H.H., Chung, J.Y., Lin, S.-C., Lo, Y.-C., da Graca, L.S., Jiang, X., and Wu, H. (2006). Caspase-9 holoenzyme is a specific and optimal procaspase-3 processing machine. Mol. Cell *22*, 259–268.

Yu, D., Baird, M.A., Allen, J.R., Howe, E.S., Klassen, M.P., Reade, A., Makhijani, K., Song, Y., Liu, S., Murthy, Z., et al. (2015). A naturally monomeric infrared fluorescent protein for protein labeling in vivo. Nat. Methods.

Zhao, Q., Schelen, B., Schouten, R., van den Oever, R., Leenen, R., van Kuijk, H., Peters, I., Polderdijk, F., Bosiers, J., Raspe, M., et al. (2012). Modulated electron-multiplied fluorescence lifetime imaging microscope: all-solid-state camera for fluorescence lifetime imaging. J. Biomed. Opt. *17*, 126020.

Zhivotovsky, B., and Orrenius, S. (2005). Caspase-2 function in response to DNA damage. Biochem Biophys Res Commun *331*, 859–867.

Zhou, R., Vander Heiden, M.G., and Rudin, C.M. (2002). Genotoxic exposure is associated with alterations in glucose uptake and metabolism. Cancer Res. *62*, 3515–3520.

Zlobovskaya, O.A., Sergeeva, T.F., Shirmanova, M. V, Dudenkova, V. V, Sharonov, G. V, Zagaynova, E. V, and

Lukyanov, K.A. (2016). Genetically encoded far-red fluorescent sensors for caspase-3 activity. Biotechniques *60*, 62–68.